ALMA MATER STUDIORUM
UNIVERSITÀ DI BOLOGNA

DOTTORATO DI RICERCA IN
ASTROFISICA

Ciclo XXXII

Tesi di Dottorato

Exploring interstellar medium conditions in AGN and star forming galaxies with integral field spectroscopy

Presentata da:
Matilde Mingozzi

Supervisore:
Dr. Giovanni Cresci

Coordinatore di Dottorato:
Prof. Francesco Rosario Ferraro

Co-supervisore:
Dr. Filippo Mannucci

Esame finale anno 2020

Settore Concorsuale: 02/C1 – Astronomia, Astrofisica, Fisica della Terra e dei Pianeti
Settore Scientifico Disciplinare: FIS/05 – Astronomia e Astrofisica

ABSTRACT

This thesis has been devoted to a research project selected and funded by INAF (the Italian National Institute for Astrophysics) within the framework of the formal agreement between INAF and the Bologna University for the PhD program in Astrophysics.

The interstellar medium (ISM), made up of ionised, neutral and molecular gas, and interstellar dust, is a fundamental ingredient of galaxy evolution. It is the "primary repository" of galaxies, where star formation (SF) takes place, depositing energy, momentum and chemical enriched material via stellar evolution events (e.g. stellar winds, supernova explosions). ISM properties can be largely influenced also by Active Galactic Nuclei (AGN) activity, that through outflows and jets is capable of heating, compressing and/or removing the gas (feedback). SF and AGN activities are part of the so-called *galaxy baryon cycle*, that encloses a variety of physical processes, driving and shaping galaxy formation and evolution. This Thesis aims at probing and interpreting ISM properties in different galaxy types, including star forming galaxies and AGN hosts, and in different conditions within a galaxy, through the use of integral field spectroscopy (IFS) and the comparison of the observed data with ionisation models.

In this context, I studied the properties and feedback mechanisms in the Measuring AGN under MUSE microscope (MAGNUM) survey. This survey comprises 9 local Seyfert galaxies, observed with the optical integral field spectrograph MUSE at the VLT, and characterised by extended outflows traced by the ionised gas. Specifically, I developed a novel approach based on the gas kinematics to disentangle high velocity gas in the outflow from gas in the disc. This allowed to spatially track the differences in the ISM properties of the two components, revealing the presence of an ionisation structure within the extended outflows that can be interpreted with different photoionisation and shock conditions, and tracing tentative evidence of positive feedback in a galaxy of the sample.

In the second part of this dissertation, I present a project focused on studying sistematically for the first time the impact of the ionisation parameter (i.e. a measure of the ionising photons with respect to the gas density) variations within galaxies on the measurement of metal abundances in the gas phase, using a sample of 2139 star forming galaxies from the integral field unit Mapping Nearby Galaxies at APO (MaNGA) survey. The idea originated from the analysis of MUSE data of a local dwarf galaxy, whose central regions are characterised by a strong star forming activity and a super solar metallicity, that has to be estimated taking into account the ionisation parameter to break any degeneracy and avoid misleading conclusions. Interestingly, this holds true also for the MaNGA sample. This allows to derive reliable gradients of metallicity, ionisation parameter and extinction, and to understand their behaviour as a function of galaxy properties, such as stellar mass.

The final part is dedicated to a project aimed at constraining the properties of molecular gas in nearby Seyfert galaxies, to assess whether and to what extent the radiation produced by the accretion onto the central black hole affects the CO line emission, mainly by comparing data from the millimeter interferometer ALMA and the far infrared satellite Herschel with photoionisation and shock models.

Overall, this Thesis demonstrates the power of multi-wavelength IFS studies to explore in detail the properties of different ISM phases in local galaxies. The use of ISM tracers from optical to submillimeter wavelengths allowed to explore the different processes that affect ISM conditions across both AGN and star forming galaxies, and to assess their impact on the evolution of their hosts. The results obtained represent also a unique test bench for the new generation of photoionisation models, given the unprecedented detail of the analysed data as well as some limitations of current models highlighted in this work.

Contents

Chapter 1

The interstellar medium in local galaxies

A variety of physical processes shape the observed distribution of galaxy properties: some of them account for galaxy growth (e.g., star formation, SF; galaxy merging), while others regulate this growth (e.g., energetic feedback from supernovae, SN and active galactic nuclei, AGN; ultraviolet, UV, radiation background). Indeed the evolution of a galaxy is a matter of synergy among these diverse physical processes. Metal poor gas is accreted from the intergalactic medium (IGM), the dilute reservoir that permeates the space between galaxies (McQuinn, 2016), triggering SF inside the galaxy. However, gas accretion and SF can also be the consequence of major and/or minor mergers. Stellar evolution, via SN explosions and stellar winds, provides chemical enrichment of the gaseous component of galaxies, referred to as the *interstellar medium* (ISM) or the *diffuse matter* (Klessen & Glover, 2016). Part of this enriched gas leaves the galaxy through galactic winds, enriching the circumgalactic medium (CGM), a large gas halo extending by hundreds of kpc in which galaxies are embedded, or the IGM, while the rest is recycled several times, in several stellar generations. Also dust plays a role in the physics of ISM, since it locks and releases metals, being continuously created and destroyed. Finally, the presence of a central AGN can largely influence the properties of the ISM and of the CGM, by heating, compressing and/or removing the gas through AGN-driven winds and jets (feedback). These processes that cause this gas flow in and out of galaxies providing the fuel both for SF and black hole (BH) accretion are known as the *galaxy baryon cycle*. Overall, since the ISM is the primary "repository" of galaxies, the study of its properties can give information on all the processes listed above (Maiolino & Mannucci, 2019).

This Chapter aims at providing a brief description of the ISM composition, and then focuses on the relations between star forming galaxies and metallicity, and on the role played by stellar and AGN feedback on galaxy evolution. Furthermore, it gives a summary of the methods that can be employed to obtain ISM properties (e.g. level of ionisation, temperature, density, metallicity, excitation source, dust extinction) through optical and molecular diagnostics. Finally, it provides an overview of the state-of-the-art of integral field spectroscopy (IFS), underlying its importance in modern astrophysics.

1.1 The ISM composition and gas phases

The ISM is mainly composed by hydrogen (H, $\approx 70\%$) and helium (He, $\approx 28\%$), while all other elements, referred to as *metals* (Z), account for the remaining $\approx 2\%$. Specifically, the primordial nucleosynthesis accounts for the origin of hydrogen, deuterium, the majority of helium and a small fraction of lithium (e.g. Cyburt et al. 2016), while all the other elements are almost entirely produced by stellar nucleosynthesis or by the explosive burning and photodisintegration related to the late stages of stellar evolution (e.g. Maiolino & Mannucci 2019 and reference therein). Matter in the ISM has long been considered to be distributed in diverse, but well-defined phases according to the chemical state of hydrogen (i.e. ionised, neutral or molecular), characterised by different temperatures, densities and ionisation states, that can coexist in approximate pressure equilibrium. The interplay between the different phases is complex, and is driven by the balance of radiative cooling with heating through the transfer of kinetic energy to atoms, molecules and ions, mainly due to radiation from stars and AGN, cosmic-rays, X-rays photons or shocks.

Generally speaking, the gas mass of a galaxy is dominated by neutral atomic gas (H I) or molecular gas (H_2), that are found mainly in the form of dense clouds, filling only $\sim 1-2\%$ of the total volume of the ISM (Klessen & Glover 2016 and references therein). The *neutral gas* is characterised by two different termally stable phases. One consists in a cold ($T \sim 50-100$ K) and dense ($n \sim 20-50$ cm^{-3}) gas, distributed in compact clouds, the so-called *cold neutral medium* (CNM), while a second relates to warm and diffuse gas ($T \sim 6000-8000$ K and $n \sim 0.1$ cm^{-3}), defined as *warm neutral medium* (WNM). Field et al. (1969) demonstrated that the CNM and the WNM could coexist in pressure equilibrium, to account for the H I 21-cm line observation either in absorption and in emission.

The transition between the dense, cold molecular gas and the tenuous, warm ionised gas typically occurs in the so-called photo-dissociation regions (PDRs, see Hollenbach & Tielens 1999 for a review), whose physics and chemistry are completely dominated by far-ultraviolet (FUV) radiation ($6\,\mathrm{eV} < h\nu < 13.6\,\mathrm{eV}$) due to stellar sources, that is not capable of ionising hydrogen anymore (see Fig. 1.1). Specifically, PDRs are bounded on the one side by an ionisation front and on the other by their surface, where the hydrogen is 50% atomic and 50% molecular. Hence, the transitions of H to H_2 and of ionised carbon (C^+) to carbon mono-oxide (CO) occur within PDRs, that enclose all the atomic and 90% of molecular gas (Hollenbach & Tielens, 1999). Alternatively, if the gas is well shielded against FUV photons but is illuminated by a strong flux of X-rays, an X-ray dominated region (XDR) forms (see Maloney et al. 1999 for a review).

The *molecular gas* is settled in giant molecular clouds (GMCs), that have masses in excess of $10^3\,\mathrm{M}_\odot$ and up to $10^6 - 10^7\,\mathrm{M}_\odot$, and a hierarchical structure, that extends from the scale of the cloud[1] ($r \approx 10 - 30\,\mathrm{pc}$) down to overdense and less massive regions ($r \approx 10^{-2}\,\mathrm{pc}$, $M \approx 1\,\mathrm{M}_\odot$), termed clumps and cores, the densest parts where SF occurs. Although H_2 represents the most abundant molecule in the Universe, its detection is very challenging because of the strongly forbidden rotational transitions due to its homopolar nature. The first accessible rotational transition is the $J+2 \rightarrow J$, where J is the rotational quantum number, in the near infrared (NIR, e.g. $J = 2-0$, $\lambda = 28.22\,\mu\mathrm{m}$; $J = 3-1$, $\lambda = 17.04\,\mu\mathrm{m}$; ... $J = 10-8$, $\lambda = 5.05\,\mu\mathrm{m}$). However, this traces only gas strongly heated by intense irradiation or shock waves, which represents only a small fraction of the overall amount of molecular hydrogen. Hence, CO, the second most abundant molecule in the Universe ($\sim 10^{-5}$ times less abundant than H_2), is widely used as tracer of molecular gas (e.g. Bolatto et al. 2013). Indeed, CO is far easier to detect, since it emits radio and sub-millimeter emission through rotational transitions. CO cooling dominates once the gas density reaches $n \simeq 1000\,\mathrm{cm}^{-3}$ at temperatures $T < 100$ K, typical values of molecular clouds. The most abundant H_2 mass tracers after CO are HCN and HCO^+, that probe the large range of physical properties within GMCs ($T \sim 15 - 100\,\mathrm{K}$, $n \sim 10^2 - 10^6\,\mathrm{cm}^{-3}$, e.g. Papadopoulos et al. 2012).

On the other hand, *ionised gas* accounts for the majority of the volume of the ISM, even though its total mass is not more than around 25% of the total gas mass. Part of this gas is very diffuse ($n \sim 3 \times 10^{-3}\ \mathrm{cm}^{-3}$) and reaches temperatures of $T \sim 10^6$ K, emitting soft X-rays, and is located in large collisionally ionised bubbles due to blast waves generated by stellar winds and SN explosions. McKee & Ostriker (1977) added this gas phase, the so-called *hot ionised medium* (HIM), to the the two-phase model proposed by Field et al. (1969). Furthermore, there is another ionised phase in the ISM, the *warm ionised medium* (WIM), composed by radiatively ionised hydrogen with temperatures around $T \sim 10^4$ K (Klessen & Glover, 2016). Part of this gas fills the so-called H II regions, located in the surroundings of massive O and B stars, characterised by a surface temperature around $T \sim 2 - 5 \times 10^5$ K, irradiating UV photons with energy $h\nu > 13.6$ eV (Fig. 1.1). These photons are capable of ionising neutral hydrogen in a sphere all around (the so-called "Strömgren sphere"). In an homogeneous medium, H II regions would appear to be spheres filled with almost fully ionised medium and sharp

---

[1] In the solar neighborhood, the mean diameter of a GMC is around 45 pc (Blitz, 1993).

edges, dividing them from almost fully neutral medium. Indeed, Strömgren spheres are ionisation bounded, which means that the nebula absorbs all ionising photons from stars (optically thick limit or Case B). Other nebulae (e.g. planetary nebulae) are instead density bounded so that some UV photons may escape the nebula (optically thin limit or Case A). H II regions are mainly traced through the He and H recombination lines (e.g. the Balmer and Paschen series in the optical and in the NIR, respectively) or forbidden lines of extremely low-density elements, such as [O III]λ5007 or [N II]λ6584. In addition, like any plasma with free electrons, photoionised gas emits via bremsstrahlung radiation, that at the typical temperatures of H II regions ($T \simeq 10^4$ K) shines at radio wavelengths[2].

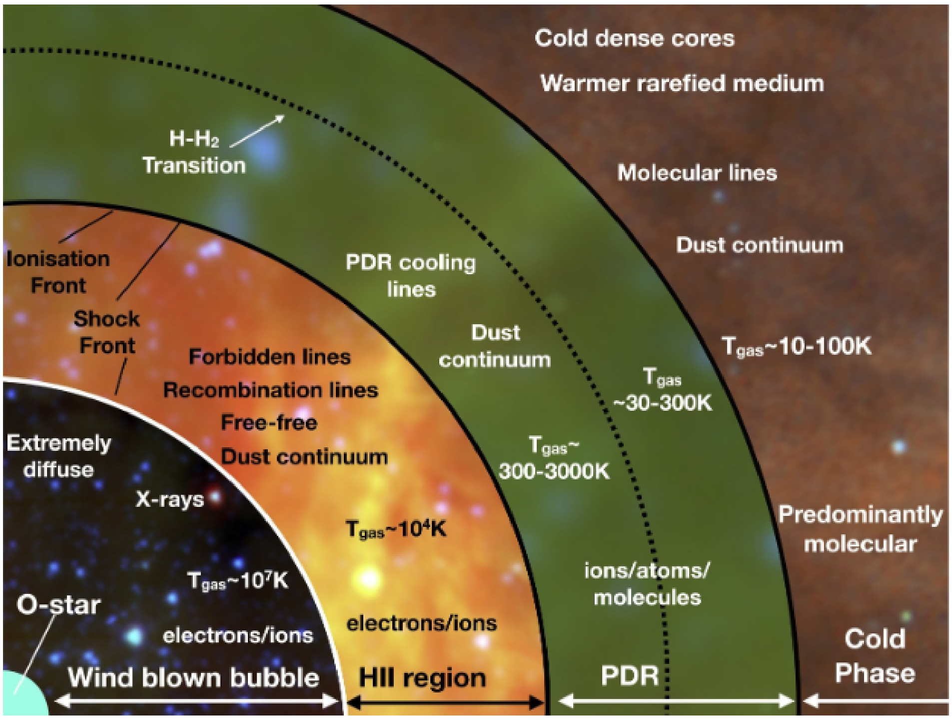

Figure 1.1: Schematic overview of the surroundings of an O star. The high velocity wind excavates a very hot, but also very diffuse bubble, out of which the gas is predominantly photoionised. FUV radiation can penetrate beyond the extent of the photoionised gas, creating a PDR. Where the medium is optically thick to the exciting O star radiation, the gas is completely molecular. This figure is taken from Haworth et al. (2018).

WIM in galaxies is also composed by a low surface brightness ionised gas, the so-called *diffuse ionised gas* (DIG). This gas, that fills the regions between H II regions and interarms in face-on spirals, is found in extraplanar regions in edge-on discs and also in spheroids (see Vale Asari et al. 2019 and references therein). Interestingly, DIG

---

[2] The bremsstrahlung spectrum is rather constant until a cut-off frequency, that depends only on the temperature of the gas and is given by the relation: $v_{cut-off} \simeq 10^{10} \times T$ Hz.

is observed to contribute to 30-60% of the total Hα flux in local spiral galaxies (Oey et al., 2007), but its properties and how it affects physical measurements of galaxies are still controversial. Its origin can be addressed to Lyman continuum photons leakage from classical H II regions, massive stars in the field and radiation from hot low-mass evolved stars, fast shocks from SN winds, and heating by cosmic rays or dust grains (e.g. Hoopes & Walterbos 2003; Oey et al. 2007; Zhang et al. 2017; Sanders et al. 2017).

As introduced above, also radiation from AGN plays a fundamental role in shaping ISM properties. Photoionised gas in AGN is characterised by a wide range of radii, ionisation states, gas densities and velocities. Specifically, AGN are characterised by a compact central source, the *super massive BH*, that provides a very intense gravitational field, whose most basic feature is the presence of an event horizon, that is a boundary from which matter and even light can never re-emerge. It is described by the gravitational radius, defined as $R_g = \frac{GM_{BH}}{c^2}$, where G is the gravitational constant, $M_{\rm BH}$ the black hole mass and c the speed of light. Around the super massive BH, an *accretion disc* forms as the gas spirals inward on scales down to a few gravitational radii, loosing angular momentum and a considerable fraction of its gravitational energy. Friction heats the gas to high temperatures ($T > 10^4$ K), that accounts for optical through soft X-ray continuum emission. A hot, rarefied gas ($T \sim 10^8 - 10^9$ K), located at $\sim 3 - 10\,R_g$ above the disc, constitutes the so-called *hot corona*. In this region, the soft thermal photons produced by the disc are upscattered to X-ray, accounting for the energetic X-ray emission from AGN. The deep gravitational potential at the center of the galaxy allows the presence of high density ($n_e \approx 10^9 - 10^{10}\,{\rm cm^{-3}}$), high velocity ($\gtrsim 2000\,{\rm km\,s^{-1}}$) gas clouds with a temperature of $\approx 10^4$ K in proximity of the central source, composing the so-called *broad line region* (BLR). The gas reprocesses the energy produced by the continuum source at ionising UV energies, through permitted emission lines (full width at half maximum $FWHM \approx 10^3 - 10^4\,{\rm km\,s^{-1}}$) due to recombination or de-excitation of photoionised atoms. The electron density is high enough to prevent forbidden lines from forming, being collisionally suppressed. Some clouds are located further away from the super massive BH, constituting the *narrow line region* (NLR), the largest spatial scale where the ionising radiation from the central source can excite the surrounding medium. Here, the electron density is sufficiently low ($10^4\,{\rm cm^{-3}}$) to allow the presence of forbidden lines, with a $FWHM \approx 10^2\,{\rm km\,s^{-1}}$. The temperature is $\sim 2.5 \times 10^4$ K. The accretion disc is surrounded by a dusty circumnuclear material, the so-called *dusty torus*, whose typical size is around $\sim 1 - 10$ pc. This region is located beyond the dust sublimation radius (the dust sublimation temperature is $\approx 1000 - 1500$ K), therefore is likely to contain dust and molecular gas. More precisely, the gas at the inner radius is ionised by the central engine, whereas at larger distances dominates the neutral and molecular material. The torus emits the reprocessed radiation in the IR band, while appears to be opaque at all the other wavelengths, obscuring the central source for certain lines of sight. Finally, the growth of super massive BHs releases an enormous amount of energy capable of accelerating outflows and jets that can significantly influence the evolution of the host galaxies. Only recently spatially resolved spectroscopic studies from optical, IR and mm facilities gave a conclusive proof of the existence of AGN galaxy-wide winds, that are now routinely detected both in the local Universe (e.g. Feruglio et al. 2010; Cicone et al. 2014) and at high-z (e.g. Cano-Díaz et al. 2012; Cresci et al. 2015a; Carniani et al. 2016). Interestingly, these outflows are ubiquitous, and are revealed on different phases (highly ionised, ionised, atomic and molecular gas) and physical scales (Cicone et al., 2018). A schematic representation of the AGN physical model is shown in Fig. 1.2, taken from Hickox & Alexander (2018).

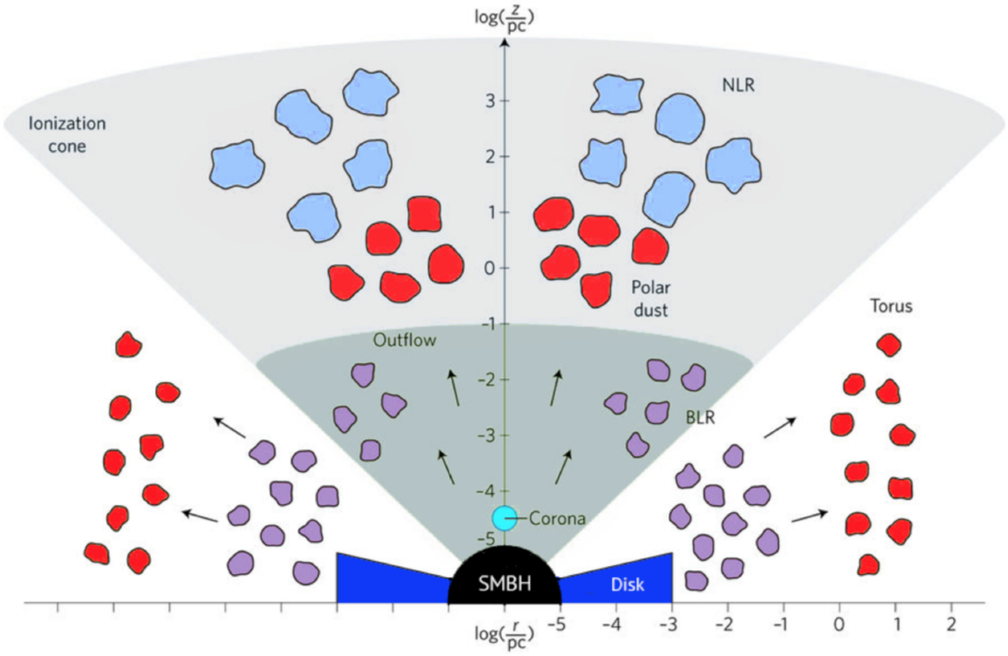

Figure 1.2: Cartoon scheme of the AGN physical model. The accretion disc, corona, BLR and dusty torus are within the gravitational influence of the super massive BH, while the NLR extends on large scales and is under the gravitational influence of the host galaxy. This figure is taken from Hickox & Alexander (2018) .

1.1.1 Dust

The reddening of starlight in the ISM and its tight correlation with the hydrogen column density point out that there is an additional component of the ISM, capable of absorbing light over a wide range of frequencies. Furthermore, measurement of elemental abundances in the local ISM reveals that a number of elements, notably silicon and iron, are considerably less abundant in the gas phase than in the Sun. Finally, mid-infrared (MIR) and far-infrared (FIR) observations show that there is a widespread continuum emission, with a spectrum close to that of a black body and an intensity that correlates well with the hydrogen column density. All these pieces of information lead to the conclusion that there must be a particulate component, which is associated to CNM and GMCs, and accounts for around 1% of the total mass of the ISM, commonly referred to as interstellar dust (see Klessen & Glover 2016 and references therein).

Dust is mostly in form of grains of graphite and silicate of micron size and plays a crucial role in several physical processes, such as the formation of molecular hydrogen and the absorption of UV and optical radiation (Draine, 2003). In addition, since it absorbs UV radiation that can dissociate molecules and, in turn, emits radiation at FIR wavelengths, it facilitates ISM chemistry and helps in cooling the gas, accelerating the process of SF. This phenomenon of absorbing and scattering part of the electromagnetic radiation emitted by an astronomical object is called extinction and is further described in Sec. 1.3.1.

1.1.2 Metals

The term "metals" refers to the fractional abundance of elements heavier than helium, that plays a fundamental role in regulating the thermal behaviour of the ISM. Oxygen is the most abundant heavy element in mass, and thus the ISM metallicity is usually expressed in terms of oxygen abundance (i.e. 12+log(O/H)), under the implicit assumption that the abundance of almost all the other chemical elements scales proportionally, maintaining the solar abundance ratios[3]. Nitrogen represents an exception because its origin is more complex, since in metal-rich environments it can be also synthesised by low- and intermediate-mass stars via the CNO cycle ("secondary" nucleosynthetic origin, Alloin et al. 1979; Considère et al. 2000; Mallery et al. 2007). Overall, in this dissertation the terms metallicity Z and oxygen abundance 12+log(O/H) are used as synonyms. The metallicity of the gas can be measured through a variety of methods, summarised in Sec. 1.3.1.

Metals are essential for cooling processes. Fig. 1.3 shows how the energy emitted per unit time and volume, that is the cooling function, changes with metallicity over temperature (10 K $< T <$ 10^8 K) taken from Maio et al. (2007). When metals are

---

[3] $12+\log(\mathrm{O/H})_\odot = 8.69 \pm 0.05$ (Asplund et al., 2009). However, the Solar (photospheric) reference is still not completely settled, but what is important is that different studies are consistently scaled to the same Solar reference value before their comparison.

not present, hydrogen-derived molecules can effectively cool gas at $T < 10^4$ K, while hydrogen and helium collisional excitations dominate at $T \sim 10^4 - 10^5$ K, creating the double peak feature in the cooling function. However, as soon as the metallicity of the gas increases (via SN explosions, stellar mass losses, stellar winds), metals become the most efficient coolants. For instance, carbon and oxygen collisional ionisation is responsible for the twin peaks at $T \sim 10^5$ K, while iron ionisation dominates at $T > 10^7$ K.

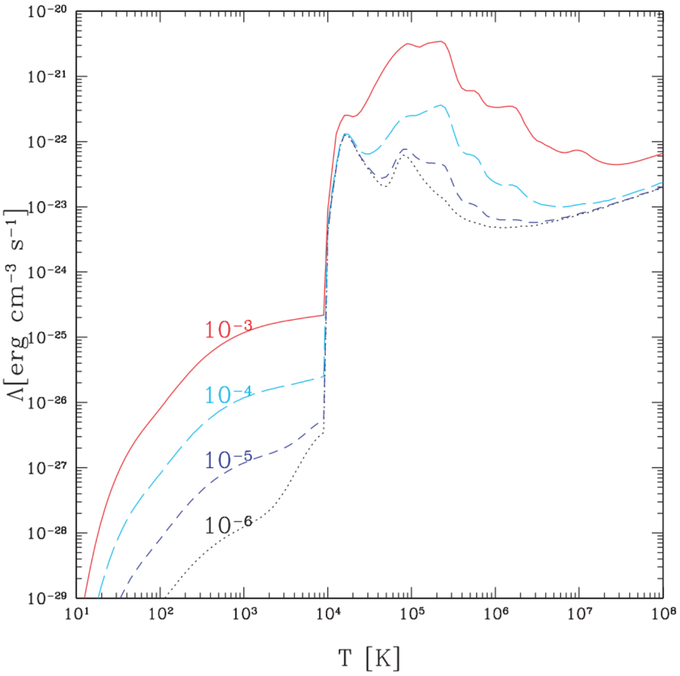

Figure 1.3: Total cooling due to H, He, metals, and H_2 and HD molecules as a function of temperature, assuming a gas density of $n \sim 1$ cm^{-3}. The different colours refer to different metal fractions: 10^{-3} (solid line), 10^{-4} (long-dashed line), 10^{-5} (short-dashed line) and 10^{-6} (dotted line). This figure is taken from Maio et al. (2007).

1.1.3 The role of metallicity in galaxies

Gas metallicity shows clear scaling relations with several integrated properties of galaxies, valid for both star forming and quiescent objects. These scaling relations stem from the fact that metallicity is a consequence of all the history of SF, gas accretion, merging, and gas outflows. Hence, they can give information on the integrated SF in galaxies, the quantity of metals lost via outflows and stripping, the presence of inflows of pristine gas, or galaxy star formation history (SFH), since different chemical elements are enriched by different populations of stars on different timescales. In the following, I will summarise the main relations between metallicity and galaxy properties, focusing on star forming galaxies in the local Universe.

Gas phase metallicity is found to primarily correlate with stellar mass, and this is known as the *mass-metallicity relation* (MZR, Lequeux et al. 1979; Tremonti et al. 2004). An example of this relation with an observed scatter of ~ 0.1 dex is shown for more than 100000 Sloan Digital Sky Survey (SDSS, York et al. 2000) galaxies in Fig. 1.4, taken from Tremonti et al. (2004). The MZR has also been extended towards low mass galaxies (e.g. Zahid et al. 2012), and is nowadays established from $\sim 10^7$ $M_\odot$ to $\sim 10^{12}$ $M_\odot$ with a steep dependence at low masses up to $\sim 10^{10}$ $M_\odot$ and a flattening towards higher values. The shape of the MZR could stem from many simultaneous processes (see e.g. Maiolino & Mannucci 2019 and references therein). A possibility is that feedback produced by outflows (see Sec. 1.2 for more details), could be very efficient in removing metal-enriched gas from the ISM towards CGM and IGM, especially in small galaxies, characterised by a shallow potential well (e.g. Tremonti et al. 2004). Recent works found higher metallicity in outflows than in the ISM (Chisholm et al., 2018), in agreement with this scenario. On the other hand, according to the "downsizing" scenario

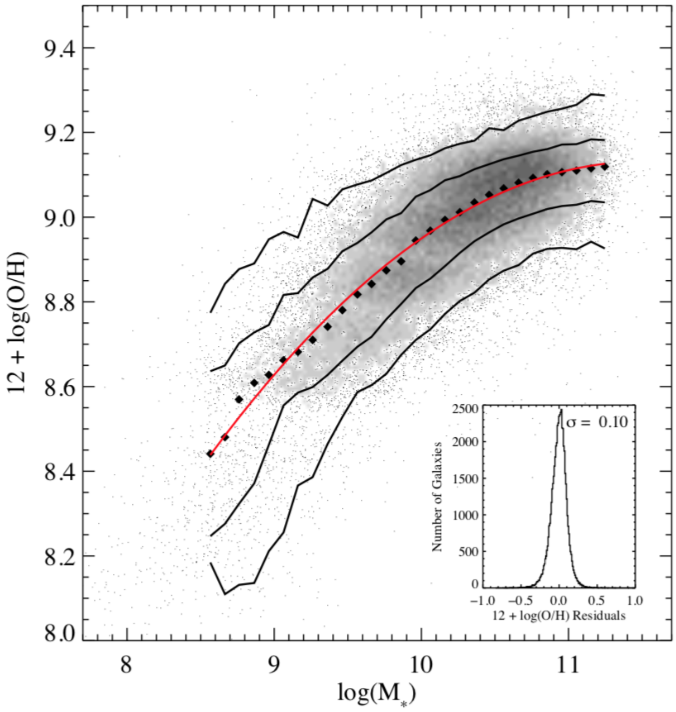

Figure 1.4: Gas phase MZR in the local Universe. The black dots are the median of the distribution of SDSS galaxies (shown as gray dots). The black lines enclose 68% and 95% of the distribution, while the red line is a polynomial fit to the data. The inset histogram shows the distribution of residuals of the fit, with a scatter of ~ 0.1 dex. This figure is taken from Tremonti et al. (2004).

(e.g. Cowie et al. 1996), high mass galaxies evolve faster and at higher redshifts than low-mass objects, and thus they are predicted to be more metal rich at the present stage (e.g. Maiolino et al. 2008). Alternatively, smaller galaxies could be affected by an ongoing infall of metal-poor gas, able to dilute their metal content, accounting for their larger gas fraction and enhancing SF (e.g. Erb et al. 2006). Another possibility is related to the shape of the initial mass function (IMF), whose high-mass end could be dependent on stellar mass, leading to a different content of metals in stars and in the metal enrichment rate (e.g. Trager et al. 2000; Lian et al. 2018). Finally, larger mass galaxies could accrete higher metallicity gas, enriched by previous episodes of SF (e.g. Ma et al. 2016).

Other scaling relations between metallicity and galaxy properties were found, such as the correlation between the metallicity residuals from the MZR and galaxy color, ellipticity, and central mass density (Tremonti et al., 2004), the dependence of the MZR shape on galaxy size (Hoopes et al., 2007), or the relation between metallicity and star formation rate (SFR) for a given stellar mass (Ellison et al., 2008). In this context, Mannucci et al. (2010) presented the so-called *fundamental metallicity relation* (FMR, see Fig. 1.5), a 3D relation between stellar mass, metallicity and SFR for the local Universe, characterised by a very low residual metallicity scatter (~ 0.05 dex). Specifically, at low stellar masses, metallicity decreases sharply with increasing SFR, while this dependence is lost at high stellar masses. Ellison et al. (2008) suggested that the dependence of metallicity on SFR and galaxy size is given by a variation in SF efficiency. On the other hand, Mannucci et al. (2010) argued that this tight relation could stem from the interplay of infall of pristine gas and outflow of enriched material. Indeed, the former provides chemically poor gas, diluting metallicity, and delivers additional fuel for SF, enhancing the SFR, whereas the latter ejects part of the enriched gas. An important issue to underline is that both the MZR and the FMR depend on how galaxies are selected and how mass, SFR, and especially metallicities are measured (see Sec. 1.3.1).

Other relations between metallicity and galaxy properties were suggested. For instance, metallicity is usually found to be anticorrelated with another fundamental parameter used to constrain the ISM, the ionisation parameter q, that quantifies the global degree of ionisation (Dopita & Evans, 1986; Freitas-Lemes et al., 2014; Pérez-Montero, 2014; Rosa et al., 2014). The ionisation parameter is defined as

$$q = \frac{Q_{\rm ion}}{4\pi r^2 n_{\rm e}} \tag{1.1}$$

where Q_{ion} is the number of photons that can ionise hydrogen, emitted per unit time

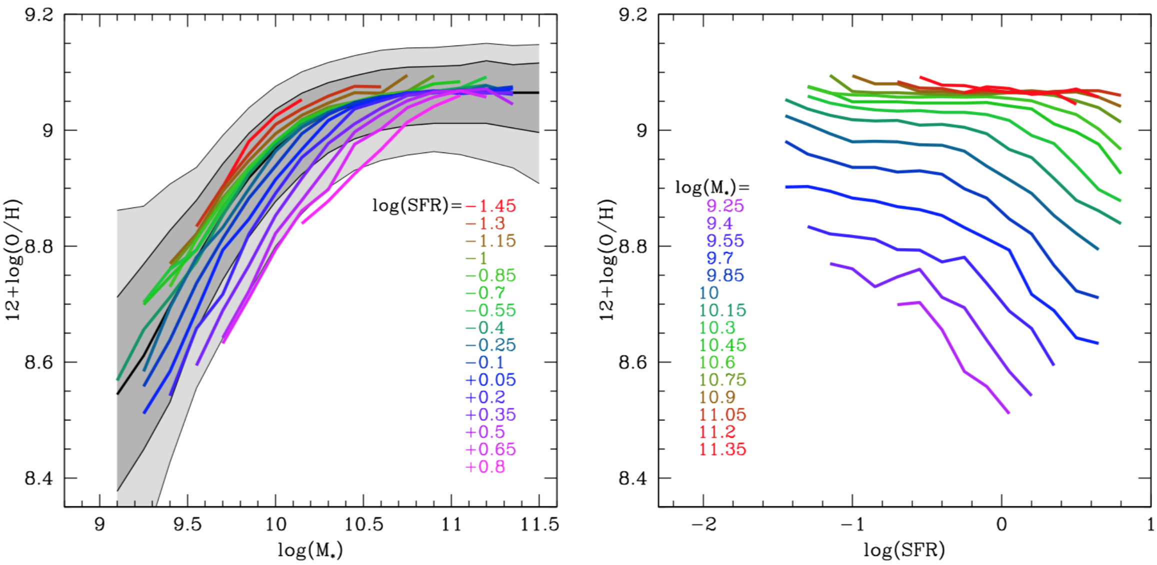

Figure 1.5: *Left*: Mass–metallicity relation of local SDSS galaxies colour-coded as a function of SFR, where the grey-shaded areas contain 64% and 90% of all SDSS galaxies, with the thick central line showing the median relation. *Right*: relation between the median metallicity and SFR, colour-coded as a function of SFR for galaxies of different stellar masses. This figure is taken from Mannucci et al. (2010).

from the central source through an area of radius r, while n_e is the gas density and is in units of [cm s^{-1}]. It can be also expressed as a dimensionless parameter $U = q/c$, dividing it by the speed of light c. According to Dopita et al. (2006b), this anticorrelation can be caused by the fact that metal-rich stellar winds are more opaque to the radiation, absorbing a greater fraction of ionising photons, while metal-rich stellar atmosphere scatter photons more efficiently. This leads to a decrease of q in the surrounding H II region ($q \propto Z^{-0.8}$). Intriguingly, metallicity and ionisation parameter were found to correlate in some works (e.g. Dopita et al. 2014), while in other they seem to be completely unrelated (e.g. Poetrodjojo et al. 2018). Nakajima & Ouchi (2014) investigated the relation between the residuals from the MZR and the ionisation parameters in a sample of local and high-z galaxies, extending the FMR into a four-dimensional relation including q (*fundamental ionisation relation*). The relations that link the ionisation parameter to metallicity and other galaxy properties is one of the topics of this dissertation, that is described in Chapter 3.

Finally, the advent of IFS (see Sec. 1.4) allowed to investigate the radial distribution of metallicity within galaxies, usually expressed in units of effective radius or half-light radius (R_e), that is the radius at which the integrated flux is half of the total one. This can provide information both on the processes that are regulating galaxy growth, and on the presence and effects of internal phenomena (e.g. radial gas inflows, stellar migration).

For instance, Fig. 1.6 shows the metallicity gradients found with 550 star forming discs from the SDSS IV Mapping Nearby Galaxies at Apache Point Observatory (MaNGA) survey (Bundy et al., 2015), as a function of galaxy stellar mass $M_\star$. Belfiore et al. (2017) revealed a dependence of metallicity gradients on the stellar mass of the galaxy, finding nearly flat gradients for low mass galaxies ($M_\star \sim 10^9$ M$_\odot$), that become progressively steeper and more negative for more massive systems. The metallicity gradients shown in Fig. 1.6 are characterised by a flattening in the central regions of the most massive spiral galaxies (see also Zinchenko et al. 2016), that can be interpreted as a consequence of a saturation of metallicity. The flattening at low stellar mass could be due to effects such as stellar migration, galaxy interactions or powerful feedback effects, recalling the flat metallicity gradients inferred for high-z galaxies. Therefore, it may favour a scenario in which metallicity gradients have become steeper with time. This would partly disagree with the *inside-out* scenario, supported by some theories, hydrodynamical simulations and chemical evolution models, that predict star forming galaxy outskirts to form later with respect to the inner parts (e.g. Larson 1974; Matteucci & Francois 1989; Molla et al. 1996; Boissier & Prantzos 1999). Indeed, a natural consequence of this scenario is that the central regions of galactic discs are formed at earlier times, and thus are more evolved, more metal rich, and show lower sSFR with respect to the outskirts (e.g.

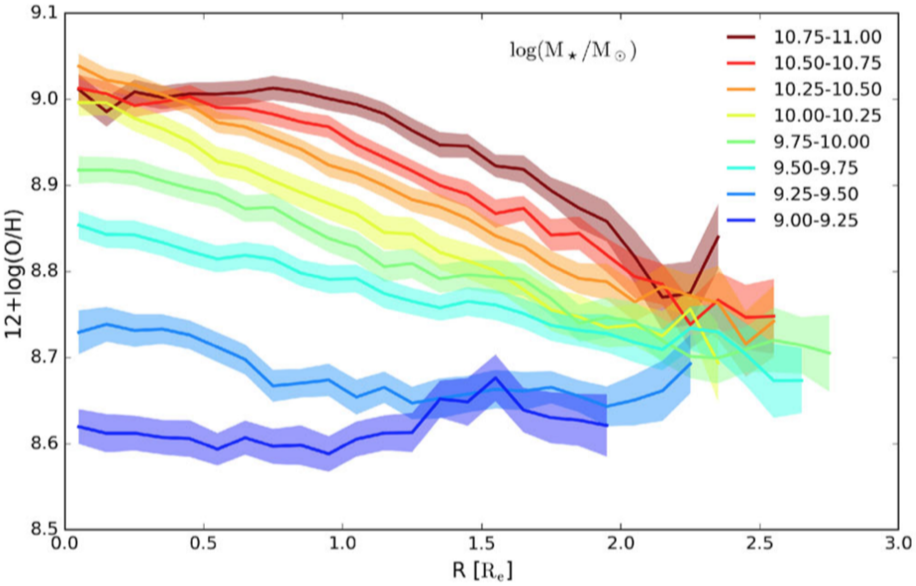

Figure 1.6: Metallicity gradients in the radial range 0.5−2 R$_e$, using the O3N2 diagnostic (Pettini & Pagel 2004, see Sec. 1.3.1) colour-coded as a function of stellar mass, as shown in the legend. The shaded region represents the error on the median gradient in each mass bin. This figure is taken from Belfiore et al. (2017).

.

Prantzos & Boissier 2000; Davé et al. 2011; Gibson et al. 2013; Pilkington et al. 2012; Belfiore et al. 2019). On the other hand, other authors, such as Sánchez et al. (2014), Ho et al. (2015) and Sánchez-Menguiano et al. (2016) found no relation between the slopes of gas metallicity radial profiles and stellar mass, using smaller samples from the Calar Alto Legacy Integral Field spectroscopy Area survey (CALIFA) survey (Sánchez et al., 2012). Chapter 3 deals also with this topic, showing new results for the metallicity gradients with the MaNGA survey and making a comparison with the main results in literature.

1.2 Feedback and outflows

The term "feedback" includes many processes including proto-stellar jets, photo-heating, stellar mass loss, radiation pressure, supernovae (Types Ia & II), cosmic ray acceleration, AGN activity and more (see e.g. Hopkins et al. 2018 and reference therein). As I introduced in the previous section, stellar and AGN radiation are a fundamental ingredient in the baryon cycle, since they strongly influence the ISM composition. For example, feedback produced by outflows is thought to contribute in regulating SF, shaping the MZR relation and the metallicity gradients within galaxies. In the following, I will describe in detail stellar and AGN feedback, explaining their role in shaping galaxy evolution.

1.2.1 Negative feedback

BHs at the center of a galaxy bulge are thought to play a major role in determining the luminosity (e.g. Kormendy et al. 1997; Magorrian et al. 1998) and final stellar mass (e.g. Ferrarese & Merritt 2000; Gebhardt et al. 2000) of their host galaxies. For instance, Fig. 1.7 shows the relation between the BH mass $M_{\rm BH}$ and the bulge velocity dispersion σ for 72 local objects (McConnell & Ma, 2013). These scaling relations span several orders of magnitudes in mass, luminosity and velocity dispersion, and are quite tight. Therefore, they provide the empirical foundation for establishing the role of BHs in galaxy formation and evolution (e.g. Hopkins et al. 2007, suggesting a symbiotic connection between the formation and growth of galaxies (directly linked to SF) and BH growth.

The process by which this may occur is called negative *AGN feedback*, and it takes place through an interaction between the energy and radiation generated by accretion onto the massive BH (i.e. the active nucleus) and the gas in the host galaxy (e.g. Silk

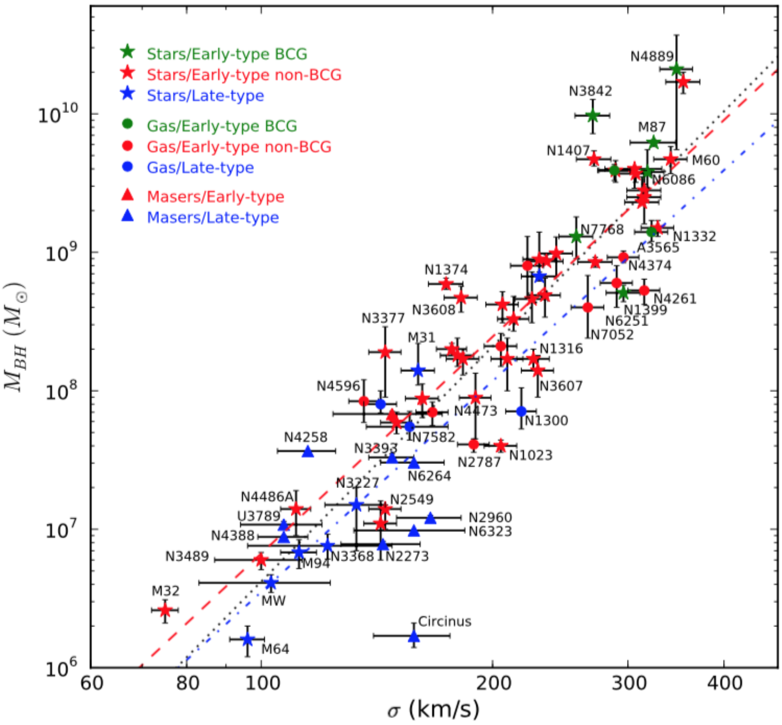

Figure 1.7: M_{BH}-σ relation for 72 galaxies, comprising brightest cluster galaxies (BCGs, in green), elliptical and S0 galaxies (in red), and late-type spiral galaxies (in blue). Error bars indicate 68% confidence intervals. The black dotted line shows the best-fitting power law for the entire sample, given by: $\log(M_{\mathrm{BH}}/\mathrm{M}_{\odot}) = 8.32 + 5.74 \times \log(\sigma/200\,\mathrm{km\,s^{-1}})$. This figure is taken from McConnell & Ma (2013).

& Rees 1998; Granato et al. 2004; King 2010; Fabian 2012). A possibility is that the intense photon and particle flux produced by the AGN sweeps away the interstellar gas from the galaxy bulge, quenching SF, and AGN activity as well, because of the lack of fuel for accretion (Fabian, 2012). Interestingly, scaling relations naturally arise when AGN feedback is taken into account in theoretical models and simulations (e.g. Silk & Rees 1998).

A further evidence that highlights the importance of feedback in galaxy evolution is given by the discrepancy between the observed stellar mass function of galaxies (i.e. the number density of galaxies having a certain stellar mass) with that predicted from the Λ-CDM models of galaxy evolution. This discrepancy emerges both at the low and at the high-mass end, as shown in Fig. 1.8. The former can be reduced by including in the models stellar feedback due to SNe (Dekel & Silk, 1986). Indeed, also *stellar feedback* plays an important role in galaxies, due to stellar and SN-driven winds that enrich the IGM and shaping the galaxy mass function, mass-metallicity relation, and other global galaxy properties (e.g. Hopkins et al. 2012). These winds progressively reheat cold disc gas and/or heat the diffuse halo surrounding the galaxy, and thus reduce the gas reservoir to form stars. Consequently, stellar feedback has been routinely included in models and simulations of galaxy formation and evolution (e.g. Kauffmann et al. 1993; Cole et al. 2000; Benson et al. 2003; Granato et al. 2004; Springel et al. 2005; Bower et al. 2012). However, this mechanism becomes inefficient at high masses, since the total energy output required to match the observed galaxy mass function largely exceeds the energy available from SN explosions. Indeed, at $\sim 3 \times 10^{10}$ $M_\odot$ the observed galaxy mass function reaches its minimum discrepancy from Λ-CDM models, and then the gap dramatically increases again. Such lack of high-mass galaxies can be explained taking into account AGN feedback mechanism, capable of suppressing SF in the galaxy through the action of outflows and jets, reconciling models with observations (e.g. Benson et al. 2003; Springel et al. 2005).

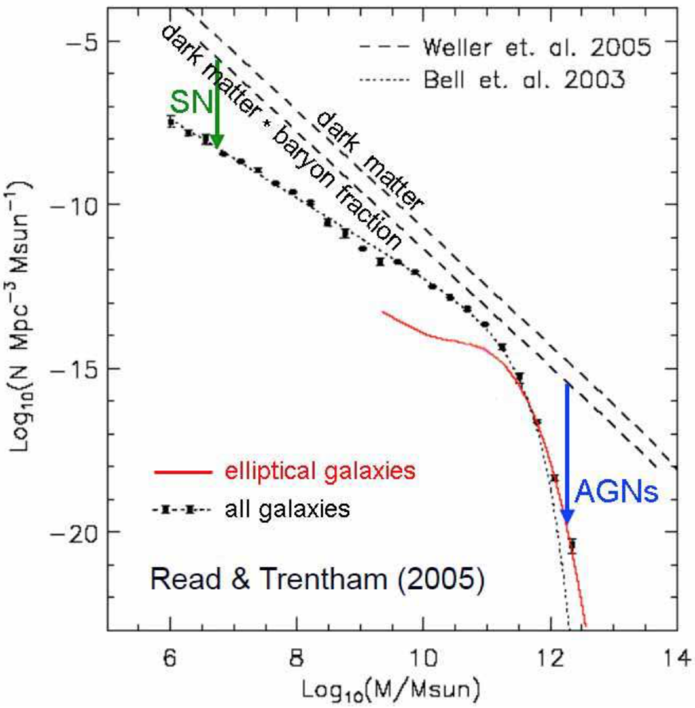

Figure 1.8: Comparison among the galaxy barionic mass function (black points for all galaxies, red curve for ellipticals only) from Read & Trentham (2005), fitted with a Schechter (1976) function (dotted curve, Bell et al. 2003), the mass function of cold dark matter halos from numerical simulations (Weller et al., 2005) and the same dark matter mass function multiplied by the universal baryon fraction of 0.163 (Hinshaw et al., 2013). Green and blue arrows represent the effect of stellar (SN) and AGN feedback, respectively, crucial for the semi-analytic models to reproduce the observed stellar mass function. This figure is taken from Kormendy & Ho (2013).

Finally, another clue in support of feedback is given by the similarity of the observed cosmic histories of BH growth and SF, as shown in Fig. 1.9. Specifically, Both BH growth and SF history peak at $z \sim 2$, meaning that the bulk of BH growth and SF took place between $z = 1 - 3$ (see Shankar et al. 2009; Delvecchio et al. 2014; Madau & Dickinson 2014; Aird et al. 2015 and reference therein). This suggests a co-evolution of the two processes, driven by a mechanism that self-regulates the SF activity in the galaxy and the growth of the BH.

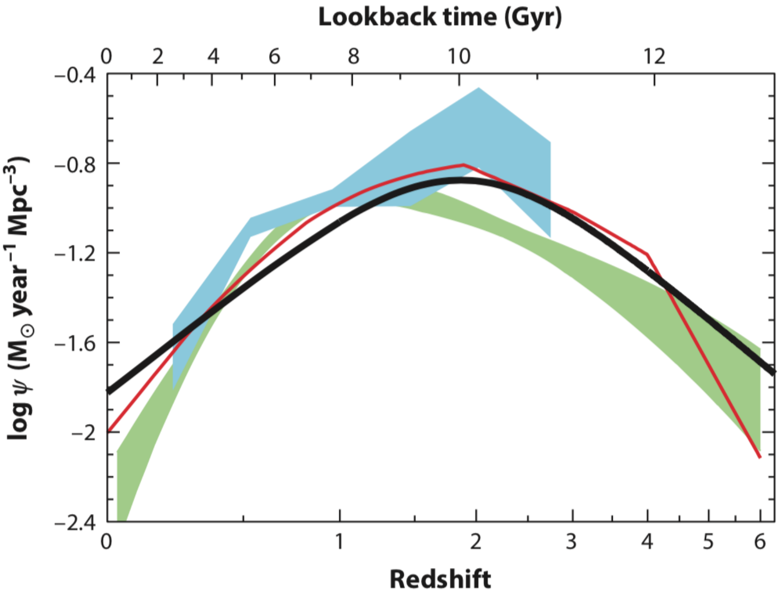

Figure 1.9: Comparison between the best-fit SF history (thick solid curve) and the massive BH accretion history from X-ray (red curve from Shankar et al. 2009; light green shading from Aird et al. 2010) and infrared (light blue shading from Delvecchio et al. 2014) data. The shading represents the $\pm 1\sigma$ uncertainty range on the total bolometric luminosity density. The radiative efficiency has been set to $\epsilon = 0.1$. The comoving rates of BH accretion have been scaled up by a factor of 3300 to facilitate visual comparison to the SF history. This figure is taken from Madau & Dickinson (2014).

In terms of energetics at least two major modes have been identified, determined by the nature of the energy outflow near the BH (see Fabian 2012 and references therein). The first is the radiative mode, also known as the quasar or wind mode, while the second is the kinetic mode, also known as the radio jet or maintenance mode (see Fig. 1.10). Radiative mode operates in a typical bulge when the accreting BH is close to the Eddington limit, pushing cold gas out of the galaxy through powerful outflows. On the other hand, kinetic mode operates when the galaxy has a hot halo (or is at the center of a group or cluster of galaxies) and the accreting BH has powerful jets, capable of heating the surrounding gas.

The "smoking gun" evidence that outflows are effectively quenching SF has been

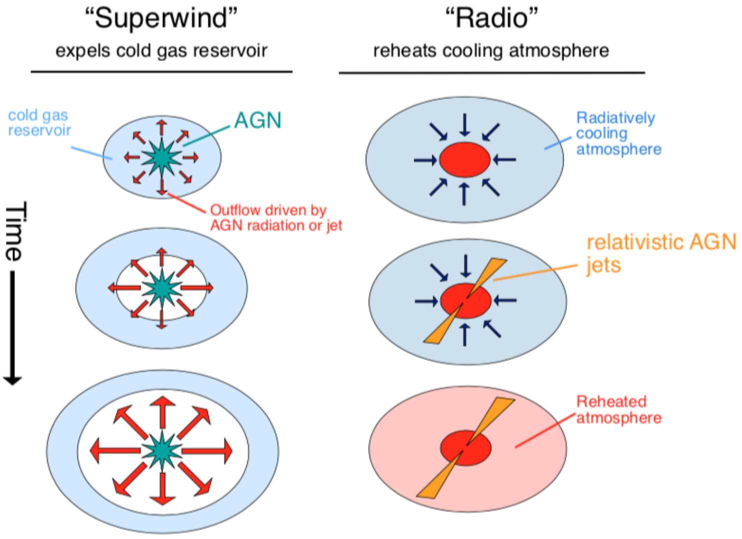

Figure 1.10: Cartoon to illustrate the two main "classical" modes of AGN feedback: radiative (superwind) to the left, and kinetic (radio) to the right. This figure is taken from Alexander & Hickox (2012).

found so far in a small amount of objects, even though the overall impact does not seem to result into a global shut down of SF (see Cresci & Maiolino 2018). For instance, NIR integral field unit (IFU) observations of $z \sim 1-3$ quasars revealed a spatial anti-correlation between the location of the fast outflowing gas (generally traced by the blue-shifted wing of the [O III]λ5007 line) and the SF in the host galaxy, traced by the narrow component of Hα (Cano-Díaz et al., 2012; Cresci et al., 2015a; Carniani et al., 2016). However, outflows appear to affect the gas reservoir only along their path, while SF remains globally high, with values of SF rates up to 100 $M_{\odot}$ yr^{-1}. Overall, the available data suggest that a significant amount of gas is entrained in AGN driven outflows, but only a minor fraction of outflowing gas may escape the host halo, while the remaining may fall back onto the galaxy at later times (Arribas et al., 2014). These considerations point towards the existence of a delayed feedback mechanism, in which SF is mainly affected in the central regions and is more slowly fading across the whole disc with a time scale of roughly $\sim$ 1 Gyr. This scenario is called *preventive feedback* and predicts that the outflow injects energy into the halo, heating the gas and preventing it from cooling, and thus halting the accretion of the fresh supply of gas needed to fuel SF (e.g., Pillepich et al. 2018; Cresci & Maiolino 2018).

1.2.2 Positive feedback

Recently, some theoretical models have proposed that outflows and jets can also have a positive feedback effect, triggering SF in the galaxy disc, compressing gas in the interstellar and circumgalactic outflows and thus fostering the fragmentation and gravitational collapse of clouds, with a consequent boost of SF (e.g. Rees 1989; Nayakshin & Zubovas 2012; Bieri et al. 2016; Zubovas & King 2016). Evidence in support of this scenario has been already revealed in few AGN at high-z with NIR integral field observations from the detection of star forming clumps in the host galaxy possibly triggered by the outflow pressure at its edges (e.g. Cresci et al. 2015a; Carniani et al. 2016). An example of this positive feedback scenario in the local Universe is given by Cresci et al. (2015b), where the nuclear region of the barred, radio-quiet Seyfert 2 NGC 5643 with a well-known ionisation cone extending eastward of the nucleus, parallel to the bar (Schmitt et al., 1994; Simpson et al., 1997; Fischer et al., 2013) is observed with MUSE as part of the Measuring AGN under MUSE microscope (MAGNUM) survey (see Chapter 2). In this galaxy, Cresci et al. (2015b) found two Hα bright, SF dominated clumps, located at the receding edge of the dust lane, where the fast outflowing gas from the central AGN encounters the dense material on the bar, possibly compressing the gas and inducing SF $SFR \sim 0.03$ M$_\odot$/yr). In the MUSE field of view (FOV), these two clumps are the youngest according to their Hα equivalent width, and are the only SF dominated regions closer to the nucleus ($\sim$ 1.2 kpc) than to the star forming ring located at the edge of the FOV ($\sim$ 2.3 kpc).

More recently, models have proposed an even more interesting scenario. Indeed, SF is expected to be triggered within the outflowing gas as a consequence of cooling and fragmentation processes (Ishibashi & Fabian, 2012; Gaibler et al., 2012; Zubovas et al., 2013; Silk, 2013; Ishibashi et al., 2013; Zubovas & King, 2014; Dugan et al., 2014; Ishibashi & Fabian, 2014; El-Badry et al., 2016; Mukherjee et al., 2018). This new SF mode can reach a few/several $\sim$ 100 M$_\odot$/yr (Ishibashi & Fabian, 2012; Silk, 2013) and differs from both SF in galactic discs and from the "standard" positive feedback scenario discussed above. Indeed, stars formed inside galactic outflows would have high velocities on nearly radial orbits, and thus may escape the galaxy and/or the halo, or become gravitationally bound (Zubovas et al., 2013). This new scenario is supported by recent observations that revealed that outflowing gas is suitable for SF, such as large quantities of cold molecular gas expelled at high velocities (e.g. Feruglio et al. 2010; Cicone et al. 2014; García-Burillo et al. 2015; Fluetsch et al. 2019), including a high fraction of dense (10^6 cm^{-3}) molecular gas (e.g. Aalto et al. 2012, 2015; Walter et al. 2017; Privon et al. 2017), that appears to be also very clumpy (e.g. Pereira-Santaella et al. 2016).

A direct observational evidence for SF in galactic outflows has been missing until recently, when it was obtained for the first time in a local luminous infrared galaxies (LIRG) at $z = 0.043$ (Maiolino et al., 2017). However, it is still not clear whether this is an isolated case, or if high molecular gas densities in galactic scale outflows could provide the appropriate physical conditions to form stars in the fast moving gas, and SF is common in galactic outflows, but difficult to identify. Consequently, Gallagher et al. (2019) investigated systematically the occurrence of this phenomenon by exploiting the statistical power of the MaNGA survey, finding stellar-like ionisation that may be tracing new stars in the high velocity gas in about 1/3 of the outflows. However, a solid proof that the ionisation source is co-spatial with the outflow is still missing.

In general, the need for high spectral and spatial resolution on a broad wavelength range (in order to detect all required diagnostics) makes the detection of these features of SF in outflows very challenging. Indeed, AGN ionisation from the bright central source may dominate over SF excitation. In addition, traditional SF tracers, such as UV or IR continuum imaging, can fail to disentangle SF occurring within outflows from the one that takes place in the galactic disc, because of spatial projection effects. The use of spectroscopic tracers, capable of separating the different star kinematic components, is thus crucial to extend the statistics of this brand new phenomena. In this context, a new tentative evidence of the two modes of positive feedback acting in a local galaxy is revealed and discussed in Chapter 2.

1.3 Probing the ISM of galaxies

The subject of this Thesis is the study of ISM properties, such as ionisation parameter, temperature, density, metallicity, extinction and excitation conditions (e.g. AGN, SF, shocks) in nearby galaxies. All these pieces of information are enclosed in galaxy spectra (see e.g. Kewley et al. 2019 for a review). I primarily exploit a set of diagnostics of the ISM available in the optical and molecular wavelength range, which are discussed in this section.

1.3.1 Optical spectroscopy

Emission lines, originating from nebulae photoionised by massive stars or gas located in the inner kiloparsecs of AGN, represent one of most powerful tracers of the ISM properties in both nearby galaxies and the high-redshift Universe. This section is focused on the methods to measure the properties of H II regions and NLRs. Measuring chemical abundances in the ISM is crucial to constrain models of stellar, galaxy, and cosmological evolution of the Universe. To do this, the structure of the emitting region must be solved, determining its properties. Different regions emit different emission lines, that can be used as diagnostics to trace the physical conditions. For instance, [O III] primarily comes from the high-ionisation zone in the inner regions of a nebula, [N II] is mostly emitted in the low-ionisation zone in the outskirts, where also [O II] and [S II] are emitted, while [S III] origins in an intermediate region between the two (e.g. Garnett 1992). Therefore, diagnostics from particular ionic species may only trace the physical conditions of a specific part of the nebula, leading to discrepancies in the inferred properties.

The ionisation parameter

The best way to determine the ionisation parameter q (Eq. 1.1, see Sec. 1.1.3) is by using the ratios of emission lines of largely different ionisation stages of the same element.

O3O2 = [O III]$\lambda\lambda$4959,5007/[O II]$\lambda\lambda$3726,29 has long been recognised as a good excitation diagnostic (e.g. Pérez-Montero & Díaz 2005; Nakajima & Ouchi 2014). The ionisation potentials of O^{++} and O^{+} are 35.1 eV and 13.6 eV, respectively. However, O3O2 is also strongly dependent on the metallicity, because the [O II] lines can only be excited by relative hot electrons, and thus disappears in cool, high metallicity H II regions. Mathis (1982, 1985) demonstrated that also the ratio between S^{++} and S^{+} (with ionisation potentials of 23.3 eV and 10.4 eV, respectively), traced by S3S2 = [S III]$\lambda\lambda 9069, 9532$/[S II]$\lambda 6717, 32$, can be used to estimate q. Furthermore, S3S2 lacks a strong metallicity dependence, since the sulfur lines are located in the red part of the spectrum, and so remain strong to much higher metallicities than the [O II]. This means that S3S2 can be considered a far better diagnostic than O3O2, as it can be appreciated by Fig. 1.11 taken from Kewley & Dopita (2002).

Temperature

The electron temperature T_e can be probed by the ratio between lines of the same species (i.e. no abundance uncertainties) from two energetically accessible levels with a difference in energy. In order to avoid any dependence on electron density, transitions with high critical densities should be chosen. Indeed, the critical density is defined as the density at which the collisional de-excitation rate and the radiative de-excitation rate are equal, and thus above its value the cooling rate becomes efficient.

In the optical, T_e is derived by the [O III]λ4363/[O III]λ5007, [N II]λ5755/[N II]λ6584

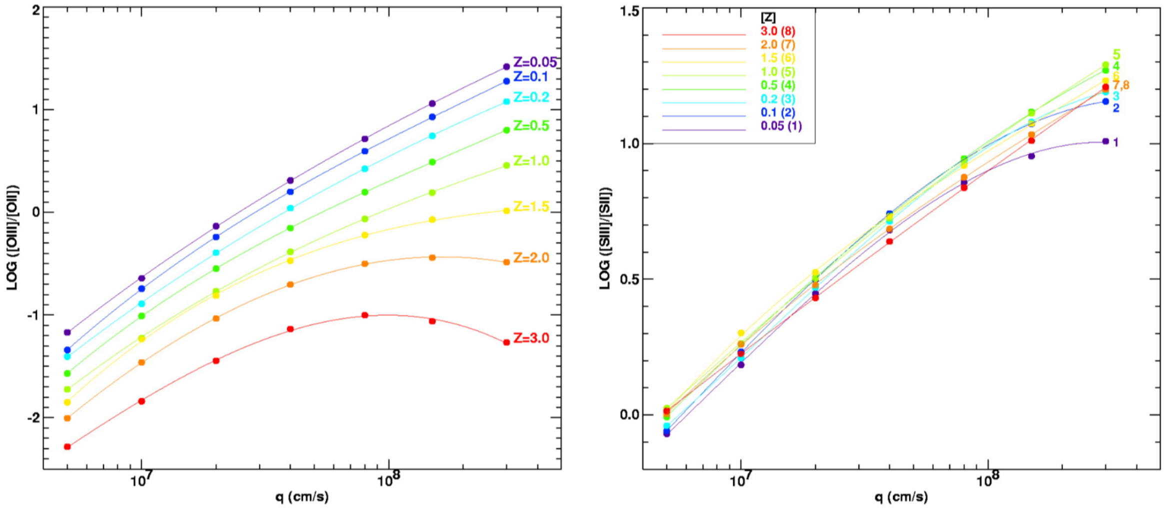

Figure 1.11: O3O2 (left) and S3S2 (right) diagnostics as a function of the ionisation parameter, colour-coded as a function of metallicity, as indicated in the legend. This figure is taken from Kewley & Dopita (2002).

and [S III]λ9532/[S III]λ6312 line ratios (see e.g. Pérez-Montero 2017). Specifically, the weaker [O III]λ4363, [N II]λ5755 and [S III]λ6312 are referred to as auroral, while the stronger [O III]λ5007, [N II]λ6584 and [S III]λ9532 are called nebular. Typically, the electron temperature is in the range 5000 K $< T_\mathrm{e} <$ 20000 K (see e.g. Osterbrock & Ferland 2006).

Density

The electron density n_e can be obtained by collisionally emission lines (CEL) of the same species (i.e. no abundance uncertainties), characterised by the same excitation energy (i.e. no temperature uncertainties) but by different collisional de-excitation rates. These diagnostics are sensitive to n_e in the density range around the critical density, while saturates at the high- and low-density regimes.

In the optical, typically the [O II]λ3726/[O II]λ3729 or the [S II]λ6717/[S II]λ6731 line ratios are used, and are sensitive to density variations in the range $\sim 50 - 10^4$ cm^{-3} (Osterbrock & Ferland, 2006). According to the spectral resolution of the observations, the two [O II] lines can be blended, as it happens for instance at the medium spectral resolution of SDSS.

The determination of chemical abundances

In the following, I provide a brief overview of the methods used to infer ISM chemical abundances of the gaseous phase. More detailed reviews on this topic are given by

Stasińska (2004), Peimbert et al. (2017) and Maiolino & Mannucci (2019).

Direct method The most reliable method to determine gas phase oxygen abundance is by measuring the electron temperature T_e of the nebula, the so-called direct or T_e method. Infact, CEL emissivity depends on the temperature T_e and the density n_e of the nebula. Typically, T_e can be estimated comparing the flux of auroral lines to the flux of nebular lines from the same species (see e.g. Pérez-Montero 2017), as described above. The density instead can be derived from the relative component intensity of density-sensitive doublets like [O II]$\lambda\lambda$3727,29 and [S II]$\lambda\lambda$6717,31, as explained above. Finally, the total elemental abundance can be estimated by assuming an ionisation correction to account for the abundance of unobserved ions. However, the direct method suffers from two main drawbacks. Indeed, auroral lines are generally too faint ($\sim 10 - 100$ times fainter than Hβ) to be easily detectable with typical sensitivity, especially at high metallicity (i.e., low T_e). Then, this method method may be sensitive to temperature fluctuations that may lead to underestimate the abundance if a correction is not applied (e.g., Peimbert & Costero 1969; Stasińska 2005).

The recombination line (RL) method The most direct way to derive metallicities is via the permitted, recombination lines (RL) of metal ions, such as O I$\lambda\lambda$8446,8447, O II$\lambda\lambda\lambda$4639,4642,4649, O IIIλ3265, O IVλ4631, N II$\lambda\lambda$4237,4242, N IIIλ4379, C IIλ4267, C IIIλ4647, and C IVλ4657 (e.g. Maiolino & Mannucci 2019). Their emissivity is characterised by a weak dependence on T_e and n_e, which reduces the impact of clumping and temperature fluctuation that can affect the direct method described above. However, similar to auroral lines, RLs are $10^{-3} - 10^{-4}$ fainter than Balmer lines, and thus are mainly accessible for bright H II regions, planetary nebulae and SN remnants (e.g. Maiolino & Mannucci 2019 and reference therein).

The strong emission lines (SEL) method An indirect way to measure metallicity stems from the calibration of ratios of strong emission lines (SEL), that are bright CELs and Balmer lines (e.g. Pagel et al. 1979; Alloin et al. 1979). Calibrations can be obtained empirically, in case the metallicity has been previously derived with the direct method (e.g. Pettini & Pagel 2004; Pilyugin & Thuan 2005; Pilyugin et al. 2012; Marino et al. 2013), but this is limited to low metallicities, at which auroral lines are observed in single objects. Alternatively, calibrations can be inferred theoretically, estimating oxygen abundance via photoionisation models (e.g. Kewley & Dopita 2002; Kobulnicky & Kewley 2004; Tremonti et al. 2004; Dopita et al. 2013, 2016). Photoionisation codes, such as CLOUDY (e.g. Ferland et al. 2017) and MAPPINGS (e.g. Dopita et al. 2013), generate grids of models out of which line ratios can be extracted and proposed as metallicity diagnostics (Kewley & Dopita, 2002; Dopita et al., 2013, 2016; Gutkin et al., 2016; Chevallard & Charlot, 2016), usually assuming a simple plane-parallel geometry, and that chemical abundances scale proportionally to solar, except for nitrogen whose abundance is assumed to scale with the global metallicity via a fixed relationship (see, e.g., Dopita et al. 2013; Nicholls et al. 2017). Generally, photoionisation models tend to predict oxygen abundances that are $0.2 - 0.3$ dex larger than those based on the direct method (e.g. Kewley & Ellison 2008; Curti et al. 2019b). To solve this issue, in recent years fully empirical calibrations based on electron temperature measurements have been developed. In those cases, the calibration is based on stacked spectra of many galaxies that are assumed to have the same metallicity, as based on their $M_\star$ and SFR (Andrews & Martini, 2013) or on their line ratios (Curti et al., 2017).

Among the most widely used metallicity diagnostics there are R23 $=$ ([O III]$\lambda\lambda$4959,5007 + [O II]$\lambda\lambda$3726,29)/Hβ (Pagel et al., 1979; Pilyugin & Thuan, 2005), O3N2 = ([O III]$\lambda\lambda$4959,5007/Hβ)/([N II]$\lambda\lambda$6548,84/Hα) (Pettini & Pagel, 2004; Marino et al., 2013; Curti et al., 2017), N2 = [N II]$\lambda\lambda$6548,84/Hα (Storchi-Bergmann et al., 1994; Denicoló et al., 2002), S3O3 = [S III]$\lambda\lambda 9069, 9532$/[O III]$\lambda\lambda 4959, 5007$ (Stasińska, 2006), together with other combinations of multiple line ratios (e.g. Pilyugin & Mattsson 2011; Pilyugin et al. 2012). Fig. 1.12 taken from Blanc et al. (2015) shows some examples. Each diagnostic has advantages and drawbacks, making it suitable in different situations. For instance, R23 is double-valued (e.g., Pagel et al. 1979; Dopita et al. 2006a), because the forbidden line flux at first increases with metallicity, then decreases towards higher abundances. This is due to the fact that the cooling by forbidden lines lowers T_e, making collisional excitation unlikely (see e.g. Dopita et al. 2006a). On the other hand, ratios of strong forbidden lines such as O3N2 can be very sensitive to q because of the very different ionisation potentials of N^{+} (14.5 eV) and O^{++} (35.1 eV), and thus is neither a clean abundance diagnostic nor a clean ionisation parameter diagnostic (see e.g. Figure 23 in Dopita et al. 2013), despite its dependence on T_e. Nevertheless, different metallicity calibrations, even when based on the same diagnostic, are generally not mutually consistent, leading to e.g. offsets of 0.2-0.6 dex in the absolute abundance scale (Kewley & Ellison, 2008; Blanc et al., 2015). The origins of this discrepancy are still largely debated in the literature. Finally, other line ratios such as O3O2 = [O III]$\lambda\lambda$4959,5007/[O II]$\lambda\lambda$3726,29, are mainly dependent on the ionisation parameter (as described above), and are only indirectly related to metallicity (see Fig. 1.12).

Overall, these line ratios do not only depend on metallicity, but also on the ionisa-

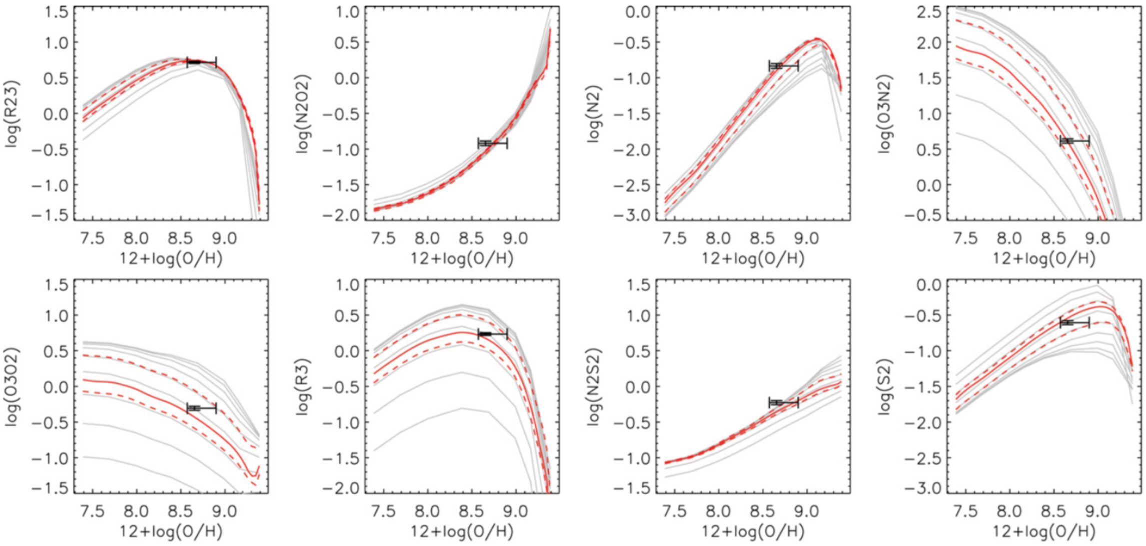

Figure 1.12: Examples of different line ratios as a function of metallicity derived from Dopita et al. (2013) photoionisation models. The different gray lines correspond to different values of the ionisation parameter q, while an example datapoint with its associated uncertainty is shown in black. The solid and dashed red lines represent the best-fit model and the 1σ confidence limits, respectively. This figure is taken from Blanc et al. (2015).

tion parameter, density, pressure or changes in abundance ratios, if different chemical species are taken into account. Moreover, in H II regions correlations exist between some of these parameters, such as the anti-correlation between metallicity and ionisation parameter (e.g. Dopita & Evans 1986; Nagao et al. 2006, see Sec. 1.1.3), and the correlation between metallicity and nitrogen abundance (Pérez-Montero & Vílchez, 2009; Pérez-Montero, 2014). Many line ratios have also to be corrected for the effect of interstellar extinction (as described below), introducing other uncertainties. Using multiple diagnostics at the same time or recursive techniques (e.g. Kobulnicky & Kewley 2004) can be useful methods to take into account these dependences. In the context of photoionisation models, SEL calibration can be made through codes that simultaneously fit multiple line ratios (Blanc et al., 2015; Chevallard & Charlot, 2016; Pérez-Montero, 2017).

Dust extinction

In the optical range, an object that suffers from dust extinction appears attenuated, but also “reddened”, since dust changes the shape of the spectrum by attenuating bluer wavelengths more than redder ones (interstellar reddening). The wavelength dependence stems from the size distribution of dust, constituted by large grains (0.1 μm) to account for the extinction at visible/NIR wavelengths, and small grains (0.016 μm) to account for the far-UV extinction at lower wavelengths. The amount of extinction measured in magnitudes at a certain wavelength is given by

$$A_\lambda = -2.5 log\left(\frac{F_\lambda}{F_{0\lambda}}\right) \tag{1.2}$$

where F_λ is the observed flux, while $F_{0\lambda}$ is the intrinsic one. The wavelength dependence of extinction is referred to as *extinction curve* $k_\lambda = A_\lambda/E(B-V)$, where $E(B-V) = A_B - A_V$ is the so-called *color excess*. Some examples of extinction curves for the Milky Way are shown in Fig. 1.13 (Li, 2006). Specifically, in the displayed wavelength range, the Galactic extinction curve can be approximated by an analytical formula involving one free parameter $R_V = A_V/E(B-V)$, that is the total-to-selective extinction ratio, with $R_V \approx 3.1$ for the Galactic average (Cardelli et al., 1989).

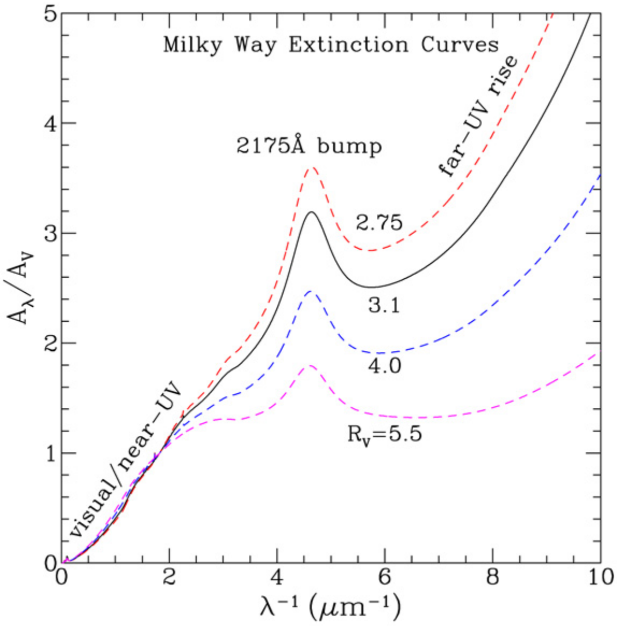

Figure 1.13: Different extinction curves for the Milky Way, as a function of R_V. This figure is taken from Li (2006).

In order to obtain the intrinsic emission line fluxes, a widely used method to infer $E(B-V)$ is based on the theoretical ratios of Balmer lines (i.e. Hα/Hβ ratio, or Balmer decrement), assuming an extinction curve:

$$E(B-V) = \frac{log(F_{H\alpha}/F_{H\beta}) - log(F_{0H\alpha}/F_{0H\beta})}{0.4(k_{H\alpha} - k_{H\beta})} \tag{1.3}$$

Given that the intrinsic Balmer decrement $F_{0H\alpha}/F_{0H\beta}$ is known from theory (2.86 for

Case B recombination, described in Sec. 1.1, assuming $T_e = 10^4$ K, Osterbrock & Ferland 2006), it is possible to infer E(B-V) from Eq. 1.3, and then, using Eq. 1.2, the intrinsic flux (e.g. Calzetti et al. 2000).

Excitation conditions in galaxies

Optical line ratios have long provided a good discriminator between AGN and SF contribution. An empirical diagnostic diagram was developed by Baldwin et al. (1981), who proposed the [N II]λ6584/Hα versus [O III]λ5007/Hβ diagram in order to discriminate H II-like sources from objects photoionised by a harder radiation field, such as a power-law continuum by an AGN or shock excitation. This classification scheme was enlarged and improved by Veilleux & Osterbrock (1987), who added the [S II]λ6717,31/Hα and the [O I]λ6300/Hα line ratios. These are known as the [N II], [S II], and [O I] Baldwin-Phillips-Terlevich (BPT) diagrams and involve line ratios that are not significantly separated in wavelength, minimising the effects of differential reddening by dust, and can discriminate among three different groups of emission line galaxies: those excited by starbursts, the Seyfert galaxies, and those found in the low-ionisation (nuclear) emission-line regions (LI(N)ERs, Heckman 1980; Belfiore et al. 2016). In addition, Kewley et al. (2001) (hereafter Ke01) created a theoretical maximum starburst line on the BPT diagrams, using a combination of stellar population synthesis models and detailed self-consistent photoionisation models. Galaxies lying above this line are likely to be dominated by an AGN. Finally, Kauffmann et al. (2003a) (hereafter Ka03) added an empirical line to divide pure star forming galaxies from Seyfert-H II composite objects, whose spectra are affected by significant contribution of both AGN and SF (see Fig. 1.14). Composite galaxies are likely to contain a metal-rich stellar population and an AGN. The [N II]/Hα line ratio is sensitive to metallicity (as described above), and thus can trace better the presence of low-level AGN than [S II]/Hα or [O I]/Hα. Indeed, owing to the saturation of [N II]/Hα ratio (at ≈ -0.5), the star forming sequence becomes almost vertical, but any AGN contribution leads to a shift towards this saturation level, allowing to distinguish them from SF-dominated galaxies (Kewley et al., 2006). Panel (a) of Fig. 1.14 shows the [N II] BPT-diagram for 85224 emission-line galaxies selected from the Sloan Digital Sky Survey the galaxy, analysed by Kewley et al. (2006). Star forming galaxies form a tight sequence, the star forming sequence, from low metallicities (low [N II]/Hα, high [O III]/Hβ) to high metallicities (high [N II]/Hα, low [O III]/Hβ). The AGN mixing sequence starts from the high metallicity end of the star forming sequence and extends towards high [O III]/Hβ and [N II]/Hα values. Fig. 1.14 panel (b) and (c) show the [S II]- and [O I]-BPT diagrams. The blue solid line represents the

Seyfert-LINER classification line (hereafter Ke06), determined by Kewley et al. (2006), that divides Seyfert galaxies and LI(N)ERs. Seyferts are AGN of low-moderate luminosity[4] and lie above the blue solid line, while LINERs are a class of characterised by very low-ionisation line emission lines, and thus lie below the Ke06 line. Their spectra are indeed dominated by low-ionisation lines such as [N II], [S II] and [O I], while higher ionisation lines (e.g. [O III]) are considerably weaker than in other AGN.

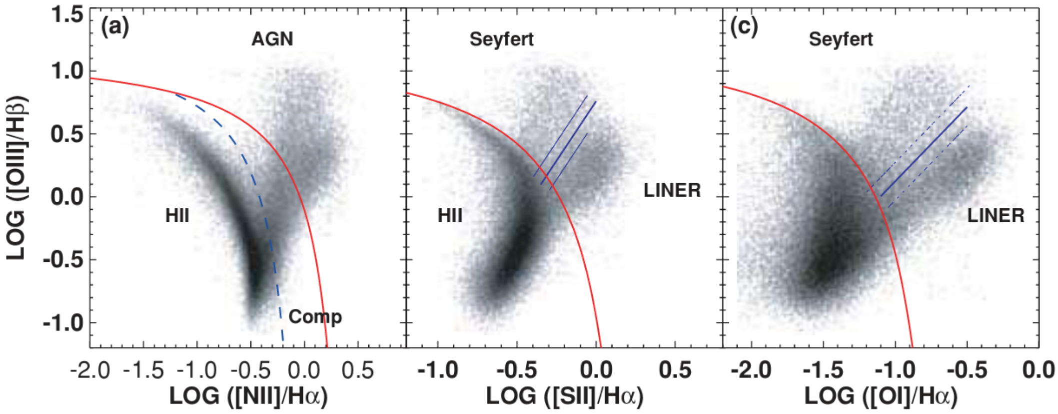

Figure 1.14: The [N II], [S II] and [O I] BPT diagrams. The red solid line represents the ke01 classification line, the blue dashed line the ka03 classification line, and the blue solid line is the ke06 classification line. This figure is taken from Kewley et al. (2006).

The development of powerful IFU spectrographs (see Sec. 1.4) has allowed to shed light on the impact of AGN activity on the host galaxy, by inspecting the spatial distribution of emission-line flux ratios. For instance, spatially resolved BPT diagrams allowed to identify in both star forming and quiescent galaxies extended (kpc scale) low-ionisation emission-line regions (LIERs), that can be confined in the central regions (cLIER) or be extended throughout the whole galaxy (eLIERs, e.g. Stasińska et al. 2008; Belfiore et al. 2016). This led to the conclusion that LIER emission is not necessarily due to a central point source but to diffuse stellar sources, identifying hot, evolved (post-asymptotic giant branch) stars as the most likely candidates Belfiore et al. (2016). Fig. 1.15 shows the galaxy classification scheme proposed by Belfiore et al. (2016), making use of spatially resolved BPT diagrams with a sample of 646 from the MaNGA survey. Panel (a) and (b) illustrate two examples of the typical star forming galaxies. The first one is characterised by prominent spiral arms populated by bright SF regions according both to the [N II]- and [S II]-BPT, that consist of several classical H II regions

---

[4] Seyfert galaxies have a bolometric luminosity of $L_{\rm bol} = 10^{42} - 10^{45}$, while the term "quasar" is often used to indicate AGN of higher luminosity. $L_{\rm bol}$ is defined as the total luminosity produced (or inferred, in case the accretion disc emission is not directly detected) by the accretion disc (Hickox & Alexander, 2018).

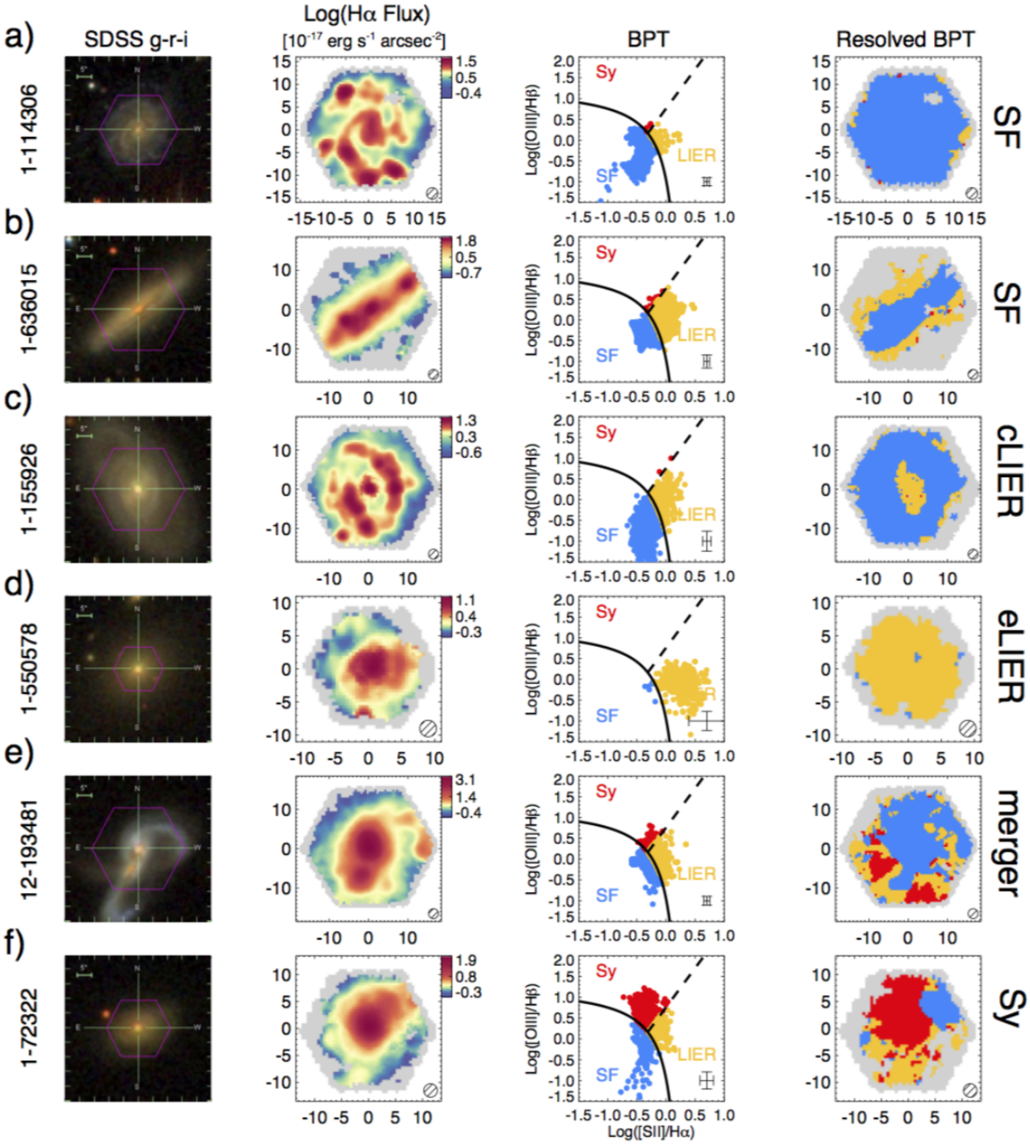

Figure 1.15: Examples of the different gas excitation conditions observed in MaNGA galaxies according to spatially resolved [S II]-BPT diagrams, with the corresponding BPT maps. SF, LIER and AGN spaxels are shown in blue, yellow and in red. According to the classification scheme explained in the text, the first two objects are classified as star forming, while the other galaxies as cLIER, eLIER, merger and Seyfert, respectively. On the left, the g-r-i images composite from SDSS with the MaNGA hexagonal FOV overlaid are shown. The hatched circle in the bottom-right corner of the MaNGA maps represents the MaNGA PSF. This figure is taken from Belfiore et al. (2016).

given the MaNGA kpc resolution (Mast et al., 2014). The second instead has the typical ionisation structure of strongly star forming edge-on discs, with a disc dominated by SF, and outskirts related to LIER excitation. Panel (c) and (d) show cLIER and eLIER, respectively, while panel (e) and (f) illustrate examples of mergers and Seyfert galaxies. Mergers are characterised by star forming spaxels in the central regions and in the tails, and LIER-like and Seyfert-like line ratios in the rest of the galaxy. Seyferts instead are generally dominated by spaxels photoionised by the nuclear source and are often associated with disturbed gas kinematics, such as outflows and other non-virial motions.

Spatially resolved BPT diagrams can be a useful tool also to investigate the ionisation properties of outflows, and thus the processes behind the often co-spatial extreme kinematics of the ionised gas (e.g. Sharp & Bland-Hawthorn 2010; McElroy et al. 2015; Karouzos et al. 2016b. This is one of the topic covered in this dissertation (see Chapter 2), that is inspired by the work of Karouzos et al. (2016b), who studied six local AGN ($z < 0.1$) using Gemini Multi-Object Spectrograph IFU, spatially and kinematically resolving [N II]-BPT maps, finding strong evidence that connects the extreme kinematic (broad) component of the ionised gas and its driving mechanism with the AGN.

1.3.2 Molecular gas diagnostics

Molecular gas plays a significant role in galaxy evolution, as it is the fuel of SF and possibly of AGN accretion. Molecular rotational lines are characteristic of the physical condition of the ISM and may be used to constrain the gas emission densities and the sources of the incident radiation field.

As introduced in Sec. 1.1, CO is one of the most abundant molecules in ISM, and thus it is considered a good tracer of the molecular gas and a fundamental tool in the study of the SF energetics and the effects of AGN activity (Mashian et al., 2015). The effective critical densities for excitation rise from 2.1×10^3 for CO(1–0) to $\approx 10^6\,\mathrm{cm}^{-3}$ for $J_{\mathrm{up}} \simeq 13$. This makes CO(1–0) the most sensitive to the total gas reservoir, including more diffuse components, whereas $J_{\mathrm{up}} > 1$ transitions are increasingly sensitive to the denser star forming gas (Daddi et al., 2015). Furthermore, the lowest three rotational transitions of CO have low excitation potentials, so they trace the cooler gas component ($T \simeq 10 - 20\,K$), and can be relatively easily observed with ground-based radio and submillimeter telescopes in many local galaxies. The mid-J CO line emission originates from warm molecular gas, as the upper-level energies range from 55 to 500 K above the ground state, and can be excited through collisions, especially with H_2 and He (Narayanan & Krumholz, 2014). The higher is the J, the higher is the density required to make collisions more likely. On the other hand, FIR CO rotational lines, with $J_{up} \geq 13$, arise from states $500 - 7000\,\mathrm{K}$ above ground. These transitions trace the warmer and denser molecular gas in the center of galaxies and are difficult to excite solely with SF. Therefore, they represent the best way to test models that distinguish between AGN and SF contribution (Mashian et al., 2015). In Tab. 1.1, the main properties of CO transitions are reported.

Table 1.1: Summary of CO rotational transitions (up to $J_{up} = 13$) fundamental parameters. E.P. is the excitation potential of the upper level above ground. The critical density is the density at which the rate of the collisional depopulation of a quantum level equals the spontaneous radiative decay rate. This table is adapted from (Carilli & Walter, 2013).

Transition	E.P. $[K]$	λ $[\mu m]$	n_{crit} $[cm^{-3}]$
J=1-0	5.5	2601.0	2.1×10^3
J=2-1	16.6	1300.0	1.1×10^4
J=3-2	33.2	867.0	3.6×10^4
J=4-3	55.3	650.3	8.7×10^4
J=5-4	83.0	520.2	1.7×10^5
J=6-5	116.2	433.6	2.9×10^5
J=7-6	154.9	371.7	4.5×10^5
J=8-7	199.1	325.2	6.4×10^5
J=9-8	248.9	289.1	8.7×10^5
J=10-9	304.2	260.2	1.1×10^6
J=11-10	364.0	237.0	$> 10^6$
J=12-11	431.3	217.0	$> 10^6$
J=13-12	503.0	200.4	$> 10^6$

Overall, the study of the CO spectral line energy distribution (SLED) shape can shed light on the properties and the heating source of molecular gas, as presented in Chapter 4 for two local Seyfert galaxies (e.g. Narayanan & Krumholz 2014). Fig. 1.16 shows different CO SLEDs, allowing the comparison among their shapes. For instance, the average SLED of (ultra) luminous infrared galaxies ((U)LIRGs, in pink), and the Milky Way SLEDs (in blue) show a relevant discrepancy at high-J transitions, where the (U)LIRGs show higher gas excitation. Indeed, (U)LIRGs, exhibiting an extremely high IR luminosity ($L_{8-1000\,\mu\mathrm{m}} > 10^{11} - 10^{12}$ $\mathrm{L}_{\odot}$ for LIRGs and ULIRGs, respectively), host an intense starburst and/or AGN activity, and are often part of a merging galaxy group (Sanders & Mirabel, 1996).

1.4 Integral field spectroscopy of nearby galaxies

Our understanding of galaxy formation was fostered by highly multiplexed spectroscopic surveys like SDSS at low redshift and with a variety of facilities at higher redshift. The statistical power of the SDSS galaxy sample has revealed how the SFRs, chemical en-

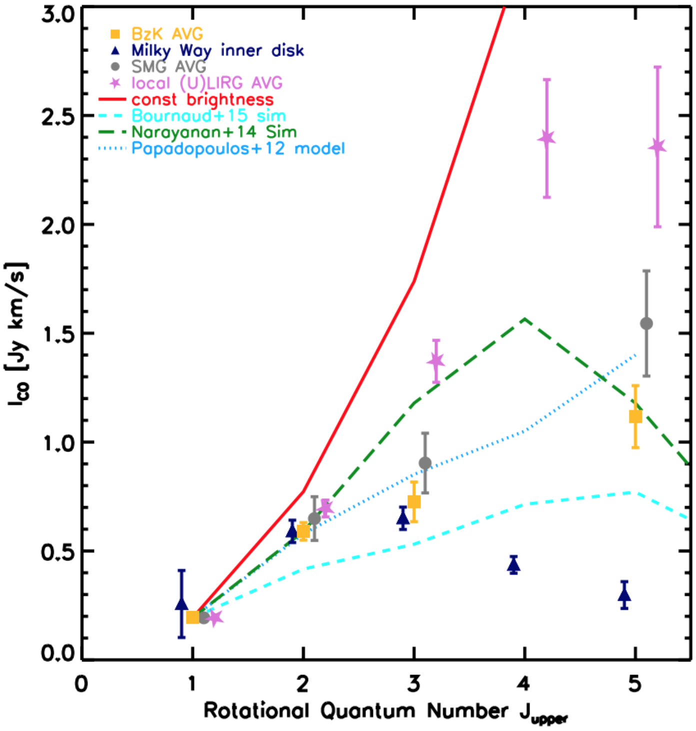

Figure 1.16: Comparison between different observed CO SLEDs, as indicated in the legend. All SLEDs are normalized to the CO(1–0) of the average BzK (star forming galaxies selected with B, z and K filters) SLED, except the Milky Way, which is normalized using CO(2–1). The dotted blue, dashed-dotted green and dashed cyan curves are models taken from Papadopoulos et al. (2012), Narayanan & Krumholz (2014) and Bournaud et al. (2015). This figure is taken from Daddi et al. (2015).

richment, stellar populations, morphologies, and BH growth rates of galaxies vary with stellar mass, environment, and cosmic time (e.g. Kauffmann et al. 2003a,b; Tremonti et al. 2004; Brinchmann et al. 2004; Kewley et al. 2006; Mannucci et al. 2010; Johansson et al. 2012). However, SDSS like all the spectroscopic surveys larger than a few hundred galaxies suffers from a serious drawback. Indeed, these surveys sample just the circumnuclear regions of each targeted galaxy (with a 3”-diameter fibre in the case of SDSS), with the aim of deriving integrated spectroscopic properties. Consequently, the complexity of galaxy internal structure (e.g. spiral arms, bulge, H II regions) is completely lost. Furthermore, the inferred measurements may not be representative of the entire galaxy, but biased by the fact that they target only its center along a particular axis. Therefore, large aperture corrections (e.g. Brinchmann et al. 2004; Salim et al. 2007) must be taken into account to derive galaxy properties, even though it is not trivial to calibrate them accurately.

IFS offers the possibility of peering inside galaxies, and thus of resolving their internal structures and kinematics. Specifically, an integral field spectrograph collects spectra over a two-dimensional FOV. Basically, it allows to observe an astronomical object in three dimensions in one go: each pixel of the image is associated with a full spectrum (i.e. spectral pixel, or "spaxel"), measuring the intensity of the light at each wavelength (that can be converted into a velocity towards or away from Earth). These instruments consist of both a spectrograph and an IFU, that divides the FOV into a continuous array. The main techniques to do this step are through a lenslet array (e.g. SAURON@CFHT, OSIRIS@Keck), fibres (e.g. PMAS@CAHA, MaNGA@APO), or an image-slicer (e.g. SINFONI and MUSE@VLT), illustrated in Fig. 1.17. In a lenslet array, first the source image is split up by a microlens array, concentrated in small dots, and then dispersed by the spectrograph. The microlens is tilted in order to prevent the spectra from overlapping, but this limits the length of the spectrum and the packing efficiency of the CCD. The technique that uses a 2D bundle of optical fibres that transfer the input light to the spectrograph (with or without lenslets) is the most common. Finally, the image-slicer technique uses mirrors to segment the source image in thin horizontal sections and to order the slices end to end to form the slit of the spectrograph.

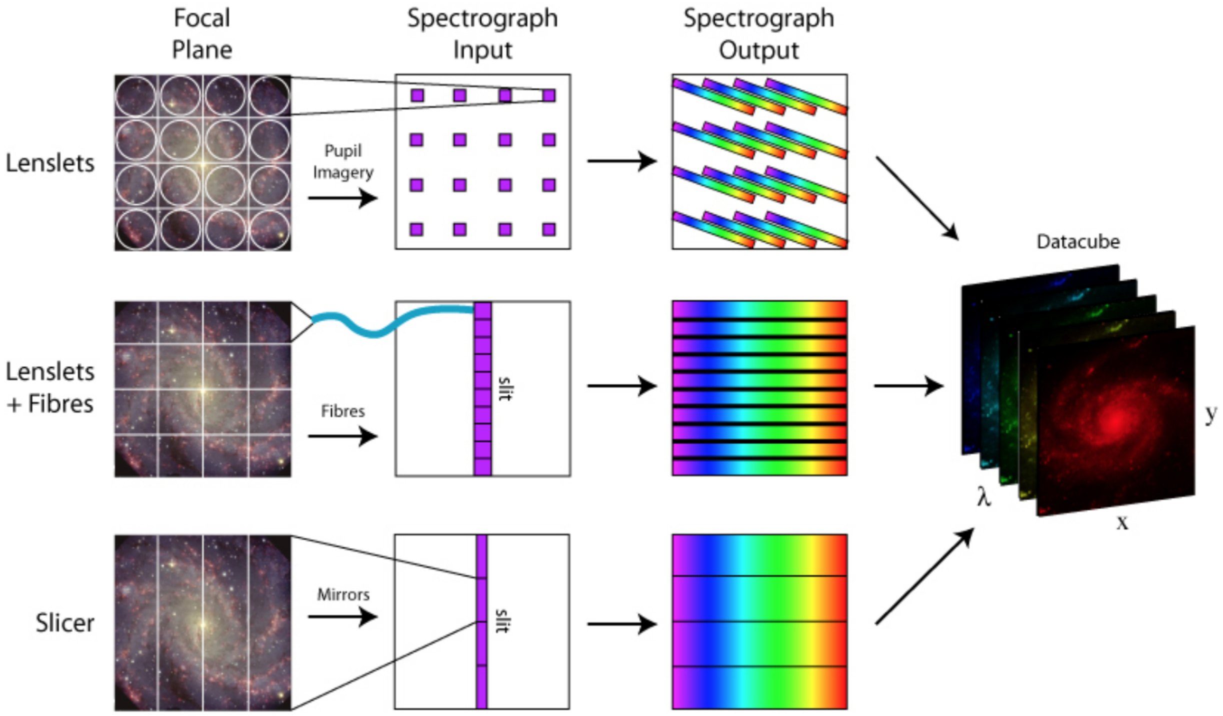

Figure 1.17: Main techniques for achieving integral field spectroscopy. Credit: M. Westmoquette, taken from INTEGRAL FIELD SPECTROSCOPY WIKI.

In the last twenty years, local galaxies have been explored through IFU spectrographs in a variety of surveys, pioneered by SAURON (72 E/S0/Sa galaxies, de Zeeuw et al. 2002) and ATLAS (260 E/S0 galaxies, Cappellari et al. 2011), that took a step forward in the classification of early-type galaxies, exploiting their IFU kinematics instead of their morphology. Subsequent surveys such as VENGA (30 spiral galaxies, Blanc et al. 2013) prioritised high spatial resolution to investigate SF and the ISM, while others such as discMass (146 face-on disc galaxies Bershady et al. 2010) optimised their sample selection and instrument setup, providing insight on the internal mass profiles and mass-to-light ratios of disc populations. Then, the development of IFS instruments in the NIR such as SINFONI (Eisenhauer et al., 2003) at the VLT has allowed to investigate spatially resolved properties of galaxies at $z \sim 2$. For instance, these observations revealed that clumpy and highly star forming high-z galaxies generally display a regular rotating discs (Förster Schreiber et al., 2009; Law et al., 2009) and gave new insights on large-scale winds and outflows (Cresci et al., 2015a; Carniani et al., 2016).

State-of-the-art instruments, such as the ALMA telescope (Wootten & Thompson, 2009) in the submillimeter wavelength range and the MUSE spectrograph (Bacon et al., 2010) in the optical at the VLT, are allowing astronomers to obtain spatially resolved observations with an unprecedented spatial sampling (e.g. of 0.2" for MUSE) on entire galaxies both in the local and high-z Universe. ALMA is an interferometer, and thus exploits a completely different technology, but still delivers data cubes, in which the third axis is frequency, and so the final data products are comparable to an IFU with up to a million spaxels. For instance, the Physics at High Angular resolution in Nearby GalaxieS (PHANGS) Collaboration is aiming at inspecting GMC scales (~ 50 pc) with ALMA and MUSE large programs, analysing CO emission at cloud scales across the discs of 74 nearby galaxies and MUSE data across a subsample of 19 galaxies (at a matched resolution) to map the ionised gas and stellar populations (e.g. Kreckel et al. 2018). This is giving new insights on the time evolution of star forming regions, thanks to the discovery of a systematic spatial offset between molecular clouds and H II regions, explained in terms of rapid evolutionary cycling between GMCs, SF, and feedback effects (Kreckel et al., 2018; Kruijssen et al., 2019). Another novel MUSE large program is GAs Stripping Phenomena in galaxies (GASP, Poggianti et al. 2017), that is aimed at studying gas removal processes in galaxies, investigating the ionised gas phase and the stellar component both in the discs and in the extraplanar tails of local jellyfish galaxies[5] in different environments (galaxy clusters and groups), as well as a control sample of disc galaxies with no morphological anomalies. Concerning high redshift galaxies instead, an

---

[5] Objects with optical signatures of unilateral debris or tails reminiscent of gas-stripping processes (e.g. Ebeling et al. 2014).

ESO Large Program among others aimed at spatially investigating their dynamics, gas excitation properties and chemical abundances is given by the KLEVER survey (Curti et al., 2019a), that exploits KMOS, first multi-IFUs spectrograph in the NIR at VLT (Sharples et al., 2006), to investigate a sample of 120 galaxies ($1.2 < z < 2.5$).

All these surveys are focused on small samples, and thus they cannot provide an unbiased view of the galaxy population in the nearby and high-z Universe. In the local Universe, this challenge has been recently addressed by the CALIFA (Sánchez et al., 2012), Sydney-AAO Multi-object Integral field (SAMI, Croom et al. 2012) and MaNGA (Bundy et al., 2015) surveys on 600, 3400 and ~ 10000 galaxies, respectively. MaNGA represents by far the largest IFS survey and is one of the three major programs of the fourth generation SDSS (SDSS-IV), with the aim of observing 10000 local ($z \sim 0.03$) galaxies within 2020. These data have been using to carry out quantitatively studies to understand the life history of present-day galaxies, from their initial birth and assembly, through their ongoing growth via SF and mergers, to their death from quenching of SF at late times (e.g. Belfiore et al. 2016, 2018).

1.5 Thesis aims

The aim of this dissertation is probing and interpreting ISM properties in different types of galaxies and in different conditions within a galaxy, both in the optical and in the molecular wavelength range, through the use of IFS, observed diagnostics and models (e.g. photoionisation, shock). Indeed, high and low ionisation emission lines (e.g. [O III]λ5007 and [N II]λ6584) in the optical, originating from nebulae photoionised by massive stars or gas located in the inner kiloparsecs of AGN represent one of most powerful tracers of density, temperature, level and source of excitation, and chemical composition of the ISM gas. In this context, in Chapter 2, I show my work on the MAGNUM survey, that aims at observing nearby galaxies hosting an AGN to investigate the physical conditions of the NLR, the interplay between nuclear activity and SF, and the properties and acceleration mechanisms of outflows. Specifically, I wanted to spatially track the variations of ISM properties and the relative contributions of different ionisation mechanisms within the extended outflows in the central regions of these local Seyferts. To do so, I used a novel approach based on the gas kinematics to differentiate between high velocity gas in the outflow and gas at rest in the disc in each spaxel of our datacubes.

In Chapter 3 I explore the ISM properties in local star forming galaxies, to investigate sistematically the impact of the ionisation condition variations in the measurement of e.g. gas phase metallicity. In particular, the first part of Chapter 3, is about the study of a local dwarf star forming galaxy, characterised by extended outflowing bubbles, demonstrating among other things the importance of taking into account ionisation parameter variations to infer the gas metallicity. This suggested to analyse the relation between the still poorly understood ionisation parameter and galaxy properties, using a larger sample of star forming galaxies, exploiting the statistic power of the MaNGA survey, as explained in the second part of Chapter 3.

On the other hand, the relative strengths of the rotational transitions of CO lines in the submillimeter wavelength range depend on the ISM properties and gas excitation mechanisms as well, meaning that a high ratio of high-excitation to low-excitation CO lines can be used for instance as a diagnostic of AGN heating. This topic is discussed in Chapter 4, in which I describe a project focused on investigating the properties of molecular gas in nearby Seyfert galaxies, and assessing whether and to what extent the radiation produced by the accretion onto the central BH affected the CO line emission, on the basis of ALMA and Herschel data.

Chapter 2

Interstellar medium properties in the nuclear region of AGN hosts and in their outflows

Mainly based on: (i) "The MAGNUM survey: different gas properties in the outflowing and disk components in nearby active galaxies with MUSE", **M. Mingozzi***, G. Cresci, G. Venturi, A. Marconi, F. Mannucci, M. Perna, F. Belfiore, S. Carniani, B. Balmaverde, M. Brusa, C. Cicone, C. Feruglio, A. Gallazzi, V. Mainieri, R. Maiolino, T. Nagao, E. Nardini, E. Sani, P. Tozzi, S. Zibetti, 2019, A&A, Volume 622, id.A146, 28 pp; (ii) "MAGNUM survey: A MUSE-Chandra resolved view on ionised outflows and photoionisation in the Seyfert galaxy NGC1365", G. Venturi, E. Nardini, A. Marconi, S. Carniani,* **M. Mingozzi***, G. Cresci, F. Mannucci et al., 2018, A&A, Volume 619, id.A74, 21 pp; (iii) the recent discovery of tentative evidence of positive feedback in one galaxy of the MAGNUM survey (***M. Mingozzi** et al. in preparation).*

The gas located in the inner kiloparsecs of active galaxies plays a crucial role in many important processes; it fuels accretion onto the central black hole (BH) in active galactic nuclei (AGN) and absorbs the energy and momentum injected in the interstellar medium (ISM) by the AGN, becoming a key ingredient in the BH-galaxy co-evolution. The AGN radiation acts as a flashlight that illuminates and ionises the nearby gas, forming the narrow-line region (NLR). Outflows powered by accretion disk winds and relativistic jets interact with the NLR gas, possibly inducing feedback effects on the host galaxy (Cresci & Maiolino, 2018). As explained extensively in Chapter 1 of this manuscript, feedback mechanisms can be both negative and positive. Negative feedback appears necessary to explain the present-day scaling relations between the host galaxy properties and BH mass and prevent galaxies from overgrowing (e.g. Silk & Rees 1998; Fabian 2012). Positive feedback instead acts through two different channels, triggering SF both in the galaxy disk, compressing the gas in the interstellar and circumgalactic galactic by outflows and jet (e.g. Rees 1989; Nayakshin & Zubovas 2012; Bieri et al. 2016; Zubovas & King 2016), and within the outflowing gas, as a consequence of cooling and fragmentation processes (Ishibashi & Fabian, 2012; Gaibler et al., 2012; Zubovas et al., 2013; Silk, 2013; Ishibashi et al., 2013; Zubovas & King, 2014; Dugan et al., 2014; Ishibashi & Fabian, 2014; El-Badry et al., 2016; Mukherjee et al., 2018).

The NLR can extend by several kpc in Seyfert galaxies (i.e. extended narrow-line regions, ENLRs, e.g. Greene et al. 2012; Sun et al. 2017, 2018) and has a relatively low-density ($n_e \sim 10^2 - 10^4$ cm^{-3}, e.g. Vaona et al. 2012). It comprises ionised and neutral gas set-up in clouds, emitting low- and high-ionisation lines, such as [S II]λ6717,31 and [O III]$\lambda\lambda$4959,5007, respectively, of elements photoionised by the non-stellar continuum emission of the AGN (e.g. Netzer 2015). These clouds are often observed to be entrained in AGN-driven outflows (e.g. Hutchings et al. 1998; Crenshaw & Kraemer 2000) that, especially in nearby Type 2 AGN, are observed to be fan-shaped, showing clearly defined biconical structures (e.g. Storchi-Bergmann et al. 1992; Das et al. 2006; Crenshaw et al. 2010; Cresci et al. 2015b; Venturi et al. 2018). Therefore, resolved NLRs are ideal laboratories for investigating in detail the effects of feeding and feedback, and for constraining the ionisation structure of the emitting regions.

There have been many studies aimed at identifying the ionisation source in Seyfert and star forming galaxies through the observed intensity ratios. Photoionisation models have had remarkable success in reproducing high-ionisation AGN lines, such as [O III]λ5007 (Ferguson et al., 1997; Komossa & Schulz, 1997), while the excitation mechanisms for low-ionisation lines (e.g. [N II], [S II], [O I]) in the region overlapping with star forming galaxies remains uncertain. Furthermore, fast radiative shocks produced by different phenomena (e.g. cloud-cloud collisions, the expansion of H II regions into the surrounding ISM, outflows from young stellar objects, supernova blast waves, outflows from active and starburst galaxies, and collisions between galaxies) can be a powerful ionising source and can provide an important component of the total energy budget, and in some circumstances dominate the line emission spectrum (Dopita & Sutherland, 1995, 1996; Allen et al., 2008).

The recent development of powerful integral field unit (IFU) spectrographs has allowed us to make a considerable step forward in understanding galaxy evolution, providing spatially resolved information on the kinematics of the gas and stars, and on galaxy properties, in terms of gas ionisation and chemical abundances (e.g. the CALIFA, Sánchez et al. 2012; SAMI, Allen et al. 2015; and MaNGA, Bundy et al. 2015 surveys, locally, and Förster Schreiber et al. 2009; Law et al. 2009; Cresci et al. 2010; Contini et al. 2012; Wisnioski et al. 2015; Stott et al. 2016; Turner et al. 2017 at high redshift). Integral field spectroscopy (IFS) is a powerful tool also for the study of outflows, both in the local Universe (e.g. Storchi-Bergmann et al. 2010; Sharp & Bland-Hawthorn

2010; Riffel et al. 2013; McElroy et al. 2015; Cresci et al. 2015b; Karouzos et al. 2016a,b) and at higher redshift (e.g. Cano-Díaz et al. 2012; Liu et al. 2013; Cresci et al. 2015a; Perna et al. 2015; Harrison et al. 2016; Carniani et al. 2016; Förster Schreiber et al. 2018). Integral field data can indeed shed light on the impact of AGN activity on the host galaxy through the kinematic signatures visible in emission-line profiles and the spatial distribution of emission-line flux ratios.

In this Chapter, I present our results obtained with the Measuring Active Galactic Nuclei Under MUSE Microscope (MAGNUM) survey (P.I. Marconi, Cresci et al. 2015b; Venturi et al. 2017, 2018, Venturi Ph.D. Thesis, Venturi et al. in preparation), which studies nearby AGN ($D_L < 50$ Mpc) by probing the physical conditions of the NLRs/ENLRs, and the interplay between nuclear activity and star formation (SF), and the properties of outflows thanks to the unprecedented combination of spatial and spectral coverage provided by the integral field spectrograph MUSE at VLT (Bacon et al., 2010).

Specifically, I use IFS to conduct detailed studies on how ISM properties (e.g. density, temperature, ionisation, reddening) and the relative contributions of different ionisation mechanisms vary within individual galaxies, all characterised by prominent conical or biconical outflows. Taking a step forward, I kinematically disentangle the disk and outflow components, and compare their gas properties. This also allowed us to detect in one galaxy of the sample, Centaurus A, two blobs dominated by SF ionisation spatially not correlated with this gas disk, but apparently embedded in the AGN ionisation cone.

2.1 The MAGNUM survey

MAGNUM galaxies are selected by cross-matching the optically selected AGN samples of Maiolino & Rieke (1995) (MR95) and Risaliti et al. (1999) (R99), and Swift-BAT 70-month Hard X-ray Survey (SB-70m, Baumgartner et al. 2013), choosing only sources observable from Paranal Observatory ($-70° < \delta < 20°$) and with a luminosity distance $D < 50$ Mpc. On the one hand, SB-70m selects optically-obscured AGN, excluded from MR95 and R99. On the other hand, the optical selection based on gas emission lines used in MR95 and R99 allows us to include also Compton-thick AGN, thanks to the spatially-extended nature of the optical line emission. This selection leads to a total sample of 72 active galaxies that will be introduced in Venturi et al. (in preparation), explaining in detail the selection criteria, data reduction, and analysis, and investigating the kinematics of the ionised gas (see also Venturi Ph.D. Thesis).

In this Chapter we present our results for the first nine MAGNUM Seyfert galaxies, selected for their broad multi-wavelength coverage, namely Centaurus A, Circinus, NGC 4945, NGC 1068, NGC 1365, NGC 1386, NGC 2992, NGC 4945, and NGC 5643, focusing on their ISM properties. These galaxies are shown in Fig. 2.1 with the MUSE field of view (FOV) superimposed in red. A large part of this sample (Centaurus A, Circinus, NGC 1068, NGC 1365, NGC 1386, NGC 2992 and NGC 4945) is part of the program 094.B-0321(A) (P.I. Marconi). IC 5063, instead, belongs to the Science Verification program 60.A-9339(A) (P.I. Marconi/Hawthorn/Salvato), while NGC 5643 is taken from 095.B-0532(A) (P.I. Carollo). Tab. 2.1 summarises their main properties, while in the following, we briefly describe their main features.

Table 2.1: Basic data of the MAGNUM survey galaxies presented in this Chapter. The columns report for each galaxy the redshift z, taken from NED, the Seyfert type, the distance (in Mpc) obtained from HYPERLEDA best distance modulus (i.e. the weighted average between the redshift distance modulus corrected for infall of the Local Group towards Virgo and the weighted average of the published z-indipendent distance measurements), and the size of the FOV (in kpc) covered by our MUSE data. This table is taken from Venturi et al. (in preparation).

Galaxy	Type	z	D [Mpc]	d_{FOV} [kpc]
Centaurus A	Sy2	0.001825	3.68 ± 0.04	1.140 ± 0.001
Circinus	Sy2	0.001448	4.2 ± 0.07	1.3 ± 0.2
IC 5063	Sy2	0.011348	46 ± 7	14 ± 2
NGC 1068	Sy2	0.003793	10.5 ± 1.7	3.3 ± 0.5
NGC 1365	Sy1.8	0.005457	17.29 ± 0.19	5.33 ± 0.06
NGC 1386	Sy2	0.002895	16.4 ± 0.8	5.1 ± 0.2
NGC 2992	Sy1.9	0.00771	32 ± 7	10 ± 2
NGC 4945	Sy2	0.001878	3.47 ± 0.03	1.069 ± 0.009
NGC 5643	Sy2	0.003999	16 ± 7	5 ± 2

2.1.1 MAGNUM galaxies

Centaurus A (Seyfert 2 - $D_L \sim 3.82$ Mpc - 1" $\sim$ 18.5 pc) is an early-type galaxy characterised by a major axis stellar component, a minor axis dust-lane, and a gas disk. The last follows the dust-lane and comprises the majority of the observed ionised, atomic, neutral, and molecular gas (Morganti, 2010). It is characterised by the presence of a spectacular double-sided radio jet revealed in both the radio and X-rays (e.g. Blanco et al. 1975; Hardcastle et al. 2003), which was found to match a diffuse highly ionised halo of [O III] (Kraft et al., 2008) first identified by Bland-Hawthorn & Kedziora-Chudczer (2003).

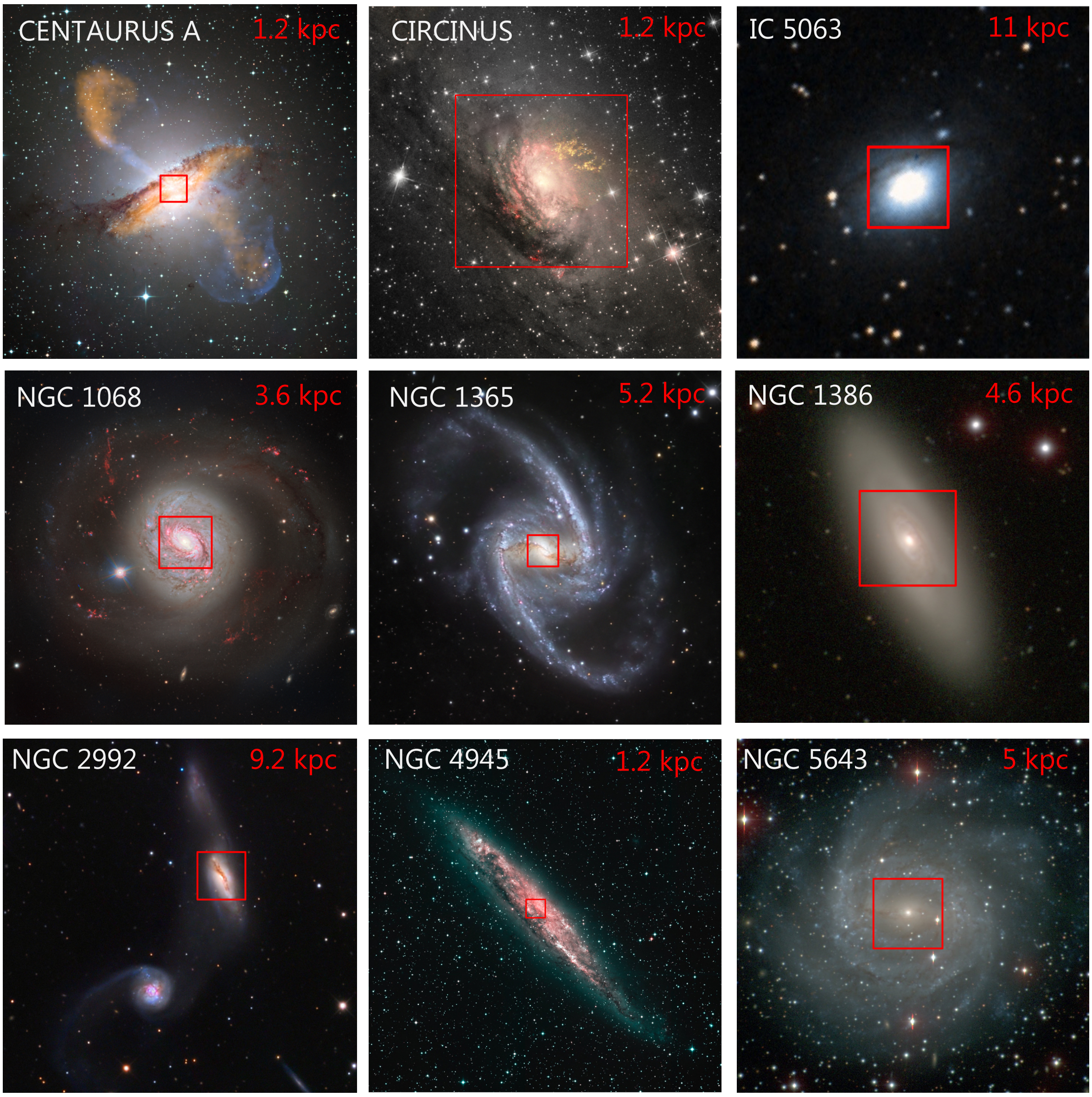

Figure 2.1: The MAGNUM survey. From top to bottom, from left to the right: composite images of Centaurus A (credit: optical, ESO/WFI; submillimetre, MPIfR/ESO/APEX/A.Weiss et al.; X-ray, NASA/CXC/CfA/R.Kraft et al.), Circinus (credit: J. Schmidt, licensed under CC BY 2.0), IC 5063 (credit: STScI/NASA, Colored & Healpixed by CDS), NGC 1068 (credit: ESO), NGC 1365 (credit: ESO/IDA/Danish 1.5 m/R. Gendler, J-E. Ovaldsen, C. Thöne, and C. Feron), NGC 1386 (credit: Ho et al. 2011), NGC 2992 (credit: Adam Block/Mount Lemmon SkyCenter/University of Arizona), NGC 4945 (credit: ESO) and NGC 5643 (credit: Ho et al. 2011). The red box indicates the MUSE FOV, whose length is reported in red on the top left corners of each image. These images are taken from Venturi Ph.D. Thesis.

Circinus (Seyfert 2 - $D_{\rm L} \sim 4.2$ Mpc - 1" $\sim$ 20.4 pc) is a nearby gas rich spiral, hosting one of the nearest Seyfert 2 nuclei known. The Seyfert 2 nature of Circinus is supported by the optical images showing a spectacular one-sided and wide-angled kpc-scale [O III] cone, first revealed by Marconi et al. (1994) (see also Veilleux & Bland-Hawthorn 1997), and the optical/IR spectra rich in prominent and narrow coronal lines (Oliva et al., 1994; Moorwood et al., 1996). Furthermore, from the X-ray spectral analysis Circinus is a highly obscured AGN, but with strong thermal dust emission dominated by heating from nuclear SF (Matt et al., 2000).

IC 5063 (Seyfert 2 - $D_L \sim 45.3$ Mpc - 1" ∼ 219.6 pc) is a massive early-type galaxy with a central gas disk and a radio jet that propagates for several hundred parsec before it extends beyond the disk plane (Morganti et al., 1998). An extended (∼ 20 kpc) [O III]-dominated double ionisation cone with an X morphology is observed (Colina et al., 1991), ubiquitously dominated by photoionisation from the AGN (Sharp & Bland-Hawthorn, 2010). In this galaxy there is one of the most spectacular examples of jet-driven outflow, with similar features in the ionised, neutral atomic, and molecular phase, since the radio plasma jet is expanding into a clumpy gaseous medium, possibly creating a cocoon of shocked gas which is pushed away from the jet axis (Morganti et al., 1998; Sharp & Bland-Hawthorn, 2010; Tadhunter et al., 2014; Dasyra et al., 2015; Oosterloo et al., 2017).

NGC 1068 (Seyfert 2 - $D_L \sim 12.5$ Mpc - 1" ∼60 pc) is one of the closest and archetypal Seyfert 2 galaxies. This galaxy also hosts powerful starburst activity (e.g. Lester et al. 1987; Bruhweiler et al. 1991) and is characterised by a large-scale oval and a nuclear stellar bar aligned NE-SW (Scoville et al., 1988; Thronson et al., 1989). NGC 1068 is known to host a radio jet, observed from X-ray to radio wavelengths (Bland-Hawthorn et al., 1997). Its activity seems confined to bipolar cones centred on the AGN, intersecting the plane of the disk with an inclination of ∼ 45°, such that the disk interstellar medium to the NE and SW sees the nuclear radiation field directly (Cecil et al., 1990; Gallimore et al., 1994). This galaxy shows clear evidence of outflowing material in both the ionised (e.g. Macchetto et al. 1994; Axon et al. 1997; Cecil et al. 2002; Barbosa et al. 2014) and molecular gas (García-Burillo et al., 2014; Gallimore et al., 2016), possibly driven by the radio jet (Cecil et al. 1990; Gallimore et al. 1994; Axon et al. 1997), located in the north-east and south-west directions.

NGC 1365 (Seyfert 1.8 - $D_L \sim 18.6$ Mpc - 1" ∼ 90.2 pc) is a local spiral, characterised by a strong bar and prominent spiral structure, displaying nuclear activity and ongoing SF. A comprehensive review about the early works on this object is given by Lindblad (1999). In Venturi et al. (2018), we carried out a detailed multi-wavelength study of the ionised gas and outflow in this galaxy, in terms of physical properties, kinematics, and ionisation mechanisms from MUSE in optical band and Chandra satellite in

X-rays. Specifically, we mapped the SE-NW biconical outflow, extended out to about 2.5 kpc in both directions, ionised by the AGN and prominent in [O III] emission. Hα emission, instead, traces SF in a circumnuclear ring and along the bar of the galaxy. Interestingly, soft X-rays are mostly due to thermal emission from the star-forming regions, but the AGN photoionised component nicely matches the [O III] emission from MUSE. Furthermore, we mapped the mass outflow rate of the galactic ionised outflow, that matches with that of the nuclear X-ray wind and then decreases with radius, implying that the outflow either slows down or that the AGN activity has recently increased. The hard X-ray emission from the circumnuclear ring instead suggests that SF might in principle contribute to the outflow.

NGC 1386 (Seyfert 2 - $D_{\rm L} \sim 15.6$ Mpc - 1" $\sim$ 76 pc), classified as a Sb/c spiral galaxy, is one of nearest Seyfert 2 galaxies and has an inclination of $\sim 65°$ with respect to the line of sight. Lena et al. (2015) analysed the gas and stellar kinematics in the inner regions (530×680 pc), obtained from IFS GEMINI South telescope observations, revealing the presence of a bright nuclear component, two elongated structures to the north and south of the nucleus, and low-level emission extending over the whole FOV, probably photoionised by the AGN. Furthermore, Lena et al. (2015) identified a bipolar outflow aligned with the radiation cone axis. This feature is resolved in HST observations (Ferruit et al., 2000) into two bright knots that represent the approaching and receding sides of the outflow, respectively. Finally, Lena et al. (2015) suggested the presence of an outflow and/or rotation in a plane roughly perpendicular to the AGN radiation cone axis, extending 2"−3" on both sides of the nucleus, characterised by an enhanced velocity dispersion and coincident with a faint, bar-like emission structure revealed by HST imaging (Ferruit et al., 2000).

NGC 2992 (Seyfert 1.9 - $D_{\rm L} \sim 31.5$ Mpc - 1" $\sim$150 pc) is a spiral galaxy hosting a Seyfert nucleus and interacting with the companion galaxy NGC 2993, located to the south-east. This galaxy is classified as a Seyfert 1.9 in the optical, on the basis of a broad Hα component with no corresponding Hβ component in its nuclear spectrum, although its type has changed between 1.5 and 2 according to past observations (Trippe et al., 2008). Looking at the optical image of this galaxy, a prominent dust lane extending along the major axis of the galaxy and crossing the nucleus stands out (Ward et al., 1980). Opposite ENLR cones extend along either side of the disk with large opening angles, and are both easily visible due to the high inclination of NGC 2992 (e.g. Allen et al. 1999). Evidence of a wide biconical large-scale outflow, extending above and below the plane of the galaxy and possibly driven by AGN activity (Friedrich et al., 2010), comes from Hα and [O III] emission and soft X-ray observations (e.g. Colina et al. 1987;

Colbert et al. 1996b,a; Veilleux et al. 2001).

NGC 4945 (Seyfert 2 - $D_{\rm L} \sim 3.7$ Mpc - 1" ~18 pc) is an almost perfectly edge-on spiral galaxy, well known for being one of the closest objects where AGN and starburst activity coexist. Its central region is characterised by a very strong obscuration, associated with a prominent dust lane aligned along the major axis of the galactic disk, revealed by near- and mid-infrared spectroscopy typical of highly obscured ultra-luminous infrared galaxies (ULIRGs) (Pérez-Beaupuits et al., 2011). This galaxy is characterised by a biconical outflow, clearly visible from the [N II] emission map that we showed in Venturi et al. (2017), where the NW lobe is far brighter than the SE lobe, which is observed only at 15" from the centre, likely being completely dust-obscured at smaller radii. The AGN presence is only supported by X-rays observations (e.g. Guainazzi et al. 2000), meaning that either its UV radiation is totally obscured along all lines of sight or that it lacks UV photons with respect to X-rays, implying in both cases a non-standard activity (Marconi et al., 2000).

NGC 5643 (Seyfert 2 - $D_{\rm L} \sim 17.3$ Mpc - 1" ~84 pc) is a barred almost face-on Seyfert 2. This galaxy is characterised by a well-known ionisation cone extending eastward of the nucleus and parallel to the bar (e.g. Schmitt et al. 1994; Simpson et al. 1997; Fischer et al. 2013), and by a sharp, straight dust lane extended from the sides of the central nucleus out to the end of the bar, roughly parallel to its major axis and clearly visible to the east of the nucleus (Ho et al., 2011). Our MUSE data of this target has been already published by Cresci et al. (2015b), who analysed the double-sided ionisation cone, revealed as a blueshifted, asymmetric wing of the [O III] emission line, up to a projected velocity of ~ -450 km s^{-1}, parallel to the low-luminosity radio and X-ray jet, and possibly collimated by a dusty structure surrounding the nucleus. Furthermore, Cresci et al. (2015b) found signs of positive feedback triggered by the outflowing gas in two star forming clumps, located at the edge of the dust lane of the bar (see Silk 2013), and also characterised by a faint CO(2–1) emission (Alonso-Herrero et al., 2018).

2.1.2 Data analysis

The data reduction was performed using the MUSE pipeline (v1.6). The final datacubes consist of $\sim 300 \times 300$ spaxels, for a total of over 90000 spectra with a spatial sampling of 0.2" × 0.2" and a spectral resolution going from 1750 at 4650 Å to 3750 at 9300 Å. The FOV of 1' × 1' covers the central part of the galaxies, spanning from 1 to 10 kpc, according to their distance. The average seeing of the observations, derived directly from foreground stars in the final datacubes, is ~ 0.8". The datacubes were analysed making use of a set of custom python scripts in order to fit and subtract the stellar continuum in each single-spaxel spectrum and fit the emission lines with multiple Gaussian components where needed. Here we summarise the main steps of the data analysis.

Stellar continuum fitting

First of all, a Voronoi adaptive binning (Cappellari & Copin, 2003), that is a technique that allows to obtain bins with different spatial extension but fixed signal-to-noise ratio (S/N) ratio in the data, was performed in order to achieve an average S/N per wavelength channel of 50 on the continuum under 5530 Å, where stellar features are more prominent. This threshold allows us to fit also the fainter regions of the FOV, preserving the maximum spatial resolution. In order to fit the stellar continuum and derive the systemic velocity and velocity dispersion of the stellar absorption lines, we applied the Penalized Pixel-Fitting (pPXF; Cappellari & Emsellem 2004) code on the Voronoi-binned spaxels. Basically, this fast and simple algorithm recovers galaxy stellar kinematics by fitting a template to an observed spectrum, applying the maximum penalized likelihood formalism (Cappellari & Emsellem, 2004). We employed as a template a linear combination of Vazdekis et al. (2010) synthetic spectral energy distributions for single stellar population models in the wavelength range $4750-7500$ Å. Note that at this stage our aim is only to reproduce the shape of the stellar features and derive the bulk velocity and velocity dispersion of the stellar population, and not to get more detailed physical information from the models. Instead, a linear baseline was used to fit the local continuum around the [S III]λ9069 emission line, since this line is not contaminated by underlying absorptions. The main emission lines lying in the selected wavelength range (Hβ - [O III]$\lambda\lambda$4959,5007 - [O I]$\lambda\lambda$6300,64 - Hα - [N II]$\lambda\lambda$6548,84 - [S II]$\lambda\lambda$6717,31) were included in the fit as well, in order to better constrain the absorption underlying the Balmer lines. Fainter lines and regions affected by sky residuals were masked. The emission lines were fitted with one, two, three, or four Gaussian components (1c, 2c, 3c or 4c) according to the peculiarities of the line profile, tying the velocity and width of each component to be the same for all the lines and leaving the intensities free to vary, apart from the [O III], [O I], and [N II] doublets, where an intrinsic ratio of 0.333 between the two lines was used (see e.g. Storey & Zeippen 2000).

A reduced χ^2 ($\tilde{\chi}^2$) selection to the different fits is made in each spaxel, in order to define where multiple components were really needed to reproduce the observed spectral profiles, with the idea of keeping the number of parameters of the fit as low as possible and using multiple components only in case of complex non-Gaussian line profiles. This happens mainly in the central parts of the galaxies and in the outflowing cones. Specifically, $\tilde{\chi}^2$ is computed in a narrow wavelength range surrounding Hβ, [O III]λ5007, Hα and [N II]$\lambda\lambda$6548,84. Then, the $\tilde{\chi}^2$ distribution is fitted with an asymmetric Gaussian and a Lévi distribution, that can reproduce its bulk and tails, respectively. If the peak of the Lévi distribution has a lower $\tilde{\chi}^2$ value with respect to the intersection between the two curves, then the $\tilde{\chi}^2$ value at the intersection is defined as "cut". Otherwise, the value of the peak itself is defined as "cut". Then, in each spaxel, if the corresponding $\tilde{\chi}^2$ of the 1c fit is lower than the "cut" of the 1c fit distribution (1c-cut), then this is chosen as best-fit. Otherwise, the 1c fit is discarded and 2c fit is taken into account, following the same methodology. However, if the 2c fit is discarded as well, but the 1c-cut is lower than the 2c-cut, then the 1c fit becomes the best-fit. If this is not the case, the 3c fit is taken into account following the same scheme, and so on.

The stellar continuum fit included also a multiplicative and an additive polynomials of degree m and a (with $7 < m < 10$ and $a = 2$) to account for any spectrum deformation not present in the models (e.g. reddening). Finally, the fitted stellar continuum in each Voronoi bin was subtracted spaxel by spaxel, rescaling the modelled continuum emission in each bin to the median of the observed continuum of each spaxel.

Broad line region fitting

Since NGC 1365 and NGC 2992 host a Seyfert 1 nucleus (i.e. an AGN showing large Balmer and Fe line components due to the presence of a broad line region, BLR), an additional template must be taken into account in the fitting procedure of those bins where the nuclear emission gives a contribution in the spectra, in order to simultaneously reproduce the BLR features and the BH accretion disk continuum. Since the BLR is unresolved in our data, this happens only in a limited circular area around the center, and thus this extra-component is fixed at zero everywhere else. This template, fixed in shape and velocity, is added to the stellar continuum and emission line fit described above, and is composed by:

- a Gaussian function to account for the broad Balmer lines, with the same velocity and width;
- a set of CLOUDY models and spectra to reproduce the [Fe II] emission lines of the BLR;
- an additive ($a = 2$) and multiplicative ($7 < m < 10$) polynomials to fit the AGN continuum.

Emission line fitting

From the continuum-subtracted cube, we generated a spatially smoothed data cube and a Voronoi-binned data cube. The former is obtained by spatially smoothing the cube with a Gaussian kernel having $\sigma = 1$ spaxel (i.e. 0.2”), without degrading significantly the spatial resolution, given the observational seeing. The latter, produced by applying a Voronoi binning in the range $\sim 4850 - 4870$ Å in the vicinity of Hβ, requiring an average S/N per wavelength channel of at least 3, is used to make comparisons among the galaxies (see Sec. 2.3).

Finally, in each spaxel (or bin in the Voronoi-binned cube), the gas emission lines (Hβ - [O III]$\lambda\lambda$4959,5007 - [O I]$\lambda\lambda$6300,64 - Hα - [N II]$\lambda\lambda$6548,84 - [S II]$\lambda\lambda$6717,31) were fitted in the same spectral range used for the stellar fitting, while the residual continuum was fitted with a linear baseline, free to vary to account for small deviations of the overall residuals from null value. To do this, we employed the MPFIT procedure (Markwardt, 2009), taking into account one, two, three, or four Gaussians to reproduce the emission line profile, tying the velocity and widths of each component to be the same for all the lines and leaving the intensities free to vary (apart from the [O III], [O I], and [N II] doublets), as described above. Note that the width of all the emission lines was forced to be greater than MUSE spectral resolution (~ 65 km/s at [O III]-Hβ wavelengths; ~ 50 km/s at [N II]-Hα-[S II] wavelengths). Then, the [S III]λ9069 emission line fit is performed analogously, fixing its velocity and width to the values obtained for the other emission lines in the previous fit. The same $\tilde{\chi}^2$ selection described above is applied to choose the best-fit in each spaxel (bin). Fianlly, the flux of each emission line is the sum of the integrated fluxes of the adopted Gaussians.

2.1.3 Spatially resolved maps

The analysis of MUSE data described above leads to map the total fitted line profiles and to trace the kinematics of the stars and the warm ionised gas. As an example, Fig. 2.2 and Fig. 2.3 show the flux and kinematic maps of one galaxy of the sample, NGC 1365, that we investigated in detail in Venturi et al. (2018).

Specifically, the left and right panels of Fig. 2.2 show the [O III]λ5007 ([O III] hereafter) and Hα emission of the total fitted line profile maps. Clearly, Hα dominates in an elongated region spanning from NE to SW parallel to the bar direction. On the other hand, [O III] is enhanced in the perpendicular direction, with a clear conical shape to the SE of the center and, even though slightly less defined in shape, to the NW, too (see also Edmunds et al. 1988; Storchi-Bergmann & Bonatto 1991; Veilleux et al.

2003; Sharp & Bland-Hawthorn 2010). Indeed, according to e.g. Hjelm & Lindblad (1996), the SE cone is in the near side, above the disk. Interestingly, the Hα spatial distribution is completely different from the [O III], since it is dominant in a $\sim$ 20” × 20” (1.6 kpc × 0.8 kpc) elongated circumnuclear ring hosting hotspots, consistent with the star-forming ring reported e.g. by Kristen et al. (1997) in narrowband HST images and by Forbes & Norris (1998) in radio. According to Lindblad (1999), star-forming rings are frequently observed in barred spirals and are ascribed to the presence of the inner Lindblad resonance (ILR, Binney & Tremaine 2008), with inflowing gas slowing down and accumulating between the outer and the inner ILR, creating a massive ring with enhanced star formation (e.g., Shlosman 1996). More details are given in Venturi et al. (2018).

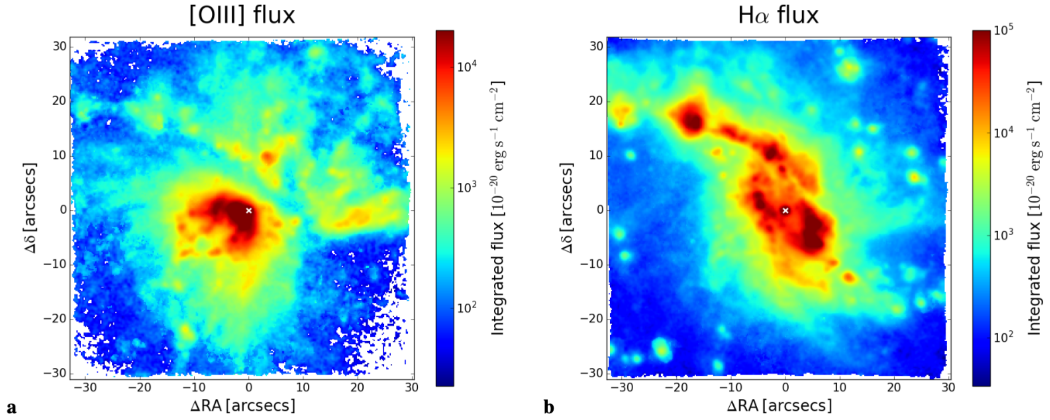

Figure 2.2: (a) [O III]λ5007 and (b) Hα emission of the total fitted line profile maps, obtained from fitting of the star-subtracted (smoothed with $\sigma = 1$ spaxel Gaussian kernel) data cube. The reported flux is per spaxel and a signal-to-noise cut of 3 has been applied. The FOV covers $\sim 5.3 \times 5.3$ kpc. This figure is taken from Venturi et al. (2018).

Fig. 2.3, instead, allows to visually appreciate the outflow shape and location within the galaxy. The stellar velocity map (Fig. 2.3a) has been obtained from the fit of stellar continuum carried out on the Voronoi-binned data cube, and clearly shows the rotation of the stars in the galactic disk, approaching the observer to the NE and receding to the SW direction. The twisted shape in the central region corresponds to the boundary where the velocity changes sign and is likely due to the presence of the bar. The [O III] velocity map (Fig. 2.3b) instead is the 1st-order moment of the [O III] total line profile resulting from the fit of the star-subtracted smoothed data cube. In addition to the rotational field, it shows other complex motions, that can be isolated and highlighted by subtracting spaxel-by-spaxel the stellar rotation (Fig. 2.3c). This reveals a clumpy double-conical outflow approximately in the SE-NW direction, with the SE and NW

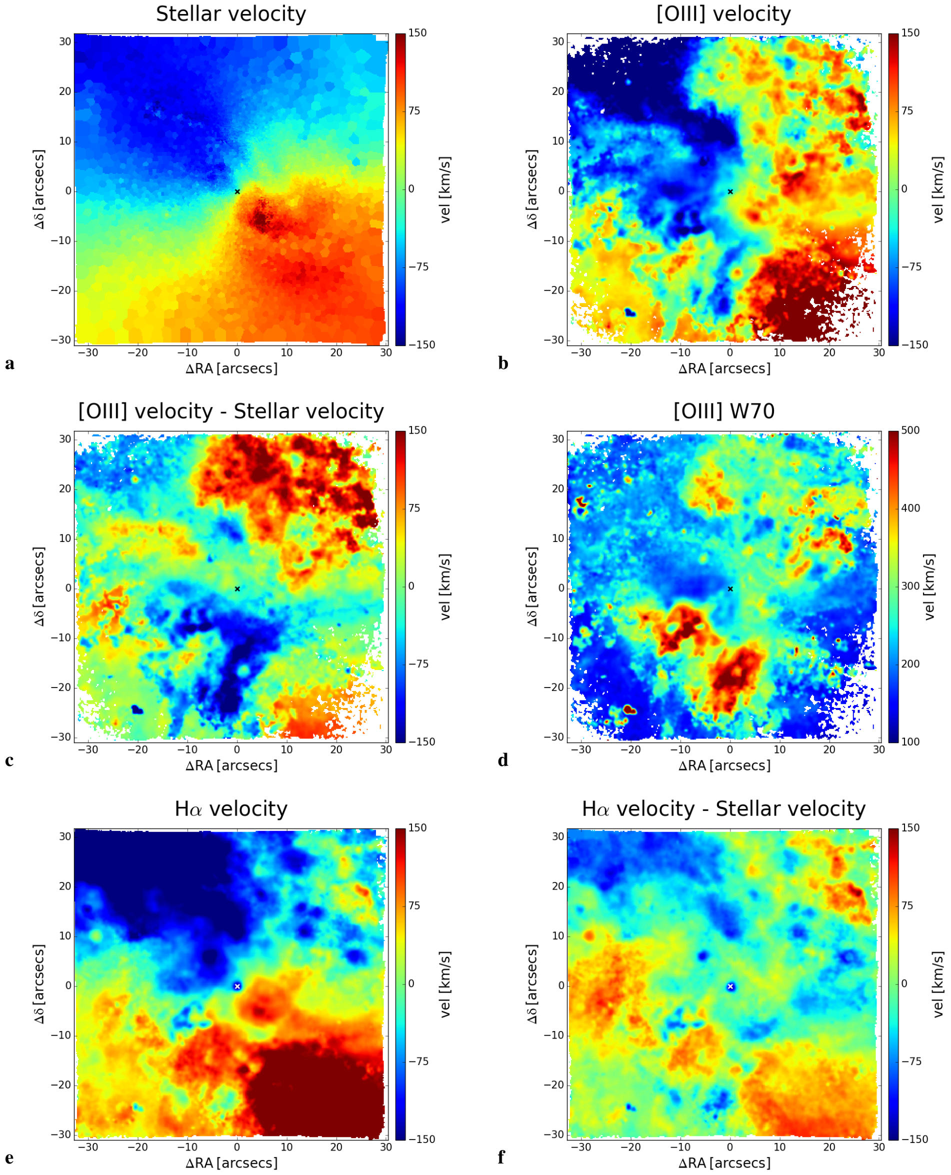

Stellar velocity

[OIII] velocity

[OIII] velocity - Stellar velocity

[OIII] W70

Hα velocity

Hα velocity - Stellar velocity

Figure 2.3: (a) Stellar velocity map of NGC 1365, with respect to the systemic velocity (1630 km s^{-1}). (b) [O III] velocity map with respect to the systemic velocity. This map has been re-smoothed with a $\sigma = 1$ spaxel Gaussian kernel for a better visual output, and a signal-to-noise cut of 3 was applied (this holds for the other maps reported in panels c, d, e, f). (c) [O III] velocity subtracted spaxel-by-spaxel by the stellar velocity. (d) [O III] W70 (i.e. difference between the 85th-percentile and 15th-percentile velocities of the fitted line profile) map. (e) Hα velocity map with respect to the systemic velocity. (f) Hα velocity map spaxel-by-spaxel subtracted by the stellar velocity. East is to the left. This figure is taken from Venturi et al. (2018).

cone having approaching and receding velocities, respectively. The shape and structure of the outflow are well-traced by the [O III] W70 velocity (Fig. 2.3d), that is the difference between the velocities including 85% and 15% of the flux of the total fitted line profile.

High W70 values come from the regions of the outflow, composed by the kinematic components belonging to disk, bar and outflow. The kinematics of the ionised gas in the disk can be better inspected from the Hα velocity map (see Venturi et al. 2018 for more details). Fig. 2.3e and Fig. 2.3f show the Hα velocity map with respect to the rest frame velocity and to the stellar velocity, respectively. The Hα kinematics is primarily dominated by two thick lanes aligned with the bar in the NE-SW direction (see Fig. 1a, Venturi et al. 2018), with opposite velocities with respect to the stellar rotation. This non-circular motions may indicate an inflow of material along the bar of NGC 1365, supported also by the presence of the star-forming ring shown in the right panel of Fig. 2.2 and described above.

2.2 Gas properties: disk versus outflow

Excitation and ionisation conditions, and dust attenuation of the ISM in each MAGNUM galaxy can be investigated through specific emission-line ratios. Thanks to IFS, we explore the different properties of the disk and the outflow of our galaxies by separating and analysing the different gas components across the MUSE FOV.

Specifically, we define velocity channels of $\sim$ 50 km/s, ranging from -1000 km/s to $+1000$ km/s around the main emission lines (Hβ - [O III] - [O I] - Hα - [N II] - [S II] - [S III]), centring the zero velocity to the measured stellar velocity in each spaxel of the MUSE FOV for all the galaxies, since the stellar velocity is generally a good approximation of the gas velocity in the disk. In order to derive the flux in each velocity bin, we integrate the fitted line profile, performed as described in Sec. 2.1.2, within each velocity channel of the emission lines taken into account. However, Centaurus A is characterised by a strong misalignment between stars and gas (e.g. Morganti 2010), and thus we consider the global systemic velocity ($v_{\rm sys}$ = 547 km/s) as a reference for the gas disk velocity.

We associate the velocity channels close to the core of the lines in the fitted line profile with the disk (hereafter disk component), and the sum of the redshifted and blueshifted channels with the outflow (hereafter outflow component). Specifically, the disk component comprises velocity in the range -100 km/s < v < 100 km/s for Circinus, NGC 1365, and NGC 1386, and -150 km/s < v < 150 km/s for the other galaxies, while the outflow component is associated with velocities v > +150 km/s and v < -150 km/s for Circinus, NGC 1365 and NGC 1386, v > +250 km/s and v < -250 km/s for NGC 1068, and v > +200 km/s and v < -200 km/s for the other galaxies. These values are chosen after an accurate spaxel-by-spaxel analysis of the spectra in the outflowing regions of the galaxies. Overall, the disk component represents the low-velocity component of the ionised gas, which is rotating similarly to the stars, while the outflow component (i.e. the high-velocity component) is moving faster than the stellar velocity, and is partly blueshifted and partly redshifted with respect to it. Since we are looking at the central regions of AGN galaxies, the NLR is present in both the disk and in the outflow components.

Figure 2.4 shows a single spaxel spectrum extracted from the Circinus galaxy datacube to exemplify our division between disk (in green) and outflow (in red) components for the [O III]$\lambda\lambda$4959,5007 doublet. In many works, disk and outflow are separated according to the width of the two Gaussian components used in fitting the lines (narrower and broader, respectively). In our analysis, this approach is not feasible since disk and outflow components are both present in many spaxels. Furthermore, in the central regions the line profiles are very complex, and their fit requires three or four Gaussians. This means that the distinction between disk and outflow through the width of the fitted components only is not trivial. Note that our approach is not a rigorous method for discriminating between the gas in the outflow and the disk, but a convenient way to analyse in detail the outflow features, as we show in the following.

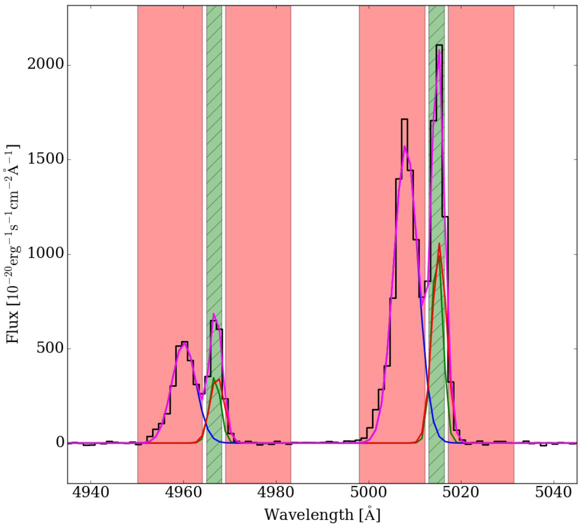

Figure 2.4: [O III]$\lambda\lambda$4959,5007 doublet in a single spaxel spectrum of the continuum-subtracted cube of the Circinus galaxy. The disk (-100 km/s $<$ v $<$ 100 km/s) and outflow (-1000 km/s $<$ v < -150 km/s and 150 km/s $<$ v $<$ 1000 km/s) components taken into account, highlighted in green and red, respectively, are superimposed to show an example of our procedure. The disk component is centred to the value of the stellar velocity in this spaxel ($\sim$ 460 km/s), obtained previously by fitting the original data cube with pPXF. The magenta line represents the result of the three-component fit (blue, green, and red Gaussians), performed with MPFIT to reproduce the observed line profiles.

Because the Hα emission is in general dominated by the disk, while the outflow is enhanced in [O III] (e.g. Venturi et al. 2018), in Fig. 2.5 we show the Hα disk component flux maps, superimposing the [O III]λ5007 outflow component flux contours (not corrected for dust reddening) for all the galaxies, using the method described above to discriminate between the two components. The blueshifted and redshifted outflowing components are indicated in blue and red, respectively. For each velocity bin, we only select the spaxels with a $S/N > 5$, computed by dividing the integrated flux in the velocity channels by the corresponding noise. The noise is estimated from the standard deviation of the data-model residuals of the fit around each line (within a range about 60 to 110 Å wide, depending on the line). Looking at Fig. 2.5, it can be seen that the disk flux maps and the outflow contours are clearly different from each other. The outflow component is often extended in a kpc-scale conical or biconical distribution, as can be clearly seen in Circinus (north-west cone), IC 5063 (north-west and south-east cones), NGC 2992 (north-west and south-east cones), NGC 4945 (north-west and south-east cones), and NGC 5643 (east and west cones). In Centaurus A the outflow component is mainly distributed in two cones (direction north-east and south-west) in the same direction of the extended double-sided jet revealed both in the radio and X-rays (e.g. Hardcastle et al. 2003), and located perpendicularly with respect to the gas in the disk component. Unfortunately, since for this galaxy the stellar velocity cannot be taken as a reference, in some regions we underestimate the gas velocity of the disk component. Consequently, a portion of the disk is still present in the outflowing component. Also in NGC 1365, the outflow component flux map has a biconical shape extended in the south-east and north-west directions, while the disk component appears to be completely different, being dominated by an elongated circumnuclear SF ring and by the bar. Unfortunately, similar to Centaurus A, a portion of the disk is still present in our outflowing gas selection, because of the high velocity reached by the gas along the bar (see Venturi et al. 2018 for more details). NGC 1068 is almost face-on, allowing us to admire the spiral arms of the disk, traced by the disk component, and preventing the outflowing component from having a clear biconical distribution, but to be broadly extended in all the inner region of the observed FOV. As reported in Sec. 2.1.1, both the ionised and molecular outflow already observed in this galaxy are observed in the north-east and south-west directions (e.g. Cecil et al. 2002; García-Burillo et al. 2014). Finally, in NGC 1386 the outflow component does not show a well-defined conical distribution, but appears to be located in the very inner region of the galaxy, with two elongated structures to the north and south of the nucleus, corresponding to nuclear bipolar outflows already revealed by Ferruit et al. (2000) and Lena et al. (2015).

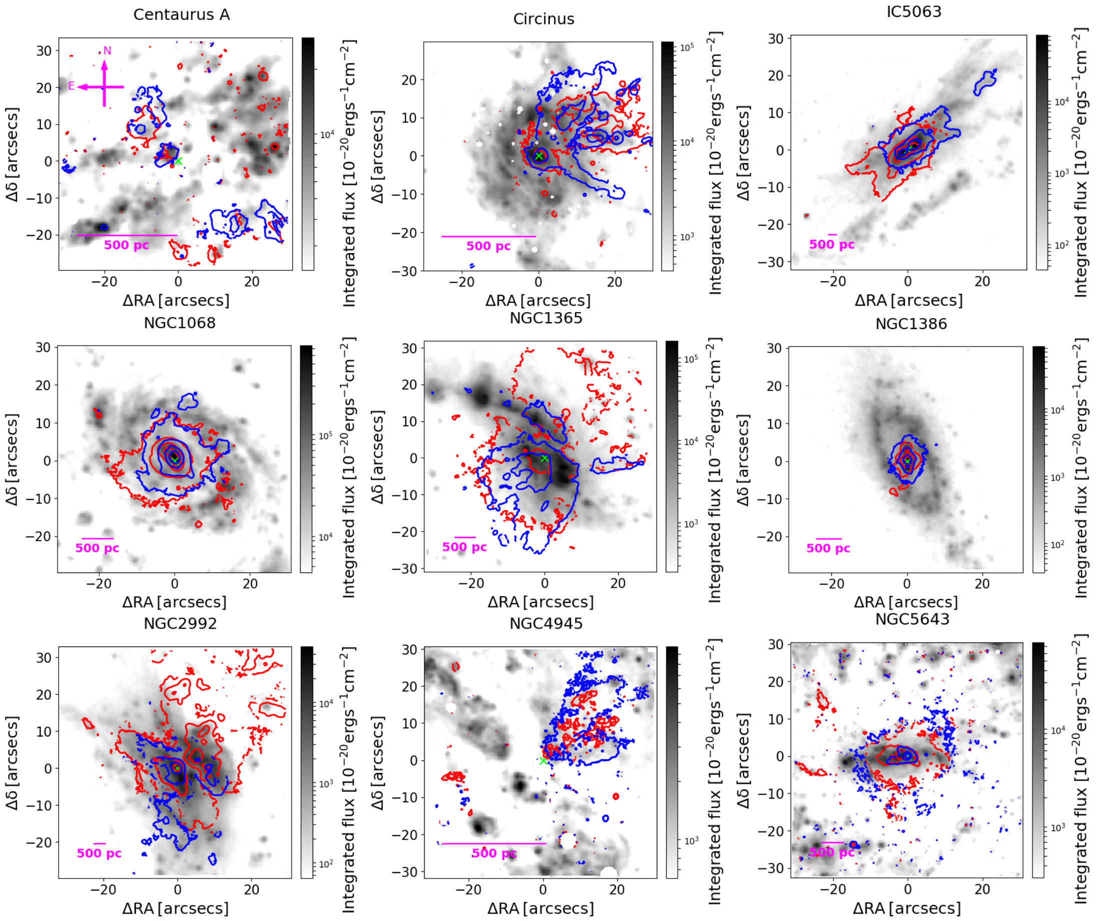

Figure 2.5: Hα disk component flux maps (not corrected for dust reddening) for all the galaxies, namely Centaurus A, Circinus, IC 5063, NGC 1068, NGC 1365, NGC 1386, NGC 2992, NGC 4945, and NGC 5643. [O III]λ5007 outflow component flux contours are superimposed for all the galaxies. The blueshifted and redshifted outflow emission (in blue and red, respectively) is often extended in a kiloparsec-scale conical or biconical distribution. For each velocity bin, we show only the spaxels with a S/N > 5. The magenta bar represents a physical scale of ∼ 500 pc. East is to the left, as shown in the first image on the left. The white circular regions are masked foreground stars. The cross marks the position either of the Type 1 nucleus (i.e. peak of the broad Hα emission), if present, or the peak of the continuum in the wavelength range 6800 − 7000 Å.

Note that in almost all galaxies the (bi)conical outflow is detected in both its blueshifted and redshifted components, which are often overlapping. For example, this can be clearly seen in NGC 4945, where the north-west cone has approaching velocities at its edges and receding ones around its axis, while the south-east cone has the opposite behaviour, with receding velocities at its edges and approaching ones around its axis. This was already revealed by Venturi et al. (2017) through the kinematical maps of the [N II] line emission.

2.2.1 Extinction, density, and ionisation parameter

We calculated the visual extinction A_V through the Balmer decrement Hα/Hβ, assuming a Calzetti et al. (2000) attenuation law, with $R_V = 3.1$ (i.e. galactic diffuse ISM) and a fixed temperature of $T_e = 10^4$ K. The top panel of Fig. 2.6 illustrates the extinction map of Circinus obtained for the total line profile (without separating disk and outflow component), where we exclude all the spaxels that have S/N < 5 on the emission lines involved. In this case, we defined the S/N of a line as the ratio between the peak value of the fitted line profile and the standard deviation of the data-model residuals of the fit around the line. The highest values $A_V \gtrsim 5$ come from the galaxy disk, while the conical outflow is characterised by $A_V \gtrsim 2$. The extinction maps for the other galaxies are shown in Fig. 2.17, showing that the highest values of A_V come mainly from dust lanes (e.g. Centaurus A and NGC 2992), gas disks as shown for Circinus (e.g. NGC 4945), spiral arms (e.g. NGC 1068 and NGC 1386), or gas flowing along the bar (e.g. NGC 1365).

In order to analyse in detail these differences, we measured two values of A_V in each spaxel for every galaxy, one for the disk and one for the outflow component. To do so, for each velocity bin we selected only the spaxels with a S/N > 5, and we discarded all the velocity bins where Hα/Hβ < 2.86 (the theoretical value associated with $A_V = 0$). The top panel of Fig. 2.7 shows the flux spatial distributions of A_V for the disk (in green) and outflow (in red) components of all the MAGNUM galaxies, with the median of the two distributions superimposed (dotted line). Interestingly, the two distributions are shifted in A_V relative to each other, with higher values of extinction in the disk (median: $A_V \sim 1.75$ - Hα/Hβ ~ 5.51) and lower in the outflow (median: $A_V \sim 1.02$ - Hα/Hβ ~ 4.16). Therefore, the majority of the outflowing gas appears to be less affected by dust extinction than the disk. We have verified that there is no large distinction between the redshifted and blueshifted outflowing gas distributions due to projection effects, probably due to the fact that redshifted and blueshifted velocities coexist in each cone of the outflow because of geometrical effects (Venturi et al. in preparation, see also Venturi Ph.D. Thesis).

In order to estimate the gas density, we make use of the optical [S II]λ6717/[S II]λ6731 ratio, converting it to an electron density, using the Osterbrock & Ferland (2006) model, assuming a temperature of $T_e = 10^4$ K. This tracer is density-sensitive in the range 50 cm^{-3} $\lesssim n_e \lesssim$ 5000 cm^{-3}, which falls within the typically estimated range of densities in the extended NLR (e.g. Perna et al. 2017). Below and above these densities, the flux ratio of the doublet saturates. The central panel of Fig. 2.6 reports the density map of Circinus, obtained for the total line profile, that

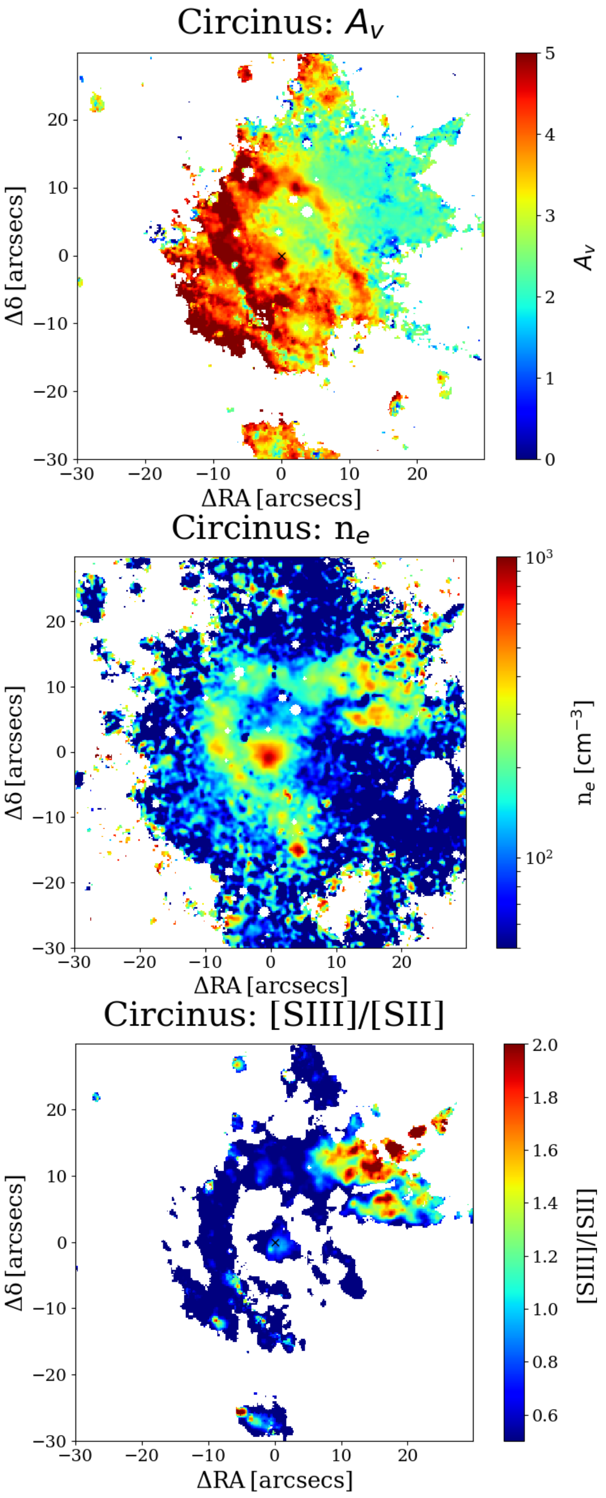

Figure 2.6: ISM properties in the Circinus galaxy. Top panel: Map of the total extinction in V band A_V obtained from the Balmer decrement Hα/Hβ. Only spaxels with Hα and Hβ S/N > 5 are shown. Central panel: Map of the total electron density measured from the [S II]λ6717/[S II]λ6731 ratio. Only spaxels with [S II]λ6717 and [S II]λ6731 $S/N > 5$ are shown. Bottom panel: Map of the [S III]$\lambda\lambda$9069,9532/[S II]$\lambda\lambda$6717,31 ratio, proxy for the ionisation parameter. Only spaxels with [S III]$\lambda\lambda$9069,9532 and [S II]$\lambda\lambda$6717,31 S/N > 5 are shown.

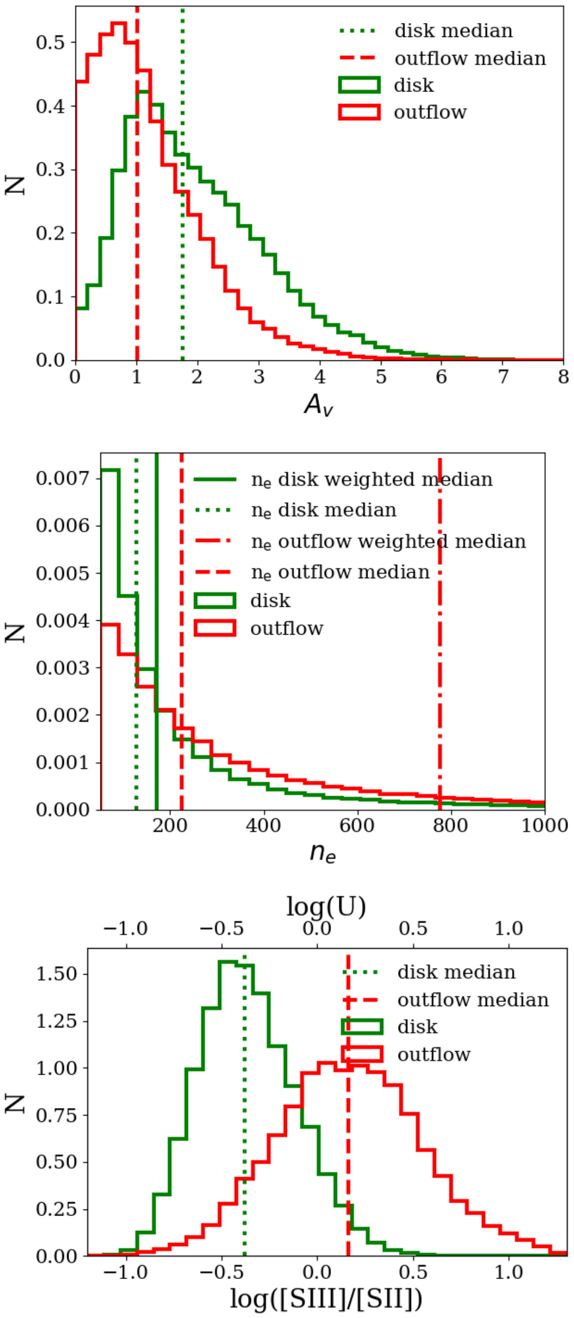

Figure 2.7: Comparison of the disk (green) and outflow (red) component distributions for all the MAGNUM galaxies in terms of visual extinction A_V, density n_e, and log([S III]/[S II]) (top, middle, and bottom panel, respectively). The two distributions are normalised such that the integral over the range is 1. For each velocity bin, we take into account only the spaxels with a $S/N > 5$ for the emission lines involved. The dotted green and dashed red lines represent the median of the disk and outflow distributions, respectively. The solid green and dash-dotted red lines in the central panel represent the median value weighted on the [S II] line flux for the disk and outflow component, respectively. The top x-axis of the bottom panel translates the [S III]/[S II] ratio into $\log(U)$, following the relation provided by Diaz et al. (1991).

appears clearly non-uniform, as found by Kakkad et al. (2018), with enhanced values of density up to $n_e \sim 10^3$ cm^{-3} located in the inner regions of the galaxy and along the north-western outflowing cone. The density maps of the other galaxies in the sample are reported in Fig. 2.18. The majority of them shows the same characteristics found in Circinus. The highest densities, with peaks of up to $n_e \sim 10^3$ cm^{-3} (e.g. IC 5063, NGC 1068, NGC 1386), are mainly found in the central regions of the galaxies. High densities (10^2 cm^{-3} $< n_e <$ 10^3 cm^{-3}) are also found along the outflowing cone axis, as is clearly visible in the north-east and south-west directions in NGC 1068 and in the double-side cone of NGC 4945 (north-west–south-east direction). On the contrary, NGC 1365 has enhanced values of density around the circumnuclear star forming ring (see also Kakkad et al. 2018; Venturi et al. 2018), consistent with recent results showing a correlation between density and the location of the SF regions (e.g. Westmoquette et al. 2011, 2013; McLeod et al. 2015). The central panel of Fig. 2.7 shows the density distribution of all the galaxies for the disk (in green) and outflow (in red) components, separately. The two distributions peak at the minimum value of the electron density range taken into account (i.e. $n_e = 50$ cm^{-3}), but the disk median value is $n_e \sim 130$ cm^{-3} against $n_e \sim 250$ cm^{-3} for the outflowing gas, and thus the outflow is generally denser than the disk gas in MAGNUM galaxies.

Previous works (e.g. Holt et al. 2011; Villar Martín et al. 2014, 2015) have found very high reddening and densities associated with ionised outflows in local objects (e.g. Hα/H$\beta \sim 4.91$ and $n_e \gtrsim 1000$ cm^{-3}, Villar Martín et al. 2014). Concerning the reddening, although we find that the outflowing gas is generally less affected by dust extinction than the disk, the median value of the total distribution is significantly affected by dust (Hα/H$\beta \sim 4.16$), with tails up to Hα/H$\beta \gtrsim 6$. We investigated possible effects due to the geometry of the outflow by comparing the A_V distributions of the blueshifted and redshifted outflow components, as shown in the left panel of Fig. 2.8. The receding part of the outflow that can be seen through the disk should increase (artificially) the A_V value associated to the outflow. However, the blueshifted and redshifted component distributions are very similar, with median values of $A_V \sim 0.93$ and $A_V \sim 1.01$, respectively. This is probably due to the fact that in almost all galaxies the (bi)conical outflow is detected in both its blueshifted and redshifted components (see Fig. 2.5), as already discussed at the end of Sec. 2.2. In NGC 1365 instead, the receding and approaching cones are dominated by the redshifted and blueshifted outflow components, respectively. Indeed, in the right panel of Fig. 2.8 it can be seen that for NGC 1365 the redshifted component distribution is shifted to higher A_V (median: $A_V \sim 1.10$) with respect to the blueshifted one (median: $A_V \sim 0.83$).

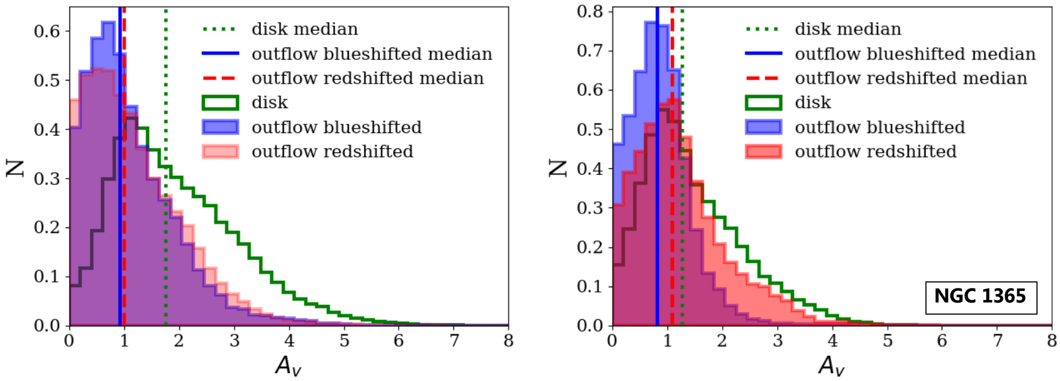

Figure 2.8: Comparison of the disk (green) and blueshifted and redshifted outflow (blue and red) component distributions for all the MAGNUM galaxies (left panel) and only for NGC 1365 (right panel) in terms of visual extinction A_V. The distributions are normalised such that the integral over the range is 1. For each velocity bin, we take into account only the spaxels with a $S/N > 5$ for the emission lines involved. The dotted green, solid blue and dashed red lines represent the median of the disk and the blueshifted and redshifted outflow distributions, respectively.

Furthermore, the outflow density of MAGNUM galaxies is higher than the values in the disk gas, but appears to be far lower than the values found by these authors. This could stem from the fact that the galaxies studied by Holt et al. 2011 are local luminous or ultra-luminous infrared galaxies (U/LIRGs), and those of Villar Martín et al. 2014, 2015 are highly obscured Seyfert 2, thus sampling sources that are more gas and dust rich compared to our sample. However, outflow median densities consistent to our findings are obtained by Arribas et al. (2014), who study ionised gas outflows properties in a large and representative sample of 75 U/LIRGs. Interestingly, our values are lower than the outflow densities found in Perna et al. (2017) ($n_e \sim 1200$ cm^{-3}), who targeted optically selected AGN from the SDSS, and Förster Schreiber et al. (2019), who presented a census of ionised gas outflows in high-z AGN with the KMOS^{3D} survey ($n_e \sim 1000$ cm^{-3}). A possible explanation could be related to the high quality of our MUSE data, which also allows us to detect the faint [S II] emission associated with lower density regions. If we calculate the median densities of the disk and outflow components, weighting for the [S II] line flux, we obtain higher values ($n_e \sim 170$ cm^{-3} and $n_e \sim 815$ cm^{-3}, for disk and outflow, respectively). This shows that previous outflow density values from the literature could be biased towards higher n_e because they are based only on the most luminous outflowing regions, characterised by a higher S/N. This could also mean that outflows at high-z could be far more extended than the values we observe.

Finally, we traced the ionisation parameter U, defined as the number of ionising photons S_* per hydrogen atom density n_H, divided by the speed of light c, making use of the [S III]$\lambda\lambda$9069,9532/[S II]$\lambda\lambda$6717,31 ratio[1] (e.g. Diaz et al. 1991). Since [S III]λ9532 is not covered by the wavelength range observed by MUSE, we adopted a theoretical ratio of [S III]$\lambda\lambda$9532/[S III]$\lambda\lambda$9069 = 2.47 (Vilchez & Esteban, 1996), fixed by atomic physics. The parameter U represents a measure of the intensity of the radiation field, relative to gas density. It can be traced using the ratios of emission lines of different ionisation stages of the same element: the larger the difference in ionisation potentials of the two stages, the better the ratio will constrain U. The [S III]$\lambda\lambda$9069,9532/[S II]$\lambda\lambda$6717,31 ratio is a more reliable diagnostic than [O III]$\lambda\lambda$4959,5007/[O II]$\lambda\lambda$3726, 28, since it is largely independent on metallicity (Kewley & Dopita, 2002). The bottom panel of Fig. 2.6 shows the [S III]/[S II] ratio map of Circinus where [S III]/[S II] reaches values as high as ~ 2 along the conical outflow. Fig. 2.19 reports the [S III]/[S II] maps for the other galaxies. Similar to Circinus, several other galaxies in our sample (NGC 1068, IC 5063, NGC 1386, NGC 2992, and NGC 5643) also show higher values of [S III]/[S II] along the outflow axis. In addition, [S III]/[S II] is high in the star forming region embedded in the gas disk in Centaurus A, and located in isolated blobs in NGC 1365. Unfortunately, the [S III]/[S II] ratio is poorly constrained in NGC 4945. The bottom panel of Fig. 2.7 shows a comparison between the distribution of [S III]/[S II] associated with the disk component (in green) and with the outflow (in red). The top x-axis translates the [S III]/[S II] ratio into log(U), following the relation provided by Diaz et al. (1991), assuming that the gas is optically thin (Morisset et al., 2016). In conclusion, log([S III]/[S II]) is observed in the range from ~ -1 to ~ 1, with higher values associated with the outflowing gas (median: log([S III]/[S II]) ~ 0.16, log(U) ~ -2.75) with respect to the disk (median: log([S III]/[S II]) ~ -0.38, log(U) ~ -3.60), where it traces mainly star forming regions. The median value found for the disk component is slightly lower than the ionisation parameters found in nearby star forming galaxies in other studies (e.g. Dopita et al. 2006c; Liang et al. 2006; Kewley & Ellison 2008; Nakajima & Ouchi 2014; Bian et al. 2016), obtained through the [O III]$\lambda\lambda$4959,5007/[O II]$\lambda\lambda$3726, 28. We also calculated the median values of the extinction and ionisation parameter distributions, weighting for the line fluxes of the involved lines, finding negligible ($\Delta A_{\rm V} \sim -0.02$, Δlog([S III]/[S II]) $\sim +0.03$) and small differences ($\Delta A_{\rm V} \sim -0.20$, Δlog([S III]/[S II]) $\sim +0.25$) with respect to the median values shown in Fig. 2.7, for the disk and outflow component, respectively.

In summary, we find that the disk and outflow are characterised by different properties. In the next section, we investigate the ionisation properties of the gas separately

---

[1] Both emission lines were corrected for dust attenuation prior to deriving the ionisation parameter.

for the two kinematic components.

2.2.2 Spatially and kinematically resolved BPT

Spatially and kinematically resolved Baldwin-Phillips-Terlevich (BPT) diagrams allow us to explore the dominant contribution to ionisation in each spaxel in the disk and outflow components separately (a similar approach has been used by e.g. Westmoquette et al. 2012; McElroy et al. 2015; Karouzos et al. 2016b).

The left and middle panels of Fig. 2.9 show the [N II]- and [S II]-BPT diagrams of Circinus for the disk and outflow components, respectively. For each velocity bin, we select only the spaxels with a $S/N > 5$, computed by dividing the integrated flux in the velocity channels for each emission line by the corresponding noise. The dashed curve is the boundary between star forming galaxies and AGN defined by Kauffmann et al. (2003a) (ka03), while the solid curve is the theoretical upper limit on SF line ratios found by Kewley et al. (2001) (ke01). The dotted line, instead, is the boundary between Seyferts and LI(N)ERs introduced by Kewley et al. (2006) (ke06). The dominant source of ionisation is colour-coded: shades of blue for SF, pink for intermediate regions in the [N II]-BPT, green for LI(N)ER regions in the [S II]-BPT, and red for AGN-like ionising spectra, as a function of the x-axis line ratios (darker shades means higher x-axis line ratios). The LI(N)ER-like excitation can be due either to shock excitation (e.g. Dopita & Sutherland 1995) or to hard-X radiation coming from AGN and to hot evolved (post-asymptotic giant branch) stars (e.g. Singh et al. 2013; Belfiore et al. 2016), as explained in Sec. 1.3.1 in Chapter 1. The corresponding position on the map of the outflowing gas component, colour-coloured based on the different sources of ionisation, is shown in the right panels of Fig. 2.9. In the background of all the pictures (black dots in the BPTs and shaded grey in the corresponding maps), we show the disk and outflow components together to allow us a better visual comparison.

Looking at Fig. 2.9, we note that the outflow spans a wider range of [N II]/Hα and [S II]/Hα, including lower and higher values compared to the disk. Specifically, the highest and lowest values of low-ionisation line ratios (LILrs; i.e. [N II]/Hα and [S II]/Hα), displayed in dark red and orange, are prominent in the AGN/LI(N)ER-dominated outflow component, while they are not observable in the disk component. This can also be seen looking at the [N II]- and [S II]-BPT diagrams of the other galaxies, shown in Figs. 2.20, 2.21, and Fig 2.22, 2.23, respectively[2]. In the following we analyse

---

[2] [N II]- and [S II]-BPT diagrams in the Appendix were made taking into account the smoothed datacubes. An exception is made for NGC 1365, where the biconical outflow can be well traced only in the Voronoi-binned cube.

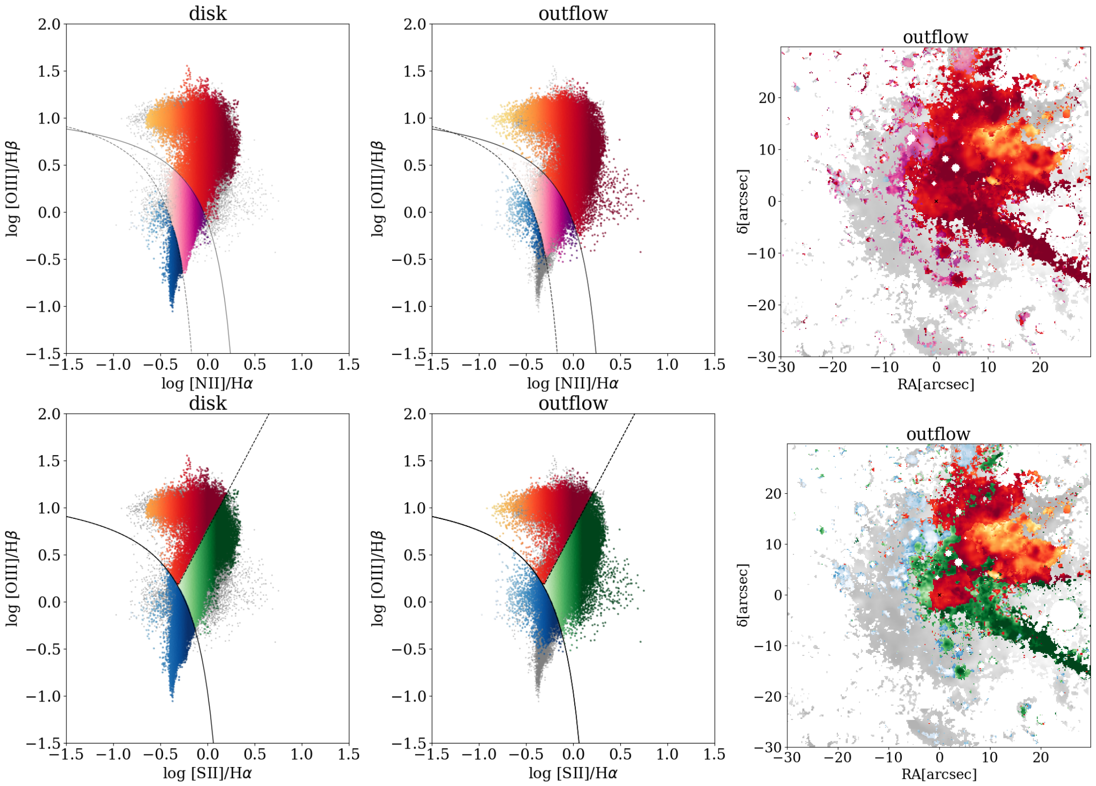

Figure 2.9: *Left and central panels*: [N II] and [S II] BPT diagrams for the disk and outflow components, on the left and on the right respectively, of Circinus. SF-dominated regions are coloured in blue, intermediate regions in the [N II]-BPT in pink, LI(N)ER in the [S II]-BPT in green, and AGN in red (darker shades means higher x-axis line ratios). The black dashed and solid curves, and the black dotted line show the ka03, ke01 and ke06 boundaries, respectively. *Right panels*: [N II] and [S II] BPT maps of the outflowing gas component, colour-coded according to BPTs. In the background of all the pictures (grey dots in the BPTs and shaded grey in the corresponding maps), we show the disk and outflow component together. For each velocity bin, we select only the spaxels with a $S/N > 5$ for all the lines involved.

the regions showing the lowest (Sec. 2.2.2) and the highest (Sec. 2.2.2) LILrs.

Outflowing gas: the lowest [NII]/Hα-[SII]/Hα line ratios

As Fig. 2.9 shows, the lowest [N II]/Hα and [S II]/Hα line ratios (in orange, with $\log([\text{N II}]/\text{H}\alpha) \lesssim -0.5$ and $\log([\text{S II}]/\text{H}\alpha) \lesssim -0.8$) in the AGN ionisation regime belong almost exclusively to the outflowing gas. Looking at the right panel of Fig. 2.9, it can be seen that these values correspond to the innermost parts of the northwestern cone (in orange)[3].

---

[3] Unfortunately, part of the outflowing gas in the west cone of Circinus is oriented along the plane of the sky, and thus has low line-of-sight velocity. Consequently, the disk component is partly contaminated by the outflow, explaining the presence of the orange dots in the left panels of the BPT diagrams

These low values of [N II]/Hα and [S II]/Hα (with logarithmic values down to ~ -1) in the AGN-dominated region are not restricted to the Circinus outflowing gas, but appear to be typical outflow signatures in almost all the galaxies of our sample (NGC 2992, NGC 1365, IC 5063, NGC 1068), and, albeit less clearly, in Centaurus A, NGC 1386, and NGC 5643 (see left panels of Figs. 2.20 and 2.21, for [N II]-BPT diagrams, Figs. 2.22 and 2.23, for [S II]-BPT diagrams). Specifically, the lowest LILrs dominate the majority of the visible north-west cone of NGC 2992, which extends out to ~ 5 kpc, and the innermost parts of the cones in most of the other galaxies (north-west cone in NGC 1365, north-west and south-east directions in IC 5063, north-east and south-west directions in NGC 1068, east and west directions in NGC 5643), highlighted in orange in the right panels of Figs. 2.20 and 2.21, Figs. 2.22 and 2.23, for the [N II]- and the [S II]-BPT diagrams, respectively. On the contrary, these features seem to be completely absent in NGC 4945.

Outflowing gas: the highest [NII]/Hα-[SII]/Hα line ratios

Looking at Fig. 2.9, the highest [N II]/Hα and [S II]/Hα line ratios (in darker red and green, respectively), with values higher than 0, appear to come from the edges of the outflowing cone.

As noted above for the other ratios, this feature is not only typical of Circinus, but appears to characterise almost all of the sample (NGC 4945, NGC 2992, NGC 1068, Centaurus A, IC 5063, NGC 1386 and NGC 5643), as can be seen in the left panels of Figs. 2.20 and 2.21, Figs. 2.22 and 2.23, for [N II]- and [S II]-BPT diagrams, respectively. For instance, it is clearly visible in NGC 4945, where – as in Circinus – the high LILrs come from the external edges of both the north-western and the south-eastern outflowing cones, even though in the latter only the edges are barely observable because of the low Hβ S/N. In NGC 1068, IC 5063 and in NGC 5643, this enhancement is extended from the edges of the cones to a region almost perpendicular to the outflow axis[4] where a conical dark red region (AGN-dominated) in [N II]-BPT and a conical dark green region (LI(N)ER-dominated) in [S II]-BPT can be distinguished.

On the contrary, it can be seen that in NGC 1365 the highest LILr stem from gas located in the disk component in the vicinity of the outflowing cone edges. However, we believe that the distinction between disk and outflow components is not completely defined in this galaxy. Part of the outflowing gas could have an apparent low line-

---

in Fig. 2.9.

[4] In NGC 1068, IC 5063 and NGC 5643 the outflow axis is in the direction north-east and south-west, north-west and south-east, and east and west, respectively.

of-sight velocity because it is oriented along the plane of sky, contaminating the disk component.

2.3 Discussion

In the analysis of the kinematically and spatially resolved BPT diagrams for our sample of galaxies (see Sec. 2.2.2), we identify two main features in the outflowing gas: a decrease and an enhancement in the [N II]/Hα and [S II]/Hα line ratios, coming from distinct regions of the outflowing cones. In the following, we discuss possible explanations for these features, such as a combination of optically thin and optically thick clouds or shocks and/or a hard filtered radiation field from the AGN. To do this, we compare ionisation state and gas velocity dispersion with [N II]- and [S II]- BPT diagrams comprising the whole MAGNUM sample; the only exception is NGC 1068, which shows a different behaviour with respect to the others concerning the [S III]/[S II] ratio (see Figs. 2.24 and 2.25) and has a far higher velocity dispersion (see Figs. 2.26 and 2.27). Therefore, it will be discussed in a forthcoming work.

2.3.1 Possible scenarios for the lowest LILr

Figure 2.10 shows the [N II]- and [S II]- BPT diagrams of all the MAGNUM galaxies (excluding NGC 1068), colour-coded as a function of the [S III]$\lambda\lambda$9069,9532/[S II]$\lambda\lambda$6717,31 ratio, which is a proxy for the ionisation parameter, as reported in the corresponding colour bars (darker shades means higher ionisation). Here, we use the Voronoi-binned cubes to increase the S/N and, for each Voronoi bin, we select only the velocity bins where the [S III] and [S II] line fluxes have a S/N > 3. The lowest LILrs (log([N II]/Hα) ~ -1 and log([S II]/Hα) ~ -1), which mainly trace the innermost regions of the outflowing gas, also correspond to the highest [S III]/[S II] line ratio ([S III]/[S II] ~ 2), which decreases to values [S III]/[S II] $\lesssim 0.5$ going towards higher LILr values.

This observed variation in the degree of excitation can be interpreted as being due to diverse proportions of two populations of line emitting clouds, characterised by different levels of opacity to the radiation, a matter-bounded (MB) and an ionisation-bounded (IB) component, first discussed by Binette et al. (1996). The former is only responsible for the high-ionisation lines (e.g. [O III]$\lambda\lambda$4959,5007), while the latter is also characterised by low-ionisation ones (e.g. [N II]$\lambda\lambda$6548,84 and [S II]$\lambda\lambda$6717,31). Specifically, a cloud is said to be MB if the outer limit to the H$^+$ region is marked by the outer

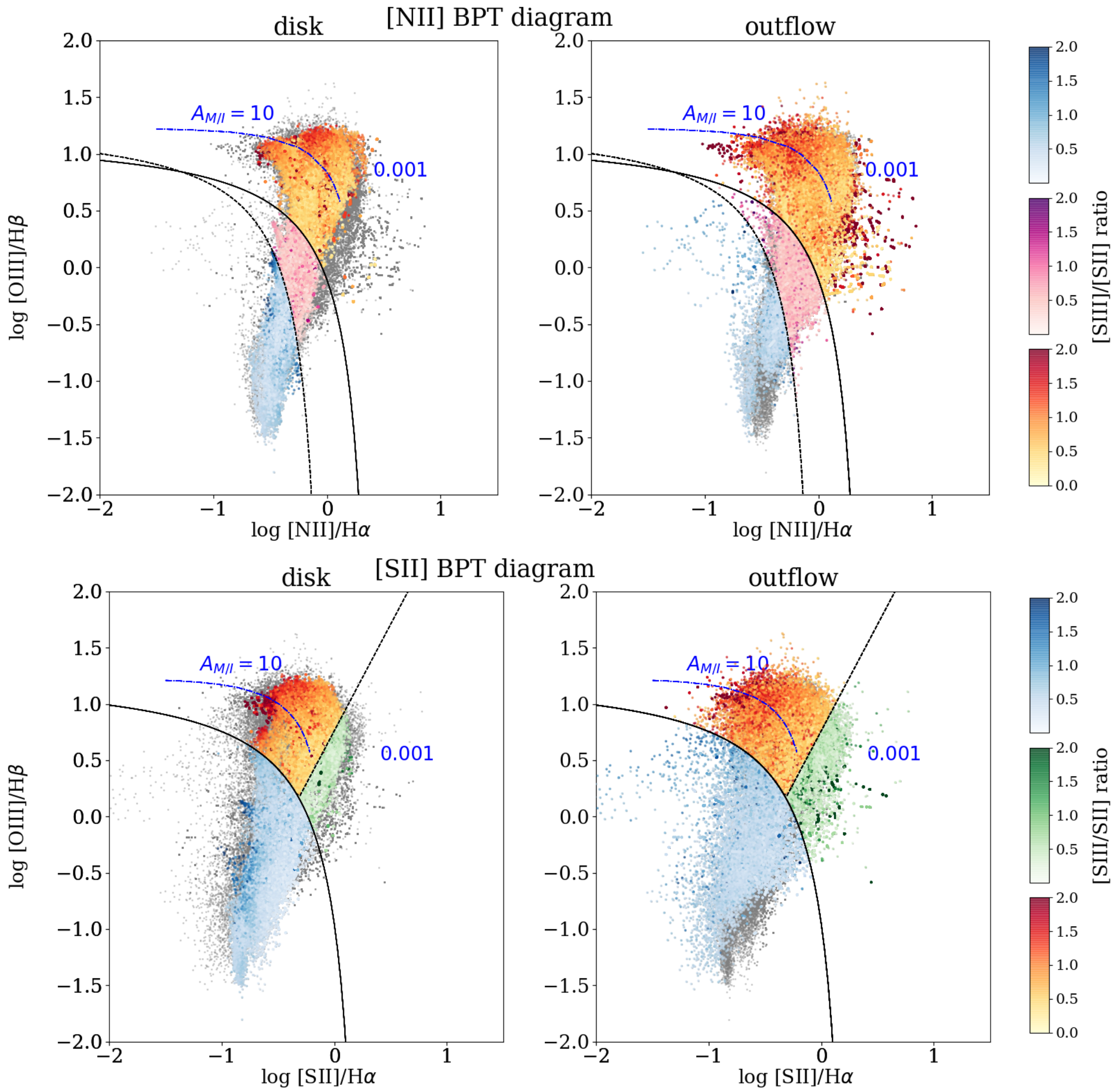

Figure 2.10: [N II]- and [S II]-BPT diagrams for the disk and outflow components, on the left and the right respectively, of all the MAGNUM galaxies, apart from NGC 1068, colour-coded as follows: shades of blue for SF, pink for intermediate regions in the [N II]-BPT, green for LI(N)ER regions in the [S II]-BPT, and red for AGN-like ionising spectra, as a function of the [S III]/[S II] line ratio (darker shades means higher [S III]/[S II] values). The black dashed curve, solid curve and dotted line show the ka03, ke01 and ke06 boundaries, respectively. The dash-dotted blue curve represents the Binette A$_{M/I}$-sequence, dominated by MB clouds in the upper left region and by IB clouds going towards higher LILrs. The black dots in the BPTs are all the spaxels taken into account (both of the disk and of the outflow component) with a S/N $>$ 3 for the line fluxes involved.

edge of the cloud, which means that it is ionised throughout and is optically thin to the incident radiation field. On the other hand, the cloud is IB (or radiation bounded) if the outer limit to the H^+ region is defined by a hydrogen ionisation front, so both warm ionised and cold neutral regions coexist, and thus the H^+ region is optically thick to the hydrogen-ionising radiation, absorbing nearly all of it. The original aspect of the Binette et al. (1996) approach is the assumption that the IB clouds are photoionised only by hard photons which have leaked through the MB clouds, meaning that the input ionising spectrum impinging on the IB clouds has been partially filtered (see Fig. 3, Binette et al. 1996). Hard photons interact much less effectively with the gas, being their energy far above the H^0 ionisation threshold. This means that, unlike the MB clouds which share the same excitation (i.e. the same ionisation parameter) being coupled with the radiation field, the IB clouds are not necessarily characterised by a unique value of ionisation parameter. Their modelling is parametrised by the ratio of the solid angles subtended by MB and IB clouds ($A_{M/I}$), which introduces a new free parameter: the geometry of the system, which is often difficult to constrain.

In Fig. 2.10, the blue dash-dotted line represents the Binette $A_{M/I}$ sequence (Binette et al., 1996; Allen et al., 1999), that closely matches the differences in the line ratios that we observe: in the upper left region ($\mathrm{A}_{M/I} \sim 10$), the MB component dominates, meaning that the gas is more optically thin, and is thus characterised by high-ionisation lines, such as [O III] and [S III], tracing the inner gas within the outflowing cones (see Sec. 2.2.2); going to higher LILrs, the optically thick IB clouds, characterised by a much lower excitation, start playing a major role ($A_{M/I} \sim 0.001$) both in the outflowing gas and in the disk gas. However, even though the MB-IB dichotomy accounts for the low LILr, it cannot explain the highest LILr that we observe in our sample.

BPT diagrams colour-coded as a function of [S III]/[S II] for each galaxy can be seen in Fig. 2.24 and Fig. 2.25, for the [N II]- and [S II]-BPT diagrams, respectively[5]. The trend found between the [S III]/[S II] line ratio and low LILr is mainly visible in Circinus, NGC 2992, and NGC 5643, but also in NGC 1386, even though less clearly because of the cut in S/N. We note that NGC 4945, which is the only galaxy that lacks the MB clouds features, is characterised either by a very strong obscuration of AGN UV radiation or by an AGN that is highly deficient in its UV with respect to X-ray emission (Marconi et al., 2000). This could explain why we see only the IB cloud component, ionised by hard photons filtered by the dust.

In the top panel of Fig. 2.11, we show the stacked spectrum in the wavelength range 4850–7500 Å of the region corresponding to the lowest LILr in Circinus. Specifically, we selected and summed the AGN- and LI(N)ER-dominated spaxels from the original data

---

[5] The [N II]- and [S II]-BPT diagrams given in the Appendix, apart from NGC 1365, are made taking into account the smoothed datacube, and not the Voronoi-binned ones that we use in this section to compare all the galaxies.

cube, where log([N II]/Hα)< -0.2 and log([S II]/Hα)< -0.4, which correspond to the innermost parts of the outflowing cone, indicated in orange in the right panels of Fig. 2.9. After fitting and subtracting the continuum with pPXF, we fitted the main emission lines with MPFIT, using one Gaussian component with the same velocity and velocity dispersion for each line. We applied the same procedure to obtain the stacked spectrum of the highest LILr in Circinus (log([N II]/Hα)> 0.1 and log([S II]/Hα)> 0), shown in the bottom panel of Fig. 2.11. In Tab. 3.1 the observed and dereddened fluxes of the fitted emission lines with respect to the Hβ are reported for the two spectra. It can be seen that the Fe coronal lines (e.g. [Fe VI]λ5146, [Fe XIV]λ5303, [Fe VII]λ5721, [Fe VII]λ6087, [Fe X]λ6374, highlighted in green) are brighter and are found almost exclusively in the lowest LILr region. These forbidden transitions are peculiar because of their high-ionisation potential (≥ 100 eV), pointing to a scenario in which the innermost parts of the outflowing gas in this galaxy are in optically thin, highly ionised regions, possibly directly illuminated by the central ionising AGN.

Furthermore, the [N II]λ5755 auroral line, which is too faint to be detected in the single spaxel spectra, is observed in the stacked spectrum in Fig. 2.11. We can then determine the electron temperature (T_e) by exploiting the temperature-sensitive auroral-to-nebular line ratio of this particular ion. The atomic structure of [N II] is such that auroral and nebular lines originate from excited states that are well spaced in energy, and thus their relative level populations depend heavily on electron temperature. From the [N II]$\lambda\lambda$6548,84/[N II]λ5755 line ratio, we obtain $T_e \sim 9.1 \times 10^3$ K. This value is lower than the few other measurements present in the literature, to the best of our knowledge, derived in outflows by Villar Martín et al. (2014), Brusa et al. (2016), Perna et al. (2017) and Nesvadba (2018) (i.e. $T_e \approx 1.5 \times 10^4$ K). This discrepancy is possibly due to the fact that these authors estimated the electron temperature on the basis of [O III] (i.e. [O III]$\lambda\lambda$4959,5007/[O III]λ4363), characterised by a higher ionisation potential with respect to [N II], which mainly traces the innermost parts of the photoionised regions and can be associated with lower temperatures (Osterbrock & Ferland, 2006; Curti et al., 2017; Perna et al., 2019).

2.3.2 Possible scenarios for the highest LILr

Figure 2.12 shows the [N II]- and [S II]- BPT diagrams of all the MAGNUM galaxies (excluding NGC 1068 as before), coloured-coded as a function of the [O III] velocity dispersion $\sigma_{[\mathrm{O\,III}]}$, as reported in the corresponding colour bars (darker shades means higher $\sigma_{[\mathrm{O\,III}]}$). Only bins from the Voronoi-binned cubes in which the [O III] line flux has a S/N > 3 are shown. It can be clearly seen that the highest values of $\sigma_{[\mathrm{O\,III}]}$

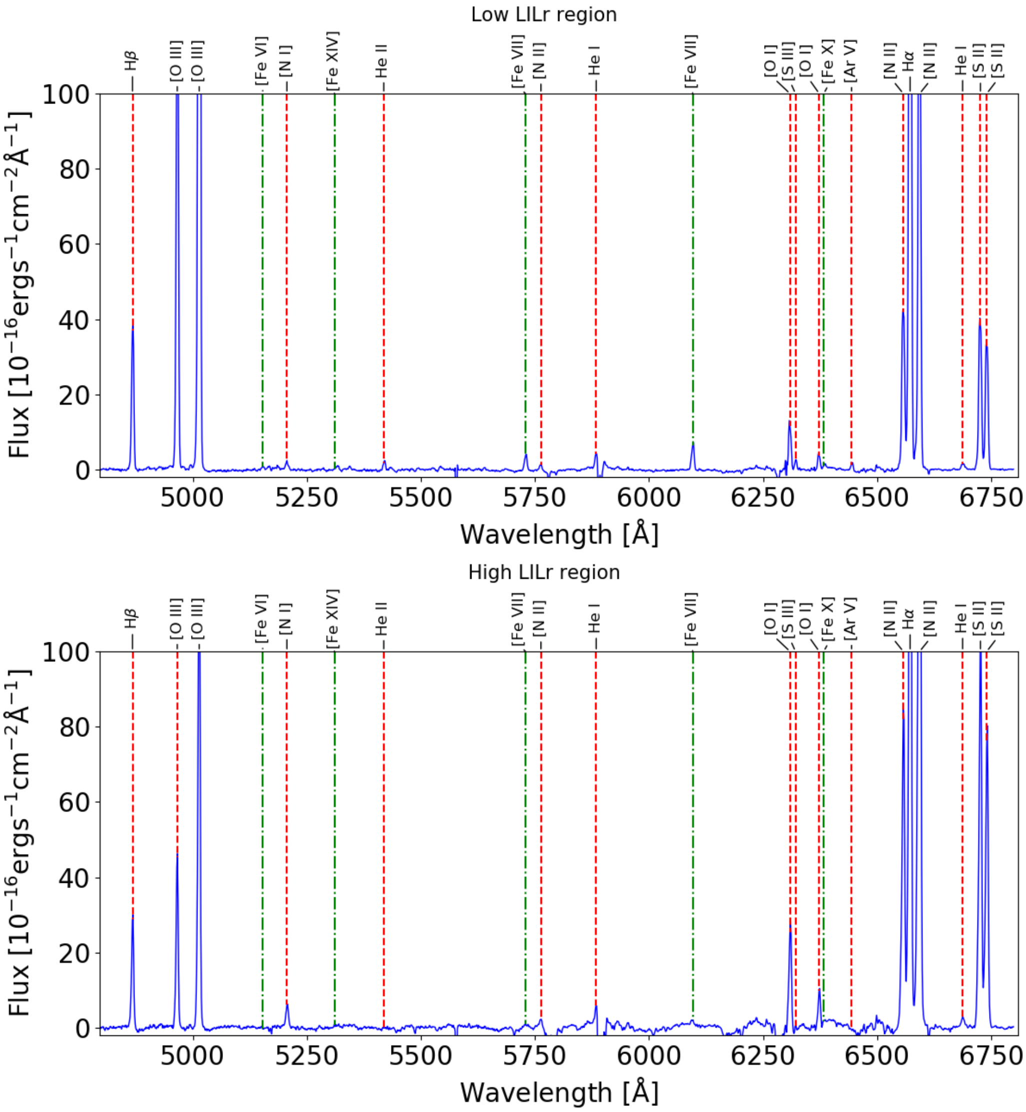

Figure 2.11: Top panel: Spectrum of the region characterised by log([N II]/Hα)< -0.2 and log([S II]/Hα)< -0.4 in Circinus, corresponding to the innermost regions of the outflowing cone. Bottom panel: Spectrum of the region characterised by log([N II]/Hα)$>$ 0.1 and log([S II]/Hα)$>$ 0 in Circinus, mainly tracing the edges of the north-western outflowing cone. High-ionisation coronal lines (in green) are observed almost exclusively in the low LILr region, supporting a scenario where the inner parts of the outflowing gas in this galaxy are in optically thin highly ionised regions.

correspond to the highest LILrs found in the outflowing gas. These mainly trace the edges of the outflowing cones and/or the region perpendicular to it (see Sec. 2.2.2). This correlation between velocity dispersion and emission-line ratio suggests that the kinematics and ionisation state are coupled, indicating that they may have the same physical origin. This trend has been already found in star forming galaxies, U/LIRGs, and AGN (e.g. Monreal-Ibero et al. 2006, 2010; Rich et al. 2011; Ho et al. 2014; Rich

Table 2.2: Circinus: observed and dereddened line fluxes (F and I), relative to Hβ (H$\beta = 1$), and electron temperatures T_e for the low LILr (log([N II]/Hα) < -0.2 and log([S II]/Hα) < -0.4) and high LILr (log([N II]/Hα) > 0.1 and log([S II]/Hα) > 0) regions, estimated by fitting the corresponding stacked spectra. Blank entries are undetected lines. Hβ flux is in units of 10^{-16} erg s^{-1} cm^{-2}, while T_e is in Kelvin.

	Low LILr region		High LILr region	
	F	I	F	I
Hβ	1	1	1	1
[O III]λ5007	11.14 ±0.04	10.17±0.03	4.69 ±0.02	4.12 ±0.02
[Fe VI]λ5146	0.022 ±0.002	0.018 ±0.002	-	-
[Fe XIV]λ5303	0.008±0.002	0.006 ±0.002	-	-
[Fe VII]λ5721	0.210 ±0.002	0.128 ±0.001	0.098±0.004	0.049 ±0.002
[N II]λ5755	0.034 ±0.002	0.021 ±0.001	0.093±0.004	0.045±0.002
[Fe VII]λ6087	0.114±0.002	0.058 ±0.001	0.037±0.004	0.014 ±0.001
[O I]λ6300	0.359±0.002	0.171 ±0.001	1.160±0.006	0.402±0.001
[S III]λ6312	0.069 ±0.002	0.033±0.001	-	-
[Fe X]λ6374	0.041 ±0.002	0.019 ±0.001	-	-
[N II]λ6584	4.23 ±0.01	1.765±0.002	10.98±0.05	3.168 ±0.002
Hα	6.79 ±0.02	2.86	9.78 ±0.04	2.86
[S II]λ6717	1.141 ±0.005	0.450 ±0.001	3.46±0.02	0.921±0.001
[S II]λ6731	1.357 ±0.005	0.532±0.001	4.62 ±0.02	1.222±0.001
Hβ flux	227.2 ±0.7	5160±40	160.9 ±0.7	13700 ±100
T_e	$(9.1 \pm 0.2) \times 10^3$		$(9.8 \pm 0.2) \times 10^3$	

et al. 2015; McElroy et al. 2015; Perna et al. 2017), and it was attributed to shocked gas components as photoionisation is not expected to cause such a trend (see Dopita & Sutherland 1995 and the detailed discussion in McElroy et al. 2015).

Therefore, we compare the observed data with a grid of MAPPINGS III shock models[6], taken from Allen et al. (2008), that comprises shock velocities in the range $v_s = 100 - 1000$ km s^{-1} and magnetic parameters $B/{n_e}^{1/2} = 10^{-2} - 10$ μG cm$^{3/2}$, taking into account solar abundances and a pre-shock density $n_e \sim 100$ cm^{-3}. It can be clearly seen that shock models can reproduce the high LILrs (up to values of ~ 0.3) that the MB-IB dichotomy could not explain. However, the models fail to reproduce the highest LILrs, possibly suggesting even more extreme conditions in the outflowing gas (see also Perna et al. 2017). We tested all the available Allen et al. (2008) shock models, but found no improvement. Since this discrepancy is more significant in the [N II]-BPT diagram, it may be partly related to a metallicity effect. Indeed, [N II]/Hα line-ratios should increase with higher metallicity due to the secondary nitrogen production (e.g.

---

[6] The values of the magnetic field, B, and magnetic parameter, $B/{n_e}^{1/2}$, were chosen by Allen et al. (2008) so as to cover the extremes expected in the ISM. Moreover, the shock velocities taken into account are consistent with those measured from the gas kinematics (Venturi et al. in preparation).

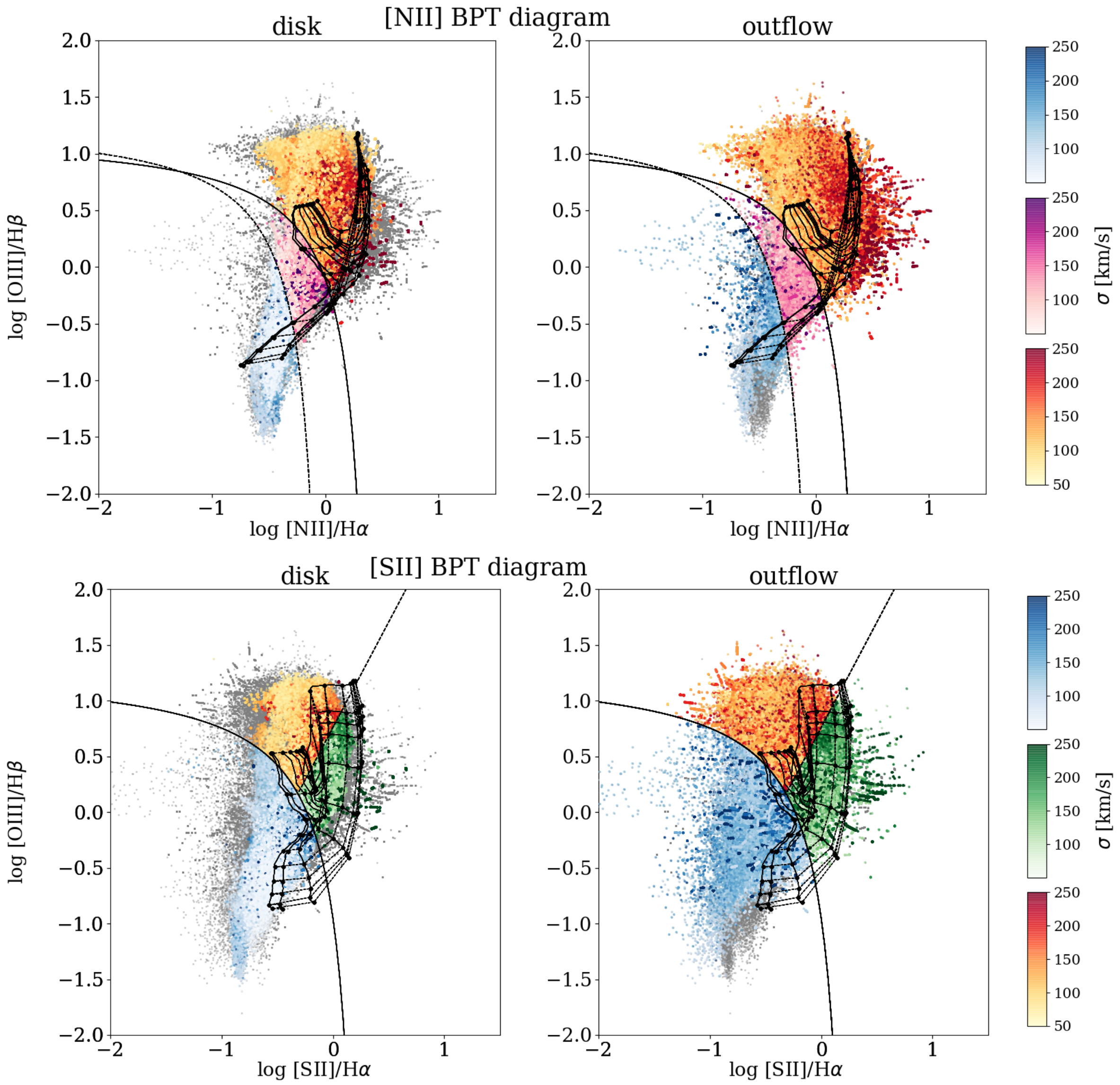

Figure 2.12: [N II]- and [S II]-BPT diagrams for the disk and outflow components, as shown in Fig. 2.10, colour-coded as a function of the [O III] velocity dispersion (darker shades means higher $\sigma_{[\mathrm{O\,III}]}$). The grid of shock models taken from Allen et al. (2008) comprises shock velocities in the range $v_s = 100 - 1000$ km s^{-1} (horizontally increasing) and magnetic parameters $B/n^{1/2} = 10^{-2} - 10$ μG cm$^{3/2}$ (vertically increasing). The black dashed curve, solid curve and dotted line show the ka03, ke01 and ke06 boundaries, respectively.

Alloin et al. 1979; Considère et al. 2000; Mallery et al. 2007).

BPT diagrams colour-coded as a function of $\sigma_{[\mathrm{O\,III}]}$ for each galaxy can be seen in Fig. 2.26 and Fig. 2.27, for [N II]- and [S II]-BPT diagrams, respectively. This correlation between [O III] velocity dispersion and high LILr is visible especially in NGC 4945, NGC 5643, and IC 5063. Also NGC 1068 shows this trend, even though it shows far higher values of [O III] velocity dispersion in all the outflowing components. The fact that this correlation is not found in Circinus does not necessarily exclude the shock scenario because, as stressed in McElroy et al. (2015), for idealised planar shock fronts we would only be observing the shock at a single velocity, implying that the observed shock velocity and velocity dispersion will not necessarily have similar values.

From the [N II]$\lambda\lambda$6548,84/[N II]λ5755 line ratio, measured from the stacked spectrum shown in the bottom panel of Fig. 2.11, we obtain $T_e \sim 9.8 \times 10^3$ K instead of the much higher temperature that we should observe if the bulk of emission were associated with shock excitation ($T_e > 10^5$ K, Osterbrock & Ferland 2006). A similar case has been found by Perna et al. (2017), who contend that a possible explanation could be that the shock accelerating the ISM gas is strongly cooled, so that the gas temperature rapidly returns to its pre-shock value (see also King 2014).

Nevertheless, some works pointed out the inefficiency of shocks in producing line emission. For example, Laor (1998) showed that shocks can reprocess only $\sim 10^{-6}$ of the rest mass to ionising radiation, with respect to a maximum conversion efficiency of $\sim 10^{-1}$ for the central continuum source, demonstrating that they can be a viable mechanism only in very low-luminosity sub-Eddington active galaxies, which are very inefficient in converting mass into radiation. An alternative explanation to account for the regions producing the strongest LILrs can be given by a hard ionising radiation field resulting from radiation filtered by clumpy, ionised absorbers located tens of parsecs or less from the nucleus, possibly consistent with the torus dimension (e.g. Netzer 2015). This scenario is consistent with our finding of lower [S III]/[S II] line ratios ([S III]/[S II] $<$ 1) in the regions characterised by the highest LILrs, with the exception of NGC 1068. Similar results have been obtained by Kraemer et al. (2008), who analysed HST images of NGC 4151 and found that the [O III]$\lambda\lambda$4959,5007/[O II]$\lambda\lambda$3726,29 – a proxy of the ionisation parameter analogous to [S III]/[S II] – is lower near the edges of the ionisation bicone observed in the galaxy than along its axis, concluding that the structure of the NLR is due to filtering of the ionising radiation by ionised gas, and is consistent with disk-wind models.

2.4 Centaurus A: an ideal local laboratory to study AGN positive feedback

As already introduced in Sec. 2.1.1, Centaurus A galaxy shows a characteristic double-sided jet observed in radio and X-rays (e.g., Hardcastle et al. 2003; Kraft et al. 2008, see Israel 1998 and Morganti 2010 for a review), expanding in a set of radio lobes from

~ 5 kpc up to ~ 250 kpc (e.g. Israel 1998). This galaxy is the best example of a radio jet emitted by the central AGN interacting with the ISM, which may have induced star formation in the outskirts of the galaxy (positive feedback). The region where this interaction appears most clearly is characterised by filaments of highly ionised gas, between about 9 and 20 kpc from the nucleus, roughly aligned along the jet direction (Blanco et al., 1975; Graham & Price, 1981; Morganti et al., 1991). Interestingly, these filaments are known to contain massive young stars, whose formation was possibly triggered by the interaction of the AGN radio plasma with a cloud of cold gas due to a recent merger, as suggested by the alignment with the jet direction and the kinematics of the gas (Graham, 1998; Mould et al., 2000; Oosterloo & Morganti, 2005; Crockett et al., 2012; Santoro et al., 2015a,b, 2016).

In this context, we investigated the central region of this galaxy, exploiting our approach of disentangling the disk from the outflow component (see also Sec. 2.2) to obtain an independent classification of their excitation properties with the BPT diagrams. The upper and lower panels of Fig. 2.13 shows the [N II] and [S II] BPT maps for the disk (on the left) and the outflow (on the right), with regions dominated by SF, AGN, Composite and LI(N)ER activity indicated in blue, red, pink and green, respectively. The direction of the inner jet, revealed both in the radio and X-rays (see Fig. 2.14, Hardcastle et al. 2003) and consistent with the location of the bi-conical outflow dominated by LI(N)ER- and AGN-like ionisation, is marked by the black arrow. An [O III] ionisation cone of ~ 500 pc along the jet axis, related to AGN or shock activities, was revealed for the first time by Bland-Hawthorn & Kedziora-Chudczer (2003). Moreover, Israel et al. (2017) discovered an outflow of gas that from the center of Centaurus A extends along an axis close to that of the northern X-ray/radio jet, detected in the neutral gas traced by CO and and C I, and in the far-infrared through fine-structure lines. Israel et al. (2017) detected also a less clear southern counterpart to the well-collimated northern outflow.

Looking back at Fig. 2.13, the SW portion of the galaxy FOV hosts a blob (solid circle, left pictures), characterised by a velocity consistent with the gas disk and by Composite and SF dominated ionisation ([N II] and [S II]-BPT, respectively), that could be interpreted as SF triggered in the ionisation cone due to compression of the galaxy ISM by the jet (as in Cresci et al. 2015b). Moreover, a nearby clump appears to have SF like ionisation, but velocities consistent with the gas in the outflow (solid square, right pictures), suggesting that in this case new stars could be formed at high velocity directly in the outflow (as in Maiolino et al. 2017). If confirmed, this would be the first example of these two types of positive feedback coexisting in the same object.

Fig. 2.15 shows the spectrum of the SF blob in the outflow (highlighted by the solid

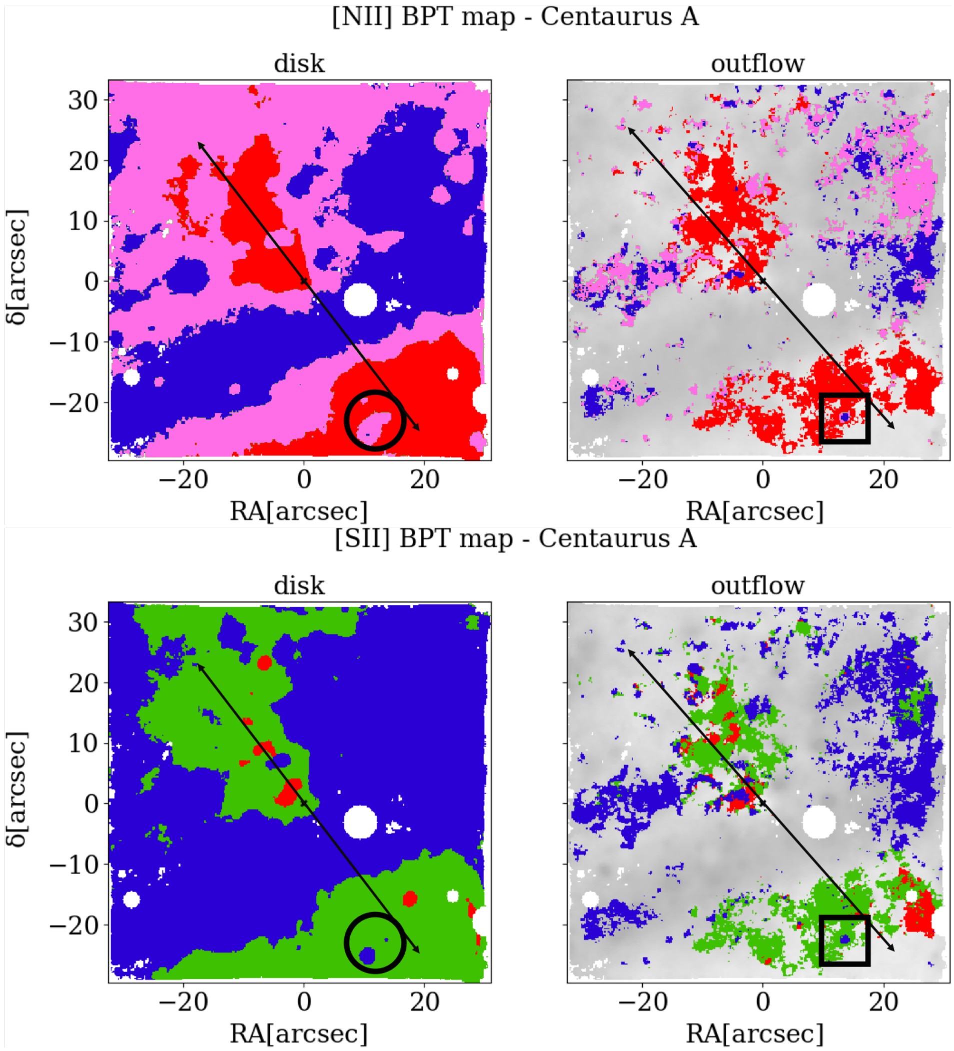

Figure 2.13: [N II] (upper panel) and [S II] (lower panel) BPT maps for the disk and outflow component of Centaurus A. To separate the two components, we divide each line profile in each spaxel of the MUSE FOV in velocity bins, associating to the disk the core of the line (-150 km/s < v < + 150 km/s) centred at Centaurus A systemic velocity ($v_{sys} \sim 547$ km s^{-1}), and the sum of the redshifted and blueshifted wings to the outflow (v > + 200 km/s – v < - 200 km/s), as already explained in Sec. 2.2. SF, AGN, Composite and LI(N)ER dominated regions are indicated in blue, red, pink and green, respectively. The black arrow indicates the direction of the outflow, while the solid circle and square highlight the position of composite/SF blobs, located in the direction of the outflow.

square in Fig. 2.13) in the wavelength range 6500 – 6650 Å, that clearly presents outflow signatures. The asymmetric line profile can be reproduced by a three Gaussian component fit as shown in the figure. Fig. 2.16 illustrates the [N II] and [S II] BPT diagrams of these three components, indicated with the same color used in the previous figure. The redshifted Gaussian component (dashed red gaussian) has a very strong Hα emission,

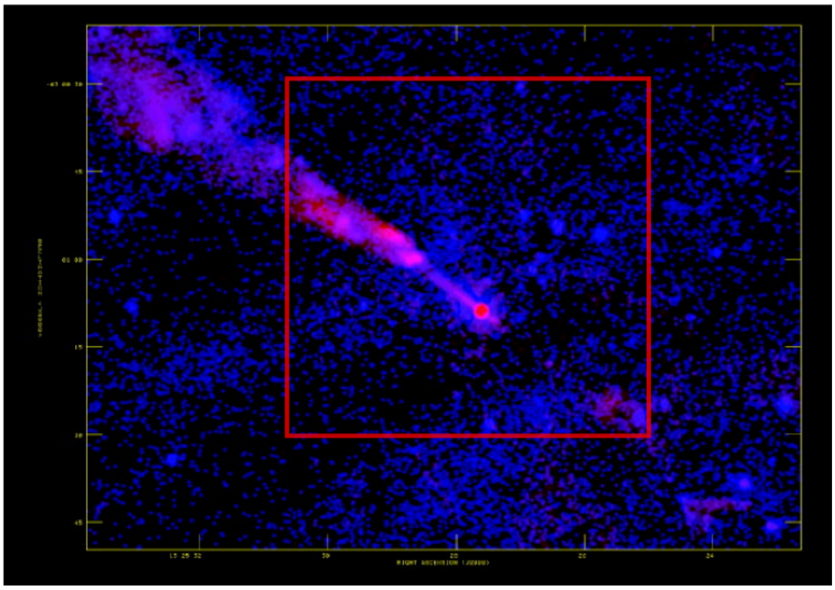

Figure 2.14: X-ray (0.4 and 2.5 keV, in blue) and radio structure (in red) of the jet in Centaurus A. This image is taken from Hardcastle et al. (2003). The red square superimposed indicates our MUSE FOV.

with log([N II]/Hα) ~ -0.6, log([S II]/Hα) ~ -0.5 and log([O III]/Hβ) ~ 0 flux ratios, indicating SF ionisation. On the other hand, the blueshifted (dashed-dotted blue gaussian) and disk (dotted green gaussian) components have AGN and Composite/LI(N)ER-like ratios, pointing towards a stellar-like ionisation source at redshifted velocities consistent with the outflow at the same location.

We estimate the star formation rate (SFR) of the two star forming blobs using the following calibration taken from Lee et al. (2009):

$$\log\left(\frac{\mathrm{SFR}}{\mathrm{M_\odot/yr}}\right) = 0.62\log\left(\frac{7.9\times10^{-42}\mathrm{L_{H\alpha}}}{\mathrm{erg/s}}\right) - 0.47 \tag{2.1}$$

Specifically, Lee et al. (2009) re-calibrated the relation between SFR and Hα luminosity of Kennicutt (1998), under the assumption that the far UV (FUV) traces the SFR more robustly. Indeed, with FUV data, they probed SFRs down to ultra-low activities on the order of 10^{-4} M$_\odot$/yr, showing that Hα emission alone could lead to underpredict up to a factor of two the SFR. From the extinction-corrected luminosity of the redshifted Hα component (shown in red in Fig. 2.15), we find a SFR $\sim 8\times10^{-3}$ M$_\odot$/yr in the outflow. Taking into account also the SF blob in the disk, we obtain a total SFR ~ 0.01 M$_\odot$/yr, which is $\sim 3\%$ of the global value of the galaxy (SFR $= 0.4$ M$_\odot$/yr Diamond-Stanic & Rieke 2012). However, we are observing just a small part of the outflow in Centaurus A, given the dust obscuration and the MUSE limited FOV due to the proximity of the

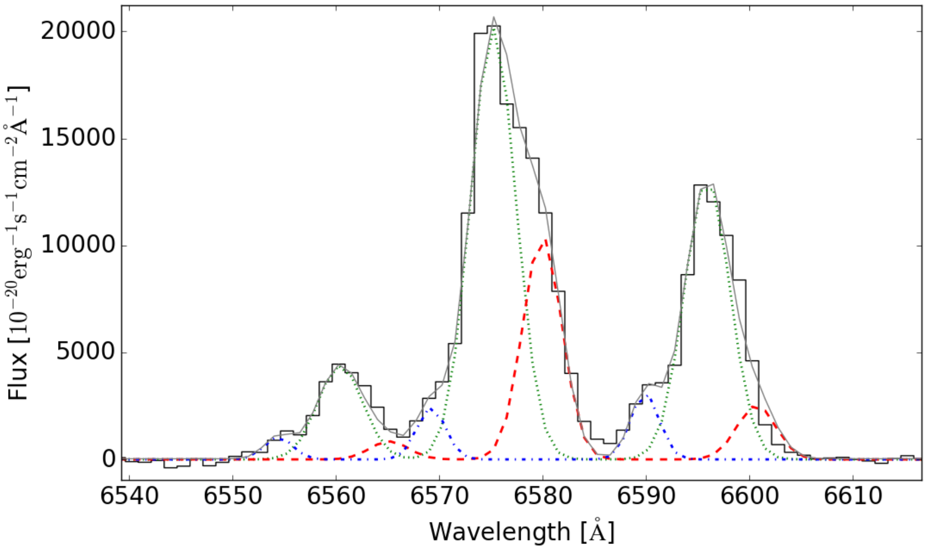

Figure 2.15: Spectrum of the SF blob in the outflow in the wavelength range 6500 − 6650 Å. The asymmetric line profile is reproduced by a three Gaussian component fit: blueshifted (dashed-dotted blue gaussian), systemic (dotted green gaussian) and redshifted (dashed red gaussian).

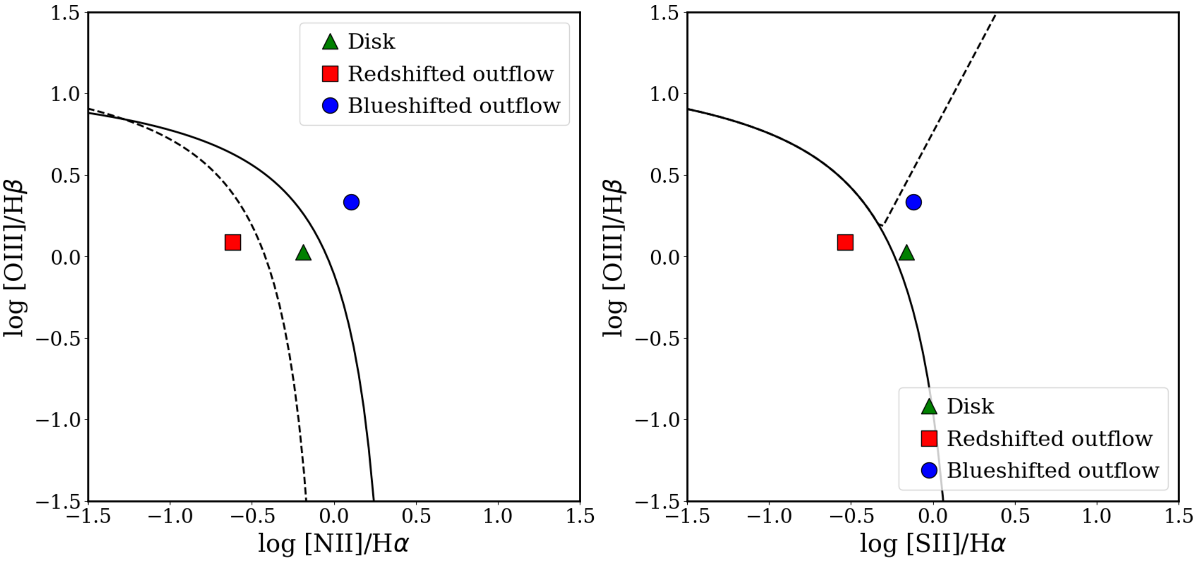

Figure 2.16: [N II] and [S II]BPT diagrams of the three Gaussian components used to fit the asymmetric line profiles shown in Fig. 2.15. Note that while the blueshifted (dashed-dotted blue gaussian) and disk (dotted green gaussian) components have AGN and Composite/LI(N)ER-like ratios, respectively, the redshifted component (dashed red gaussian) is SF dominated.

source, which means that there could be many more SF clumps embedded in the outflow. Even if the contribution to the total SFR might seem irrelevant, it remains that Centaurus A could be a local test bench to explore in detail the structure and kinematic of the gas, improving our knowledge on positive feedback and possibly confirming that it is not a rare mechanism. Indeed, this phenomenon may play a significant role in the formation of the spheroidal component of galaxies at high redshift, where AGN-driven outflows are more prominent and, possibly, the associated SF inside those very massive outflows much higher (Gallagher et al., 2019; Rodríguez del Pino et al., 2019).

Overall, these two blobs could represent the first evidence of the two modes of positive feedback in the nuclear region of this galaxy. However, Maiolino et al. (2017) demonstrated that only the combination of X-Shooter (D'Odorico et al., 2006; Vernet et al., 2011) and MUSE data allow to undoubtedly identify the signatures of SF in the outflow. Indeed, X-shooter has a broad-band spectral coverage able to cover IR diagnostics, such as the [Fe II]$\lambda 1.64\mu$m/Br$\gamma\lambda 2.16\mu$m versus the $H_2(1-0)S(1)\lambda 2.12\mu$m/Br$\gamma$ and the [Fe II]$\lambda 1.25\mu$m/Pa$\beta\lambda 1.28\mu$m versus [P II]$\lambda 1.18\mu$m/Paβ diagrams (Oliva et al., 2001; Colina et al., 2015), that can further discriminate among SF, AGN and shock ionisation. Typically, in star forming regions these ratios are expected to be very low, since shocks could enhance the emission of [Fe II] and H_2, while the Brγ and the [P II] are direct tracers of the AGN UV and soft-X ionising radiation, respectively. Moreover, X-shooter high spectral resolution allows to investigate the presence of young stars formed in the outflow. To do this, the stellar absorption features, such as the Balmer series down to $\lambda \sim 4000$ Å (tracing young hot O-B-type stars), the Ca II triplet at $\lambda \sim 8500$ Å (in case of recent SF, dominated by young red supergiants and young asymptotic giant branch stars) and, possibly, the weak absorption feature of HeIλ4922 Å(unambiguous tracer of B-type stars and of young stellar populations) can be taken into account. Hence, we successfully asked for observations with the X-Shooter spectrograph (0102.B-0292(A), P.I. Mingozzi). The observations were carried out during the nights of April 1-2 and of August 3-5 2019, making use of the 0.8" slit, orientated in order to observe the two SF blob simultaneously, and will be analysed in the next months.

2.5 Conclusions

In this Chapter, we explored the gas properties (e.g. density, ionisation parameter, reddening and source of ionisation) of the outflowing gas in the (E)NLR of the 9 nearby Seyfert galaxies that are part of the MAGNUM survey, all characterised by prominent conical or biconical outflows. Exploiting the very high spatial resolution of the optical integral field MUSE spectrograph at VLT, we were able to disentangle the outflow component from the disk component in order to analyse its peculiarities through spatially and kinematically resolved maps. To do this, we divided the main emission lines (Hβ, [O III], [O I], Hα, [N II], [S II] and [S III]) in velocity bins, associating the core of the lines (centred on the stellar velocity in each spaxel) with the disk, and the blueshifted and redshifted wings with the outflow. In the following, we report our main results:

- In Sec. 2.2.1, we show that the outflow component is characterised by higher median densities and [S III]/[S II] ratio, which is a proxy for the ionisation parameter ($\langle A_V \rangle \sim 0.9$, $\langle n_e \rangle \sim 250$ cm^{-3}, $\langle \log([\mathrm{S\,III}]/[\mathrm{S\,II}]) \rangle \sim 0.16$) with respect to the gas in the disk, which instead is more affected by dust extinction ($\langle A_V \rangle \sim 1.75$, $\langle n_e \rangle \sim 130$ cm^{-3}, $\langle \log([\mathrm{S\,III}]/[\mathrm{S\,II}]) \rangle \sim -0.38$). Our median outflow density is lower with respect to what we found in the literature. However, calculating the median density weighting for the [S II] line flux, we obtain higher values ($\langle n_e \rangle \sim 170$ cm^{-3} and $\langle n_e \rangle \sim 815$ cm^{-3}, for disk and outflow, respectively). Therefore, many values of outflow density found in the literature could be biased towards higher n_e because they are based only on the most luminous outflowing regions and are characterised by a higher S/N.

- In Sec. 2.2.2, we analyse the ionisation state of the (E)NLR of MAGNUM galaxies, by making spatially and kinematically resolved BPT diagrams. We find that the AGN/LI(N)ER-dominated outflow is characterised by the lowest and highest values of low-ionisation line ratios (LILrs, $\log([\mathrm{N\,II}]/\mathrm{H}\alpha) \sim -1$, $\log([\mathrm{S\,II}]/\mathrm{H}\alpha) \sim -1$ and $\log([\mathrm{N\,II}]/\mathrm{H}\alpha) \sim 0.5$, $\log([\mathrm{S\,II}]/\mathrm{H}\alpha) \sim 0.5$, respectively), which are not observed in the disk. The lowest LILrs mainly come from the innermost regions of the outflowing cone, near the outflow axis, also characterised by the highest [S III]/[S II] line ratios ([S III]/[S II] ~ 2), meaning high excitation. On the other hand, the highest LILr appear to come from the edges of the outflowing cones and/or from the regions perpendicular to the axis of the outflow, typically characterised by high values of [O III] velocity dispersion ($\sigma_{[\mathrm{O\,III}]} > 200$ km/s).

- In Sec. 2.3, we make a comparison of our spatially and kinematically resolved BPT diagrams with photoionisation and shock models. Specifically, we found that the matter and ionisation bounded (MB and IB) dichotomy first introduced by Binette et al. (1996) could reproduce well most of the observed features. MB clouds, characterised by high-ionisation lines (e.g. high [O III]/Hβ) and high excitation (i.e. high [S III]/[S II]) could account for both the [N II]/Hα, [S II]/Hα decrease and the [S III]/[S II] enhancement observed in the majority of MAGNUM galaxies. On the other hand, IB clouds, optically thick and characterised by a much lower excitation, could be responsible for higher [N II]/Hα and [S II]/Hα line ratios, found both in the outflowing and in the disk components. Shocks may explain the highest

[N II]/Hα and [S II]/Hα line ratios and the [O III] velocity dispersion enhancement. Consistently, we show the stacked spectrum of the region dominated by the lowest LILr of Circinus, characterised by the presence of coronal lines (e.g. [Fe VI]λ5146, [Fe XIV]λ5303, [Fe VII]λ5721, [Fe VII]λ6087, [Fe X]λ6374), suggesting a very high excitation.

- In Sec. 2.4, we illustrate the detection of two blobs embedded in the ionisation cone of Centaurus A, that could represent the first evidence of the two modes of positive feedback in act in the nuclear region of this galaxy. We will soon analyse X-shooter data with the aim of unambiguously confirming the presence of positive feedback and fast moving young stars forming in the outflow.

We speculate that the gas in the outflowing cones of our galaxies is set up in clumpy clouds characterised by higher density and ionisation parameters with respect to the disk gas. The innermost regions of the cone are optically thin to the radiation, being characterised by high excitation, and are possibly directly heated by the central ionising AGN. The edges of the cones and the regions perpendicular to the outflow axis could instead be dominated by shock excitation probably because of the interaction between the outflowing gas and the ISM. Alternatively, these regions, generally characterised by low excitation ([S III]/[S II] < 1) could be impinged by an ionising radiation filtered by clumpy, ionised absorbers. Although these conclusions apply to the MAGNUM sample as a whole, some details may differ in individual galaxies. As an example, NGC1068 is the only galaxy that shows an enhancement of the [S III]/[S II] line ratio in the regions characterised by the highest LILr. The next step of our analysis will be a detailed modelling of each MAGNUM galaxy, also making use of the photoionisation code CLOUDY (Ferland et al., 2017) to better investigate the different scenarios that we propose to interpret our findings.

2.6 Additional material

2.6.1 Extinction maps

We derive the dust extinction map for each galaxy, making use of the Balmer decrement Hα/Hβ, assuming a Calzetti et al. (2000) attenuation law and a fixed temperature of 10^4 K. The resulting extinction map for the MAGNUM galaxies Centaurus A, IC 5063, NGC 1068, NGC 1365, NGC 1386, NGC 2992, NGC 4945, and NGC 5643 are shown in Fig. 2.17. We show only the spaxels in which the Hα and Hβ lines are detected with S/N > 5.

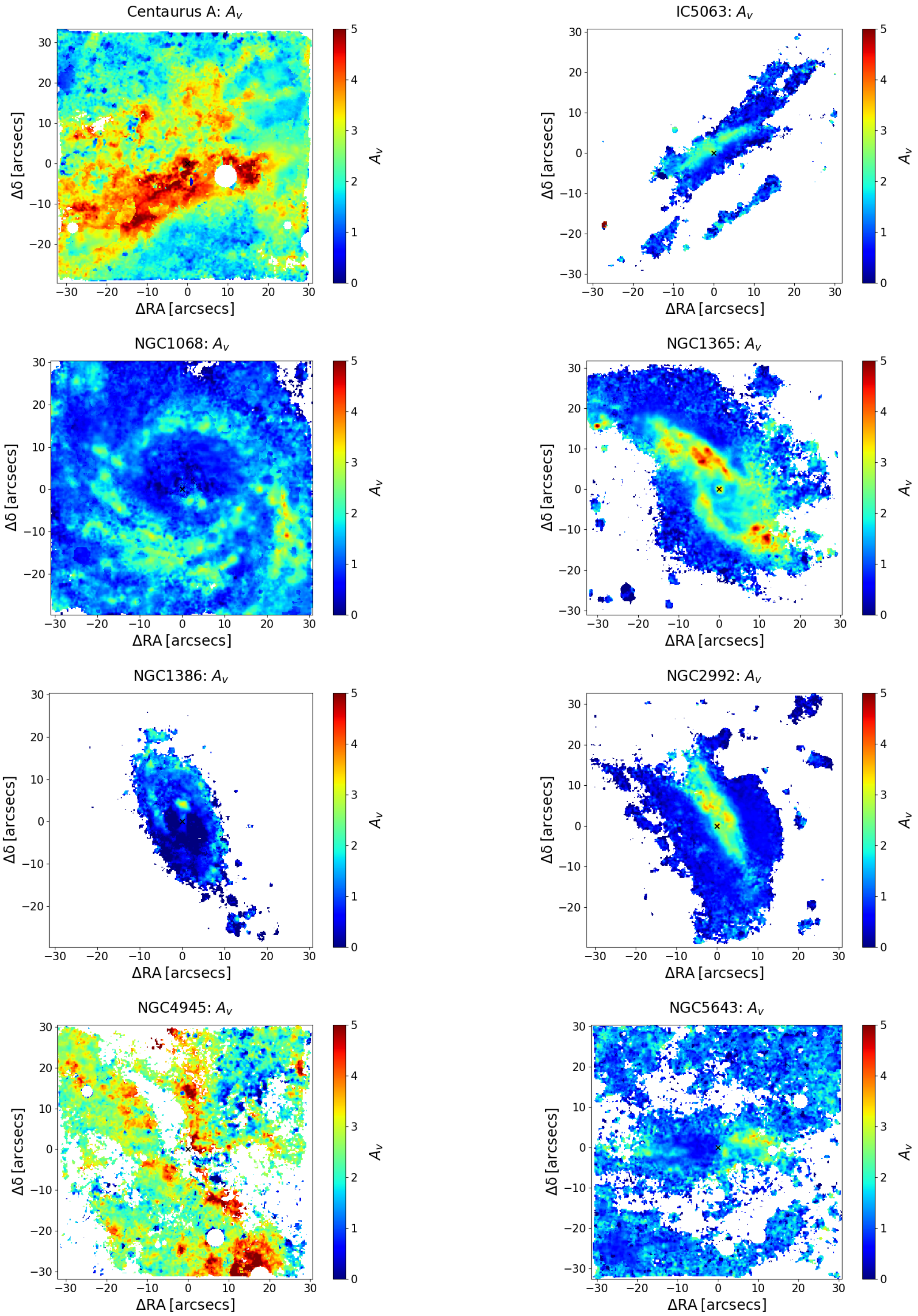

Figure 2.17: Maps of the total extinction in V band A_V, obtained from the Balmer decrement $H\alpha/H\beta$, for Centaurus A, IC 5063, NGC 1068, NGC 1365, NGC 1386, NGC 2992, NGC 4945, and NGC 5643. Only spaxels with $H\alpha$ and $H\beta$ $S/N > 5$ are shown.

2.6.2 Electron density maps

We have computed the [S II]$\lambda\lambda$6717,31 line ratio in each spaxel where the [S II] lines are detected with S/N > 5, and converted it to an electron density using the Osterbrock & Ferland (2006) model, sensible to the density variations in the range 50 cm^{-3} $<$ $n_e < 5000$ cm^{-3}, assuming a temperature of 10^4 K. The resulting electron density maps of the MAGNUM galaxies Centaurus A, IC 5063, NGC 1068, NGC 1365, NGC 1386, NGC 2992, NGC 4945, and NGC 5643 are shown in Fig. 2.18.

2.6.3 [SIII]/[SII] maps

We computed the [S III]$\lambda\lambda$9069,9532/[S II]$\lambda\lambda$6717,31 line ratio in each MUSE spaxel where the line fluxes are detected with S/N > 5 since it is a proxy for the ionisation parameter (e.g. Diaz et al. 1991). The resulting maps for the MAGNUM galaxies Centaurus A, IC 5063, NGC 1068, NGC 1365, NGC 1386, NGC 2992, NGC 4945, and NGC 5643 are shown in Fig. 2.19.

2.6.4 Spatially and kinematically resolved BPT diagrams

The left panels of Figs. 2.20, 2.21, and Figs. 2.22, 2.23 show the [N II]- and [S II]-BPT diagrams for the disk and outflow components of Centaurus A, Circinus, IC 5063, NGC 1068, NGC 1365, NGC 1386, NGC 2992, NGC 4945, and NGC 5643, respectively. The black dashed curve, solid curve and dotted line show the ka03, ke01 and ke06 boundaries, respectively. The dominant source of ionisation is colour-coded: blue for SF, green for intermediate regions in the [N II]-BPT and LI(N)ER in the [S II]-BPT, and red for AGN-like ionised spectra. The colours are shaded as a function of the x-axis line ratios (darker shades means higher x-axis line ratios). The corresponding position on the map of the galaxy, colour-coded according to the different source of ionisation, is shown in the right panels. In the background of all the pictures (black dots in the BPTs and shaded grey in the corresponding maps) are reported the disk and outflow components together to allow us a better visual comparison.

Moreover, Figs. 2.24 and 2.25 show the [N II]- and [S II]-BPT diagrams colour-coded as a function of the [S III]/[S II] line ratio, which is a proxy of the ionisation parameter (darker shades means higher [S III]/[S II] line ratios). Finally, Figs. 2.26 and 2.27 show the [N II]- and [S II]-BPT diagrams colour-coded as a function of the [O III] velocity dispersion $\sigma_{\text{[O III]}}$ (darker shades means higher $\sigma_{\text{[O III]}}$).

For each velocity bin, we selected only the spaxels with a S/N > 5 on each emission

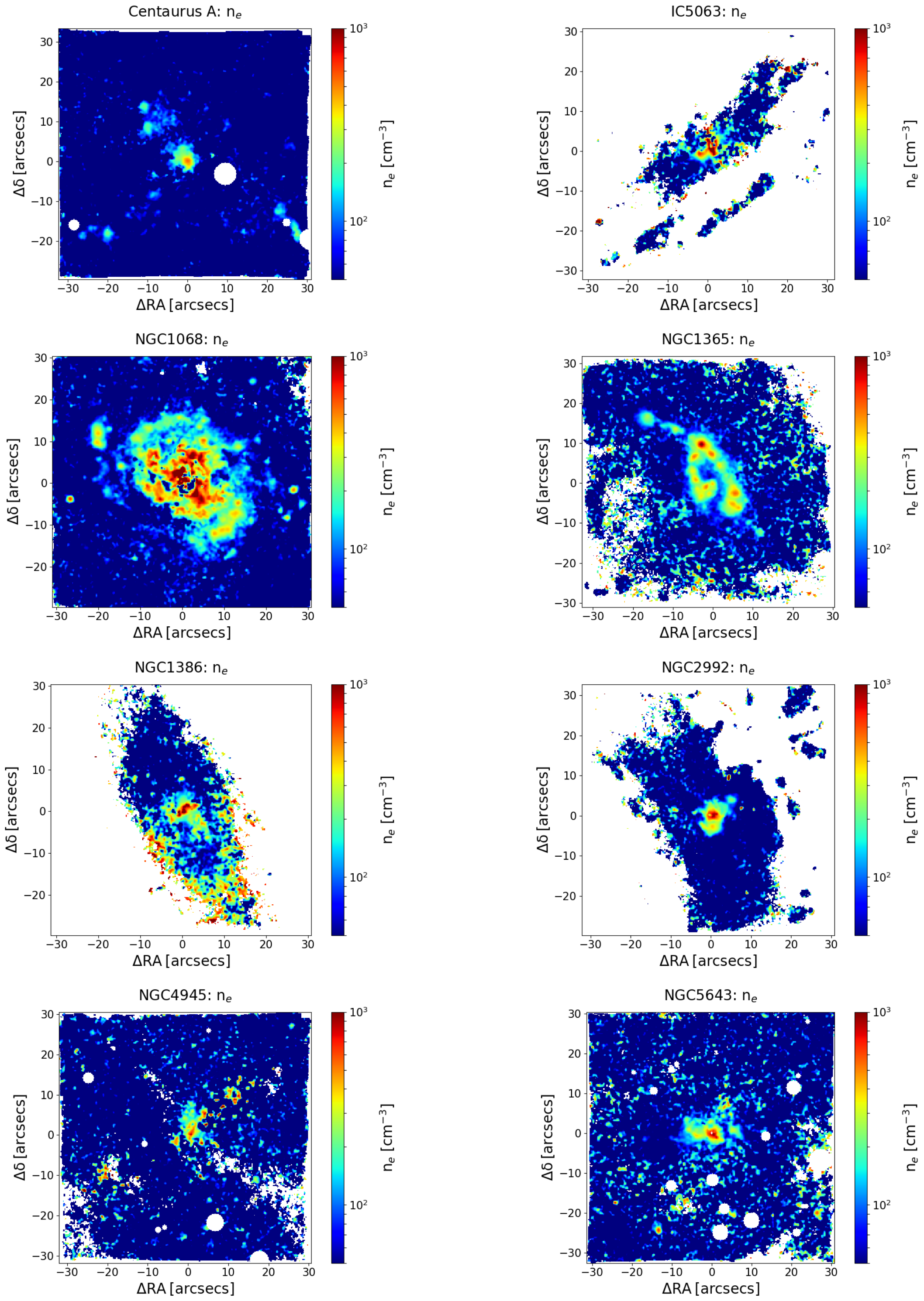

Figure 2.18: Maps of the total electron density n_e, measured from the [S II]λ6717/[S II]λ6731 ratio, for Centaurus A, IC 5063, NGC 1068, NGC 1365, NGC 1386, NGC 2992, NGC 4945, and NGC 5643. Only spaxels with [S II]λ6717 and [S II]λ6731 S/N > 5 are shown.

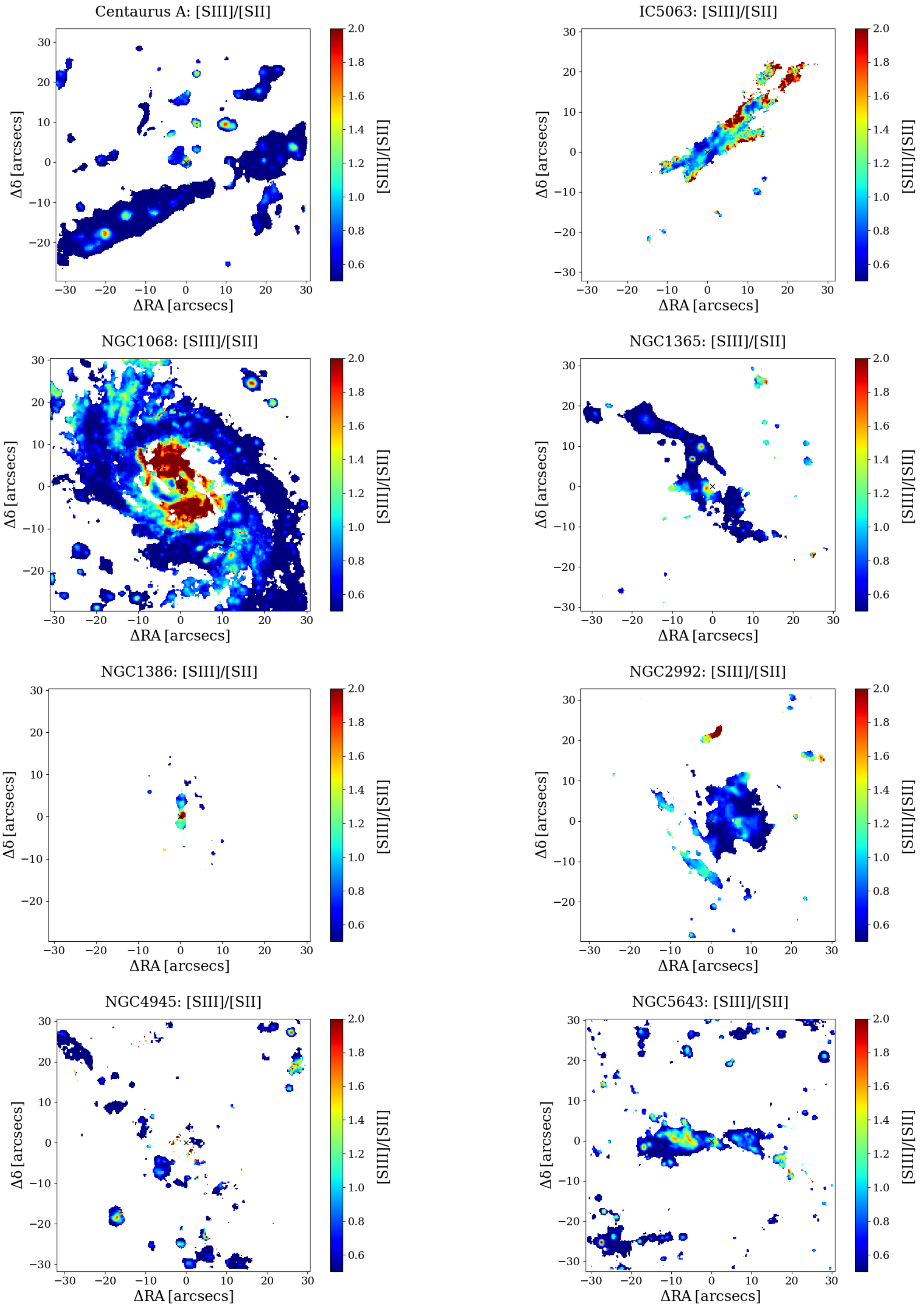

Figure 2.19: Maps of [S III]λλ9069,9532/[S II]λλ6717,31 ratio, a proxy for the ionisation parameter, for Centaurus A, IC 5063, NGC 1068, NGC 1365, NGC 1386, NGC 2992, NGC 4945, and NGC 5643. Only spaxels with [S III]λ9069 and [S II]λλ6717,31 S/N > 5 are shown.

line involved in the given diagram, computed by dividing the flux integrated in the velocity channels considered by the corresponding noise.

For NGC 1365, we show the BPT diagrams obtained from the Voronoi-binned cube in order to detect the biconical outflow, which would be too weak to be detected in Hβ otherwise.

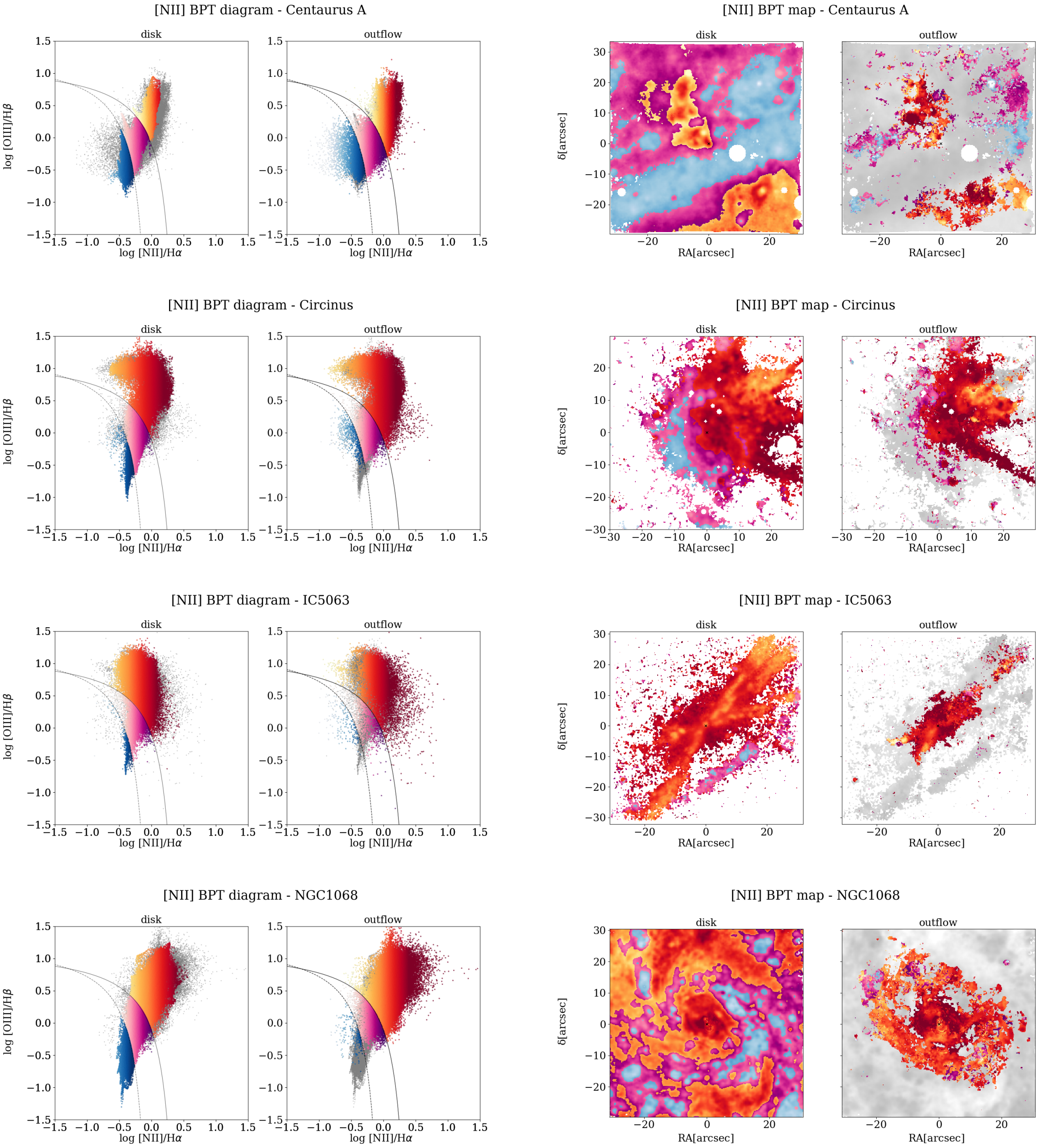

Figure 2.20: Left panels: [N II]-BPT diagrams for the disk (left) and outflow (right) components of Centaurus A, Circinus, IC 5063 and NGC 1068 (shades of blue for SF, pink for composite regions, and red for AGN-like ionising spectra), coloured-coded as a function of the [N II]/Hα line ratio (darker shades means higher [N II]/Hα). The black-dashed and solid curves indicate the Ka03 and Ke01 boundaries, respectively. Right panels: [N II]-BPT maps, colour-coded according to the BPT classification. In the background the disk and outflow components are shown in gray. For each velocity bin, we select only the spaxels with a S/N > 5 for all the flux line ratios.

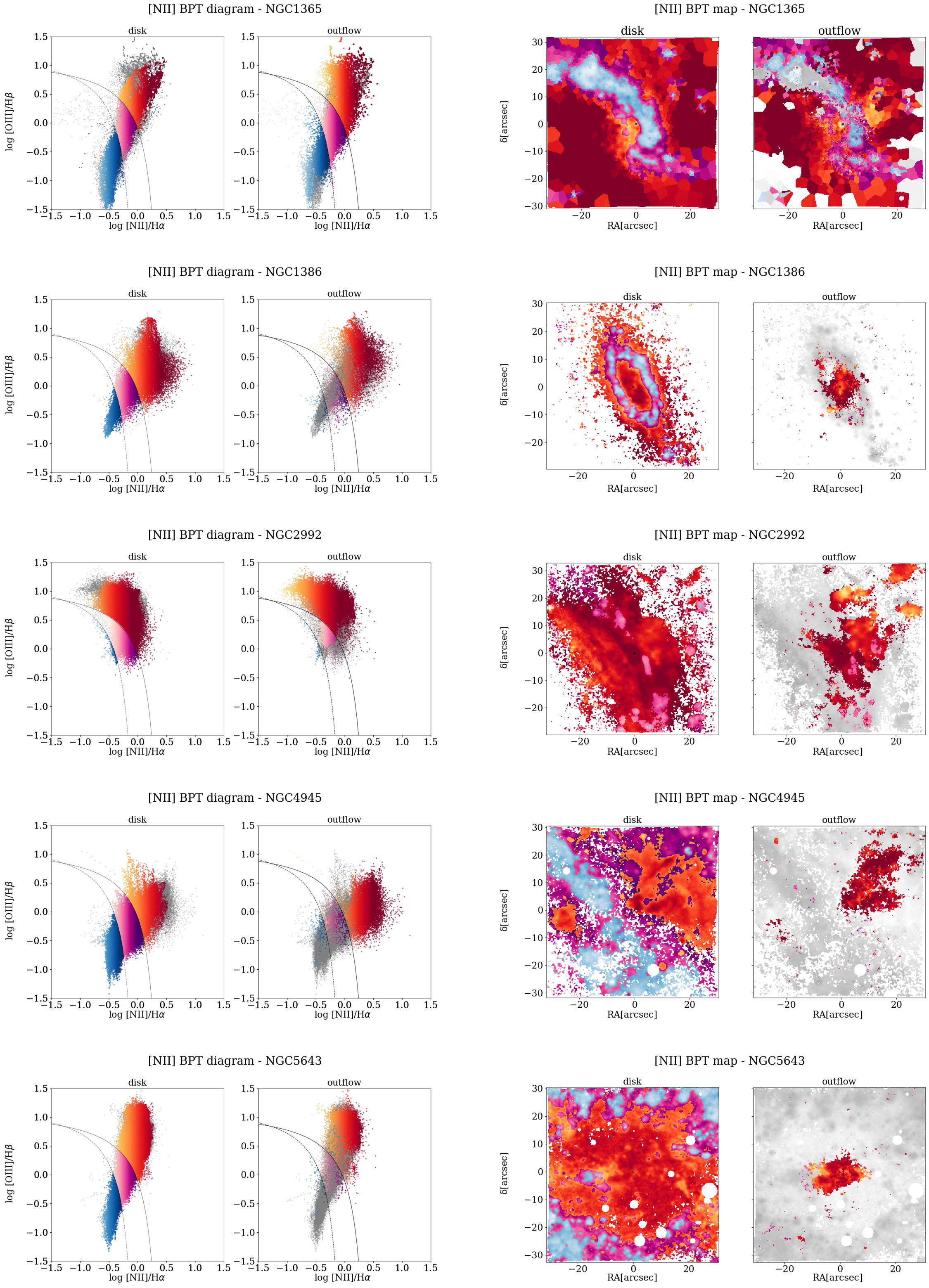

Figure 2.21: Same as Fig. 2.20, but for NGC 1365, NGC 1386, NGC 2992, NGC 4945, and NGC 5643.

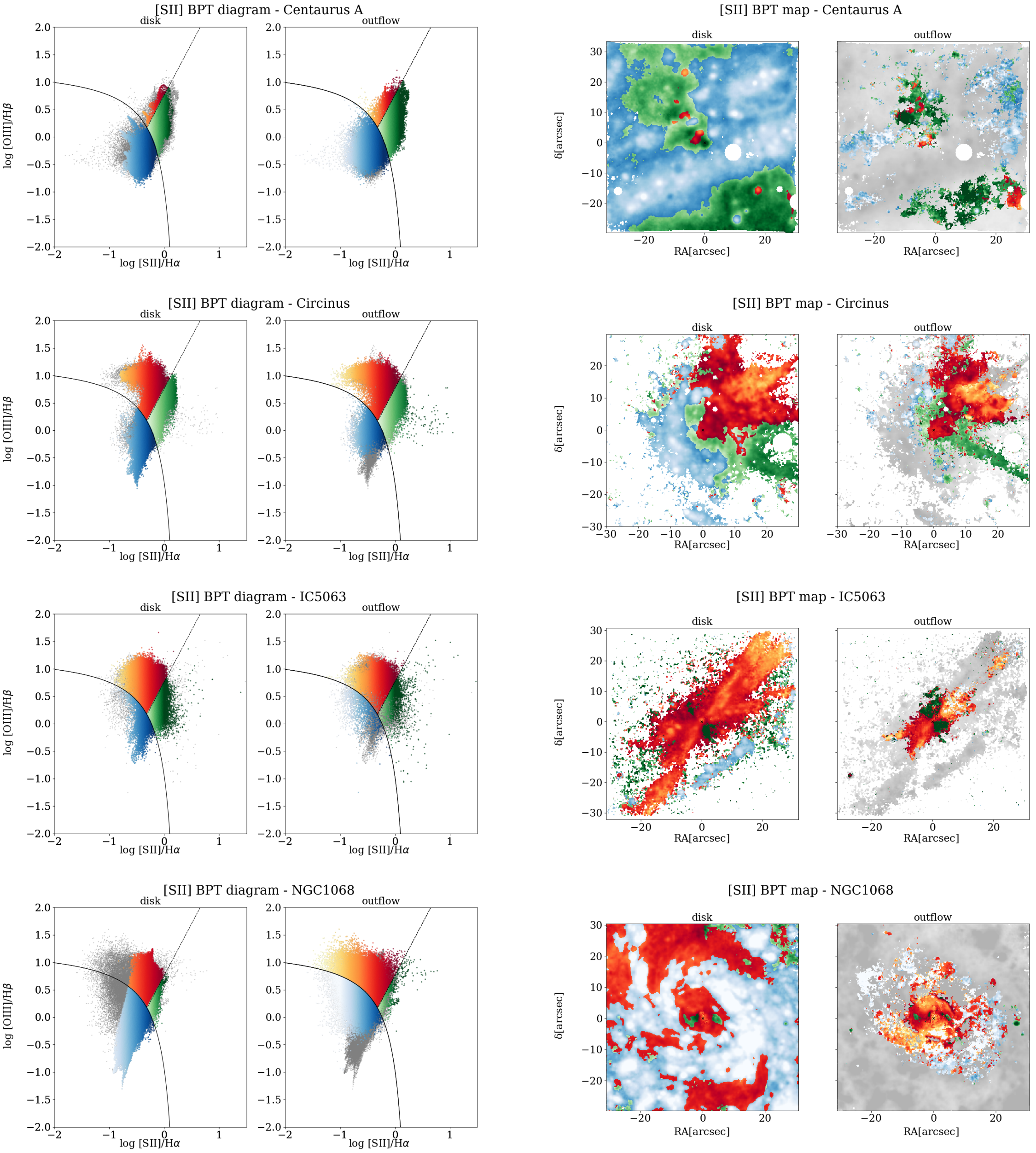

Figure 2.22: Left panels: [S II]-BPT diagrams for the disk (left) and outflow (right) components of Centaurus A, Circinus, IC 5063 and NGC 1068 (shades of blue for SF, green for LI(N)ER, and red for AGN-like ionising spectra), colour-coded as a function of the [S II]/Hα line ratio (darker shades means higher [S II]/Hα). The black-solid curve and the black-dotted line indicate the Ke01 and Ke06 boundaries, respectively. Right panels: [S II]-BPT maps, colour-coded according to the BPT classification. In the background the disk and outflow component are shown in gray. For each velocity bin, we select only the spaxels with a S/N > 5 for all the flux line ratios.

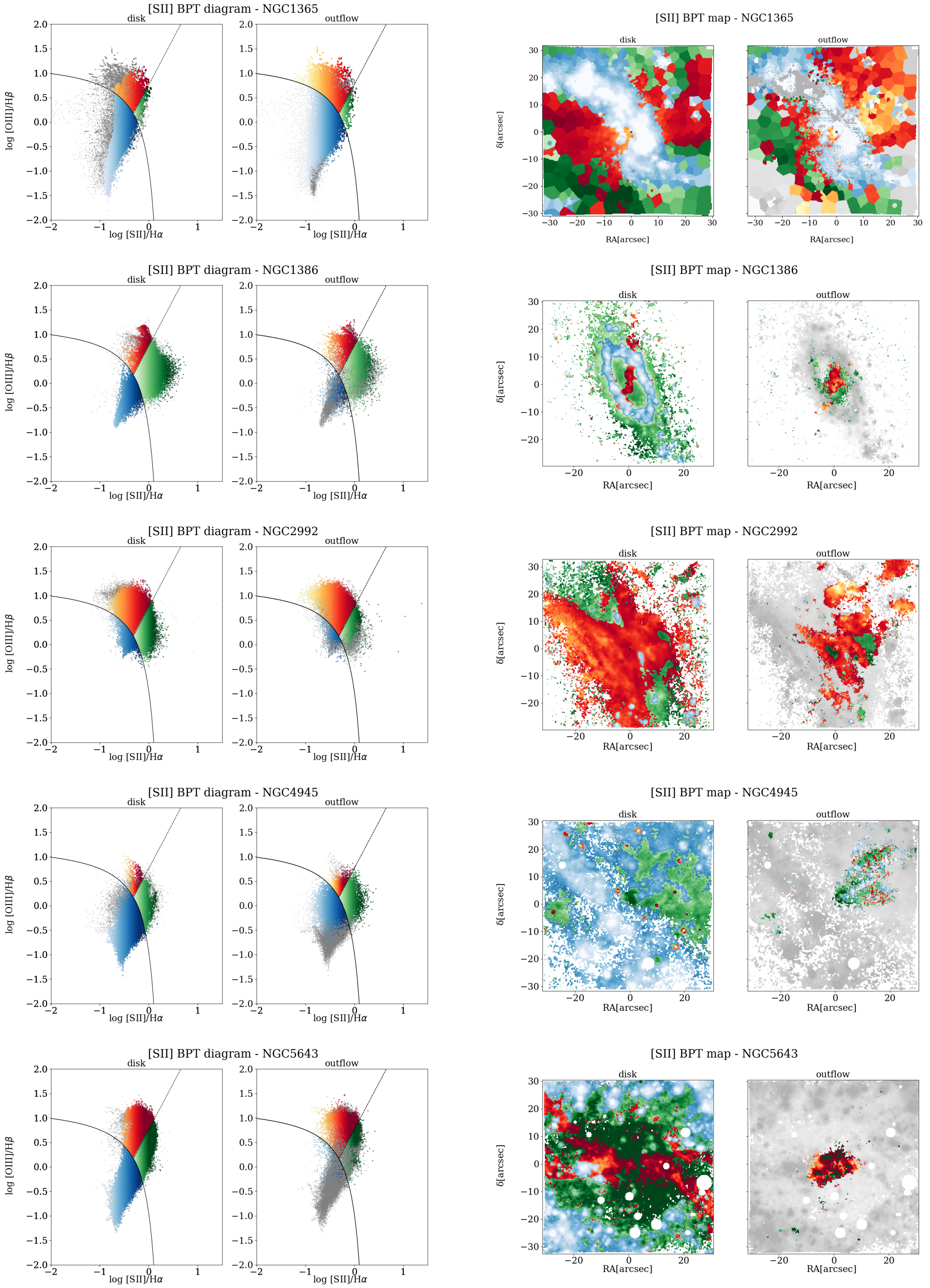

Figure 2.23: Same as Fig. 2.22, but for NGC 1365, NGC 1386, NGC 2992, NGC 4945 and NGC 5643.

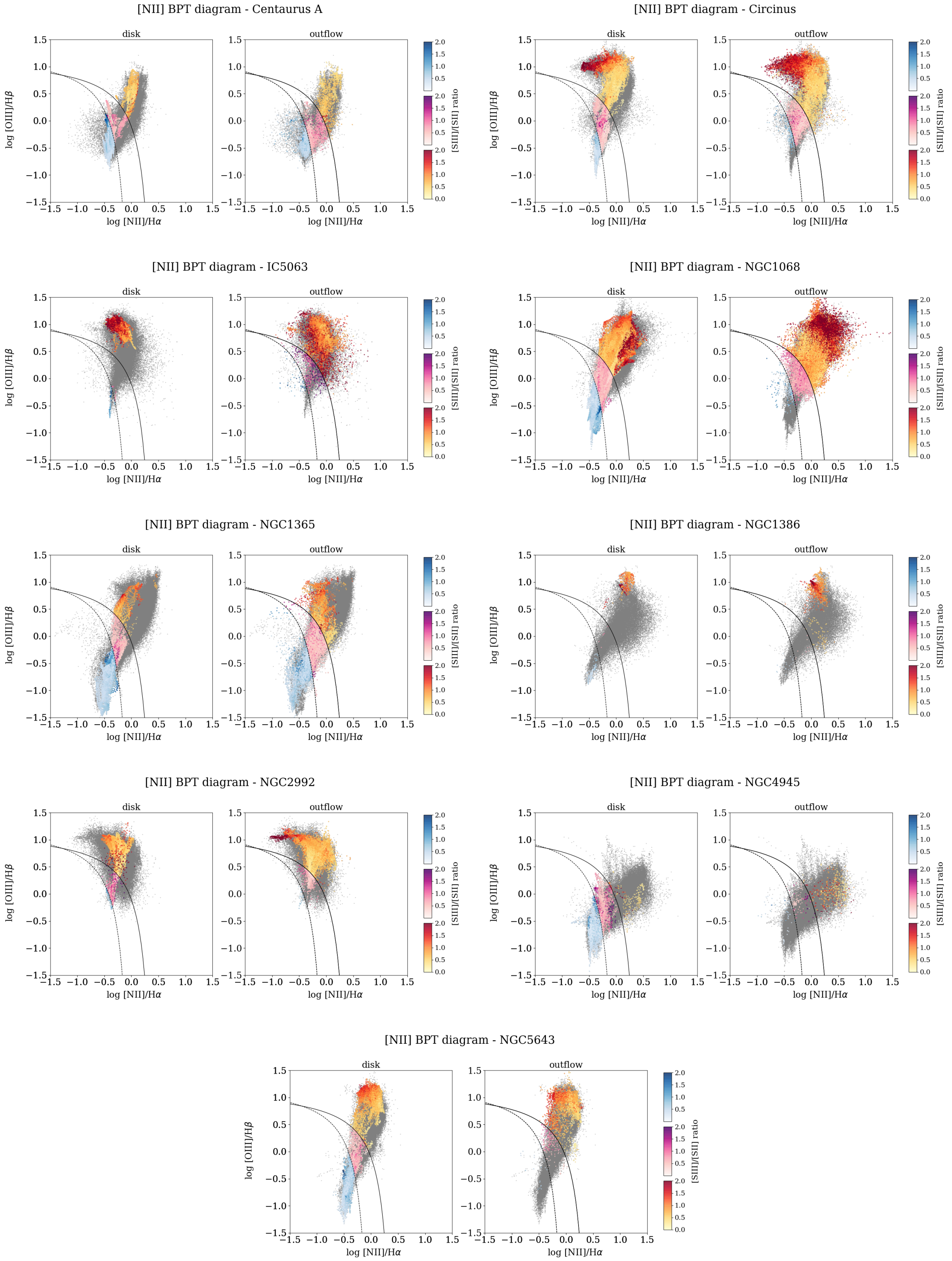

Figure 2.24: [N II]-BPT diagrams for the disk and outflow components for all the MAGNUM galaxies, colour-coded as a function of the [S III]/[S II] line ratio (darker shades means higher [S III]/[S II]).

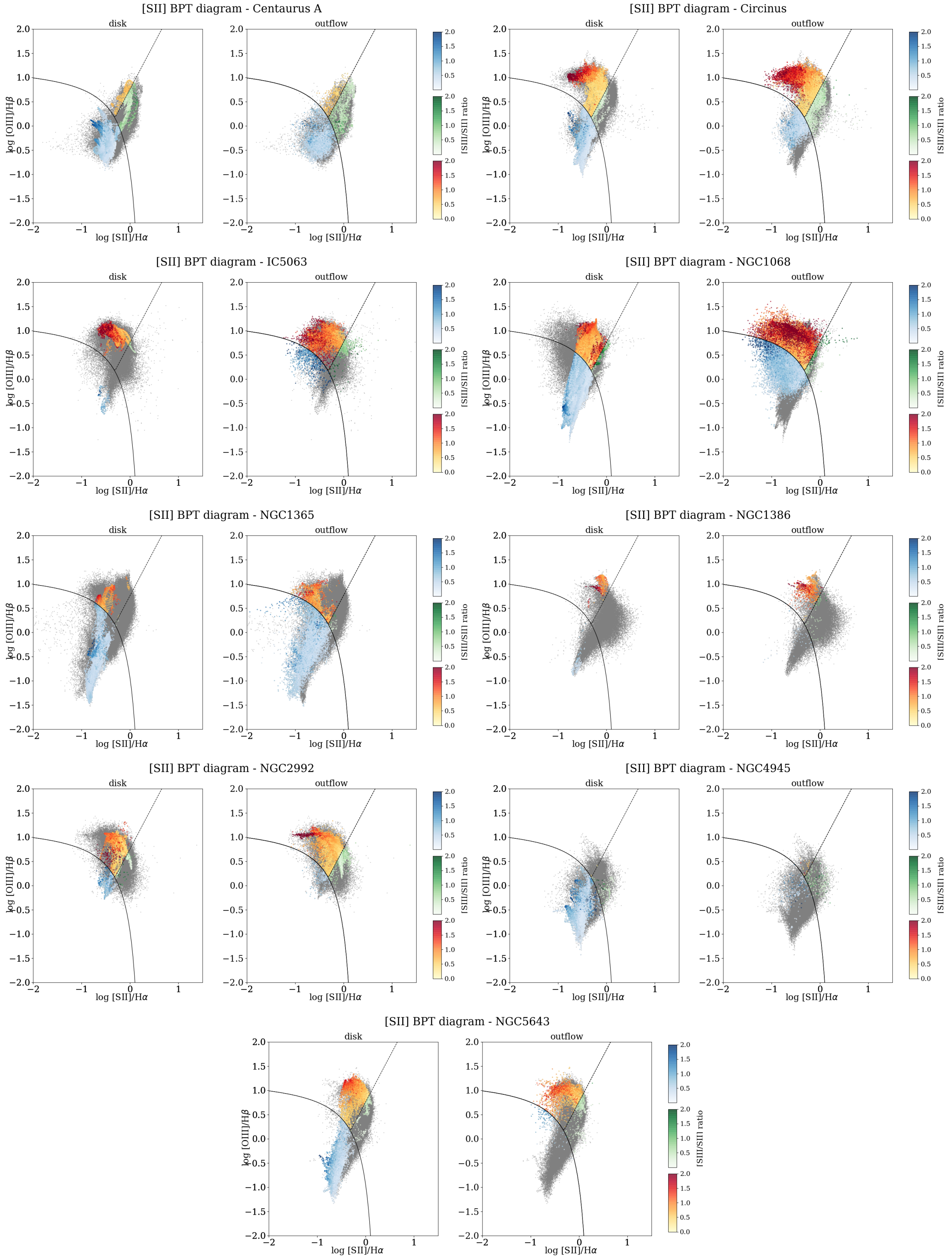

[SII] BPT diagram - Centaurus A

[SII] BPT diagram - Circinus

[SII] BPT diagram - IC5063

[SII] BPT diagram - NGC1068

[SII] BPT diagram - NGC1365

[SII] BPT diagram - NGC1386

[SII] BPT diagram - NGC2992

[SII] BPT diagram - NGC4945

[SII] BPT diagram - NGC5643

Figure 2.25: [S II]-BPT diagram for the disk and outflow components for all the MAGNUM galaxies, colour-coded as a function of the [S III]/[S II] line ratio (darker shades means higher [S III]/[S II]).

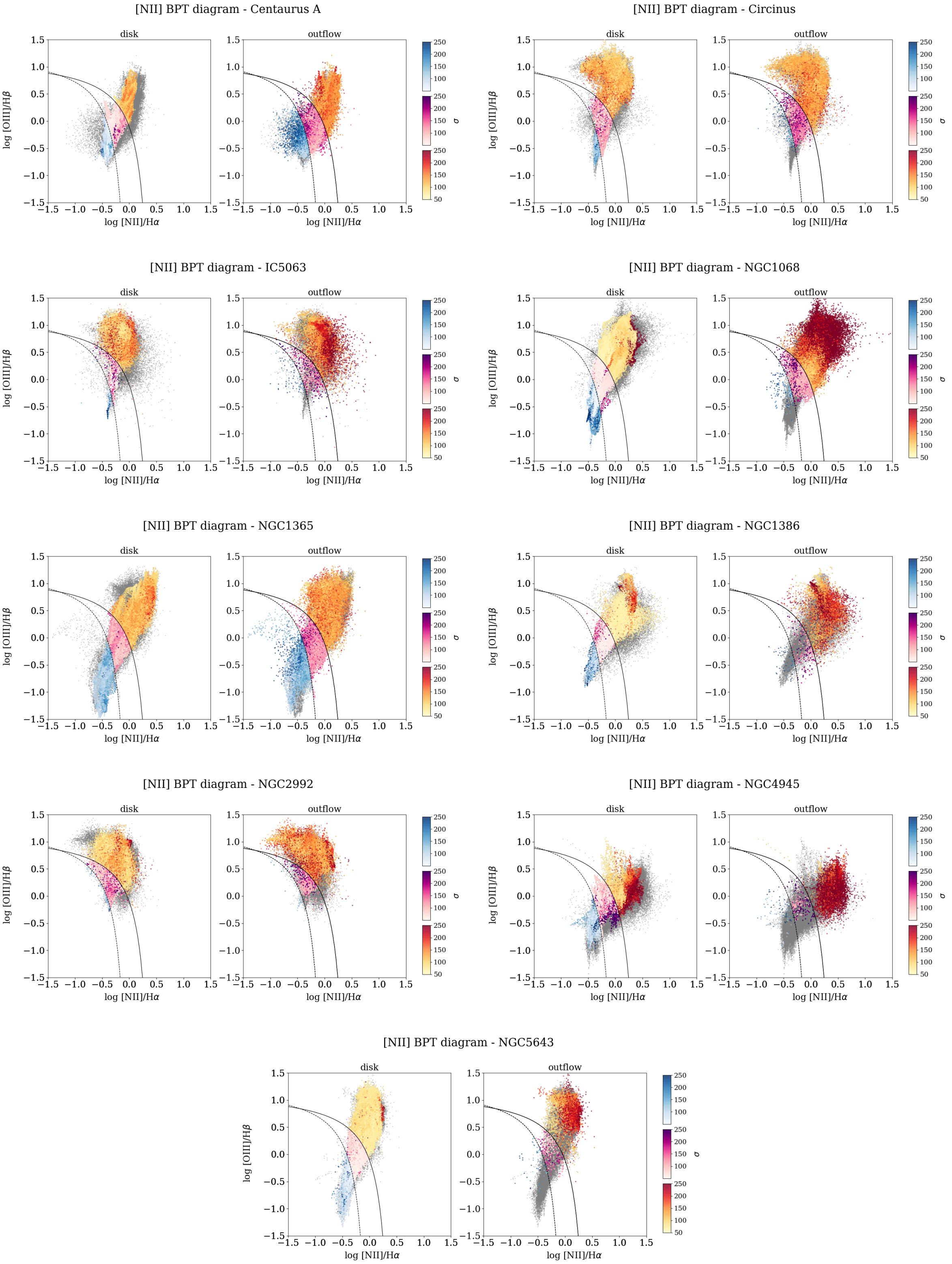

Figure 2.26: [N II]-BPT diagram for the disk and outflow components for all the MAGNUM galaxies, colour-coded as a function of the [O III] velocity dispersion $\sigma_{[\mathrm{O\,III}]}$ (darker shades means higher $\sigma_{[\mathrm{O\,III}]}$).

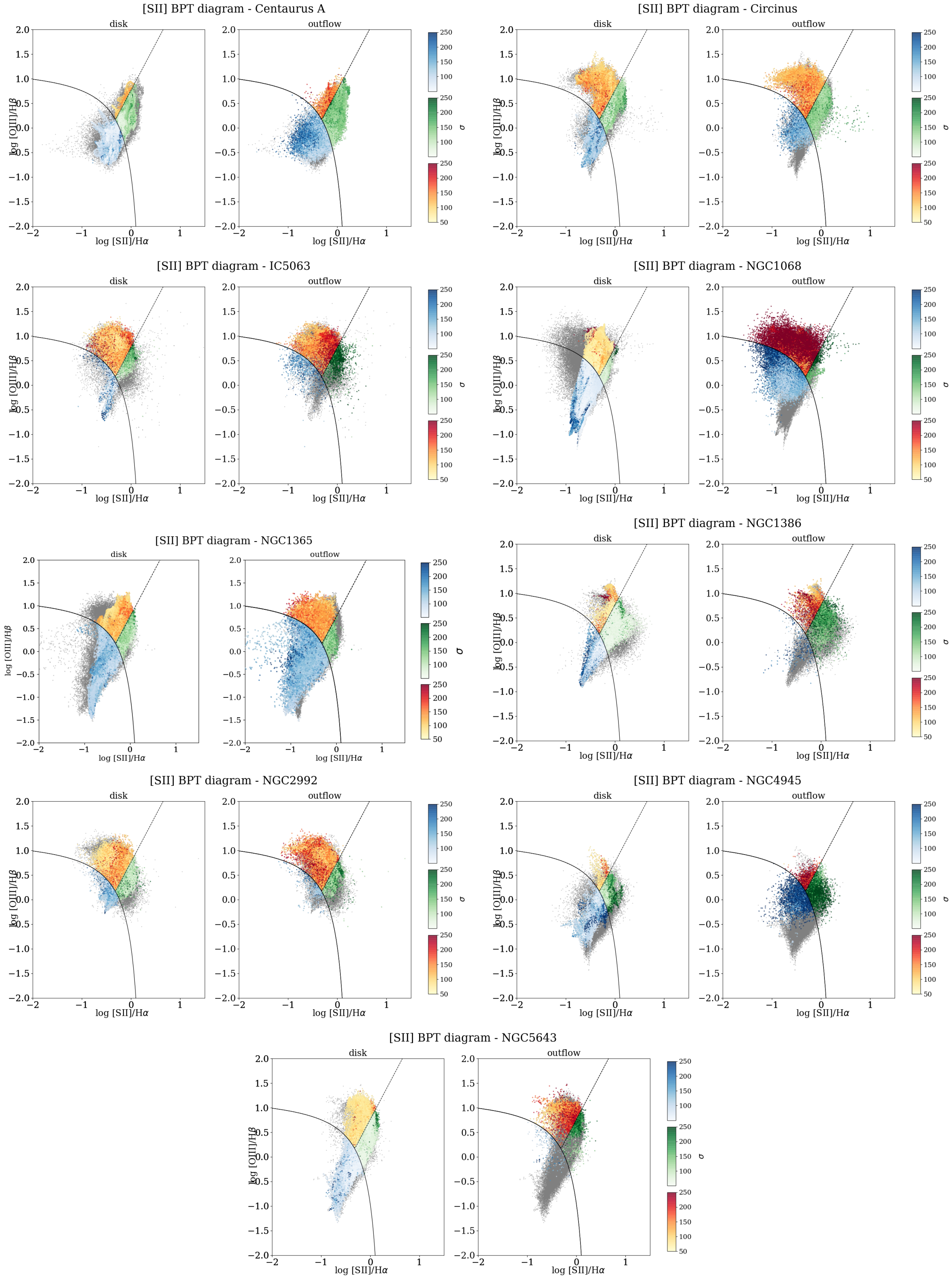

Figure 2.27: [S II]-BPT diagram for the disk and outflow components for all the MAGNUM galaxies, colour-coded as a function of the [O III] velocity dispersion $\sigma_{[\mathrm{O\,III}]}$ (darker shades means higher $\sigma_{[\mathrm{O\,III}]}$).

Chapter 3

Metallicity and ionisation parameter in local star forming galaxies

Adapted from: (i) "SDSS IV MaNGA - Metallicity and ionisation parameter gradients of local star forming galaxies from Bayesian fitting to photoionisation models", **M. Mingozzi***, F. Belfiore, G. Cresci, K. Bundy, M. Bershady, D. Bizyaev, G. Blanc, M. Boquien, N. Drory, H. Fu, R. Maiolino, R. Riffel, A.Schaefer, E. Telles, C. Tremonti, T. Storchi-Bergmann, N. Zakamska, and K. Zhang, resubmitted to A&A (arXiv:2002.05744); (ii) "The MUSE view of He 2-10: no AGN ionisation but a sparkling starburst", G. Cresci, L. Vanzi, E. Telles, G. Lanzuisi, M. Brusa,* **M. Mingozzi***, M. Sauvage and K. Johnson, 2017, MNRAS, Volume 604, id.A101, 11 pp.*

The metal content in galaxies is mainly governed by the interplay of metal production via stellar nucleosynthesis, gas (and metal) inflow, and outflows via galactic winds. Because of these connections, the abundance and distribution of metal in a galaxy interstellar medium (ISM) provides strong constraints on current models of galaxy evolution (e.g. Lilly et al. 2013; Maiolino & Mannucci 2019).

As discussed in Chapter 1 (Sec. 1.3.1), metallicity measurements in extragalactic sources at even modest redshifts and in large galaxy surveys are usually based on strong nebular emission lines (SEL), following the pioneering works of Pagel et al. (1979) and Alloin et al. (1979), given the faintness of auroral and metallicity-sensitive recombination lines (see e.g. Pettini & Pagel 2004; Curti et al. 2017).

An important limitation of the "strong-line approach" to determining metallicity is the secondary dependence of metallicity diagnostics on other parameters of the ISM, such as the ionisation parameter q or $U = q/c$, where c is the speed of light (see Sec. 1.3.1 and Eq. 1.1 in Chapter 1). Across a large sample of H II regions, once all the other parameters are kept fixed, metallicity and ionisation parameter are expected to be anti-correlated (e.g. Dopita & Evans 1986), because the ionising photon flux of a star increases with decreasing metallicity (e.g. Freitas-Lemes et al. 2014; Pérez-Montero 2014 and Rosa et al. 2014). This physical link between the two key parameters of H II regions is implicitly assumed in empirical calibration that relate SEL diagnostics to metallicity and the effect of q is included in the scatter of the relations (e.g. Maiolino & Mannucci 2019) because these calibrations are based on observed samples of H II regions.

Empirically the ionisation parameter is best determined by ratios of emission lines of different ionisation stages of the same element (see Sec. 1.3.1, Chapter 1), with O3O2 = [O III]λ5007/[O II]$\lambda\lambda$3726,29 being the most widely used proxy in the optical wavelength range (Díaz & Pérez-Montero, 2000; Kewley & Dopita, 2002; Kobulnicky & Kewley, 2004). However, O3O2 is strongly dependent on metallicity as well, as shown for example in Kewley & Dopita (2002), since the [O II] lines can only be excited by relatively hot electrons, disappearing in cooler, high-metallicity H II regions. Kewley & Dopita (2002) demonstrated that [S III]$\lambda\lambda 9069, 9532$/[S II]$\lambda 6717, 32$ (S3S2) provides a more accurate measure of the ionisation parameter, as already suggested by Mathis (1982, 1985). Given the redder wavelengths of the sulphur emission lines, and consequently their lower excitation energies with respect to the oxygen lines, S3S2 is roughly independent on metallicity (Kewley & Dopita, 2002).

Until recently however, the near-infrared [S III]$\lambda\lambda 9069, 9532$ lines (from now just the [S III] lines), have rarely been used to investigate the ionisation parameter (e.g. Díaz & Pérez-Montero 2000; Kehrig et al. 2006; Cresci et al. 2017; Mingozzi et al. 2019) because they are weaker than their oxygen counterparts and no large spectroscopic survey of nearby galaxies covered the required wavelength range. This situation is now changing with new spectroscopic surveys and facilities covering the full wavelength range between 6000 and 10000 Å (including the X-shooter and MUSE instruments on the VLT, or the SDSS-IV MaNGA survey) and the first detection of the [S III] lines at high redshift with near-IR instruments (e.g. Curti et al. 2019 submitted).

In this Chapter, I will summarize two projects I was involved with concerning this topic.

- The first (Sec. 3.1) is focused on a local H II galaxy published by Cresci et al. (2017), in which I contributed to analyse MUSE data with the aim of studying the spatially resolved ISM properties of the galaxy, whose large scale dynamics is dominated by extended outflowing bubbles, probably due to massive gas ejection from the central star forming regions. Classical emission line diagnostics were used to trace the dust extinction, electron density, metallicity and ionisation conditions all across the galaxy, confirming the extreme nature of the highly star forming knots in the core of the galaxy. A special remark that stems from this work is the importance of taking into account the strong variation of the ionisation parameter to get a reliable estimate of the metallicity.

- The second project (Sec. 3.2) instead is aimed at investigating statistically how the still poor understood ionisation parameter is related with metallicity and other properties of galaxies, such as stellar mass ($M_\star$), star formation rate (SFR) and specific SFR ($sSFR = SFR/M_*$), to what extent the inclusion of the [S III]$\lambda\lambda$9069,9532 lines can help to determine metallicity and ionisation parameter, and how different photoionisation model grids can relate with the observed line ratios (Mingozzi et al., submitted to A&A). To do this, I made use of the MaNGA survey (Bundy et al., 2015), part of the last generation Sloan Digital Sky Survey IV (July 2014–ongoing), that will observe 10000 local galaxies up to $z \sim 0.15$, across a wide range in M_* and environment with uniform radial coverage, within 2020. The wavelength range observed by MaNGA (3600–10300 Å) allows us to present the first study of the [S III] lines within 2139 local galaxies.

3.1 The MUSE view of Henize 2-10

The physical and dynamical properties of the ionised gas in the prototypical H II galaxy Henize 2-10 (He 2-10, Allen et al. 1976) can be derived using MUSE integral field spectroscopy. Specifically, nearby H II galaxies are local dwarf starburst objects, characterised by low chemical abundances, large gas and dust content. Moreover, they are dominated by very young stellar populations in massive star clusters that cause high current SFR and sSFR. Therefore, these sources represent a unique test bench to investigate in detail the physical mechanisms that drive SF and galaxy evolution in nearly pristine environments similar to those in high-z galaxies, since their peculiar conditions can be studied at a very high spatial resolution.

3.1.1 A prototypical HII galaxy

He 2-10 is located at a distance of 8.23 Mpc (Tully et al. 2013, 1" $\sim$ 40 pc), and its optical extent is less than 1 kpc, characterised by a complex and irregular morphology. Despite its low mass[1], it hosts an intense burst of star formation (SFR = 1.9 $M_\odot$/yr Reines et al. 2011), as traced by classical indicators such as strong optical and infrared emission lines excited by young stars (Vacca & Conti, 1992; Vanzi & Rieke, 1997), the detection of Wolf-Rayet features (Schaerer et al., 1999), intense mid-IR emission (Sauvage et al., 1997; Vacca & Conti, 1992) and far-IR continuum (Johansson, 1987). The galaxy is gas rich, with a molecular gas mass of $\sim 1.6 \times 10^8$ $M_\odot$ and an atomic

---

[1] $M_\star = 3.7 \times 10^9$ $M_\odot$, Reines et al. 2011, although Nguyen et al. 2014 revised this value to $M_\star = 10 \pm 3 \times 10^9$ $M_\odot$ using deep optical imaging of the outer regions.

gas mass of $\sim 1.9 \times 10^8$ $M_\odot$ (Kobulnicky et al., 1995a), suggesting a gas fraction of about 3-10%. Apart from the central 500 pc characterized by blue colors and irregular morphology, the outer part of the galaxy appears to be redder and dominated by an older stellar population, consistent with an early-type system (Nguyen et al., 2014). The stellar component seems to be dispersion dominated also in the central part, further supporting the spheroidal nature of the older stellar population (Marquart et al., 2007).

The recent burst ($\sim 10^7$ yr, Beck et al. 1997) was probably triggered by a massive gas infall due to an interaction, or to a merger with a companion dwarf, as inferred by the tidal CO and H I plumes extended up to 30" to the southeast and northeast of the core (Kobulnicky et al., 1995b; Vanzi et al., 2009). The galaxy is also surrounded by a complex kiloparsec-scale superbubble centered on the most intense star forming core, and evident in HST narrowband Hα images (Johnson et al., 2000). The estimate of the energy of the bubbles is compatible with the expected mechanical energy released by Supernovae (SN) and stellar winds in the central starburst, suggesting a stellar driven galaxy wind (Méndez et al., 1999). The outflowing material was also detected in absorption as blueshifted interstellar lines up to 360 km/s, that were used to compute a lower limit on the mass of the outflowing material of $M_{\rm out} \geq 10^6$ $M_\odot$ (Johnson et al., 2000).

The most actively star forming regions are concentrated in an arc-like structure of about 3" in radius (120 pc) in the core of the galaxy. The area was investigated in optical and UV, revealing a resolved young super massive star clusters, with masses up to 10^5 $M_\odot$ and ages of ~ 10 Myr (e.g. Cresci et al. 2010). These clusters lie at the center of a cavity depleted of both cold molecular gas and warm line emitting ionised gas, whose emission is instead concentrated in two regions at East and West of the arc (knot 4 and 1+2 in Fig. 3.1), harbouring actively star forming, dust embedded young star clusters, prominent at mid-IR wavelength. The only notable exception is a non-thermal radio source located in the line emitting bridge between the two Hα brightest clumps (designated as knot 3 in Johnson & Kobulnicky 2003, see Fig. 3.1) that has been identified as an actively accreting super massive black hole, with $\log(M/M_\odot) = 6.3 \pm 1.1$ by Reines et al. (2011). However, in this work no sign of AGN ionisation is traced in the galaxy, leading to the conclusion that this non-thermal radio source is a Supernova Remnant, as also supported by the re-analysis of the X-ray data that were used to propose the presence of the AGN (more details on this topic are given in Sec. 5 of Cresci et al. 2017).

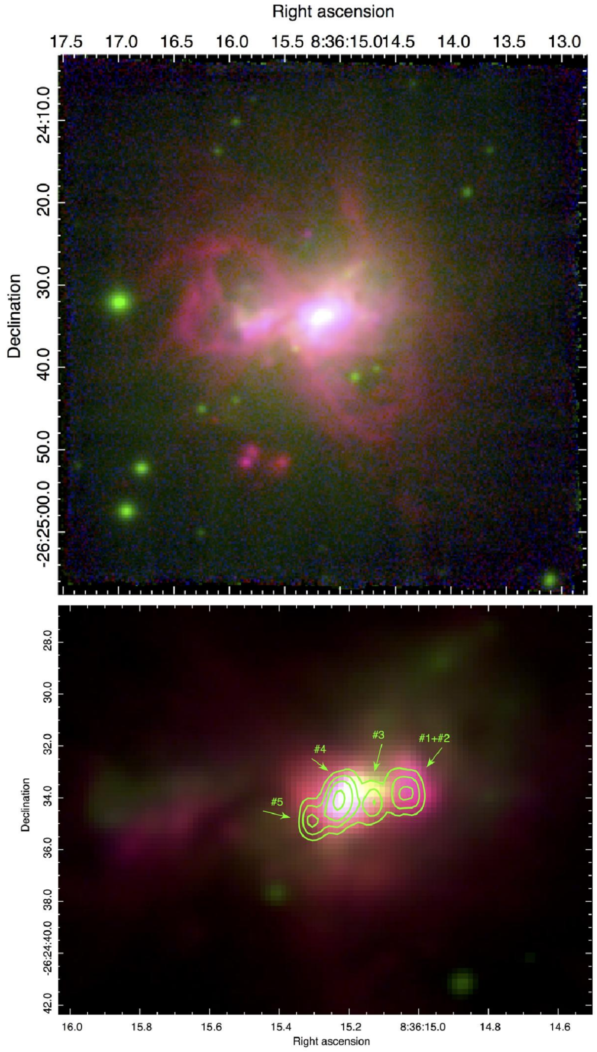

Figure 3.1: Three color MUSE images of the galaxy He 2-10. The full MUSE FOV is shown in the upper panel: the continuum over the entire spectral range is shown in green, the [O III]λ5007 emission in blue, and the Hα emission in red. An enlarged view of the central regions of the galaxy (20"×15") is instead shown in the lower panel, with the radio continuum contours at 3.6 cm obtained by Johnson & Kobulnicky (2003) overplotted, along with their notation for the main radio knots $1-5$. North is up and East is left. This figure is taken from Cresci et al. (2017).

3.1.2 Observations and data analysis

He 2-10 was observed with MUSE on May 28, 2015, under program 095.B-0321 (P.I. Vanzi). The galaxy was observed with four dithered pointings of 30 s each, for a total of 2 minutes on source, with the background sky sampled with 3 equal exposures in between. The data reduction was performed using the recipes from the latest version of the MUSE pipeline (1.6.2), as well as a collection of custom IDL codes developed to improve the sky subtraction, response curve and flux calibration of the data. Further details on the data reduction can be found in Cresci et al. (2015b) and references therein. The final datacube consists of 321×328 spaxels, for a total of over 100000 spectra with a spatial sampling of 0.2" and a spectral resolution going from 1750 at 465 nm to 3750 at 930 nm. The field of view (FOV) of 1'×1' is sufficient to sample the optical extent of the source, as shown in Fig. 3.1. The average seeing during the observations, derived directly from foreground stars in the final datacube, was FWHM = 0.68" ± 0.02".

The obtained datacube was analyzed using a set of custom python scripts, developed to subtract the stellar continuum and fit the emission lines with multiple Gaussian components where needed. The details about the procedures used to obtain the emission lines fluxes, velocities and velocity dispersions are described in Sec. 2.1.2 of Chapter 2, while here we just summarise the steps followed to obtain the emission lines fluxes.

The underlying stellar continuum was subtracted using a combination of MILES templates (Sánchez-Blázquez et al., 2006) in the wavelength range 3525−7500 Å covered by the stellar library. This wavelength range covers most of the emission lines considered in the following, with the exception of [S III]λ9069, for which we used a polynomial fit to the local continuum given that this line is not contaminated by underlying absorptions. The continuum fit was performed using the pPXF code (Cappellari & Emsellem, 2004) on binned spaxels using a Voronoi tessellation (Cappellari & Copin, 2003) to achieve a minimum $S/N > 50$ on the continuum under 5530 Å rest frame. The main gas emission lines included in the selected range (Hβ, [O III]λ4959, [O III]λ5007, He Iλ6678, [O I]λ6300, [O I]λ6363, [N II]λ6548, Hα, [N II]λ6584, He Iλ7065, [S II]λ6717, [S II]λ6731) were fitted simultaneously to the stellar continuum using multiple Gaussian components to better constrain the absorption underlying the Balmer lines. Fainter lines as well as regions affected by sky residuals were masked out of the fitting region. The fitted stellar continuum emission in each bin is then subtracted on a spaxel-to-spaxel basis, rescaling the continuum model to the median of the observed continuum in each spaxel. The continuum subtracted datacube was finally used to fit the emission lines in each spaxel. The velocity and widths of the Gaussian components were bound to be the same for each emission line of the different species, while the intensities were left free to vary with the exception of the [O III]$\lambda\lambda$4959,5007, [O I]$\lambda\lambda$6300,6363 and [N II]$\lambda\lambda$6548,84 doublets for which the intrinsic ratio between the two lines was used. Each fit was performed three times, with one, two and three Gaussian components per each emission line, in order to reproduce peculiar line profiles where needed. A selection based on the reduced χ^2 obtained using each of the three different fits in each spaxel was used to select where a multiple components fit was required. This choice allows us to use the more degenerate multiple components fits only where it is really needed to reproduce the observed spectral profiles. These conditions apply only in the central part of the galaxy and in some knots of the outflowing filaments where double peaked lines are detected.

The stellar and gas dynamics are described in details in Cresci et al. (2017) Sec. 3, while in the following I discuss He 2-10 gas properties.

3.1.3 Gas properties

The excitation, physical conditions, dust and metal content of the interstellar gas in He 2-10 can be explored using selected ratios between the measured emission lines.

Dust extinction, electron density and gas excitation

The left panel of Fig. 3.2 illustrates the dust extinction map, derived through the Balmer decrement Hα/Hβ, assuming a Calzetti et al. (2000) attenuation law and a fixed temperature of $T_{\rm e} = 10^4$ K. The dust attenuation shows the highest values in the two star forming clumps detached $\sim$ 18” to the SW of the main galaxy and in the Eastern region where the line and continuum emission is less prominent. These locations correspond to the position of the CO gas (Kobulnicky et al., 1995b). Moreover, the extinction is high on one of the central star forming regions ($A_{\rm V} = 2.3$, knot 1+2). It is interesting to compare Fig. 3.2 with the extinction map obtained by near-IR IFU data for the central region of the galaxy by Cresci et al. (2010) from the Br12/Brγ line ratio, in which the the extinction towards the two brightest star forming region at the center of the galaxy was $A_{\rm V} = 7 - 8$. This difference is probably due to the fact that IR observations are capable to probe deeper in the highly embedded star forming clusters. The right panel of Fig. 3.2 shows the electron density $n_{\rm e}$ map, estimated using the [S II]λ6717/[S II]λ6731 ratio (Osterbrock, 1989). The highest $n_{\rm e}$ values ($n_{\rm e} \sim 1500$ cm^{-3}) come from the Western central star forming region (knot 4), while the density distribution appears to be flat in the rest of the galaxy ($n_{\rm e} \sim 100$ cm^{-3}).

The dominant ionisation source for the line emitting gas in each MUSE spaxel can be explored using the [N II], [S II] and [O I] BPT diagrams (e.g. Baldwin et al. 1981; Kewley et al. 2006), in which spatially resolved regions of galaxies dominated by SF, AGN (Seyfert-type), low ionisation emission line Regions (LI(N)ERs, Belfiore et al. 2016), or shocks populate different regions. The three BPT diagrams for the spaxels with $S/N > 3$ for all the lines involved with the corresponding maps are shown in Fig. 3.3, in which the dominant source of ionisation is marked with different colors. Clearly, all the line emitting gas in the galaxy, even at the location of the compact radio source, is dominated by ionisation from young stars, as different sources are limited to few noisier

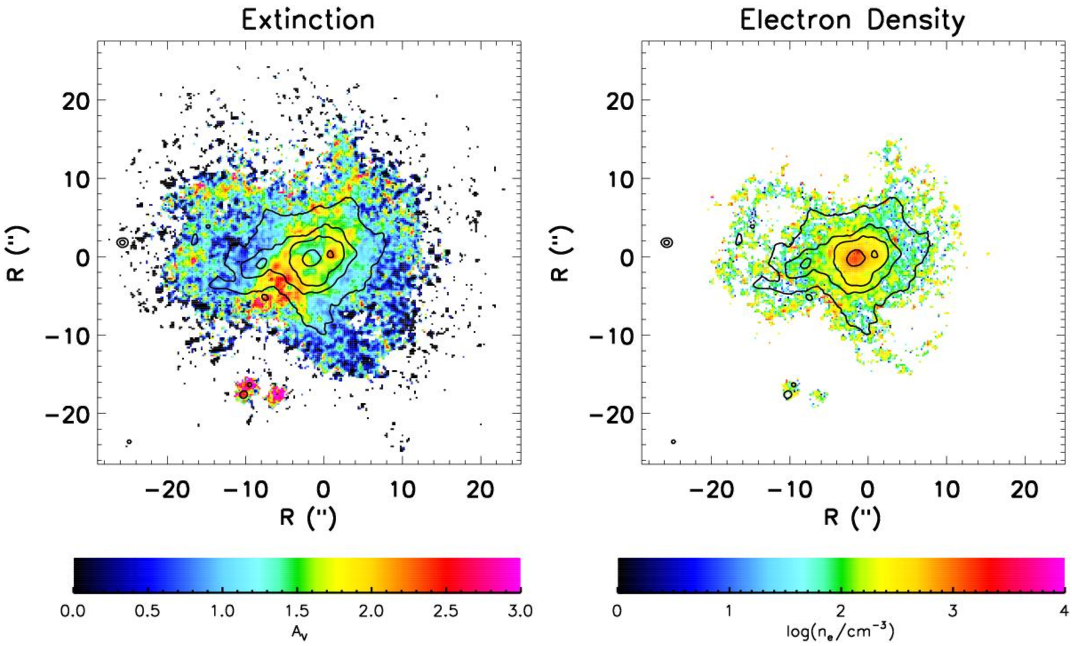

Figure 3.2: Extinction map as derived from the Hα/Hβ line ratio (left panel) and electron density n_e from [S II]λ6716/[S II]λ6731 (right panel) with Hα contours overplotted. Both maps are displaying the spaxels with $S/N > 3$ in all the emission lines involved. This figure is taken from Cresci et al. (2017).

spaxels at the edges of the galaxy. Assuming that all the line emitting gas is ionised by young stars, the total SFR in the galaxy can be estimated from the integrated stellar continuum subtracted spectrum extracted in an aperture of 120 spaxels in radius (24" or 960 pc). An intrinsic Hα luminosity of $L(\mathrm{H}\alpha) \sim 1.48 \times 10^{41}$ erg/s, after correcting for the dust extinction derived from the Balmer decrement ($\mathrm{A_H} = 1.32$. This value of $L(\mathrm{H}\alpha)$ converts into a $SFR = 0.76$ M$_\odot$/yr, using the calibration by Kennicutt & Evans (2012).

These pieces of evidence confirm that the central regions of He 2-10 host dense, dust embedded, young and highly star forming star clusters, a common feature in starburst galaxies (see e.g. Vanzi & Sauvage 2006) and possibly in galaxies in general (e.g. Förster Schreiber et al. 2011).

Metallicity and ionisation

Since the gas ionisation is dominated by young stars across all the galaxy, it is possible to use selected line ratios of the most intense lines to derive the chemical enrichment of the interstellar gas (i.e. SEL). The integrated metal abundance of He 2-10 was already derived by Kobulnicky et al. (1999), yielding a super solar abundance of $12 + \log(\mathrm{O/H}) = 8.93$. Such a high value is not unexpected given the relative higher mass of He 2-10 and

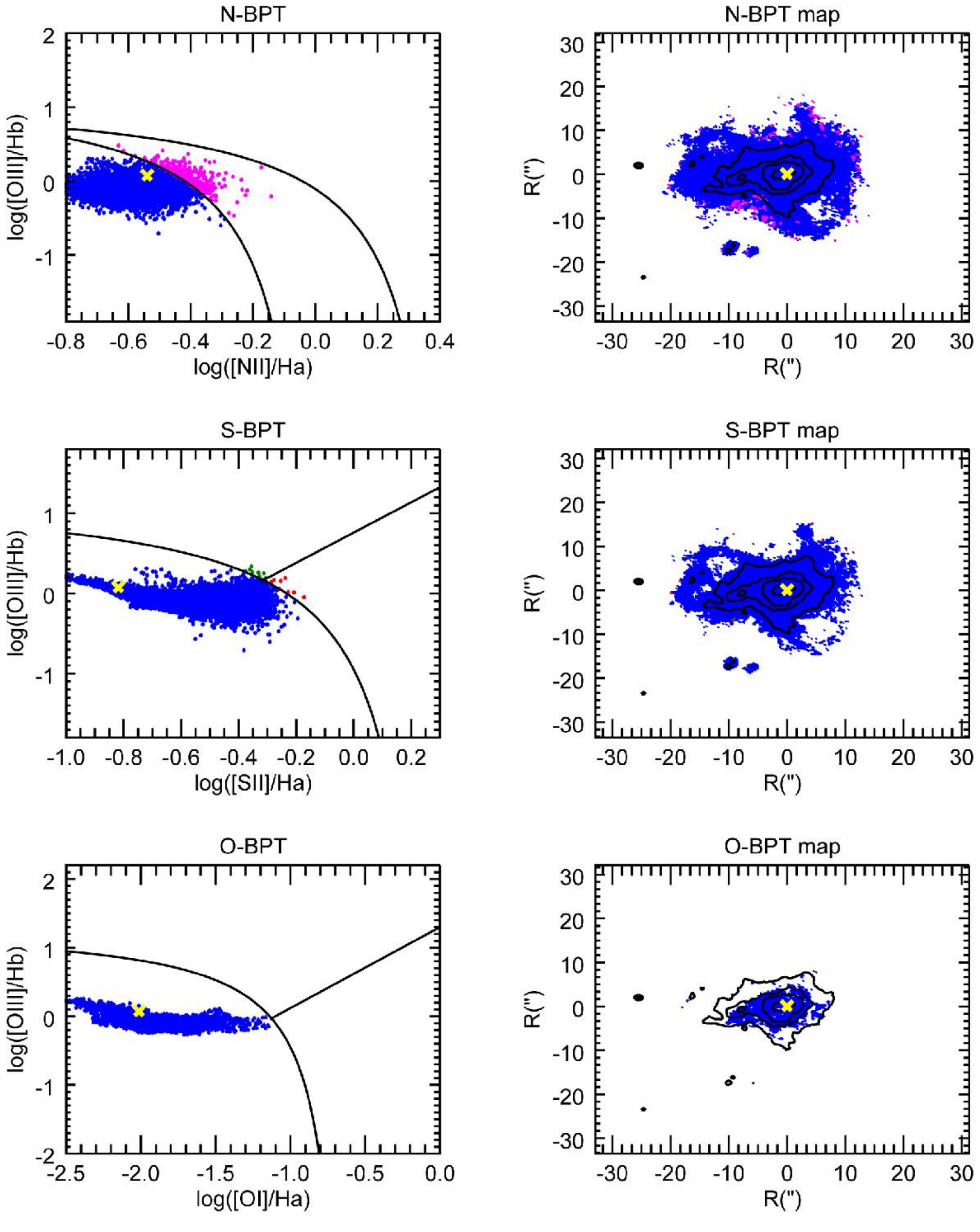

Figure 3.3: Resolved BPT diagrams for He 2-10. The [N II], [S II] and [O I] BPT diagrams for each spaxel with $S/N > 3$ in each line are shown on the left, while the corresponding maps, marking each spaxel according to the dominant excitation, are shown on the right (SF in blue, AGN in green, and LINER/shock in red and composite regions in magenta). The contours of Hα line emission are overplotted in black, and the location of the nuclear radio source classified as accreting BH by Reines et al. (2011) is marked with a yellow cross. This figure is taken from Cresci et al. (2017).

the well known relation between mass and metallicity. As an example, assuming the mass metallicity relation of Tremonti et al. (2004) and taking into account a stellar mass of 1×10^{10} $M_\odot$, the oxygen abundance would be $12 + \log(O/H) = 8.95$, while if the SFR is assumed as third parameter in the relation, following Mannucci et al. (2010), $12 + \log(O/H) = 8.70$, somehow lower than the measured value. However, Esteban et al. (2014) obtained a new measure of the oxygen metallicity of $12 + \log(O/H) = 8.55 \pm 0.02$ integrated on the central 8”×3”, using faint pure recombination lines. The new metallicity value by Esteban et al. (2014) is again comparable with what is expected by a computation of the mass metallicity relation obtained with such new diagnostics, as Andrews & Martini (2013) would predict $12{+}\log(O/H) \sim 8.65$ using only the stellar mass and $12 + \log(O/H) \sim 8.50$ taking into account the SFR as well.

The first row of Fig. 3.4 shows the spatial variation of the diagnostic ratio O3N2 and the corresponding metallicity map, using the calibrations by Curti et al. (2017), on the left and on the right, respectively. The global average metallicity in the disk is compatible with the value derived by Esteban et al. (2014), while the eastern region of the galaxy and the central highly star forming regions show lower metallicity values ($12 + \log(O/H) = 8.2 - 8.3$). Highly star forming regions with lower gas metallicity than the surrounding galaxy have been interpreted as signatures of pristine, low metallicity gas accretion, that dilutes the metal content of the ISM and boosts star formation, both locally (e.g. Sánchez Almeida et al. 2014) and at high-z (Cresci et al., 2010). However, in the case of He 2-10 the abundance gradient amplitudes is of the same order of magnitude of the intrinsic scatter in the calibrations (e.g. 0.2 dex for O3N2, probably due to variation in the ionisation in different sources).

The map of the ionisation parameter can be derived trough the calibration of Kewley & Dopita (2002) using the line ratio [S III]$\lambda\lambda$9069,9532/[S II]$\lambda\lambda$6717,31[2] (Fig. 3.4, third panel). It can be seen from Fig. 3.4 (third panel) that this parameter is one order of magnitude higher in the two nuclear star forming region, further suggesting that the line ratio variation is due to ionisation effects in extreme environments such as these embedded, highly star forming regions and not to a metallicity variation.

To further explore this, the fourth panel of Fig. 3.4 shows the metallicity map obtained from the new diagnostic diagram by Dopita et al. (2016) (shown in Fig. 3.5) which makes use of [O III]λ5007, Hβ, [N II]λ6584, [S II]$\lambda\lambda$6717,31 and Hα lines to constrain both metallicity and the ionisation parameter using photoionisation models. In Fig. 3.5, the different grids shows the variation of metallicity and log(U) for different values of ISM pressure, while the spaxels corresponding to the central star forming regions

---

[2] Since [S III]λ9532 is not covered by the wavelength range observed by MUSE, a theoretical ratio of [S III]$\lambda\lambda$9532/[S III]$\lambda\lambda$9069 = 2.47 (Vilchez & Esteban, 1996), fixed by atomic physics, can be adopted.

define two clear sequences towards high metallicity and high U, reported in magenta and blue. The location of these spaxels are plotted in the upper right panel superimposed to the Hα map of He 2-10. The spaxels with metallicity $12 + \log(\mathrm{O/H}) < 8.55$ are marked in green, both in the left and in the right panel. This confirms that the Eastern part of the galaxy has lower metallicity than the rest by 0.2 dex, possibly in agreement with the merger interpretation of the origin of He 2-10, while the different line ratios in the central star forming regions are due to higher ionisation parameter.

In the Dopita et al. (2016) diagram the two star forming regions actually show very high supersolar metallicities, probably due to efficient metal enrichment in those extreme environments. As shown in Fig. 3.5, lower right panel, these regions form a definite structure in the BPT diagram as well. This result suggests caution in the interpretation of a single line ratio as a variation in metallicity of the ISM, and confirms the importance of a large wavelength range to exploit multiple physical diagnostics.

3.1.4 Conclusions

In this Section, we presented the analysis of MUSE observations to inspect the dynamics and properties of the warm ionised gas in the prototypical nearby H II galaxy He 2-10. The central star forming regions show the highest values of electron density ($n_{\mathrm{e}} \sim 1500$ cm^{-3}) and ionisation parameter ($\log(U) \sim -2.5$), and a super solar metallicity. This confirms the extreme conditions in these environments.

An interesting conclusion that stems from this work is the importance of taking into account the ionisation parameter variations to measure the gas metallicity. Indeed, given the large variation of the ionisation parameter across the galaxy traced by S3S2, the use of a single line ratio (e.g. O3N2, Pettini & Pagel 2004) to derive the metallicity can lead to misleading conclusions. Indeed, O3N2 carries a strong dependence on the ionisation parameter, because of the very different ionisation potentials of N^{+} (14.5 eV) and O^{++} (35.1 eV) (Alloin et al., 1979). This can cause to underestimate systematically $12 + \log(\mathrm{O/H})$ for higher ionisation parameters and to overestimate it in regions characterised by lower ionisation parameter values (see also Krühler et al. 2017). In this context, the diagram proposed by Dopita et al. (2016) allows us to account simultaneously to the variation of these two parameters, finding a strong negative metallicity gradient across the galaxy.

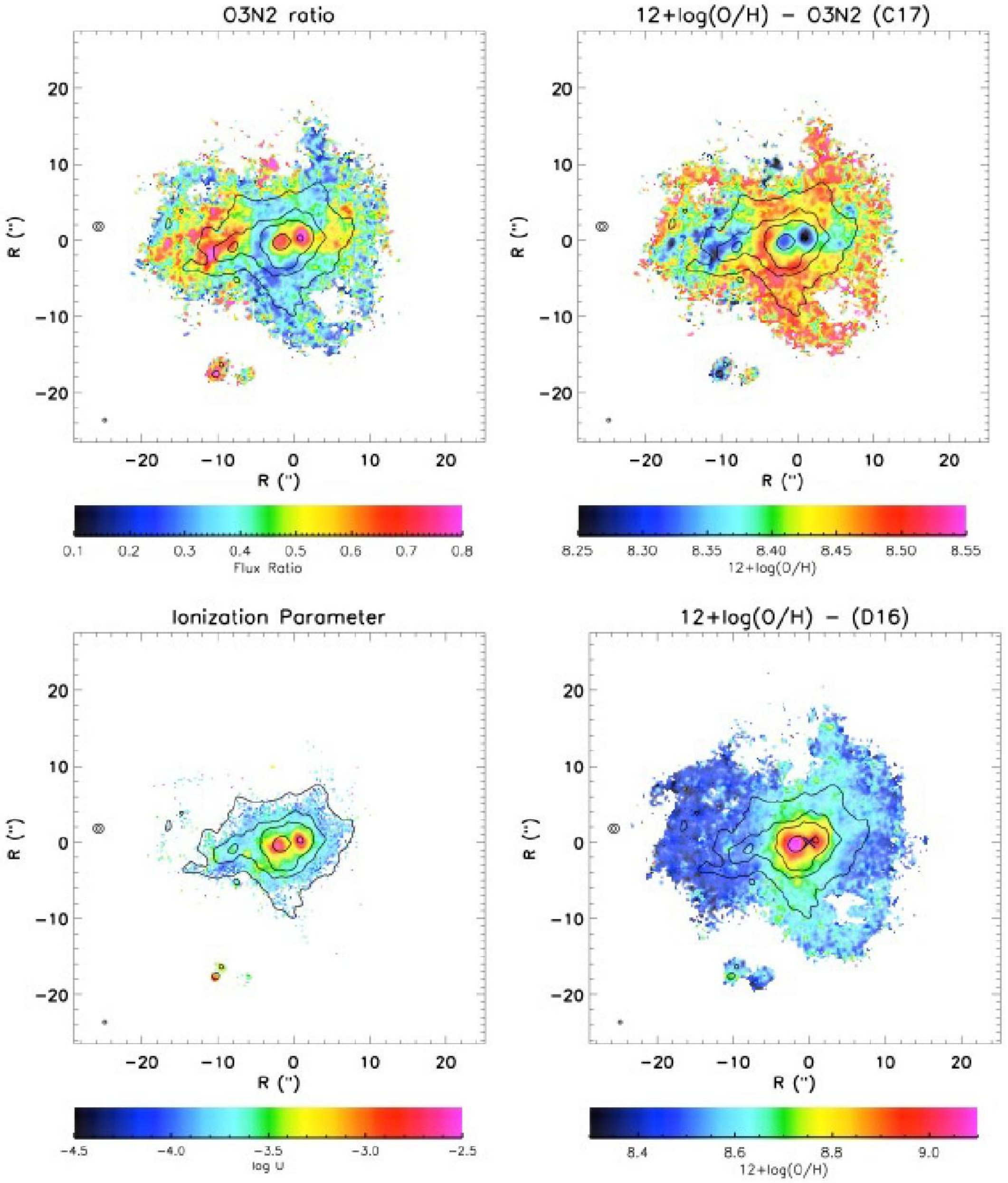

Figure 3.4: Spatial dependence of the O3N2 line ratio (upper left panel), the corresponding metallicity map derived from Curti et al. (2017) calibration (upper right panel), ionisation parameter from the [S III]$\lambda\lambda$9069,9532/[S II]$\lambda\lambda$6717,31 line ratio (lower left panel) and metallicity map using the diagnostic by Dopita et al. (2016) (lower right panel). All maps are displaying the spaxels with $S/N > 3$ in all the emission lines involved. This figure is taken from Cresci et al. (2017).

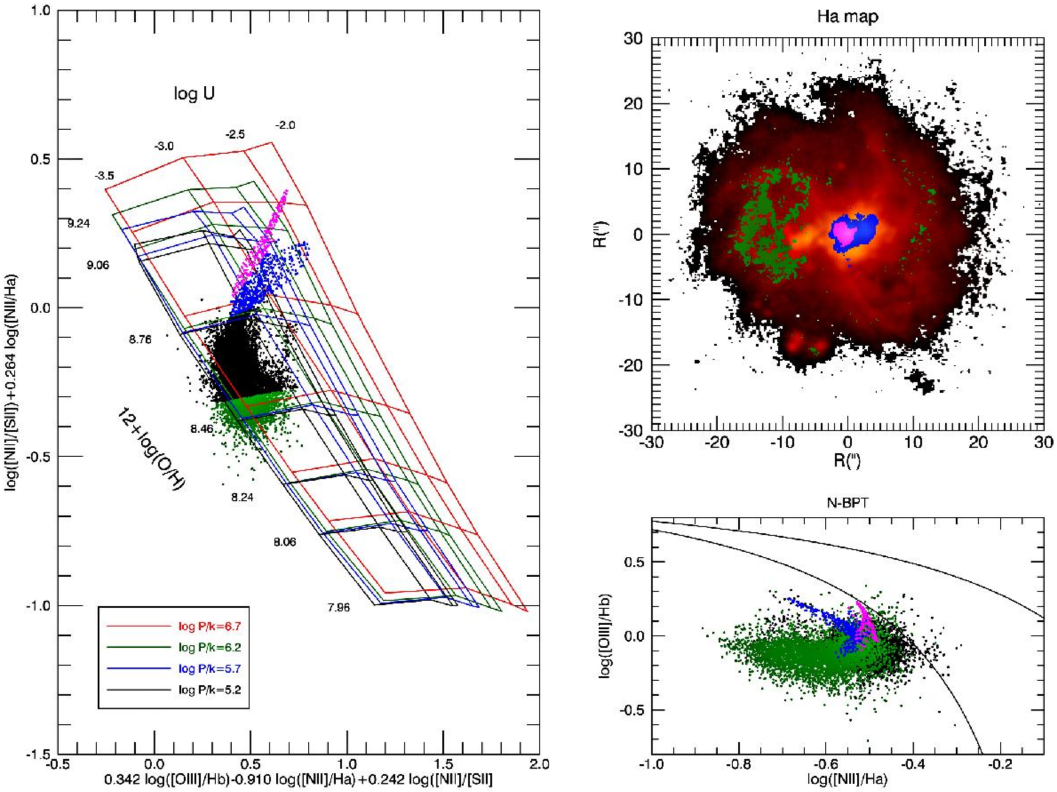

Figure 3.5: The spatially resolved emission line diagnostic by Dopita et al. (2016) for spaxels in He 2-10 with $S/N > 3$ in all the emission lines involved. The diagnostic diagram is shown in the left panel, where each point corresponds to a MUSE spaxel. The metallicity scale (increasing along the vertical axis) and ionisation parameter scale (increasing along the horizontal axis) are shown on the different grids, corresponding to different values of the ISM pressure. The spaxels whose metallicity in the Dopita et al. (2016) scale is lower than $12 + \log(O/H) = 8.5$ are marked in green, while the two horn like structures at high metallicity and ionisation parameter are shown in magenta and blue. These regions are marked with the same color in the upper right panel, overplotted on the Hα map of the galaxy. The lower right panel shows the position of the regions selected on the diagnostic diagram on the [N II]-BPT. This figure is taken from Cresci et al. (2017).

3.2 From Bayesian fitting to photoionisation models with the MaNGA survey

To assess whether the degeneracy between metallicity and ionisation parameter found in He 2-10 generally persists in a larger sample of galaxies, in this Section I analyse galaxies from the MaNGA survey. In particular, I move past the traditional SEL diagnostics of metallicity and instead make use of a Bayesian approach, based on Blanc et al. (2015), and inspired by the previous work of Charlot & Longhetti (2001), Brinchmann et al. (2004) and Tremonti et al. (2004). In this framework, observed SEL fluxes are directly compared with a grid of photoionisation models. This approach has the advantage of modelling all the available SEL ratios self-consistently, but is also subject to specific limitations. First, the current generation of photoionisation models are not capable of correctly reproducing all the observable SEL ratios (D'Agostino et al., 2019). Second, photoionisation models are based on a large number of simplifying assumptions and it is not guaranteed that the obtained solution is unique and that the real uncertainties are correctly estimated. Moreover, any physical correlation between metallicity 12+log(O/H) and ionisation parameter q, which is hard-wired into empirical models, cannot be easily ported to Bayesian methods. When using a Bayesian approach it is therefore necessary to use a wide enough set of SELs to break the well-known degeneracy between metallicity 12+log(O/H) and q. Specifically, I derive simultaneously metallicity, ionisation parameter and extinction gradients in galaxies, to understand the degeneracy between the different parameters affecting previous similar studies.

Throughout this work, we use a Λ cold dark matter cosmology with $\Omega_{\mathrm{M}} = 0.3$, $\Omega_{\Lambda} = 0.7$ and $H_0 = 70$ km^{-1} s^{-1} Mpc^{-1}.

3.2.1 The MaNGA survey

The galaxy sample

The MaNGA survey is one of the three components of SDSS-IV (Blanton et al., 2017). Observations are carried out at the 2.5 m telescope at Apache Point Observatory (Gunn et al., 2006). The survey aims to map 10000 galaxies in the redshift range $0.01 < z < 0.15$ by 2020. MaNGA galaxies are selected to be representative of the overall galaxy population for $\log(\mathrm{M}_{\star}/\mathrm{M}_{\odot}) > 9$. The sample is drawn from an extended version of the NASA-Sloan catalogue (NSA `v1_0_1`[3], Blanton et al. 2011). MaNGA observations are carried out with 17 hexagonal fiber-bundle integral field units (IFUs) that vary

---

[3] https://www.sdss.org/dr15/manga/manga-target-selection/nsa/

in diameter from 12" (19 fibers) to 32" (127 fibers). Each fiber has a diameter of 2" (Drory et al., 2015). The IFUs feed light into the two dual-channel BOSS spectrographs, that provide simultaneous wavelength coverage in the 3600–10300 Å wavelength range, with a resulting spectral resolution of $R \sim 1400$ at $\lambda \sim 4000$ Å and $R \sim 2600$ near $\lambda \sim 9000$ Å ($R \sim 2000$ corresponds to a velocity dispersion of $\sigma \sim 70$ km/s, Smee et al. 2013). A uniform radial coverage to radii of 1.5 R_e and 2.5 R_e is achieved for 2/3 (primary sample) and 1/3 (secondary sample) of the final sample, respectively. In order to compensate for light loss during observations, a three-point dithering pattern is used, allowing also to obtain a uniform point spread function (PSF, Law et al. 2015).

The data analysed in this work are part of the fifteenth SDSS Data Release (DR15, Aguado et al. 2019), reduced according to the algorithms described in Law et al. (2016) and Yan et al. (2016) and subsequent updates. The data release includes the output of the MaNGA data analysis pipeline (DAP, Westfall et al. 2019; Belfiore et al. 2019) for a sample of 4688 spatially-resolved galaxies observed until July 2017. Integrated galaxy global properties such as redshift, total stellar mass (M_*), elliptical effective radius (R_e) and inclinations are drawn from the extended version of NSA v1_0_1, i.e. the parent targeting catalog described in Section 2 of Wake et al. (2017), which includes the calculation of elliptical Petrosian aperture photometry. Elliptical Petrosian effective radii and inclinations are used throughout this work to construct de-projected radial gradients.

From this initial sample of galaxies, we selected 4099 objects with $z < 0.08$, in order to have access to the [S III]λ9532 line within the observed wavelength range. We select star-forming galaxies according to the 'excitation morphology', as described in Belfiore et al. (2016). This scheme makes use of the classical Baldwin-Phillips-Terlevich (BPT) diagnostic diagram (Baldwin et al., 1981; Veilleux & Osterbrock, 1987; Kauffmann et al., 2003b; Kewley et al., 2006) to map the excitation source of the ISM throughout galaxies. In particular, we exclude galaxies that show central or extended low-ionisation emission-line regions (cLIERs and eLIERs), line-less galaxies (no line emission detected), and galaxies with Seyfert-like central regions. We retain only objects classified as star-forming, defined as objects dominated by star formation (SF) at all radii. This selection cut limits our sample to mostly main-sequence galaxies, while eliminating the majority of green valley objects (Belfiore et al., 2018) and all passive galaxies. Finally, we exclude highly inclined systems, namely galaxies with minor to major axis ratio (b/a) less than than 0.4, leading to a final sample of 1795 galaxies.

In the rest of this work we further exclude spaxels which are not classified as star-forming according to either the [N II]- or the [S II]-BPT diagrams (i.e. all the spaxels above the demarcation lines defined by Kauffmann et al. 2003b and by Kewley et al. 2001, respectively), for which we assume that the Hα flux is contaminated by other physical processes aside from star formation.

Spectral fitting

We make use of the flux measurements obtained by Gaussian fitting for the [O II]$\lambda\lambda$3726,29, Hβ, [O III]$\lambda\lambda$4959,5007, [N II]$\lambda\lambda$6548,84, Hα, [S II]λ6717 and [S II]λ6731 emission lines in stellar-continuum subtracted spectra from the MaNGA DAP v2.2.1. In the fit performed by the DAP the flux ratios of doublets are fixed when such ratios are determined by atomic physics, with transition probabilities taken from Osterbrock & Ferland (2006) (e.g. intrinsic ratios of 0.340 and 0.327 for [O III] and [N II] doublets, respectively). Furthermore, in DR15 the velocities of all the fitted emission lines are tied, while the velocity dispersions are free to vary, with the exception of the doublets with fixed flux ratios and the [O II]$\lambda\lambda$3726,29 lines. Belfiore et al. (2019) (see Sec. 2.2.3) found that the impact of these algorithmic choices on the line fluxes is negligible.

In DR15, the stellar continuum fitting is limited by the spectral range of the adopted MILES stellar library (Sánchez-Blázquez et al., 2006; Falcón-Barroso et al., 2011). Because of the absence of a continuum model redder than ~ 7400 Å the DAP does not fit the [S III]$\lambda\lambda$9069,9532 lines. We therefore performed a bespoke fitting process.

Since the red part of the spectrum around the lines of interest does not feature prominent stellar absorption features, we use a linear baseline to account for the local continuum ± 30 Å around the [S III] emission lines. Each line is then fitted with a single Gaussian, making use of MPFIT (Markwardt, 2009) and masking the remaining part of the spectrum. We fixed the flux ratio of the two [S III] lines to the theoretical ratio of 2.47 determined from the transition probabilities used in PYNEB (Luridiana et al., 2015) and their velocities to the velocity obtained by the DAP for the previously fitted emission lines. Lower (~ 40 km/s) and upper (~ 400 km/s) limits are imposed on the velocity dispersion in order to reduce the probability of fitting sky lines, or noise features in the spectra. All line fluxes are corrected for Galactic foreground extinction using the maps of Schlegel et al. (1998) and the reddening law of O'Donnell (1994).

The top panel of Fig. 3.6 shows the g-r-i image composite from SDSS of MaNGA galaxy 8150-6103 with the MaNGA hexagonal field of view (FoV) overlaid (on the left), and an example of our fitting procedure for the [S III] lines for one spaxel (on the right). The observed spectrum is reported in black, while the best-fit is highlighted by the dashed-dotted red line. The regions in grey were masked before fitting. The bottom panel of Fig. 3.6 presents maps of the [S III]λ9532 flux, velocity and velocity dispersion for the same galaxy.

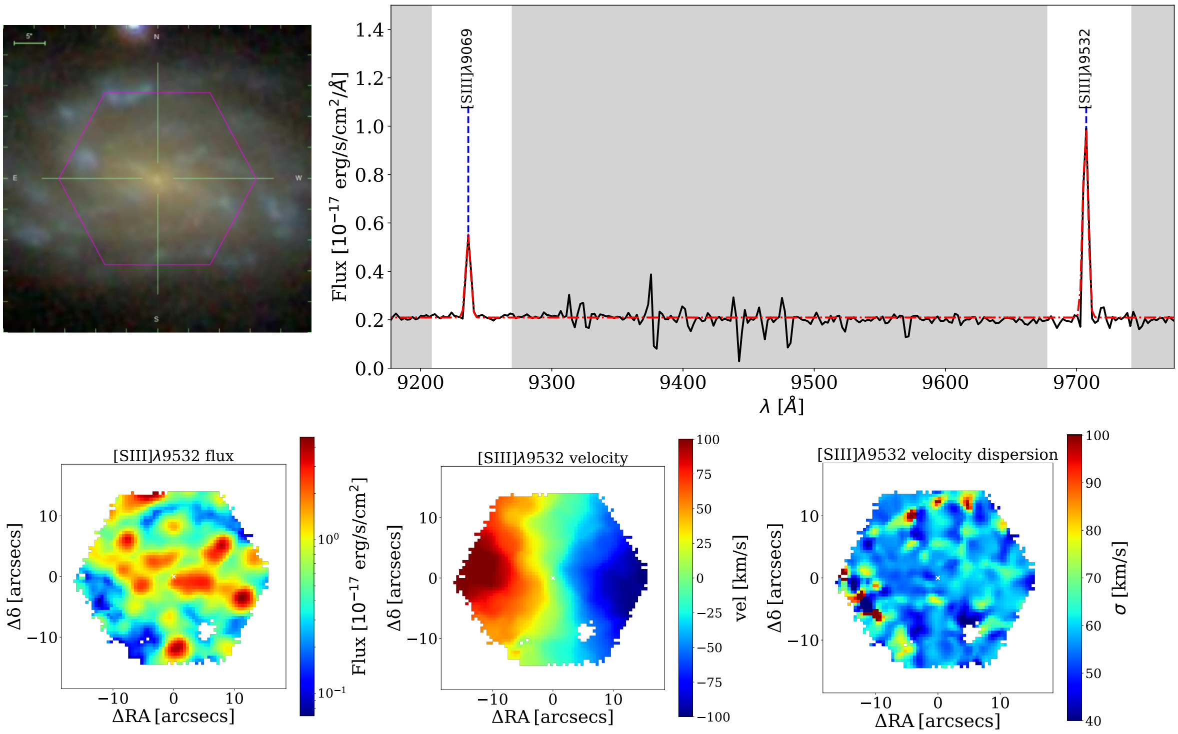

Figure 3.6: *Top left*: $g-r-i$ image composite from SDSS for MaNGA galaxy 8150-6103, with the MaNGA IFU hexagonal FoV overlaid. East is to the left. *Top right*: An example of our fitting procedure for the [S III] lines for one representative spaxel in this example galaxy. The black solid line is the observed spectrum, while the dashed-dotted red line is the best-fit. The regions in grey were masked before fitting. *Bottom panels*: [S III]λ9532 flux, velocity and velocity dispersion maps of MaNGA galaxy 8150-6103.

In Sec. 3.2.5, we present a comparison between the emission line fluxes considered in this work and those computed by the Pipe3D code (Sánchez et al., 2016, 2018), which performs independent continuum subtraction and emission-line measurements of the MaNGA data. There is a good overall agreement between the two (see also the Appendix of Belfiore et al. 2019), up to the [S III]λ9069 emission line. However, we find a larger discrepancy with respect to the other emission lines for the [S III]λ9532, likely associated with a failure in the extrapolation of the continuum performed by Pipe3D (S. F. Sánchez, private communication).

Signal-to-noise selection

In this work, we define the signal-to-noise of each emission line $S/N_{\rm line} = {\rm Flux}/{\rm Err}_{\rm flux}$, as in Belfiore et al. (2019). This quantity is equivalent to the classical amplitude-over-noise ratio often used for line detection. In order to obtain reliable measurements for the

ISM parameters of interest we exclude from further analysis spaxel with $S/N(\mathrm{H}\alpha) < 15$. We follow this approach, based on the work of Mannucci et al. (2010), because a high $S/N(\mathrm{H}\alpha)$ ensures that the main optical lines are generally detected with $S/N > 1.5$ without introducing metallicity biases. According to Belfiore et al. (2019), the fluxes computed by the DAP with $S/N \leq 1.5$ are unreliable. We therefore consider them as upper limits. This cut on $S/N(\mathrm{H}\alpha)$ selects 85% of the star-forming spaxels of the galaxy sample. In Appendix 3.2.5, we show the S/N radial profiles for MaNGA galaxies as a function of stellar mass. Overall, all strong lines of interest have $S/N > 5$ at $R < 2$ $\mathrm{R_e}$, except the [S III] lines, which are particularly weak ($S/N \sim 2-4$) at large radii and for massive galaxies.

Aside from emission from H II regions, galaxies are observed to contain low surface brightness diffuse ionised gas (DIG). The origin of this ionised gas emission is likely to be a combination of different processes, such as radiation leaking from classical H II regions, massive stars in the field and radiation from hot evolved stars (Hoopes & Walterbos, 2003; Oey et al., 2007; Zhang et al., 2017; Sanders et al., 2017; Wylezalek et al., 2018). In this work we only consider H II region models. It is therefore necessary to minimize the contribution of DIG to our observed line fluxes.

Previous works have demonstrated the existence of a tight relation between diagnostic line ratios and Hα equivalent width (EW) in emission (e.g., Sánchez et al. 2014; Belfiore et al. 2016; Zhang et al. 2017; Lacerda et al. 2018; Vale Asari et al. 2019). Specifically, Lacerda et al. (2018) argue that $EW(\mathrm{H}\alpha) < 3$ Å traces emission from hot low-mass evolved stars (Stasińska et al., 2008), while gas with $EW(\mathrm{H}\alpha) = 3-14$ Å may include a mixture of DIG and emission from star forming regions. Because of our selection in BPT classification and signal-to-noise described above, virtually all the spaxels taken into account in this work have $EW(\mathrm{H}\alpha) > 3$ Å, and are therefore dominated by flux from HII regions.

3.2.2 Methods

Bayesian approach to determining ISM properties

Our method to derive the oxygen abundance and the ionisation parameter of ionised nebulae is based on the software tool IZI presented by Blanc et al. (2015). In brief, IZI compares an arbitrary set of observed SELs (and their associated errors) with a grid of photoionisation models, calculating the joint and marginalised posterior probability density functions (PDFs) for 12 + log(O/H) and $\log(q)$. This method allows us to include flux upper limits (see Blanc et al. 2015 for details), and it provides a self-consistent way of inferring the physical conditions of ionised nebulae using all available information. In particular, this approach makes it straightforward to test the effect of either a particular choice of SELs (as commonly done in traditional metallicity diagnostics) or a particular set of photoionisation models.

For this work we have re-written the original IDL IZI code in Python and added several modifications to the original code. The main innovation of our revisited version of IZI is the simultaneous estimate of a third parameter, the gas extinction $E(B-V)$. The gas extinction along the line-of-sight towards star-forming regions can be directly probed with Balmer recombination line flux ratios, comparing the observed and intrinsic Balmer decrements (e.g. Calzetti 1997). E(B-V) is usually derived assuming a fixed un-attenuated case B recombination, and generally an intrinsic Balmer decrement of Hα/Hβ $= 2.86$, appropriate for an electron density $n_e = 100$ cm^{-3} and electron temperature $T_e = 10^4$ K (Osterbrock, 1989). The intrinsic ratio depends weakly on density, with Hα/Hβ $= 2.86 - 2.81$ over four orders of magnitude in electron density ($n_e = 10^2 - 10^6$ cm^{-3}, Osterbrock 1989). However, the dependence on temperature is relatively larger, leading to Hα/Hβ intrinsic ratio value between $3.04 - 2.75$ for $5000 - 20000$ K (Dopita et al., 2003). Consequently, adopting a single intrinsic Balmer ratio neglects the direct effect of metallicity and ionisation parameter on the temperature of the nebula. For instance, Brinchmann et al. (2004) pointed out that ignoring the metallicity-dependence of the case B Hα/Hβ ratio leads to an overestimate of the dust attenuation by up to ~ 0.5 mag for the most metal rich galaxies (see e.g. Fig. 6 Brinchmann et al. 2004). Therefore, in this work we estimate dust extinction together with metallicity and ionisation parameter, assuming a foreground screen attenuation, a Calzetti attenuation law with $R_V = 4.05$ (see Calzetti et al. 2000) and adopting the intrinsic Balmer decrements self-consistently calculated within the photoionisation model grids. Another big advantage of inferring gas extinction, metallicity and ionisation parameter simultaneously is that we are self-consistently taking into account the covariance in dust-corrected line fluxes after applying a dust correction.

We make use of the Markov chain Monte Carlo (MCMC) Python package `emcee` to evaluate the PDF of the three parameters (Foreman-Mackey et al., 2013). Since photoionisation models cannot fully reproduce all observed line ratios, following Blanc et al. (2015), Kewley & Ellison (2008) and Dopita et al. (2013) we adopt a systematic fractional error in the flux predicted by the photoionisation model of 0.1 dex, except for the Hα line, for which we took into account 0.01 dex, in order to weight it more when constraining E(B-V). This intrinsic uncertainty is the dominant source of the error term in IZI, being generally larger than the measurement error associated to observed fluxes.

Consequently, signal-to-noise levels of the strong lines have a minor effect on the IZI output. Despite the differences from the publicly-available IDL code, for the rest of this work we refer to our rewritten and modified code as IZI unless otherwise noted.

As discussed by Blanc et al. (2015), it is not trivial to define a 'best-fit' solution for a specific parameter if its PDF is not Gaussian (e.g. strong asymmetries and/or multiple peaks). In these cases the mean is not a reliable estimator because it can be significantly different from the most likely solution, given by the mode. We choose as 'best-fit' value the marginalized median (i.e. 50^{th} percentile) of the PDF for each parameter. The upper and lower errors of the best-fit solution are obtained by computing the 16^{th} and 84^{th} percentiles of the distribution, respectively, and are defined as $\Delta_{up} = 84^{\mathrm{th}} - 50^{\mathrm{th}}$ and $\Delta_{down} = 50^{\mathrm{th}} - 16^{\mathrm{th}}$. If the PDF is Gaussian, these two values are equal and correspond to the standard deviation.

As our default photoionisation models set, we use the photoionisation model grids presented in Dopita et al. (2013) (D13 models hereafter). These models are computed with the MAPPINGS-IV code, which with respect to the previous version includes new atomic data, an increased number of ionic species treated as full non-local-thermodynamic-equilibrium multilevel atoms, and the ability to use electron energy distributions that differ from a simple Maxwell-Boltzmann distribution (Nicholls et al., 2013; Dopita et al., 2013). The grids that we use here are, however, calculated assuming a Maxwell-Boltzmann distribution, in light of the ongoing controversy on whether the use of alternative distributions is justified for H II regions Draine & Kreisch (2018).

In D13 models, the input ionising spectrum is computed through the population synthesis code STARBURST99 (Leitherer et al., 1999), taking into account the Lejeune/Schmutz extended stellar atmosphere models (Schmutz et al., 1992a; Lejeune et al., 1997a), a constant star formation history (SFH), a Salpeter initial mass function (IMF, lower and upper mass cut-off at 0.1 $\mathrm{M}_{\odot}$ and 120 $\mathrm{M}_{\odot}$, respectively), and an age of 4 Myr. D13 models are isobaric with an electron density $n_e \sim 10$ cm^{-3} and are computed for a spherical geometry. The assumed gas phase abundances are taken from Asplund et al. (2009), except for nitrogen and carbon. For these elements empirical fitting functions as a function of O/H are adopted (see Table 3 in Dopita et al. 2013). Furthermore, D13 models include dust physics and radiative transfer, assuming a population of silicate grains following Mathis et al. (1977) size distribution and a population of small carbonaceous grains within the ionised regions, as described in detail in Dopita et al. (2005). The metallicities vary in the range 12+log(O/H) = [7.39−9.39] (the solar oxygen abundance is 8.69), while the ionisation parameter varies in the range $\log(q) = [6.5{-}8.5]$. Intrinsic Balmer decrement values vary in the range $= [2.85 - 3.48]$, and are systematically higher than the standard Case B recombination value, as reported by Dopita et al. (2013).

In Fig. 3.7 we show as an example the comparison between the [N II]- and [S II]-BPT diagrams for our sample of MaNGA star-forming spaxels with the grid of D13 models described above. The dashed curve represents the demarcation line defined by Kauffmann et al. (2003b) (Ka03), while the solid curve is the theoretical upper limit on SF line ratios proposed by Kewley et al. (2001) (Ke01). The dotted line, instead, is the boundary between Seyferts and low-ionisation (nuclear) emission-line regions (LI(N)ERs) introduced by Kewley et al. (2006). We noticed that [S II] lines are predicted to be weaker by ~ 0.1 dex (see Fig. 3.7) than observed, as already reported in Dopita et al. (2013) (a lower discrepancy is observed also between observed and modelled [N II]/Hα line ratios). This is due to the fact that [S II] ions are much more sensitive than [N II] ions to the diffuse radiation field in H II regions (Dopita et al., 2006a; Kewley et al., 2019). This issue is also discussed in Levesque et al. (2010), where the authors suggest that their models probably do not produce sufficient flux in the far-ultraviolet ionising spectrum. They argue that [S II] requires a larger partially ionised zone generated by a harder radiation field than the one present in the models.

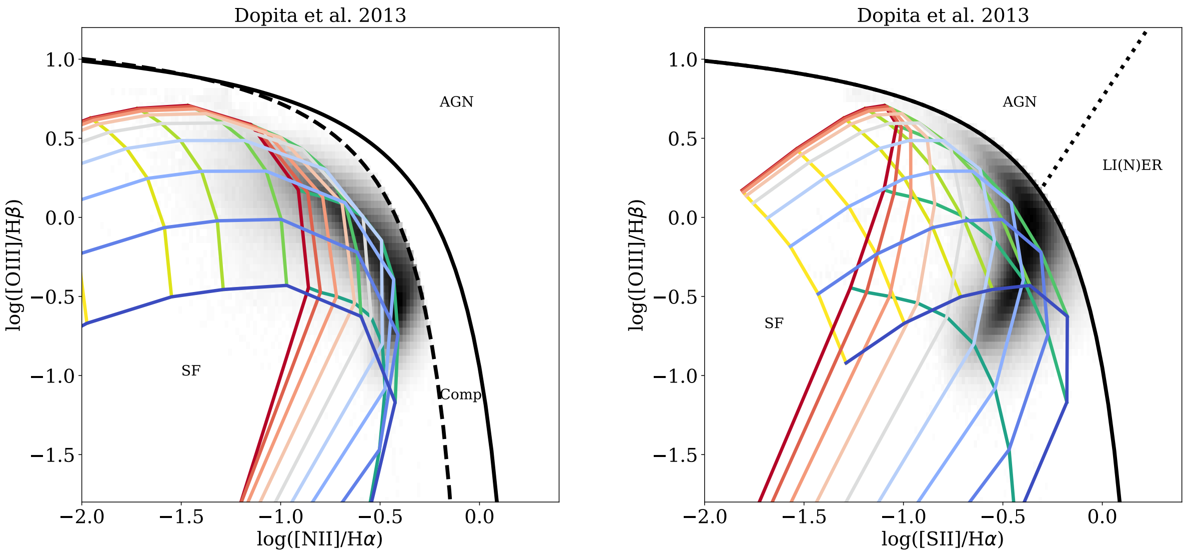

Figure 3.7: [N II]- and [S II]-BPT diagrams for our sample of MaNGA spaxels compared with D13 models, for metallicities in the range [7.39–9.39] (increasing from yellow to green) and ionisation parameters in the range [6.5–8.5] (redder means higher log(q) and bluer lower log(q)). D13 models generally well-reproduce the observed line ratios in MaNGA spaxels as ensembles.

Considering the above caveats, the optical line ratios in MaNGA spaxels are generally well-reproduced by the D13 models as ensembles. We have also reproduced all the diagnostics plots based on optical emission lines presented in Dopita et al. (2013) and find the MaNGa data global distribution to be well-covered by the model grids. As a caveat, we stress that this test does not demonstrate whether single galaxies are also well-reproduced by the models in all the diagnostic plots.

The failure of photoionisation models in reproducing the observed [SIII] lines

Stasińska (2006) suggested that S3O3 = $[\mathrm{S\,III}]\lambda\lambda9069, 9532/[\mathrm{O\,III}]\lambda\lambda4959, 5007$ versus S3S2 represents a useful diagnostic plot, where the horizontal axis is mostly tracing metallicity while the vertical axis traces the ionisation parameter. Indeed, S3O3 is found to vary monotonically with metallicity, similarly to the more commonly employed O3N2 diagnostic (Dopita et al., 2013).

Fig. 3.8 shows S3O3 versus S3S2 of all the selected MaNGA spaxels (black contours), the brightest MaNGA star-forming regions $[EW(\mathrm{H}\alpha) > 100\ \text{Å}]$ (red contours) and single H II regions analysed in Kreckel et al. (2019)[4] within eight galaxies from the Physics at High Angular resolution in Nearby GalaxieS[5] (PHANGS) survey (grey dots), in comparison with different sets of photoionisation models (described below). The observed line ratios are corrected for reddening assuming a Calzetti attenuation law with $R_V = 4.05$ (see Calzetti et al. 2000) and adopting the intrinsic Balmer decrement of 2.86. As shown in the top left panel of Fig. 3.8, the D13 models largely overestimate the [S III] fluxes (black contours), being consistently shifted both horizontally and vertically with respect to our data. In order to test whether this discrepancy is caused by any specific feature of the D13 models, we consider three other sets of photoionisation models, based on different ingredients and assumptions: the Levesque et al. (2010) models (Fig. 3.8, upper right panel), two different versions of the Byler et al. (2017) models (Fig. 3.8, lower left and right panels), and the Pérez-Montero (2014) models.

Levesque et al. (2010) (L10) photoionisation models are computed with MAPPINGS-III, adopting a version of the STARBURST99 population synthesis code (Vázquez & Leitherer, 2005) that uses the Pauldrach/Hillier stellar atmosphere models (Pauldrach et al., 2001; Hillier & Miller, 1998), and evolutionary tracks produced by the Geneva group (Schaller et al., 1992). Therefore, these models are characterised by a detailed non local thermal equilibrium modelling of metal line blanketing, which significantly affects the shape of the ionising spectrum, unlike the Lejeune/Schmutz models used in D13.

---

[4] Private communication.

[5] `https://www.phangs.org`

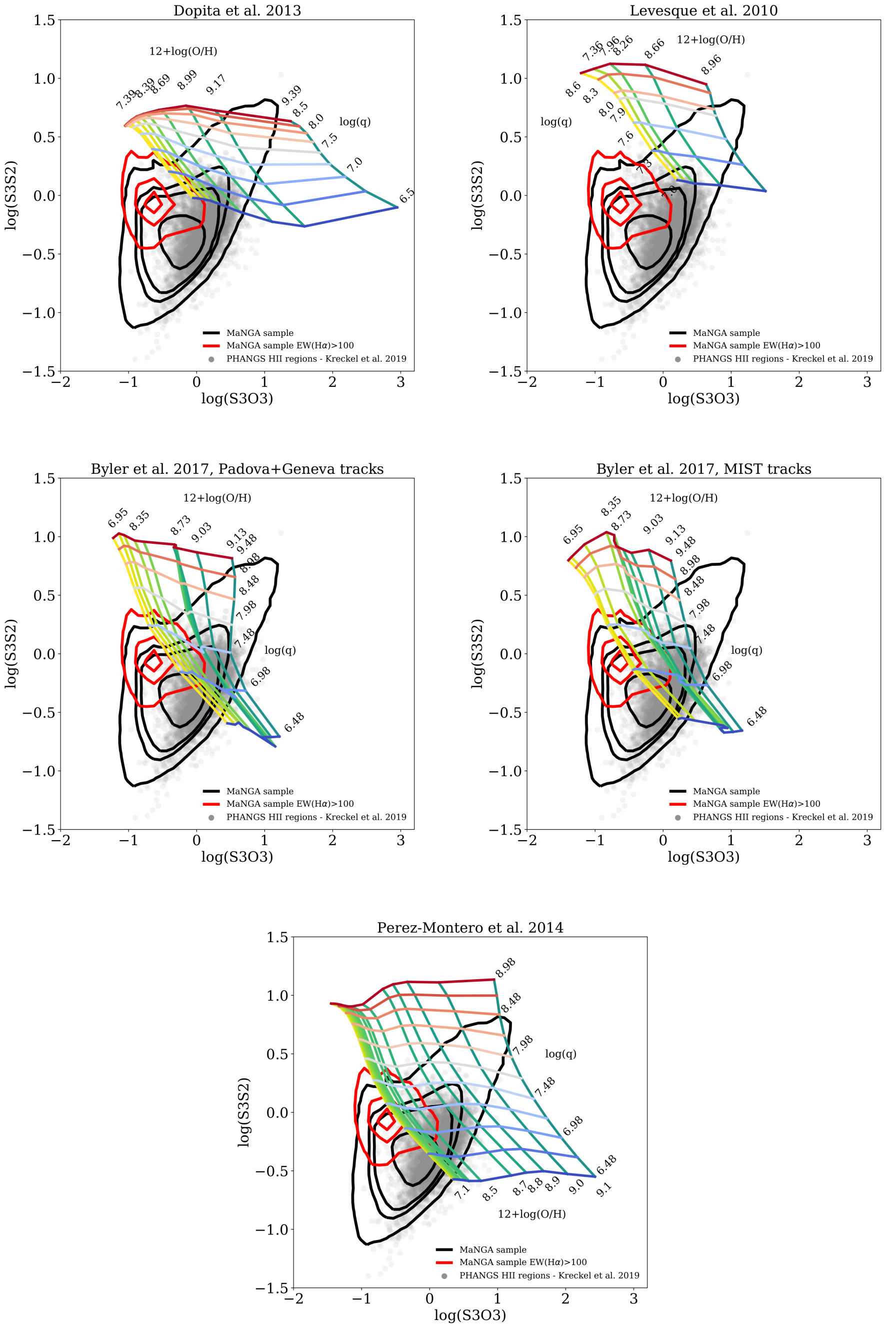

Figure 3.8: [S III]/[O III] versus [S III]/[S II] diagnostic diagrams introduced by Stasińska (2006) showing the density contours for all the star-forming spaxels of our sample (in black), with superimposed Dopita et al. (2013), Levesque et al. (2010), Byler et al. (2017) pdva+geneva, Byler et al. (2017) MIST, and Pérez-Montero (2014) models respectively. Metallicity increases horizontally from yellow to green, while ionisation parameter increases vertically [redder means higher log(q) and bluer lower log(q)]. The red contours correspond to the brighest MaNGA star-forming regions [$EW(\mathrm{H}\alpha) > 100$], while the grey dots are the H II regions analysed by Kreckel et al. (2019) with the PHANGS survey. Current photoionisation models fail to reproduce the observed [S III] lines.

Byler et al. (2017) (B17) photoionisation models, instead, are obtained with version 13.03 of CLOUDY (Ferland et al., 2013), using the Flexible Stellar Population Synthesis code (FSPS; Conroy et al. 2009), based on Padova+Geneva and MESA isochrones and stellar tracks (MIST; Choi et al. 2016; Dotter 2016) evolutionary tracks, where the latter include stellar rotation. Stellar rotation affects stellar lifetimes, luminosities, and effective temperatures through rotational mixing and mass loss, implying harder ionising spectra and higher luminosities (see Choi et al. 2016; Byler et al. 2017 for further details). B17 models are characterised by a spherical shell cloud geometry and a constant gas density of $n_\mathrm{e} = 100$ cm^{-3}. The assumed gas phase abundances are taken from Dopita et al. (2000), which are based on the solar abundances from Anders & Grevesse (1989).

Finally, Pérez-Montero (2014) (PM14) photoionisation models are obtained with version 13.03 of CLOUDY (Ferland et al., 2013) as well, assuming a plane-parallel geometry with a constant electron density of $n_\mathrm{e} = 100$ cm^{-3}. The input ionising spectrum is derived from PopStar (Mollá et al., 2009) evolutionary synthesis models. The assumed gas phase abundances are taken from Asplund et al. (2009), except for nitrogen, that is considered a free parameter, varying in the range [-2,0]. The grid shown in Fig. 3.8 corresponds to log(N/O)=-0.875, close to the solar value log(N/O)=-0.86 (Asplund et al. 2009; note that this choice does not take into account the detailed shape of the N/O versus O/H sequence, but this is of little importance to the [S III] line fluxes).

Interestingly, taking into account these different sets of photoionisation models does not resolve the discrepancy with our observations. The Levesque et al. (2010) grids are even more further removed from the data than the Dopita et al. (2013) grids. The two Byler et al. (2017) and Pérez-Montero (2014) grids appear to provide a better fit, since they predict log([S III]/[S II]), line ratios as low as $\sim$ -0.75, in better agreement with the data, but still overestimate log([S III]/[O III]). As a consequence of the latter fact, only low-metallicity models can be superimposed with the data.

We then test whether this observed discrepancy persists in the high-S/N regime. This regime is also worth exploring because low surface brightness and low $EW(\mathrm{H}\alpha)$ regions in MaNGA galaxies tend to be increasingly contaminated by DIG, which is known to display different line ratios than classical H II regions. We therefore select only the brightest star-forming regions by looking for spaxels with $EW(\mathrm{H}\alpha) > 100$ Å (red contours), and still find a significant difference between observed and predicted fluxes.

Since MaNGA data have a kpc scale resolution, H II regions, characterised by sizes between $10 - 100$ pc (Azimlu et al., 2011; Gutiérrez et al., 2011; Whitmore et al., 2011) cannot be resolved, and spatial averaging could lead to loose significant information.

In order to show that this issue is not the cause of the discrepancy between models (designed for H II regions) and the data with regards to the [S III] lines, we also take into account single H II regions analysed by Kreckel et al. (2019) with the PHANGS survey (grey dots in Fig. 3.8). For these galaxies, we estimated the [S III]λ9069,9532 flux from the extinction-corrected [S III]λ9069 reported in Kreckel et al. (2019), assuming an intrinsic value between the two [S III] lines of 2.47 (Luridiana et al., 2015). The fact that the discrepancy holds also in this case allows also to exclude that it is related to the presence of DIG.

The discrepancy between observed and modelled [S III] fluxes has been already reported in the literature (e.g. Garnett 1989; Dinerstein & Shields 1986; Ali et al. 1991). Specifically, Garnett (1989) showed that the [S III]/[S II] ratio was over-predicted by their photoionisation models. Their models produced [O II]/[O III] ratios comparable to observations, suggesting the discrepancy may be due to limitations in modelling stellar atmospheres and/or in the atomic data for sulfur. Very recently, Kewley et al. (2019) discuss the use of [S III]/[S II] as an ideal ionisation parameter diagnostic, but come to the same conclusions with regards to the limitations in the modelling effort so far. Kewley et al. (2019) however, only discuss modelling issues with regards to the [S II] lines, since no large sample of galaxies with [S III] observations was available to date. In this work we finally provide such a dataset and confirm that the discrepancy between models and observations of the [S III] lines is a lingering problem, which persists in observations of a large sample of local galaxies and latest-generation photoionisation models based on independent state-of-the-art codes.

Applying IZI to the MaNGA data

Given that the [S III] lines are not well-reproduced by photoionisation models, we first run IZI excluding the [S III] line fluxes. In particular, we consider the fluxes of [O II]$\lambda\lambda$3726,29, Hβ, [O III]$\lambda\lambda$4959,5007, [N II]$\lambda\lambda$6548,84, Hα, [S II]λ6717 and [S II]λ6731 and make use of the D13 models. We stress that, even though E(B-V) is derived assuming a screen attenuation, the IZI output takes into account also the internal dust taken into account in D13 models (see Sec. 3.2.2). Indeed, the internal dust modifies the thermal structure of the H II region, and thus the emission-line spectrum, particularly in the high-excitation regions, affecting the abundances derived by the model (e.g. Dopita et al. 2000). We assume uniform priors for metallicity and the log(q) within the range provided by the selected photoionisation models. The extinction E(B-V) is also assumed to follow a flat prior in the range [0, 1] mag. We have checked that adding the [S III] lines to the list of strong lines ratios does not change the IZI output. This

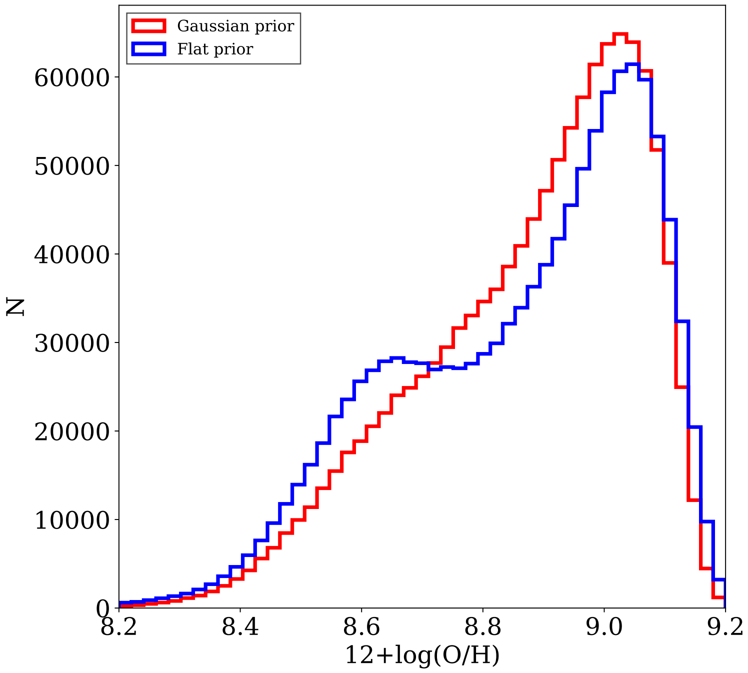

Figure 3.9: Distribution of the best-fit values of 12+log(O/H) for all MaNGA spaxels considered in this work. Metallicities are derived by IZI with a Gaussian (red) and a flat (blue) prior on the ionisation parameter, respectively. Specifically, the mean of the Gaussian prior is given by the Diaz et al. (1991) calibration, that links [S III]/[S II] line and ionisation parameter.

is because the [S III] lines are so badly reproduced by the models that they are unable to provide useful information on the best-fit parameter values. If the [S III] lines are introduced in the fit they are characterised by a large χ^2 $(10-25)$ compared to all other lines, highlighting how the D13 models are generally capable of reproducing all strong line ratios except those including [S III].

Fig. 3.9 shows in blue the histogram of the best-fit values of the metallicity obtained by IZI without taking into account the [S III] lines. Interestingly, the metallicity distribution tends to be bimodal, peaking at 12+log(O/H) $\sim$ 9 and at 12+log(O/H) $\sim$ 8.6, with a gap around 12+log(O/H) $\sim$ 8.8. As we discuss below, we argue that the peak at 12+log(O/H) $\sim$ 8.6 could be due to an underestimation of metallicity, because of the degeneracy between 12+log(O/H) and log(q). The results of taking into account the [S III]/[S II] line ratio to determine the ionisation parameter are described in the next section and are shown with the red line.

In order to better visualise the origin of the bimodality in the metallicity distribution of spaxels and its possible relation to intrinsic degeneracies in the fitting process, we show as an example different tests performed on one spaxel of the galaxy 7990-12703, chosen as a random spaxel with best-fit metallicity close to the lower-metallicity peak in the bimodal metallicity distribution of all MaNGA spaxels (Fig. 3.9, 12+log(O/H) = 8.7). In the upper panel of Fig. 3.10 we show in blue the posterior PDFs of 12+log(O/H), log(q) and E(B-V), inferred by IZI without taking into account the [S III] lines. Strong degeneracy between metallicity and ionisation parameter is evident from the figure. The 12+log(O/H) PDF is found to be very wide, characterised by likely values in the range [8.6,8.9] (best-fit median value of 12+log(O/H) = 8.7). We believe that the inability of constraining the metallicity in this example is due to the lack of a strong ionisation parameter diagnostic capable of tightly constraining log(q), as suggested by the wide PDF of this parameter, covering the range [6.8,7.4]. The lower panel of Fig. 3.10 displays in green and orange the PDFs calculated using only [O II]$\lambda\lambda$3726,29, Hβ and [O III]$\lambda\lambda$4959,5007 (i.e., R23), and Hβ, [O III]$\lambda\lambda$4959,5007, [N II]$\lambda\lambda$6548,84 and Hα, (i.e. O3N2), respectively. In both cases, there is a clear degeneracy between a low-metallicty low-ionisation parameter and a high-metallicity, high-ionisation parameter solution. Indeed, R23 is known to be double-valued (e.g., Pagel et al. 1979; Dopita et al. 2006a). O3N2 is commonly used as metallicity diagnostic, but it carries a strong dependence on the ionisation parameter, because of the very different ionisation potentials of N^+ (14.5 eV) and O^{++} (35.1 eV) (Alloin et al., 1979). This leads to a systematic underestimation of 12+log(O/H) for higher ionisation parameters and overestimation of 12 + log(O/H) in regions characterised by lower ionisation parameter values (e.g. Cresci et al. 2017; Krühler et al. 2017).

Imposing a prior on log(q) based on the [SIII]/[SII] line ratio

The discrepancy between model predictions and [S III] emission line fluxes prevents us from introducing them directy in our method together with all the other emission lines. Hence, in order to understand if and to what extent the [S III]$\lambda\lambda$9069,9532 lines can help in the determination of the ionisation parameter and in breaking the degeneracy with metallicity illustrated in Fig. 3.9 and Fig. 3.10, we compute a second run of IZI using the [S III]/[S II] ratio to set a Gaussian prior on log(q). Specifically, we choose to set the mean of this Gaussian prior by linking [S III]/[S II] and ionisation parameters via a commonly-used calibration obtained by using a large grid of single-star photoionisation models by Diaz et al. (1991) (D91 hereafter),

$$\log(q) = -1.68 \times \log([S\,\textsc{ii}]/[S\,\textsc{iii}]) + 7.49, \tag{3.1}$$

taking into account a standard deviation of 0.2 dex. Recently, Morisset et al. (2016) recalibrated this relation using an updated version of CLOUDY (Ferland et al., 2013) and atomic data, finding reasonable agreement with Eq. 3.1. This approach allows the [S III]

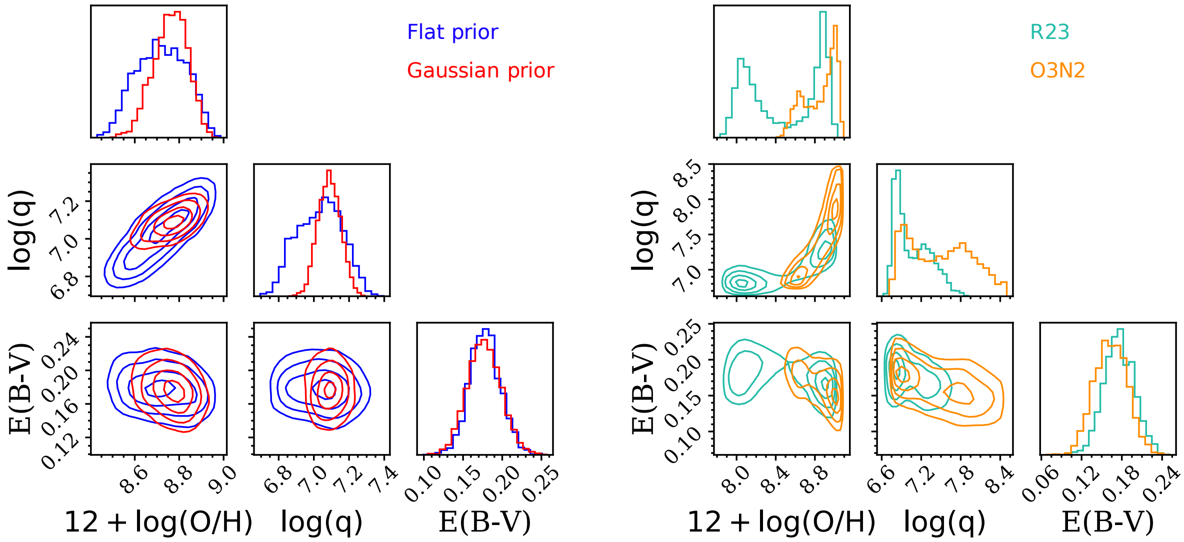

Figure 3.10: *Left panel*: Posterior PDFs relative to 12+log(O/H), log(q) and E(B-V), inferred with a Gaussian (red) and a flat (blue) prior on the ionisation parameter, respectively, with D13 models, for a single spaxel of the galaxy 7990-12703. *Right panel*: Posterior PDFs relative to the three parameters, inferred only taking into account [O II]$\lambda\lambda$3726,29, Hβ and [O III]$\lambda\lambda$4959,5007 (i.e., R23, in green), and Hβ, [O III]$\lambda\lambda$4959,5007, [N II]$\lambda\lambda$6548,84 and Hα, (i.e. O3N2, in orange), respectively.

lines to add extra information to the fit, while at the same time not fully constraining log(q) to the value obtained via the D91 calibration. We stress that since we do not fix the ionisation parameter to the value inferred by Diaz et al. (1991), the use of Morisset et al. (2016) calibration would not change our results, given that Diaz et al. (1991) and Morisset et al. (2016) are reasonably consistent within ±0.2 dex. The Gaussian prior can be applied only in those spaxels in which [S III]λ9532, [S II]λ6717, [S II]λ6731, Hα and Hβ are observed with $S/N > 1.5$, which are $\sim 80\%$ of the total.

Fig. 3.11 shows log(q) inferred with IZI with the flat prior on the ionisation parameter as a function of the observed log(S3S2). The green dashed line illustrates the log(q) values obtained with Eq. 3.1, while the green dotted lines represent the ±0.2 dex scatter around this relation. D13 models are shown for comparison (from red to blue going from high to low metallicity). Given the range of log(S3S2) observed in our data, the ionisation parameters obtained via the D91 calibration are broadly in the same range as the ionisation parameter inferred by IZI using all other strong lines except [S III] within ±0.2 dex.

The reason why the D91 calibration, which is itself based on photoionisation models, is in better agreement with the data than all the other models considered in the previous

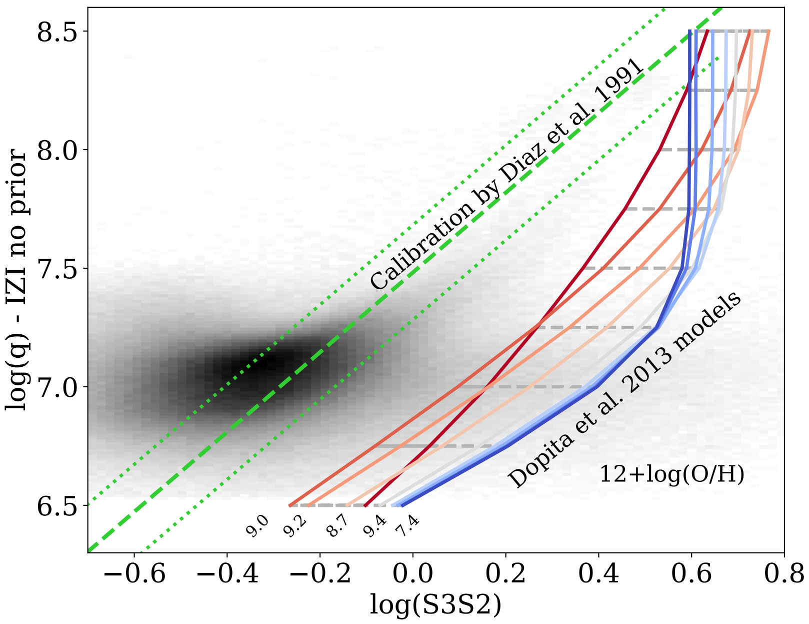

Figure 3.11: The distribution of log(q) as a function of log(S3S2) inferred with IZI with a flat prior on the ionisation parameter is shown in shades of grey. The green dashed line shows the log(q) values obtained with Eq. 3.1 (Diaz et al. (1991)), while the green dotted lines represent the ±0.2 dex scatter around this relation. D13 models are shown in colour (red-blue, going from higher to lower metallicity).

section is still an unresolved problem. The main discrepancy between D13, D91 and Morisset et al. 2016 photoionisation models, however, could be related to the input ionising spectrum (see also Sec. 4.1 and Fig. 5 in Morisset et al. 2016), but also to the underlying assumptions of the models (e.g. changes in atomic data, inclusion/exclusion of dust physics).

The differences between our two IZI runs (with a Gaussian and a flat prior on the ionisation parameter) can be appreciated from the three panels of Fig. 3.12. These figures compare the best-fit values (i.e. the median of the PDF computed by IZI, see Sec. 3.2.2) of metallicity, ionisation parameter and gas extinction obtained without taking into consideration the [S III] lines (x-axis) and imposing a Gaussian prior on log(q) based on S3S2 (y-axis), respectively. The metallicity distributions of the two runs are consistent at values 12+log(O/H) $>$ 8.9, but below this threshold metallicities inferred by the IZI run with the Gaussian prior tend to be higher than those inferred by IZI with the flat prior. The distribution of ionisation parameters of all considered spaxels is found to be wider when taking into account the prior, since the best-fit values tend to be lower for log(q) $<$ 7 and higher for log(q) $>$ 7.2. Finally, as expected, the prior on the ionisation parameter has no effect on the gas extinction.The reason why the

D91 calibration, which is itself based on photoionisation models, is in better agreement with the data than all the other models considered in the previous section is still an unresolved problem. The main discrepancy between D13, D91 and Morisset et al. 2016 photoionisation models, however, could be related to the input ionising spectrum (see also Sec. 4.1 and Fig. 5 in Morisset et al. 2016), but also to the underlying assumptions of the models (e.g. changes in atomic data, inclusion/exclusion of dust physics).

The differences between our two IZI runs (with a Gaussian and a flat prior on the ionisation parameter) can be appreciated from the three panels of Fig. 3.12. These figures compare the best-fit values (i.e. the median of the PDF computed by IZI, see Sec. 3.2.2) of metallicity, ionisation parameter and gas extinction obtained without taking into consideration the [S III] lines (x-axis) and imposing a Gaussian prior on $\log(q)$ based on S3S2 (y-axis), respectively. The metallicity distributions of the two runs are consistent at values 12+log(O/H) > 8.9, but below this threshold metallicities inferred by the IZI run with the Gaussian prior tend to be higher than those inferred by IZI with the flat prior. The distribution of ionisation parameters of all considered spaxels is found to be wider when taking into account the prior, since the best-fit values tend to be lower for $\log(q) < 7$ and higher for $\log(q) > 7.2$. Finally, as expected, the prior on the ionisation parameter has no effect on the gas extinction.

Coming back to Fig. 3.9, the histogram of the best-fit values of the metallicity obtained by the IZI run with the Gaussian prior on the ionisation parameter is shown in red. Note that the bimodality discussed in Sec. 3.2.2 disappears when the Gaussian prior is imposed. Indeed, in the upper panel of Fig. 3.10, the degeneracy is broken introducing the Gaussian prior based on the Diaz calibration (shown in red as well), in which a higher metallicity (8.8 vs 8.7) and a higher ionisation parameter (7.1 vs 7.0) solution is preferred.

As explained in Sec. 3.2.2, the errors provided by IZI are obtained by computing the 16^{th}, 50^{th} and 84^{th} percentiles of the PDFs, and are defined as $\Delta_{up} = 84^{\text{th}} - 50^{\text{th}}$ and $\Delta_{down} = 50^{\text{th}} - 16^{\text{th}}$. The difference between Δ_{up} and Δ_{down} indicates how much these PDFs differ from a symmetric distribution. In general this difference would be greater than zero if the distribution is tailed towards higher values with respect to its median value, considered as the best-fit, and vice-versa. Fig. 3.13 shows the distribution of the difference between Δ_{up} and Δ_{down} for the metallicity (left panel) and ionisation parameter (right panel), in the case with a flat (blue) and a Gaussian (red) prior on the ionisation parameter, for all the spaxels considered in this work. In the case with the flat prior, these distributions are shifted towards negative values both for 12+log(O/H) and $\log(q)$ Δ_{up} - Δ_{down}, meaning that the majority of the spaxels have an asymmetric PDF

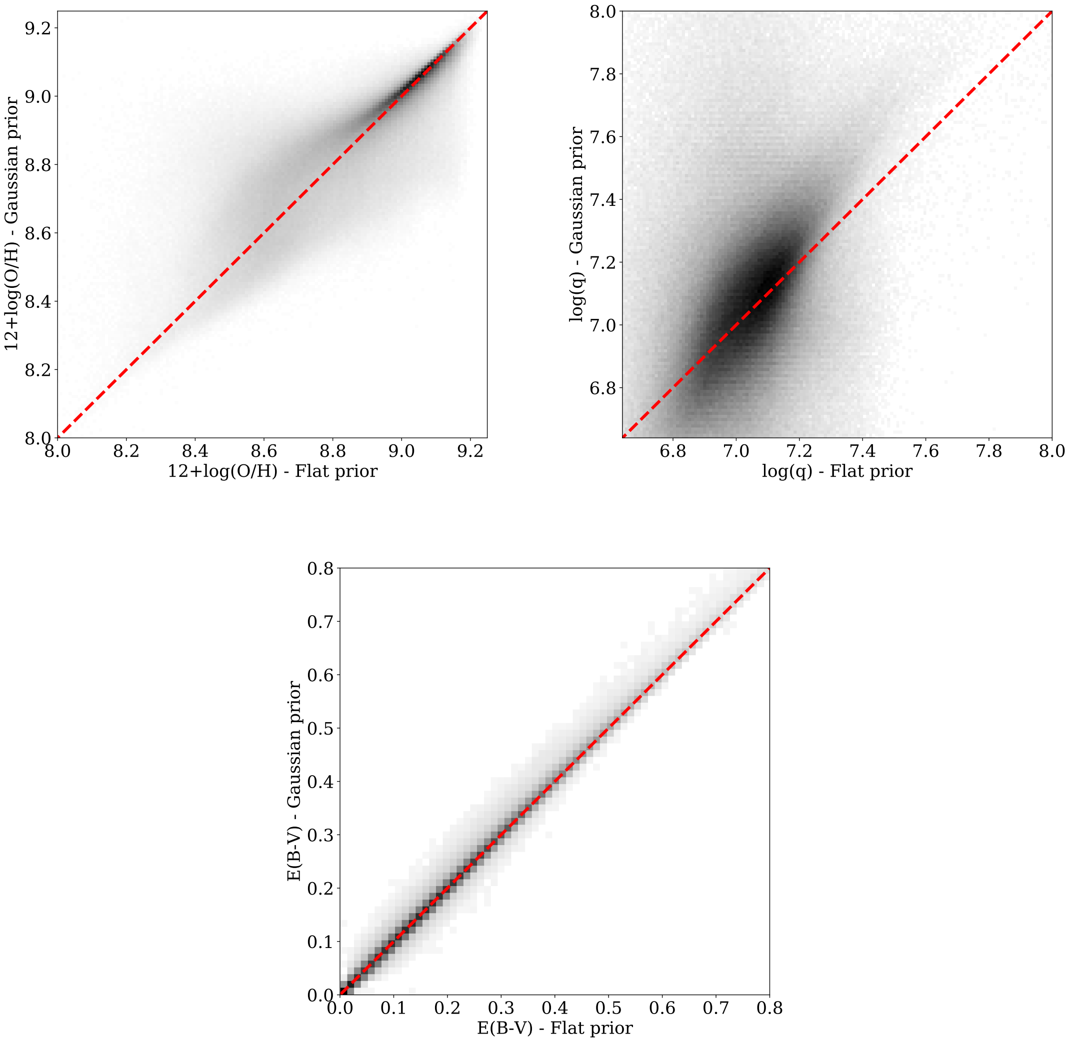

Figure 3.12: Comparison between the results obtained with IZI with a flat (x-axis) and a Gaussian (y-axis) prior on the ionisation parameter, for metallicity, ionisation parameter and gas extinction, respectively. The red dashed line represents the one-to-one relation.

tailed towards lower values with respect to the best-fit. Moreover, these distributions show a cut-off around 0 (this is more visible for 12+log(O/H)), with a considerable tail at positive values to $\sim$ 0.075, implying that some spaxels have an asymmetric PDF tailed towards higher values with respect to the best-fit. This leads to the bimodality discussed above.

In the case with the Gaussian prior, the log(q) Δ_{up} - Δ_{down} distribution is almost Gaussian, centered on zero, mirroring the prior itself. The metallicity distribution remains slightly shifted towards negative values (i.e. high values of metallicity), but shows a much less conspicuous tail compared to the case with the flat prior, indicating a general

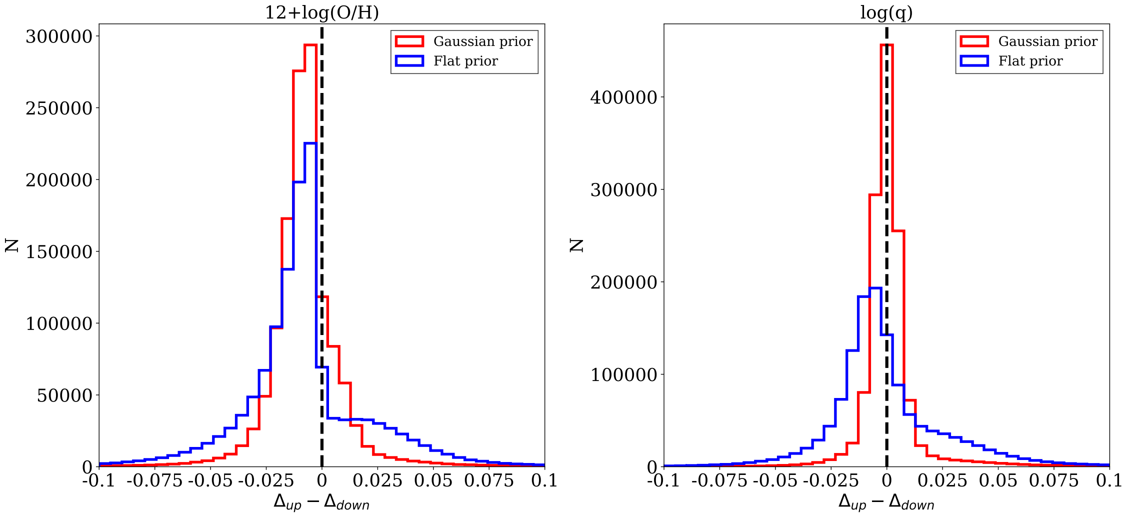

Figure 3.13: Distribution of the difference between $\Delta_{up} = 84^{\text{th}} - 50^{\text{th}}$ and $\Delta_{down} = 50^{\text{th}} - 16^{\text{th}}$ for the metallicity (left panel) and ionisation parameter (right panel), in the case with a flat (in blue) and a Gaussian (in red) prior on the ionisation parameter, respectively), for all the spaxels of all the galaxies.

significant reduction in the effect of the 12+log(O/H) − log(q) degeneracy.

Fig. 3.14 shows the metallicity inferred for each galaxy at 0.8 R_e, obtained by interpolating the metallicity profile as a function of galactocentric distance. This characteristic metallicity is shown as a function of the total stellar mass, colour-coded on the basis of the ionisation parameter (also at 0.8 R_e) for the case with the flat and the Gaussian prior on the ionisation parameter, respectively. We present the corresponding metallicity distributions as grey histograms on the right. We comment here on this well-known scaling relation between mass and metallicity (MZR, Lequeux et al. 1979; Tremonti et al. 2004) to highlight the importance of breaking the degeneracy between metallicity and ionisation parameter when investigating secondary trends.

As the left panel of Fig. 3.14 shows, in the case with the flat prior we find the hint of a bimodality in the metallicity distribution, shown in the grey histogram, with values around 12+log(O/H) ∼ 8.8 being less probable. This feature creates a steeper slope for the mass-metallicity relation in the range $9.5 < \log(M_\star/M_\odot) < 10$, with respect to the case with the prior, and in agreement with the even larger bimodality in the mass-metallicity relation derived by Blanc et al. (2019) with IZI and the Levesque et al. 2010 models.

More strikingly, at fixed mass there is a strong correlation between metallicity and ionisation parameter (a smoothing has been applied to the colour-coding for ease of visualisation, using the LOESS recipe from Cappellari et al. 2013). This correlation disappears when a Gaussian prior based on [S III]/[S II] is used (right panel of Fig. 3.14).

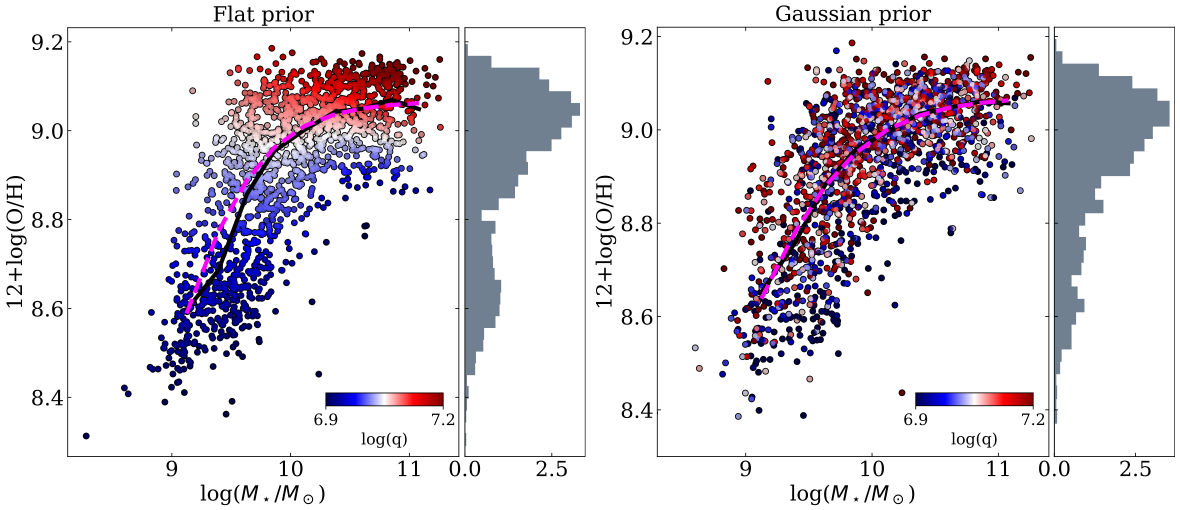

Figure 3.14: The mass-metallicity relation for the MaNGA star-forming galaxies considered in this work without using the [S III] lines (left) and by using the [S III] lines via an ionisation parameter prior as discussed in the text (right). Metallicities are computed for each galaxy at 0.8 R_e. The colour-coding indicates the ionisation parameter (at 0.8 R_e). A histogram of the metallicity distributions for all galaxies is shown in grey on the right. In the case where the [S III] lines are not used (left panel) there is a striking correlation at fixed mass between the metallicity and ionisation parameter. To visually highlight this correlation the colour-coding has been smoothed according to the LOESS recipe of Cappellari et al. (2013). The solid black lines show the median metallicity in bins of $M_\star$, while the dashed magenta lines are the best-fit using the parametrisation proposed in Curti et al. (2019b).

We argue, therefore, that this secondary dependence of metallicity on $\log(q)$ seen in the case with the flat ionisation parameter prior is solely due to the degeneracy between the two parameters.

In Tab. 3.2.2 we report the best-fit parameter values for the MZR shown in Fig. 3.14, using the new parametrisation proposed in Curti et al. (2019b) (C19):

$$12 + \log(\mathrm{O/H}) = Z_0 - \gamma/\beta \times \log\left(1 + \left(\frac{M}{\mathrm{M}_0}\right)^{-\beta}\right) \tag{3.2}$$

In this equation, Z_0 is the metallicity at which the relation saturates, quantifying the asymptotic upper metallicity limit, while M_0 is the characteristic turnover mass above which the metallicity asymptotically approaches the upper metallicity limit (Z_0). At stellar masses $M_\star < M_0$, the MZR reduces to a power law of index γ. In Eq. 3.2, β quantifies how "fast" the curve approaches its saturation value. The parameters that we obtain for the two different MZRs, shown on the left and right of Fig. 3.14, are consistent within the errors, and the scatter around the best-fit relations are 0.12 dex

Table 3.1: Best-fit values for the parameters of the MZR shown in the right panel of Fig. 3.14 derived with IZI, putting a Flat and a Gaussian prior on the ionisation parameter based on [S III]/[S II], assuming the new parametrisation proposed in Curti et al. (2019b) (Eq. 3.2).

MZR C19 - Flat prior			
Z_0	$M_0/\mathrm{M}_\odot$	γ	β
$9.07^{+0.06}_{-0.04}$	$9.3^{+0.1}_{-0.2}$	$1.3^{+0.4}_{-0.4}$	$1.1^{+0.5}_{-0.4}$
MZR C19 - Gaussian prior			
Z_0	$\log(M_0/\mathrm{M}_\odot)$	γ	β
$9.06^{+0.05}_{-0.04}$	$9.3^{+0.1}_{-0.2}$	$1.1^{+0.5}_{-0.4}$	$1.2^{+0.5}_{-0.4}$

and 0.10 dex, respectively.

In App. 3.2.5, we show the comparison between the observed value of Hα, [N II]λ6584, [O II], [O III]λ5007, [S II]λ6717 and [S II]λ6731 and the fluxes of the the best-fitting model retrieved by IZI (all normalised to Hβ, and divided by the error), as a function of the Petrosian effective radius and stellar mass, for all the spaxels of all the galaxies taken into account. Overall, the stellar-mass- and radius-dependent variations are consistent within the errors taken into account.

3.2.3 Metallicity, ionisation parameter and gas extinction in MaNGA galaxies

In this section we show the results obtained with the IZI run which makes use of the Gaussian prior on the ionisation parameter, as described in Sec. 3.2.2. In all the plots, only the spaxels classified as star-forming according to both the [N II]- and the [S II]-BPT diagrams with S/N(Hα) > 15 and in which the prior based on the S3S2 line ratio can be used are shown.

Example maps for low- and high-mass galaxies

Fig. 3.15 and Fig. 3.16 show an example of a low-mass (8147-9102, $\log(\mathrm{M}_\star/\mathrm{M}_\odot) = 9.10$) and a high-mass (9041-12701, $\log(\mathrm{M}_\star/\mathrm{M}_\odot) = 10.93$) galaxy in our sample. The quantities displayed are: $g-r-i$ image composite from SDSS with the MaNGA hexagonal FoV overlaid, the logarithm of equivalent width of Hα [EW(Hα)], the log(S3S2) and log(O3O2) line ratios, the IZI best-fit metallicity 12+log(O/H), ionisation parameter $\log(q)$ and gas extinction E(B-V), and the logarithm of the resulting luminosity of Hα per spaxel corrected for extinction [l(Hα)].

In the low-mass galaxy, the S3S2 line ratio map, used as a prior for the ionisation

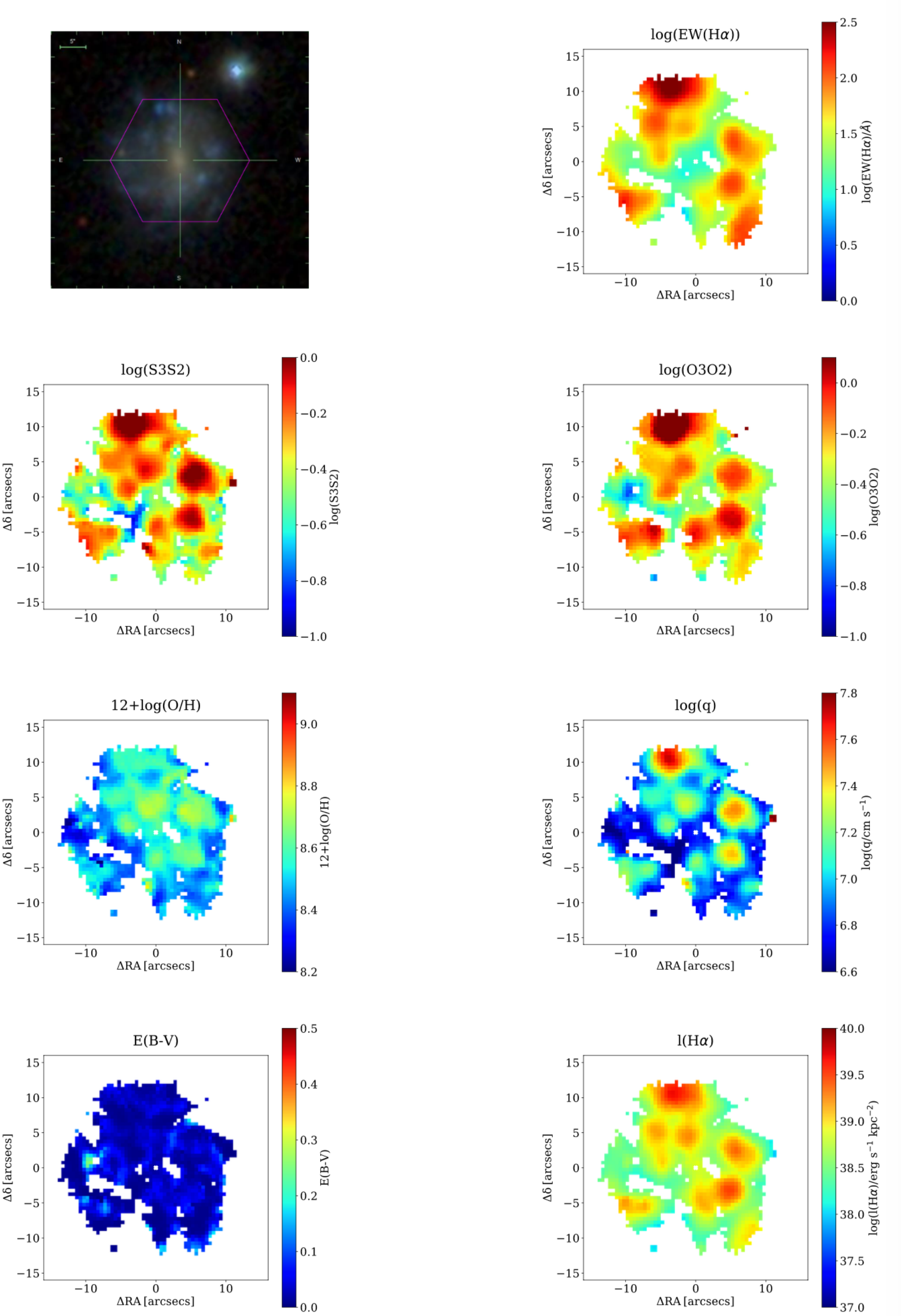

Figure 3.15: Maps for the galaxy 8147-9102, with a stellar mass $\log(\mathrm{M}_{\star}/\mathrm{M}_{\odot}) = 9.10$. The $g-r-i$ image composite from SDSS with the MaNGA hexagonal FoV overlaid, equivalent width of Hα, S3S2, O3O2, IZI metallicity 12+log(O/H), IZI ionisation parameter $\log(q)$, IZI gas extinction E(B-V) and Hα luminosity per spaxel $L(\mathrm{H}\alpha)$ maps are reported, respectively. East is to the left.

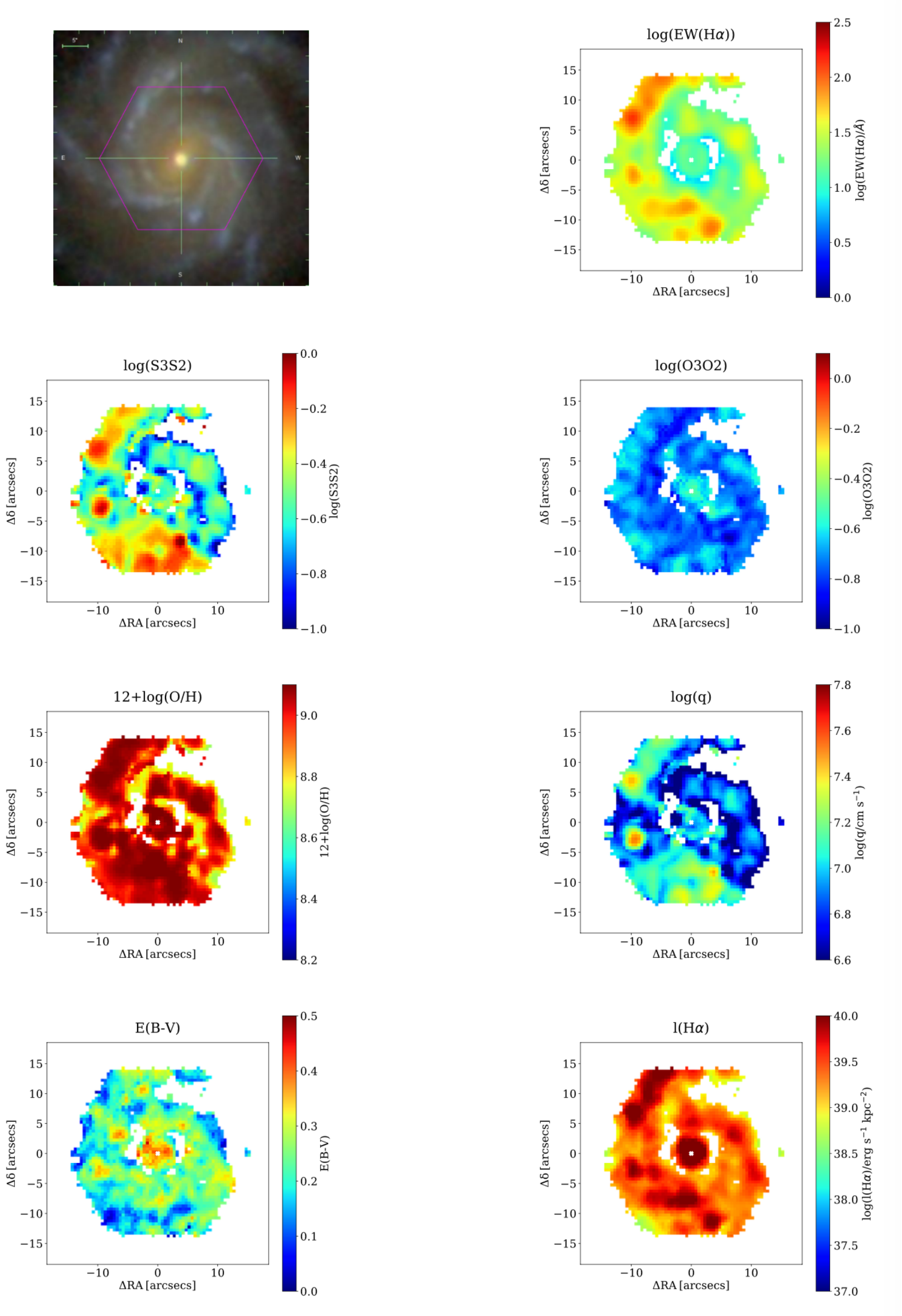

Figure 3.16: Same as Fig. 3.15 for the galaxy 9041-12701, with a stellar mass in the range $10.75 < \log(M_\star/M_\odot) < 11$.

parameter, and the O3O2 line ratio map look very similar. Interestingly, both the S3S2 and O3O2 line ratios tend to trace the regions with higher values of $EW(\mathrm{H}\alpha)$ and $l(\mathrm{H}\alpha)$, and thus show a clumpy distribution.

On the other hand, in the high-mass galaxy the S3S2 and O3O2 maps look qualitatively different. The S3S2 line ratio map is clumpy with an enhancement in the eastern direction, while the O3O2 line ratio is higher in the center, but shows a roughly flat profile over the FoV. The similarity between S3S2 line ratios and $EW(\mathrm{H}\alpha)$ persists, while there is no clear correlation between S3S2 and $l(\mathrm{H}\alpha)$. Indeed, the central regions in which $l(\mathrm{H}\alpha)$ is enhanced are characterised by lower values of S3S2. The discrepancy between S3S2 and O3O2 in the high mass galaxy, could be due to the strong dependence of O3O2 on metallicity (e.g. Fig. 1, Kewley & Dopita 2002), as already mentioned in Sec. 1.3.1. Specifically, in the low-mass galaxy the highest metallicities (up to 12+log(O/H) $\sim$ 8.8) are found in several clumps all around the field of view. The high-mass galaxy, in contrast, displays higher metallicities (with values up to 12+log(O/H) $\sim$ 9.1) and an almost regular metallicity gradient, with some deviations only in the inter-arm regions. In this high-metallicity regime the O3O2 line ratio is only marginally sensitive to $\log(q)$ (Kewley & Dopita, 2002), and thus the higher values of the O3O2 line ratio observed in the centre can be explained by the metallicity enhancement.

Interestingly, in these two galaxies the ionisation parameter does not show a monotonic and smooth radial profile, but, similarly to the S3S2 line ratio map, is enhanced in 'structures' which follow the $EW(\mathrm{H}\alpha)$ maps, concentrated along the spiral arms visible in the $g-r-i$ images.

Finally, the gas extinction is low across the entire FoV of the lower-mass galaxy, with values below E(B-V) $\sim$ 0.1, but shows a radial gradient in the high-mass galaxy, with values up to E(B-V) $\sim$ 0.5 in the central regions.

The shape of the metallicity gradients

In the following, we analyse the radial profiles and gradients of metallicity, ionisation parameter and gas extinction for all the 1795 galaxies, keeping in mind that some of these quantities may have trends not well reproduced by a simple radial average, as shown in the example maps.

To determine the radial gradients, we used the deprojected distance of each spaxel derived by Belfiore et al. (2017), taking into account the inclination from the measured semi-axis ratio, assuming a constant oblateness of 0.13. Following the approach of Sánchez et al. (2014), Ho et al. (2015) and Belfiore et al. (2017), we adopt as a scale length to normalise the gradients the elliptical Petrosian effective radius (henceforth

R_e), which is the most robust measure of the photometric properties of MaNGA galaxies provided by the NSA catalogue. The median radial profile of each quantity is computed for every galaxy in the range $0.5-2$ R_e (in bins of 0.2 dex) as the median of the quantity measured in the spaxels lying in each bin. Then the median profiles are divided in eight bins of stellar mass, in the range $\log(M_\star/M_\odot) = 9 - 11$ (in bins of 0.25 dex). The radial range is chosen to minimise the effects of inclination and beam-smearing on the metallicity gradients (Belfiore et al., 2017), and because of significant deviations from a linear fit are observed out of this range (Sánchez et al., 2014; Sánchez-Menguiano et al., 2016). The shaded regions in the following figures represent the 16th and 84th percentiles of the distribution in each stellar mass bin, divided by $\sqrt{N}$, where N is the number of galaxies lying in the bin. For each mass bin, a profile is computed only if more than 100 galaxies have a valid measured radial profile.

Fig. 3.17 displays the metallicity radial profiles computed with IZI for galaxies of different stellar mass (stellar mass bins as reported in the legend). The main observed features are the following:

- The mean oxygen abundance radial profiles are negative at all stellar masses in the range [-0.05, -0.10] dex $R_e{}^{-1}$.
- The metallicity profile shape of galaxies with $\log(M_\star/M_\odot) > 10.25$ is characterised by a flattening in the central regions ($R < 0.5$ R_e);
- Galaxies with $\log(M_\star/M_\odot) < 10$ show a mild flattening of the radial metallicity profile in the outer regions ($R > 1.5$ R_e).
- The average slope shows a weak non-linear trend with stellar mass.

The negative abundance gradients are consistent with infall models of galaxy formation, that predict that spiral discs build up through accretion of material, which leads to an inside-out growth (Matteucci & Francois, 1989; Molla et al., 1996; Boissier & Prantzos, 1999; Belfiore et al., 2019). In this scenario, accretion brings gas into the inner regions of the discs, where high density leads to efficient star formation. The fast reprocessing of gas in the inner regions leads to a population of old, metal-rich stars in a high-metallicity gaseous environment. The outer regions, on the other hand, are characterised by younger, metal-poor stars surrounded by less enriched material (e.g., Davé et al. 2011; Gibson et al. 2013; Prantzos & Boissier 2000; Pilkington et al. 2012). The vertical offset between the different profiles is due to the mass-metallicity relation (Tremonti et al., 2004; Curti et al., 2019b).

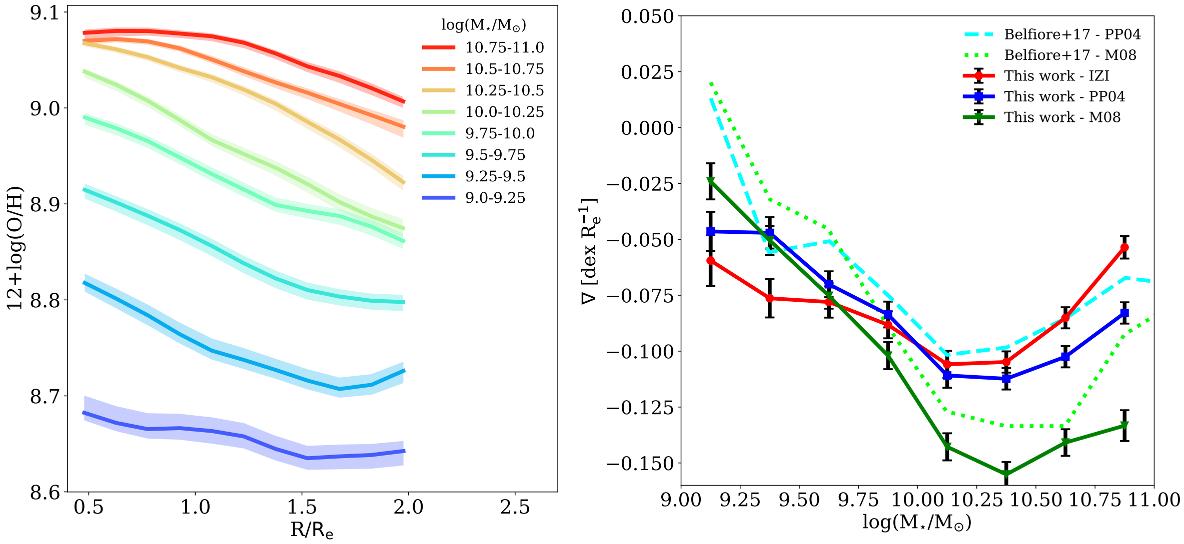

Figure 3.17: *Left*: Oxygen abundance 12+log(O/H) as a function of the radius (in units of R_e), colour-coded as a function of the stellar mass $\log(M_\star/M_\odot)$, as reported in the legend. The shaded regions represent the upper and lower errors of the radial gradients, obtained by calculating the 16th and 84th of the distribution in each stellar mass bin taking into account the number of galaxies lying in the bin. *Right*: Metallicity gradient estimated in the radial range 0.5–2 R_e from a linear fit of the corresponding radial profiles in different mass bins as a function of stellar mass (in red). The metallicity gradients estimated with M08 and PP04 calibrations are reported in green and blue, respectively, while those taken by Belfiore et al. (2017) are reported in lime and cyan.

A decrease or a nearly flat distribution of the abundance in the innermost region of discs was first observed by Belley & Roy (1992), while several works reported a flattening in the gradient in the outer regions (e.g. Martin & Roy 1995; Vilchez & Esteban 1996; Roy & Walsh 1997). This behaviour deviates from the pure inside-out scenario and could be due to the presence of radial migration (e.g. Minchev et al. 2011, 2012). Furthermore, the flattening of the metallicity gradient in the central region of the most massive spiral galaxies, found also in other works using CALIFA (e.g. Zinchenko et al. 2016) and MaNGA data (e.g. Belfiore et al. 2017), can be a consequence of the metallicity saturating in the central most metal rich regions and can readily be explained by classical inside-out chemical evolution models (Belfiore et al., 2019). One should also consider the possibility that contamination from the central LIER-like emission in massive galaxies may still contaminate the measured line fluxes (e.g., Maiolino & Mannucci 2019).

In Fig. 3.17, right panel, we show the metallicity profile slopes, estimated from a linear fit to the median profile in each mass bin, as red circles as a function of stellar mass. We observe a slight steepening with stellar mass in the range $\log(\mathrm{M}_\star/\mathrm{M}_\odot) = 9 - 10.25$, going from -0.06 dex $\mathrm{R_e}^{-1}$ to -0.1 dex $\mathrm{R_e}^{-1}$, and then a flattening down to -0.04 dex $\mathrm{R_e}^{-1}$ towards $\log(\mathrm{M}_\star/\mathrm{M}_\odot) = 11$.

These mass trends may appear in contrast with the conclusions from Belfiore et al. (2017), who analysed gas-phase metallicity gradients using 550 star-forming MaNGA galaxies from a previous SDSS data release (data release 13). The metallicity gradients in Belfiore et al. (2017) are nearly flat for low-mass galaxies ($\log(\mathrm{M}_\star/\mathrm{M}_\odot) = 9$) and become progressively steeper (more negative) for more massive galaxies until slopes ~ -0.15 dex $\mathrm{R_e}^{-1}$ at $\log(\mathrm{M}_\star/\mathrm{M}_\odot) = 10.25$. A steepening of the metallicity gradient as a function of stellar mass - though weaker than the one observed by Belfiore et al. (2017) - is also inferred by Poetrodjojo et al. (2018), using data from the SAMI survey and an iterative process based on R23 and O3O2 to estimate 12+log(O/H) and $\log(q)$ (see Kobulnicky & Kewley 2004 for more details). This steepening is not per-se in contrast with the inside-out galaxy formation scenario (Belfiore et al., 2019), but may also point towards redistribution of metals in the early stages galaxy formation (see e.g. Maiolino & Mannucci 2019).

While the current sample of galaxies is larger than the one considered in Belfiore et al. (2017) and we make use of a different S/N selection criterion, the main discrepancy between the current work and Belfiore et al. (2017) is the method applied to infer metallicities. Indeed, in Belfiore et al. (2017) two strong-line ratio diagnostics were used, namely a calibration of R23 from Maiolino et al. (2008) (M08) and the well-established

O3N2 calibration from Pettini & Pagel 2004 (PP04). To allow for a fairer comparison with Belfiore et al. (2017), in Fig. 3.17 we show the average metallicity gradients obtained applying the PP04 (blue squares) and M08 (green triangles) calibrations to the data presented in this work. The cyan dashed and the lime dotted lines are the results obtained by Belfiore et al. (2017) using PP04 and M08, respectively, and are fairly consistent with the gradients obtained with the current data set. At low stellar masses [$\log(\mathrm{M}_\star/\mathrm{M}_\odot) < 9.75$], both the PP04 and M08 calibration find flatter gradients than IZI, in accordance to the findings in Belfiore et al. (2017). It is reassuring that some of the qualitative features (e.g. the flattening in the central regions of massive galaxies) are found for different choices of calibrator. It seems, moreover, that the slope of the metallicity gradients for low-mass galaxies was found to be too shallow in Belfiore et al. (2017). Further work may be warranted to better understand the chemical abundance distribution on the low-mass end, especially in light of recent work pointing out the diversity of metallicity gradients exhibited by low-mass star-forming galaxies (Bresolin, 2019).

The ionisation parameter on resolved scales

The ionisation parameter changes within galaxies are still surprisingly poorly understood, despite the importance of determining q for correctly utilising ISM diagnostics. Dopita et al. (2006b) argued that in the local universe ionisation parameter gradually decreases with $M_\star$ (see also Brinchmann et al. 2008). Some studies presented a possible correlation between ionisation parameter and star formation rate (SFR, e.g. Dopita et al. 2014; Kaplan et al. 2016), while others argue for a better correlation with specific SFR (sSFR = $\mathrm{SFR}/\mathrm{M}_*$, e.g., Kewley et al. 2015; Bian et al. 2016; Kaasinen et al. 2018). On the other hand, Ho et al. (2015) investigated ~ 50 galaxies from the CALIFA survey, finding indications of a smooth increase in the ionisation parameter from their centres to the outskirts, which they interpret as a radial change in the properties of the ionising radiation. Kaplan et al. (2016), instead, analysed the ionisation parameter distribution in 8 nearby galaxies with the VENGA survey (Blanc et al., 2013), finding a peak in the central parts and regions of localised enhancements in the outer disc of their galaxies. Finally, Poetrodjojo et al. (2018), analysying 25 face-on star-forming spiral galaxies from the SAMI survey, found that the ionisation parameter does not have clear radial or azimuthal trends, showing a range of different distributions ranging from weak gradients, to flat or clumpy distributions. All these authors estimated $\log(q)$ using the O3O2 diagnostic following the iterative method proposed by Kobulnicky & Kewley (2004), apart from Dopita et al. (2014), who used the method developed by Dopita et al.

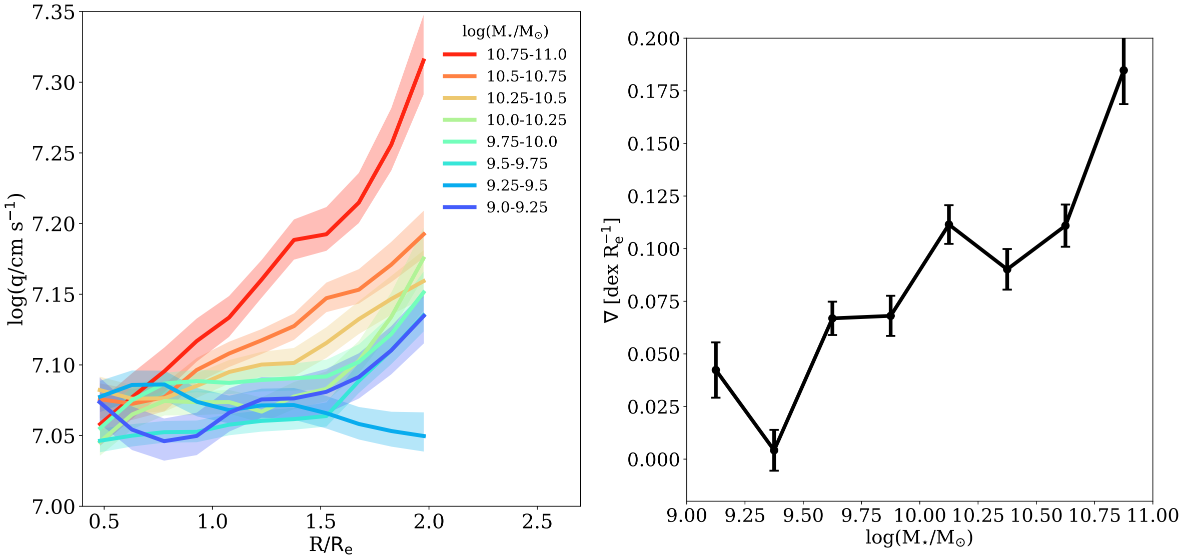

Figure 3.18: *Left*: Ionisation parameter radial distribution (in units of R_e), colour-coded as a function of the stellar mass $\log(M_\star/M_\odot)$, as reported in the legend. The shaded regions represent the 16th and 84th pecentiles of the distribution in each stellar mass bin taking into account the number of galaxies lying in the bin. *Right*: $\log(q)$ radial profile slopes as a function of stellar mass in units of dex ${R_e}^{-1}$.

(2013), `pyqz`, that performs a two-dimensional fit to a given diagnostic grid, estimating metallicity and ionisation parameters for a given set of diagnostics

The left panel of Fig. 3.18 shows the radial profiles of ionisation parameter estimated by IZI, colour-coded as a function of stellar mass bins as reported in the legend. The right panel shows the slope of the radial profiles as a function of stellar mass. We highlight two main features from these figures:

- the ionisation parameter radial profiles are approximately flat at low stellar masses ($\log(M_\star/M_\odot < 10)$, with slopes becoming more positive and steeper at increasing $M_\star$, up to 0.15 dex ${R_e}^{-1}$ at $\log(M_\star/M_\odot) = 11$;
- in the central regions, galaxies of all masses show similar values of $\log(q)$ around $\log(q/\mathrm{cm\,s^{-1}}) \sim 7.05 - 7.1$, while at large radii, higher stellar mass galaxies tend to have higher average values of $\log(q)$ (with values up to $\log(q/\mathrm{cm\,s^{-1}}) \sim 7.3$).

The steepening with stellar mass and increasingly positive slopes of $\log(q)$ profiles echo the $EW(\mathrm{H}\alpha)$ radial distributions as a function of stellar mass (see Fig. 3, Belfiore et al. 2018). These are found to be flat for low mass galaxies, becoming increasingly positive towards higher stellar masses. As discussed in Leitherer (2005), the equivalent width of the strongest hydrogen recombination lines, such as $EW(\mathrm{H}\alpha)$, can be very powerful age indicators, measuring the ratio of the young, ionising stars over the old, non-ionising population (see also Kewley et al. 2015; Kaasinen et al. 2018). Therefore, $EW(\mathrm{H}\alpha)$ is a good proxy for the sSFR, that is defined as the number of massive young (O,B) stars with respect to the total number of formed stars. A similarity between $\log(q)$ and $EW(\mathrm{H}\alpha)$ was already suggested by analysing Fig. 3.15 and Fig. 3.16.

In light of this, we investigated the dependence of the ionisation parameter on $EW(\mathrm{H}\alpha)$, finding a strong correlation at all stellar masses, as shown in the left panel of Fig. 3.19, obtained dividing all the spaxels of each galaxy in $EW(\mathrm{H}\alpha)$ bins of 0.15 dex, and then separating the galaxies in bins of stellar mass $M_\star/\mathrm{M}_\odot$, as reported in the legend. For $EW(\mathrm{H}\alpha) > 14$ Å (above the threshold of a possible DIG contamination; Lacerda et al. 2018), $\log(q)$ increases with $EW(\mathrm{H}\alpha)$ following a nearly universal relation for galaxies of different masses. We quantify this relation with a linear slope in the log-log plane as

$$\log(q) = 0.56 \times \log(EW(H\alpha)) + 6.29 \tag{3.3}$$

with a scatter of 0.12 dex (dashed line in Fig. 3.19). This relation could be useful to constrain $\log(q)$ in order to calculate metallicity from a limited set of emission lines (e.g. [N II] and Hα in high-z galaxies). We also test the presence of a correlation between $\log(q)$ and $l(\mathrm{H}\alpha)$. $l(\mathrm{H}\alpha)$ traces the number of ionising photons produced by young and massive stars, and thus the current star formation on timescales of ~ 10 Myr (Calzetti et al., 2005, 2012). The right panel of Fig. 3.19 shows the ionisation parameter as a function of $l(\mathrm{H}\alpha)$, dividing all the spaxels in this work in $l(\mathrm{H}\alpha)$ bins of 0.15 dex, and then separating the galaxies in bins of stellar mass $\log(\mathrm{M}_\star)/\mathrm{M}_\odot$. No universal relation is found between $\log(q)$ and $l(\mathrm{H}\alpha)$. Indeed, $\log(q)$ increases with $l(\mathrm{H}\alpha)$ at the lowest stellar masses ($\log(\mathrm{M}_\star)/\mathrm{M}_\odot = 9$), while it decreases at the highest stellar masses ($\log(\mathrm{M}_\star)/\mathrm{M}_\odot = 11$).

Interestingly, Pellegrini et al. (2019) found a good correlation between ionisation parameter and the age of the stellar population (i.e. with $EW(\mathrm{H}\alpha)$), that they explain in terms of a correlation between q and the hardness of the spectrum, without finding any correlation between q and SFR, in agreement with our findings.

We note that, as evidenced in Fig. 3.18, the majority of spaxels have $\log(q)$ in the range $\log(q/\mathrm{cm\ s}^{-1}) = 7.05 - 7.15$, while the correlation with $EW(\mathrm{H}\alpha)$ observed in in Fig. 3.19 only starts to appear for all masses for $\log(q) > 7.2$. This indicates that the correlation is driven by spaxels corresponding to the brightest H II regions. The flat $\log(q)$ radial profiles are the result of averaging a very clumpy distribution in $\log(q)$ with a large scatter, as highlighted in Fig. 3.15 and Fig. 3.16. Therefore, the radial averages used here to derive radial trends might not be ideal to understand the variations of q across the galaxy discs, that seem to be dominated by sSFR variations traced by

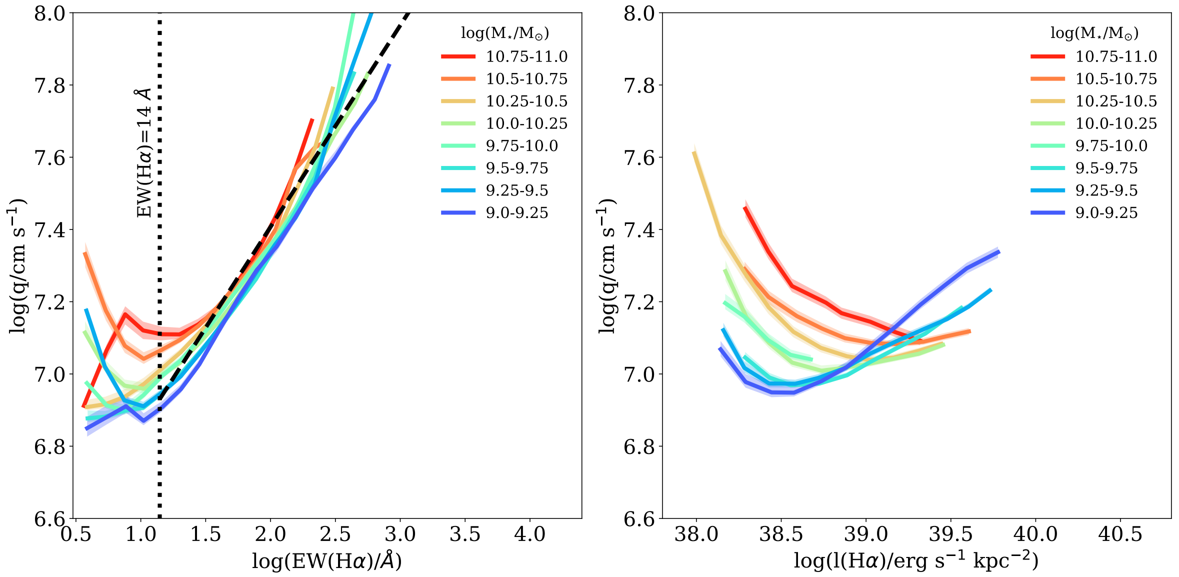

Figure 3.19: *Left*: Ionisation parameter log(q) as a function of Hα equivalent width [EW(Hα)/Å] dividing all the spaxels used in this work in bins of 0.15 dex, and then separating the galaxies in bins of stellar mass, as reported in the legend. A nearly-universal power-law relation is evident between the two quantities for $EW(\mathrm{H}\alpha) > 14$ Å (labelled with a dotted vertical line). *Right*: Same as the left panel but for Hα luminosity per spaxel [l(Hα)/erg s^{-1}]. No universal relation is found in this case.

EW(Hα).

The left and right panels of Fig. 3.2.3 show log(S3S2) and log(O3O2) radial distributions in stellar mass bins, derived analogously to Fig. 3.18. These line ratios are both proxies for the ionisation parameter, and consistently show that low-mass galaxies are characterised by higher values of log(S3S2) and log(O3O2) and by flatter radial profiles. High-mass galaxies, on the other hand, tend to show positive slopes.

Interestingly, we used S3S2 line ratios as a prior for log(q), so the log(q) radial distribution should closely follow the same trend. However, comparing the right panels of Fig. 3.18 and Fig. 3.2.3 the log(q) distribution obtained with IZI shows higher values for higher mass galaxies. On the one hand, this "flip" with stellar masses could be due to the residual dependence of these line ratios on metallicity. Up to $\log(q/\mathrm{cm\ s^{-1}}) = 7.5$ (where the majority of spaxels lies) the log(q) values retrieved by IZI are slightly lower with respect to the prediction of Eq. 3.1, and the discrepancy depends on metallicity. Interestingly, this happens even though the input prior is not metallicity-dependent. IZI, however, will predict a metallicity dependence of the relation between log(S3S2) and ionisation parameter as a consequence of the information provided by the other emission lines. Above $\log(\mathrm{q/cm\ s^{-1}}) = 7.5$, log($q$) retrieved by IZI is fairly consistent with D91. This leads to a "re-calibrated" relation between log(S3S2) and log(q), highlighted by the

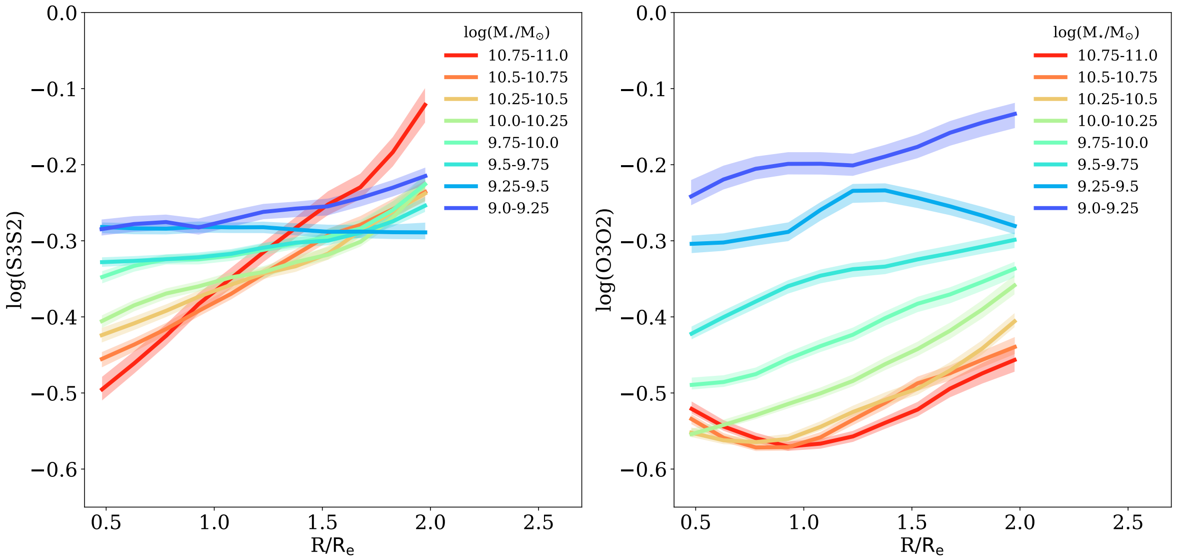

Figure 3.20: log(S3S2) and log(O3O2) radial distributions, in bins of stellar mass $\log(M_\star)/M_\odot$, as reported in the legend, respectively.

magenta dotted line in Fig. 3.21 and given by

$$\log(\mathrm{S3S2}) = 0.76 \times \log(\mathrm{q}) - 5.70, \tag{3.4}$$

with a scatter of 0.11 dex, obtained using all the selected spaxels. On the other hand, this residual dependence of log(S3S2) on metallicity after adding a prior on the ionisation parameter could also point to the fact that IZI still suffers from a certain degree of degeneracy between the 12+log(O/H) and log(q). Another possibility is that the difference between the [S III]/[S II] derived value for q and the IZI output could be due to residual problems of the photoionisation models used in reproducing the observed line ratios. Therefore, a new generation of photoionisation models, designed to reproduce the sulfur emission lines as well, is required to better asses this issue.

Finally, Fig. 3.22 shows the relation between EW(Hα) and ionisation parameter in bins of metallicity, obtained by IZI, indicating that at fixed EW(Hα) there is a clear correlation between log(q) and 12+log(O/H). However, this correlation disappears going towards the highest value of EW(Hα) (EW(Hα)>150 Å). A correlation between the two quantities is in contrast with the theoretical relation presented in Dopita & Evans (1986) and Dopita et al. (2006b) [$\log(q/\mathrm{cm\ s^{-1}}) \propto 12+\log(\mathrm{O/H})^{-0.8}$]. However, Ho et al. (2015), Kaplan et al. (2016) and Poetrodjojo et al. (2018) do not find any clear radial trend between ionisation parameter and gas metallicity, both when considering regions at different galactocentric distances and in the 2-D maps, while Dopita et al. (2014) found a positive correlation between the two quantities. Dopita et al. (2014)

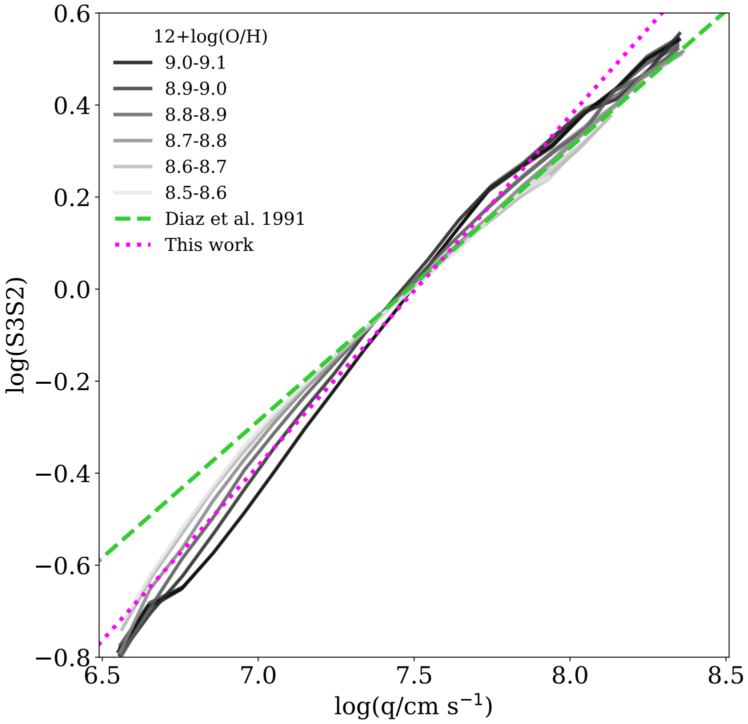

Figure 3.21: Distribution of log(S3S2) as a function of log(q) inferred with IZI is shown in shades of grey, while its linear fit is given by the dotted magenta line. The green dashed line illustrates the D91 calibration, used as a prior.

explained the positive correlation between 12+log(O/H) and log(q) as a consequence of the positive correlation that they find between SFR density and ionisation parameter. They conclude that the correlation between SFR density and log(q) is mainly caused by geometrical effects (i.e. overlapping between H II regions or non-spherical geometries), but is also due to the presence of dense gas in the vicinity of H II regions. On the other hand, Cresci et al. (2017) investigated the physical properties of the ionised gas in the prototypical H II galaxy He 2-10, finding that the central extreme star forming knots are highly enriched with super solar metallicity and characterised by a large ionisation parameter, highlighting again a correlation between the two quantities.

Gas extinction

The left panel of Fig. 3.23 illustrates the radial profiles of gas extinction E(B-V) estimated by IZI, colour-coded as a function of stellar mass bins as reported in the legend, while the right panel shows the radial profile as a function of stellar mass. We report on these profiles only briefly in this work, since they will be the subject of future work by our team. Here we only highlight two main features of these figures:

- the E(B-V) radial profiles show a strong dependence on stellar mass, with slopes

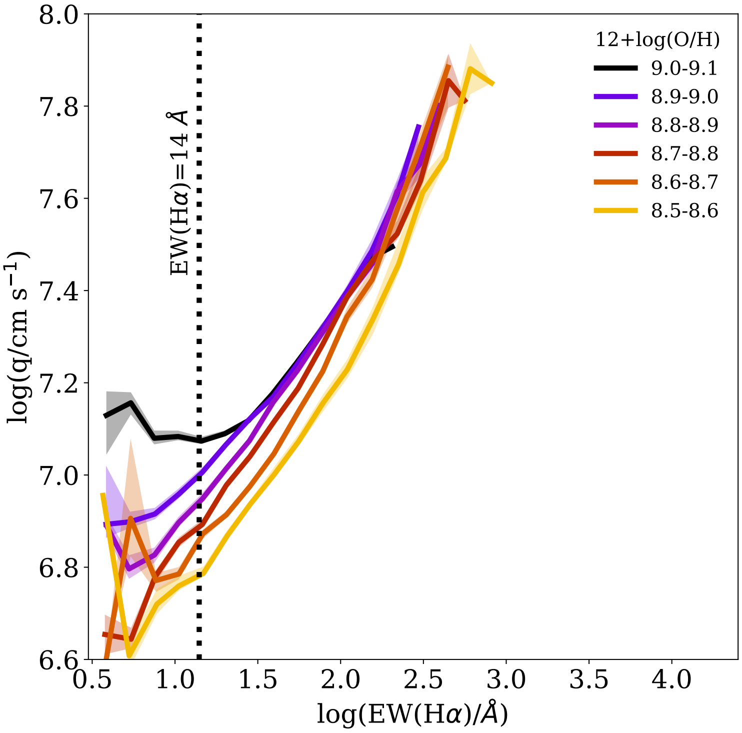

Figure 3.22: Ionisation parameter $\log(q)$ as a function of $\log(EW(\mathrm{H}\alpha))$ dividing all the spaxels used in this work in bins of 0.15 dex, and then separating the galaxies in bins of metallicity, as reported in the legend.

around -0.02 dex $\mathrm{R_e}^{-1}$ at $\log(\mathrm{M_\star/M_\odot}) = 9$ and increasingly negative and steeper slopes in the range up to ~ -0.13 dex $\mathrm{R_e}^{-1}$ at larger stellar masses;

- E(B-V) $\sim$ 0.07 for the lowest mass galaxies and reaches values as high as E(B-V) $\sim$ 0.4 in the central regions of the more massive galaxies.

Indeed our findings in this section are not surprising, since more massive galaxies usually have larger dust reservoirs, especially in the central regions (Bell & de Jong, 2000). Since dust is formed from metals, a correlation between dust and the gas-phase oxygen abundance is expected and observed both in the local universe (e.g., Heckman et al. 1998; Zahid et al. 2013) and at high redshift (e.g., Reddy et al. 2010). A follow-up study of the relation between gas extinction and other galaxy properties will be presented in a forthcoming work.

Fig. 3.24 shows the histogram of the difference between gas extinction obtained by assuming a fixed Hα/Hβ line ratio of 2.86 and the one retrieved by IZI [ΔE(B-V)]. The two quantities are pretty consistent, but in general IZI tends to retrieve slightly lower E(B-V) values, in agreement with Brinchmann et al. (2004).

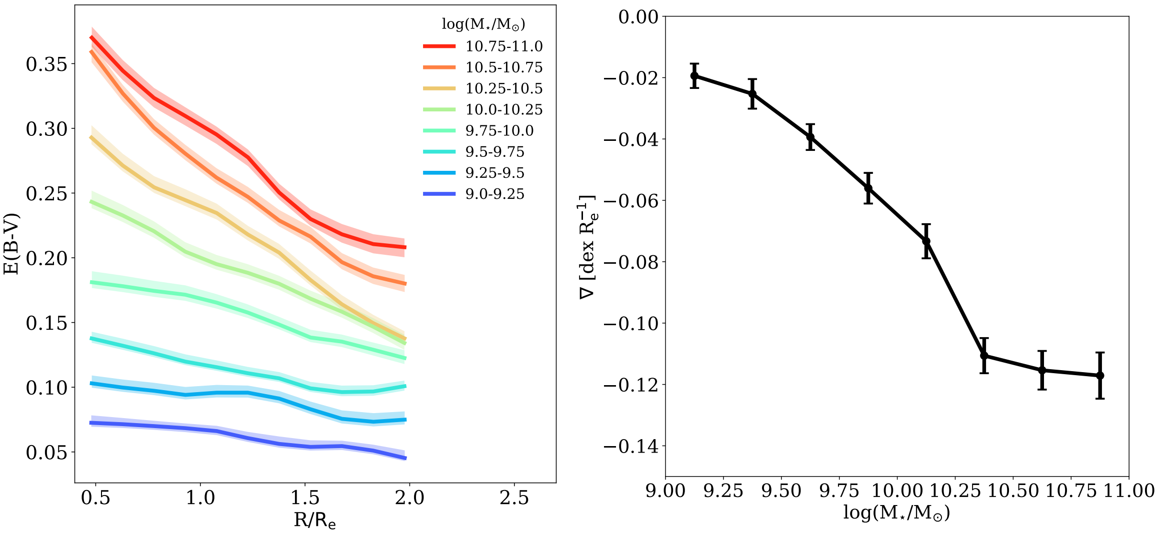

Figure 3.23: *Left*: Gas extinction radial distribution (in units of R_e), colour-coded as a function of the stellar mass $\log(M_\star/M_\odot$, as reported in the legend. The shaded regions represent the 16th and 84th percentiles of the distribution in each stellar mass bin taking into account the number of galaxies lying in the bin. *Right*: Slope of the radial profiles of E(B-V) in units of mag/R_e as a function of stellar mass.

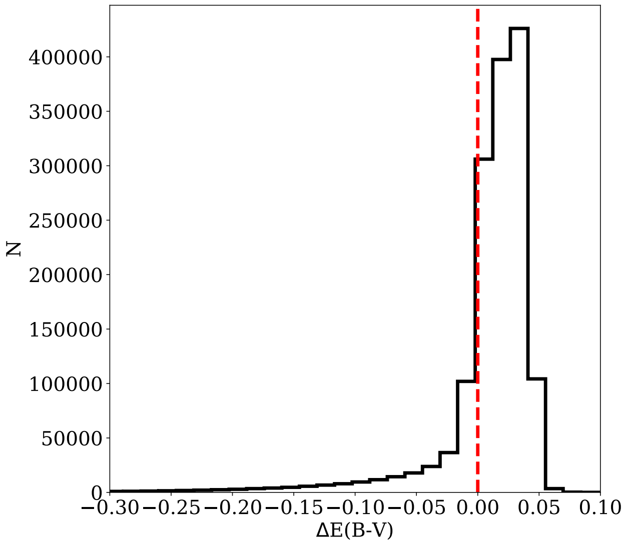

Figure 3.24: Histogram of the difference between the E(B-V) obtained by assuming a fixed Hα/Hα line ratio of 2.86 and the one retrieved by IZI.

3.2.4 Conclusions

In this Section we investigated the gas phase metallicity, ionisation parameter and gas extinction for a sample of 1795 local star forming galaxies, spanning the stellar mass range $10^9 - 10^{11}$ $M_\odot$, by exploiting integral field spectroscopy from the SDSS-IV MaNGA DR 15. We selected star forming galaxies following the classification scheme proposed in Belfiore et al. (2016), further excluding spaxels which are not classified as star forming according to both the [N II]- and the [S II]-BPT diagrams. Moreover, we excluded spaxels with S/N(Hα) $<$ 15, which assures that the main optical emission lines (i.e. [O II]$\lambda\lambda$3726,29, Hβ, [O III]$\lambda\lambda$4959,5007, [N II]$\lambda\lambda$6548,84, Hα, [S II]λ6717, [S II]λ6731 and [S III]$\lambda\lambda$9069,9532) are generally detected with $S/N > 1.5$ without introducing metallicity biases. We characterise self-consistently the gradients of metallicity, ionisation parameter and gas extinction with a method that consists in an update of the software tool IZI (Blanc et al., 2015), which compares an arbitrary set of observed emission lines with photoionisation model grids. Our revised version takes as input observed (as opposed to de-reddened) fluxes and simultaneously estimates the dust extinction (E(B-V)).

In the following we summarise our main findings.

- We confirm the existence of a discrepancy between models and observations of the [S III] lines already reported in the literature that persists with observations of a large sample of local galaxies and latest-generation photoionisation models (based on both the MAPPINGS and CLOUDY codes) (Fig. 3.8).

- We argue that the set of emission lines comprising [O II]$\lambda\lambda$3726,29, Hβ, [O III]$\lambda\lambda$4959,5007, [N II]$\lambda\lambda$6548,84, Hα, [S II]λ6717 and [S II]λ6731 is not sufficient to break the degeneracy between metallicity and ionisation parameter with the current photoionisation models. We therefore used the [S III] lines to add extra information to the fit performed with our revised version of IZI, taking into account a Gaussian prior based on the D91 calibration, that links S3S2 to q (Sec. 3.2.2).

- The oxygen abundance radial profiles (in the range 0.5–2 R$_\mathrm{e}$) have negative slopes [$-0.1\,\mathrm{dex\,R_e^{-1}}$ to $-0.04\,\mathrm{dex\,R_e^{-1}}$], and show a flattening in more massive systems. Galaxies with $\log(\mathrm{M_\star/M_\odot}) > 10.25$ show a flat gradient in the central regions ($R \sim 0.5$ R$_\mathrm{e}$), while galaxies with $\log(\mathrm{M_\star/M_\odot}) < 10$ tend to have a flatter gradients in the external regions ($R > 1.5$ R$_\mathrm{e}$) (Fig. 3.17).

- The ionisation parameter gradients are approximately flat at low stellar masses ($\log(\mathrm{M_\star/M_\odot}) < 10$), and tend to steepen (more positive slopes) at increasing M$_\star$. In galaxy outskirts, higher stellar mass galaxies tend to have higher average values of $\log(q)$ than less massive objects. All galaxies, however, show a median value around $\log(q) \sim 7.05 - 7.1$ in the central regions (Fig. 3.18).

- A tight correlation between $\log(EW(\mathrm{H}\alpha))$ and $\log(q)$ is observed at all stellar masses, expressed by a simple power-law relation for $EW(\mathrm{H}\alpha) > 14$ Å. A clear correlation between $l(\mathrm{H}\alpha)$ (i.e. SFR) and $\log(q)$ is only found in low-mass galaxies, but this correlation does not hold for the whole galaxy sample (Fig. 3.19).

- A correlation between metallicity and ionisation parameter is found at fixed $EW(\mathrm{H}\alpha)$ up to $EW(\mathrm{H}\alpha) < 150$ (Fig. 3.22).

- The gas extinction radial gradients strongly depend on stellar mass. E(B-V) slopes are approximately flat at $\log(\mathrm{M}_\star/\mathrm{M}_\odot) = 9$ with values of E(B-V) ~ 0.07 mag. The profiles steepen towards higher stellar masses, and E(B-V) reaches values as high as ~ 0.4 mag in the central regions of the more massive systems (Fig. 3.23).

The work presented in this Section can be seen as a first step in the simultaneous study of 12+log(O/H) and q within a large set of galaxies. As such, it is affected by some limitations. For example, at this stage we have not included in our analysis the variation of N/O ratio and the effective temperature of the stellar cluster. Indeed, the nucleosynthetic origin of nitrogen is more complex than that of oxygen, and its nucleosynthesis is metallicity-dependent, implying a non-linear relation between O/H and N/O (see e.g. Belfiore et al. 2017; Schaefer et al. 2019). Furthermore, the effective temperature of the exciting stars is related to both metallicity and ionisation parameter since it increases as metallicity is lowered, but the mechanical energy flux in the stellar winds decreases towards lower metallicity, causing changes in the ionisation parameter (see e.g. Pérez-Montero & Díaz 2005; Dopita et al. 2006b,a; Pérez-Montero 2014). Since these fundamental parameters of H II regions are not independent, more physical H II region models, such as WARPFIELD-EMP (Rahner et al., 2017; Pellegrini et al., 2019), that allows to model the time evolution of feedback in molecular clouds taking into account the physical processes regulating the emission from the clouds (e.g. stellar winds, radiation, supernovae, gravity, thermal conduction, cooling), may be helpful in reducing the size of the parameter space to be explored.

However, the main drawback of the current approach lies in the limitations of the current photoionisation models. Even though the model grids are generally able to reproduce the bulk properties of H II regions in galaxies, we have shown here that S3S2 is not well reproduced by any of the state-of-the art model grids taken into account in this work. This fact severely limits the usefulness of S3S2 at present as a tracer of the ionisation parameter.

3.2.5 Additional material

Comparison with Pipe3D

Pipe3D code (Sánchez et al., 2016, 2018) provides a valid point of comparison to the DAP, since it performs an independent continuum subtraction and emission-line measurements. An overview of the data products released by these two pipelines is provided by Aguado et al. (2019). The output of Pipe3D code on MaNGA data is presented in the MaNGA Pipe3D value-added catalog (VAC)[6]. The MaNGA VAC generated by the Pipe3D team uses MIUSCAT templates for spectral fitting, instead of the MILES models used by the DAP as reported in Sec. 3.2.1. Specifically, MIUSCAT is a set of simple stellar-population (SSP) models generated according to Vazdekis et al. (2012), that extend the wavelength range of MILES models to cover the range $3465 - 9469$ Å. The Pipe3D VAC therefore contains line fluxes for [S III]λ9069. Intriguingly, the publicly-available VAC also contains line fluxes for the [S III]λ9532, which lies outside the MIUSCAT wavelength coverage. It appears that Pipe3D in this case performs a extrapolation of the model continuum for ~ 100 Å (S. Sanchez, private communication).

Fig. 3.25 shows the comparison between the emission line fluxes taken into account in this work (y-axis) with the ones obtained with Pipe3D (x-axis) (see also Appendix A, Belfiore et al. 2019) for all the star forming spaxels characterised by a signal-to-noise S/N(Hα) > 15. In general there is good agreement between the two pipelines, since the majority of the measurements lie in the vicinity of the red dashed line one-to-one line. However, there is a larger spread in the comparison of the [S III] lines with respect to the other transitions, especially for [S III]λ9532. Overall, our [S III]λ9532 measurements are slightly larger than those performed by Pipe3D, while in few cases Pipe3D measurements have values up to two orders of magnitude higher than the ones derived by us. There is good agreement for the [S III]λ9069 emission line, instead. In contrast to Pipe3D, in our fitting procedure we fixed the flux ratio of the two [S III] lines to the intrinsic value of 2.47 (Luridiana et al., 2015), as explained in Sec 3.2.1. Therefore, the fact that there is good agreement for the [S III]λ9069 but not for the [S III]λ9532 suggests that Pipe3D is underestimating the [S III]λ9532 line flux in the majority of the spaxels, on top of showing a high failure rate of spaxels with clearly nonphysically [S III] line ratios. We therefore strongly recommend against the use of the Pipe3D [S III]λ9532 line fluxes.

---

[6] `https://www.sdss.org/dr15/manga/manga-data/manga-pipe3d-value-added-catalog/`

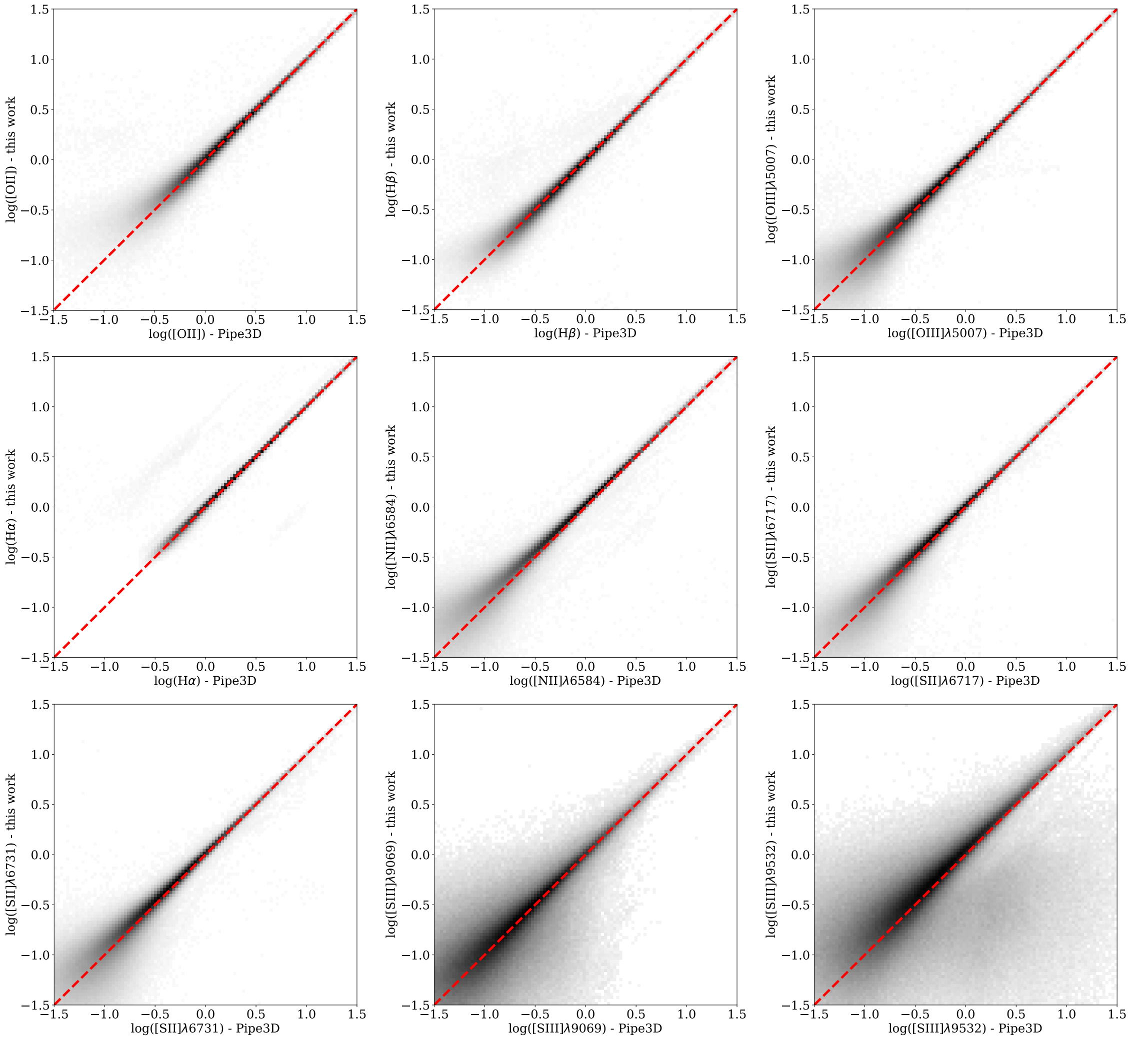

Figure 3.25: Spaxel-by-spaxel comparison between the emission line fluxes taken into account in this work (y-axis) and the results of Pipe3D (x-axis): namely [O II], Hβ, [O III]λ5007, Hα, [N II]λ6584, [S II]λ6717, [S II]λ6731, [S III]λ9069, [S III]λ9532. The fluxes are in units of 10^{-17} erg s^{-1}Å^{-1} cm^{-2} and are expressed in logarithm. The red dashed line represents the one-to-one line.

Signal-to-noise radial profiles

Fig. 3.26 shows the S/N radial gradients of Hα, Hβ, [N II]λ6584, [O II], [O III]λ5007, [S II]λ6717, [S II]λ6731 and [S III]λ9532. To compute these gradient we considered all the spaxels in our galaxy sample, subdivided in bins of stellar mass, as reported in the legend. The radial distance is normalised to the elliptical Petrosian effective radius (R$_e$), like for all other gradients presented in this work. For each stellar mass bin, the radial profile is computed as the median of the galaxies contributing to the bin at that radius. The upper and lower error bars are obtained by calculating the 16th and 84th percentiles of the distribution for the sample and dividing by $\sqrt{N}$, where N is the number of profiles at each radius. The figure highlights that the MaNGA galaxy sample used in this work shows sufficient S/N in all the strong lines considered, except for [S III]λ9532 at large radii and for high-mass galaxies.

Quality test

In order to show the reliability of our method in Fig. 3.27 we show the distribution of the difference between the logarithm of the observed value of the emission line fluxes (Hα, [N II]λ6584, [O II], [O III]λ5007, [S II]λ6717 and [S II]λ6731) and that of the best-fitting model (both normalised to Hβ) obtained with IZI, taking into account D13 models and a Gaussian prior on the ionisation parameter (See Sec. 3.2.2), for all the spaxels used in this work, as a function of radius and stellar mass. The radial distributions are divided in eight bins of stellar mass, in the range $\log(\mathrm{M}_\star/\mathrm{M}_\odot) = 9 - 11$ in bins of 0.25 dex, as reported in the legend. The shaded areas represent the 16^{th} and 84^{th} percentiles of the distribution in each stellar mass bin divided by $\sqrt{N}$, where N is the number of galaxies lying in each bin. For each mass bin, a profile is computed only if more than 100 galaxies have a valid measured radial profile. Specifically, the Hα and [O III]λ5007 line fluxes are faithfully reproduced at all radii and stellar masses. However, IZI tends to overpredict the [N II]λ6584 and [O II] line fluxes at low stellar masses and to underestimate the [N II]λ6584 at high stellar masses, and the [S II]λ6717 and [S II]λ6731 line fluxes at low stellar masses. Interestingly, concerning the [S II] lines there is a dependence also on radius, since in the most massive galaxies the observed [S II] fluxes are slightly overestimated at radii $R < 1$ $\mathrm{R_e}$, while they are slightly underestimated at radii $R > 1.5$ $\mathrm{R_e}$. Overall, we claim that these stellar-mass- and radius-dependent discrepancies are not affecting the results shown in this Chapter, because all the radial distributions shown in Fig. 3.27 lie in the range [-0.1,0.1] dex, meaning that they are all consistent within the assumed uncertainty of the photoionisation models of 0.1 dex (0.01 dex for Hα).

Fig. 3.28 instead shows the distribution of the difference between the logarithm of the observed flux of the [S III]λ9532 and that of the best-fit model (both normalised to Hβ) predicted by IZI, taking into account D13 models and a Gaussian prior on the ionisation parameter, for all the spaxels used in this work, as a function of radius and stellar mass, analogously to Fig. 3.27. Unlike the other emission lines, [S III]λ9532 is largely overestimated, with differences between observed and predicted fluxes up to 0.8 dex. Similarly to [S II] lines, there is a dependence also on radius, since in the inner regions ($R < 1$ $\mathrm{R_e}$) of the most massive galaxies the observed [S III] fluxes are

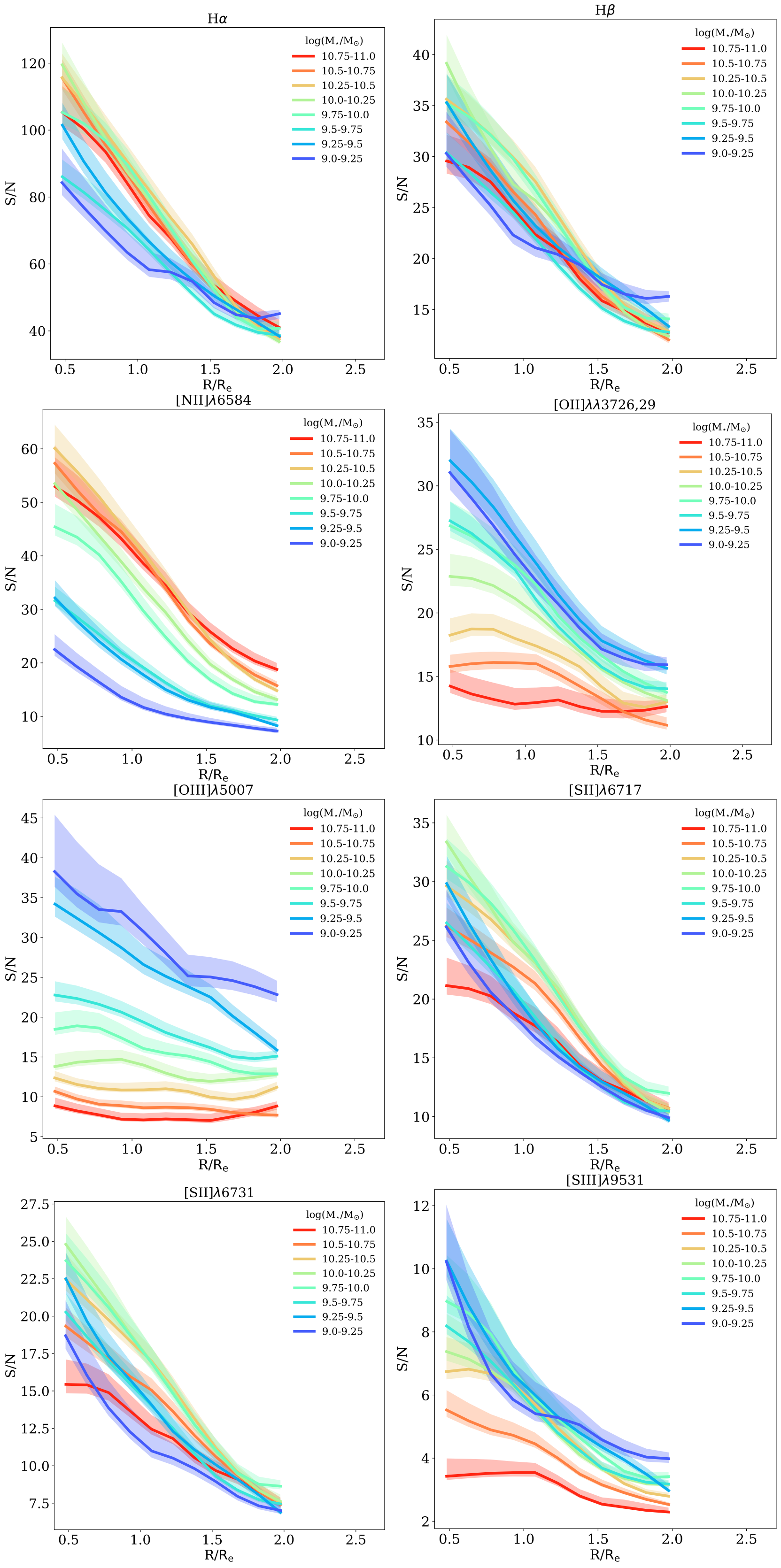

Figure 3.26: Radial distribution of the signal to noise of Hα, Hβ, [N II]λ6584, [O II], [O III]λ5007, [S II]λ6717, [S II]λ6731 and [S III]λ9532, in eight stellar mass $M_\star$ bins, as reported in the legend.

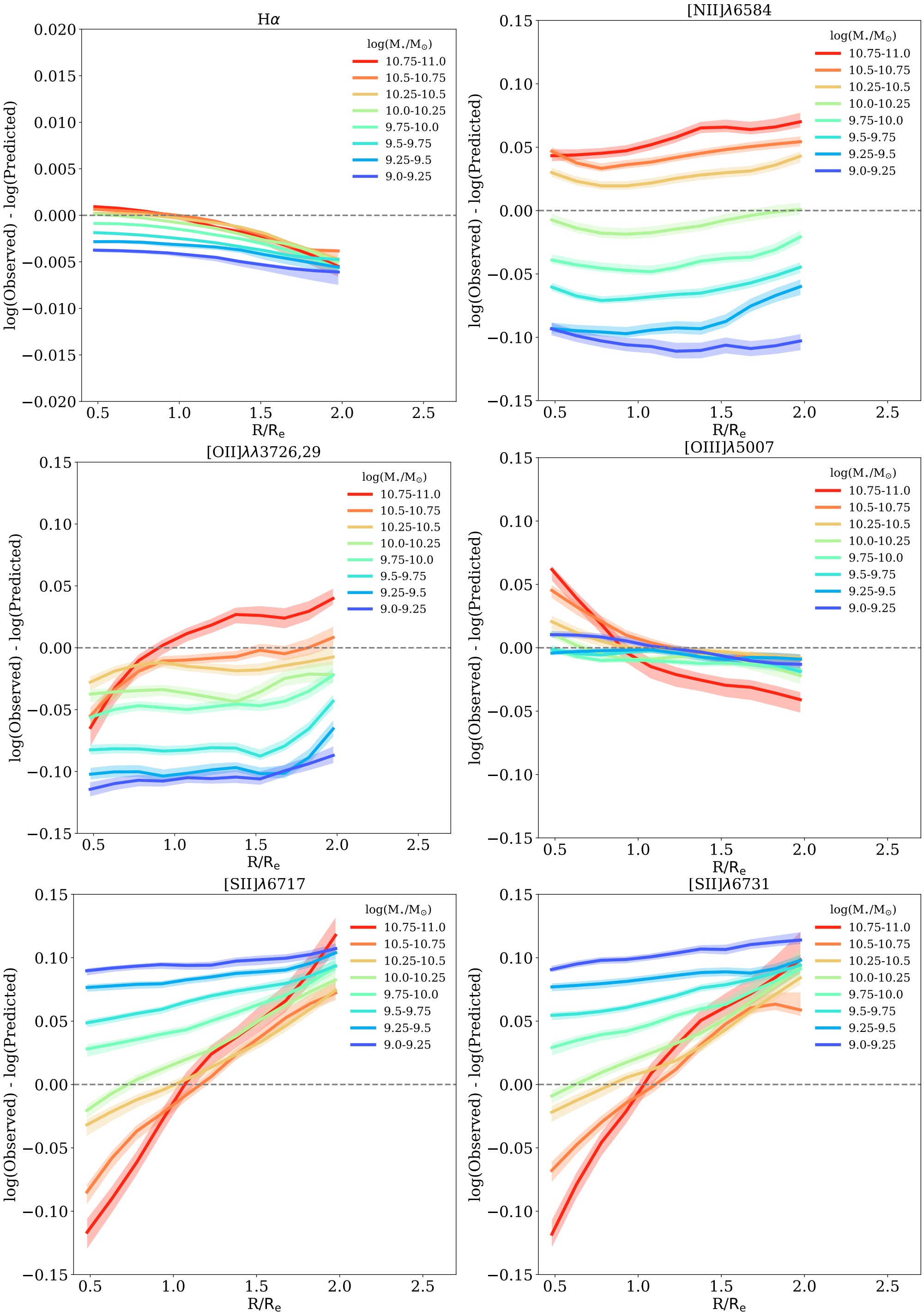

Figure 3.27: Radial distribution of the difference between the logarithm of the observed flux and that of the best-fit model (both normalised to Hβ) obtained with IZI and a Gaussian prior on the ionisation parameter, for all the emission lines taken into account, in eight stellar mass $M_\star$ bins, as reported in the legend. Since these radial distributions lie in the range [-0.1,0.1] dex, it means that they are all consistent within the intrinsic error taken into account for the models.

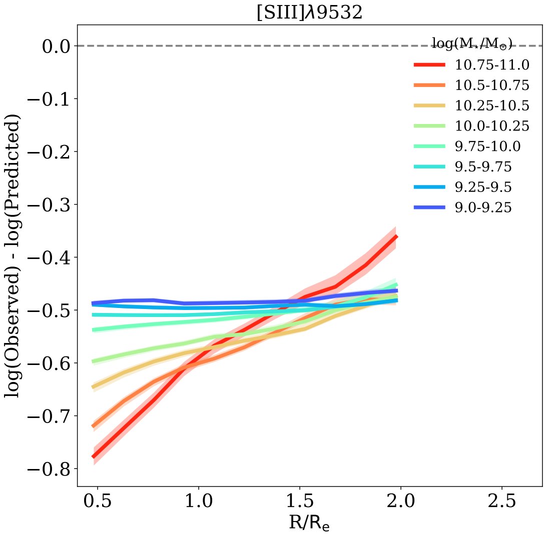

Figure 3.28: Radial distribution of the difference between the logarithm of the observed [S III]λ9532 flux and that of the best-fit model (both normalised to Hβ) predicted by IZI, in eight stellar mass $M_\star$ bins, as reported in the legend. This clearly shows that [S III]λ9532 is largely overestimated, with differences between observed and predicted fluxes up to 0.8 dex.

overestimated of 0.3 dex more with respect to the values in the outer regions ($R > 1$ R$_\mathrm{e}$).

CHAPTER 4

Investigating local galaxies ISM by exploiting CO excitation

Based on: (i) "CO excitation in the Seyfert galaxy NGC 34: stars, shock or AGN driven?", **M. Mingozzi***, L. Vallini, F. Pozzi, C. Vignali, A. Mignano, C. Gruppioni, M. Talia, A. Cimatti, G. Cresci, M. Massardi, 2018, MNRAS, Volume 474, Issue 3, p.3640-3648; (ii) "CO excitation in the Seyfert galaxy NGC 7130", F. Pozzi, L. Vallini, C. Vignali, M. Talia, C. Gruppioni,* **M. Mingozzi***, M. Massardi, P. Andreani, 2017, MNRAS, Volume 470, Issue 1, p.L64-L68.*

The previous chapters are focused on the warm, ionised gas component of the interstellar medium (ISM). However, molecular gas is another key component of the ISM, as it is the fuel of star formation (SF) and possibly of Active Galactic Nucleus (AGN) accretion.

The molecular gas mass in galaxies is dominated by molecular hydrogen, H_2. Given the lack of a permanent dipole moment, the lowest rotovibrational transitions of molecular hydrogen are forbidden and have high-excitation requirements ($T_{\rm ex} \approx 500$ K above the ground, significantly higher than kinetic temperatures in molecular clouds (MCs, $T_{\rm kin} \sim 15 - 100$ K). This is the reason why the molecular phase is generally traced through carbon monoxide (CO) rotational transitions (e.g., McKee & Ostriker 2007; Carilli & Walter 2013) being the CO the second most abundant molecule after H_2 in the Universe ($CO/H_2 \approx 1.5 \times 10^{-4}$ at solar metallicity Lee et al., 1996).

More importantly, the study of the so called CO Spectral Line Energy Distribution (CO SLED) – i.e. the CO line luminosity as a function of the CO upper rotational level – allows us to constrain the physical properties of the molecular gas, both at $z > 1$ (e.g., Weiss et al. 2007; Gallerani et al. 2014; Daddi et al. 2015), thanks to sub-millimeter facilities such as CARMA and IRAM-PdBI interferometers, and in local sources (e.g., Rosenberg et al. 2015; Mashian et al. 2015; Lu et al. 2017; Pereira-Santaella et al. 2014; Pozzi et al. 2017), with Herschel. In the last few years, the ALMA advent has represented a breakthrough making it possible to reach a spatial resolution of $50-100$ pc when targeting CO lines in the nearby Universe (e.g., Xu et al. 2014, 2015; Zhao et al.

2016.)

As explained in Sec. 1.3.2 (Chapter 1), the CO SLED shape is determined by (i) the gas density and (ii) the heating mechanism acting on the molecular gas. The heating agents can be either far-ultraviolet (FUV, $6 - 13.6$ eV) photons, X-ray photons, or shocks (e.g. Narayanan & Krumholz, 2014). Regions whose molecular physics and chemistry are dominated by FUV radiation, e.g. from OB stars, are referred to as *Photo-Dissociation Regions* (PDRs, Hollenbach & Tielens 1999), while those influenced by X-ray photons ($1 - 100$ keV), possibly produced by an AGN, are referred to as *X-ray-Dominated Regions* (XDRs, Maloney et al. 1999). Interstellar shock waves, instead, originate from the supersonic injection of mass into the ISM by stellar winds, supernovae, and/or young stellar objects, that compress and heat the gas, producing primarily H_2, CO, and H_2O line emission, and relatively weak dust continuum (Hollenbach et al., 1989). In PDRs, the CO emission saturates at a typical column densities of $\log(N_{\rm H}/{\rm cm}^{-2}) \approx 22$ (Hollenbach & Tielens, 1999) and the resulting CO SLED considerably drops and flattens at high-J transitions (van Dishoeck & Black, 1988). On the contrary, the smaller cross sections of X-ray photons allow them to penetrate deeper than FUV photons[1]. Because of that, the XDRs are characterised by column densities of warm molecular gas, where high-J CO can be efficiently excited. The resulting CO SLEDs are thus peaked at higher-J rotational transitions compared to those resulting from PDRs. The same holds true for shock-heated molecular gas. Shocks can heat the gas above $T \approx 100\,{\rm K}$, and at such high temperatures the high-J CO rotational energy levels become more populated and the resulting CO SLED peaked at high-J.

The goal of this chapter is to shed light on the "ambiguous" nature of the local galaxy NGC 34, exploiting the peculiarities of its CO SLED. NGC 34 has been either classified as a starburst galaxy, because of the lack of high-ionisation emission lines, such as the [Ne V] (12.3 μm and 24.3 μm) and the O IV (25.89 μm), in the infrared (IR) spectrum, and as a Seyfert 2 galaxy, owing to the optical spectrum properties and X-ray observations.

We aim at assessing whether and to what extent the CO emission is influenced by the radiation produced by the accretion onto the black hole. To do that we analyse the X-ray and CO emission, using mainly archival data from XMM-*Newton*, NuSTAR, ALMA, and Herschel. On the one hand, the X-ray data allow us to properly include the effect of AGN radiation in the modelling of the CO SLED, on the other hand, the CO emission, traced by ALMA in the central region of NGC 34 at high spatial resolution, is crucial to spatially constrain the region where the contribution of the AGN actually

---

[1] A 1 keV photon penetrates up to a typical column of $N_{\rm H} \simeq 2 \times 10^{22}$ cm^{-2}, whereas a 10 keV photon penetrates $N_{\rm H} \simeq 4 \times 10^{25}$ cm^{-2}, (Schleicher et al., 2010)

dominates.

4.1 Data

4.1.1 NGC 34: a nearby ambiguous object

NGC 34 is a local object ($z \simeq 0.0196$, D_L=85.7 Mpc, $2.2' \times 0.8'$, 1" $\sim$ 0.4 kpc), classified as a Luminous Infrared Galaxy (LIRG; $\log(L_{8-1000\,\mu\mathrm{m}}) \simeq 11.44\,\mathrm{L}_\odot$, Sanders et al. 2003).

Riffel et al. (2006) studied NGC 34 near-infrared (NIR; $0.8 - 2.4$ μm) spectrum, that appears to be dominated more by stellar absorption features rather than emission lines (e.g., [S III], typical of Seyfert 2 spectra), suggesting that this source is not a "genuine" AGN or that it has a buried nuclear activity at a level that is not observed at NIR wavelengths. Additional support to this conclusion comes from the lack of high-ionisation lines in the Spitzer-IRS spectrum, such as the [Ne V] (12.3 μm and 24.3 μm) and the O IV (25.89 μm), that are exclusively excited by AGN, and can be considered AGN spectral signatures (Tommasin et al., 2010). Consequently, Riffel et al. (2006) infer that NGC 34 is a starburst galaxy.

Mulchaey et al. (1996) analyse the optical emission lines of NGC 34, inferring that it is a rather weak emitter of [OIII]λ5007, when compared to other Seyfert galaxies in their sample, while it shows a strong Hα emission. Therefore, they conclude that the ionisation of the gas is not related to any Seyfert activity. Nevertheless, a later work by Brightman & Nandra (2011b) reports new optical emission line ratios, confirming the presence of a Seyfert 2 nucleus through optical diagnostic diagrams (BPT, Baldwin et al. 1981). Vardoulaki et al. (2015) confirmed the presence of an AGN, analysing the radio spectral index maps. Furthermore, NGC 34 appears to have an intrinsic X-ray luminosity of $\log(L_{2-10\,\mathrm{keV}}) \simeq 42\,\mathrm{erg\,s^{-1}}$ on the basis of XMM-*Newton* data (Brightman & Nandra, 2011a). Assuming the Ranalli relation (Ranalli et al., 2003), this large X-ray luminosity can be explained only by a $SFR > 100\,\mathrm{M}_\odot\,\mathrm{yr}^{-1}$, while NGC 34 SFR is $\simeq 24\,\mathrm{M}_\odot\,\mathrm{yr}^{-1}$ (Gruppioni et al., 2016). Another indication of the presence of an AGN has been reported by Gruppioni et al. (2016), who carried out a SED decomposition analysis, suggesting the presence of circumnuclear dust (i.e., dusty torus component) heated by a central AGN. Moreover, the mid-infrared (MIR; $5 - 20\,\mu$m) intrinsic luminosity corresponding to the torus appears to correlate with the X-ray luminosity in the 2–10 keV band, reinforcing the hypothesis of an AGN (Gandhi et al., 2009).

4.1.2 X-ray data

NGC 34 was observed by XMM-*Newton* on Dec. 22^{nd}, 2002. After cleaning the data to remove periods of high background, the cleaned exposure time was 9.87 ks in the pn camera and 17.12 ks and 16.75 ks in the MOS1 and MOS2 cameras, respectively. The source spectra were extracted from circular regions of radius 30" for the pn and 18" for the MOS cameras, centered on the optical position of the source; background spectra were extracted from larger regions, free of contaminating sources, in the same CCD as the source spectra. The number of net (i.e., background-subtracted) counts is 670 (pn), 280 (MOS1) and 240 (MOS2). Then the spectra from the two MOS cameras were summed using MATHPHA to increase the statistics in each spectral bin, along with the corresponding background and response matrices. pn (MOS1+2) spectra were binned to 20 (15) counts/bin to apply χ^2 statistics; in the following X-ray spectral analysis (carried out using XSPEC; Arnaud 1996), errors and upper limits are reported at the 90% confidence level for one parameter of interest (Avni, 1976).

NuSTAR observed NGC 34 on July 31^{st}, 2015, for an exposure time of 21.2 ks. Data were reprocessed and screened using standard settings and the NUPIPELINE task, and source and background spectra (plus the corresponding response matrices) were extracted using NUPRODUCTS. A circular extraction region of 45" radius was selected, while background spectra were extracted from a nearby circular region of the same size. The source net counts, ≈130 and ≈120 in the FPMA and FPMB cameras, respectively, were rebinned to 20 counts per bin. The source signal is detected up to ≈25 keV.

At first we verified that no large flux variability occurs between XMM-*Newton* and NuSTAR data, being well within a factor of two. Then the four datasets were fitted simultaneously with the same modelling. The advantage of using all datasets is to achieve a proper source modelling over a broad energy range. To this goal, we adopted a model consisting of an absorbed power-law, accounting for the continuum emission above a few keV, and a thermal plus scattering component below 2 keV. Due to the limited photon statistics, we fixed the power-law photon indices (of the nuclear and scattered components) to $\Gamma = 1.9$, as typically found in AGN and quasars (e.g., Piconcelli et al. 2005). For the thermal emission, likely related to the host galaxy, we used the MEKAL model, obtaining kT=0.7±0.1 keV. The obscuration towards the source is $N_{\rm H} = 5.2^{+1.3}_{-1.1} \times 10^{23}\,{\rm cm}^{-2}$, consistent with previous analyses of the XMM-*Newton* datasets (Guainazzi et al. 2005; Brightman & Nandra 2011a) and the recent one conducted on XMM-*Newton* and NuSTAR data by Ricci et al. (2017). About 4% of the nuclear emission is scattered at soft X-ray energies. An upper limit to the iron Kα emission line of 110 eV is derived. The best-fitting model and data−model residuals are reported in Fig. 4.1. The observed 2–10 keV flux is 3.2 $\times 10^{-13}$ erg cm^{-2} s^{-1}, while the intrinsic (i.e., corrected for the obscuration) rest-frame 2–10 keV and 1–100 keV luminosities are 1.3 $\times 10^{42}$ erg s^{-1} and 4.0 $\times 10^{42}$ erg s^{-1}, respectively. Given that, the AGN appears to contribute to a 10% to the bolometric luminosity of the galaxy.

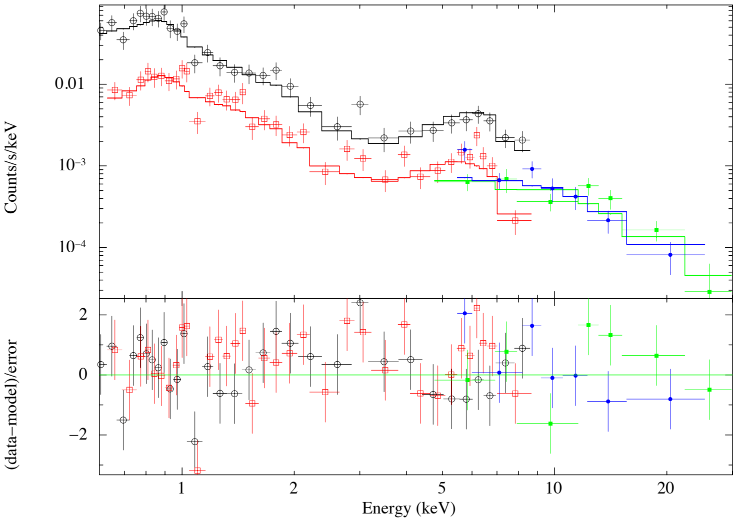

Figure 4.1: Top panel: XMM-*Newton* pn and MOS (black and red points, respectively) and NuSTAR FPMA and FPMB (green and blue points, respectively) spectral data and BF modelling (continuous lines); see text for details. Bottom panel: spectral residuals in units of σ.

4.1.3 ALMA data

NGC 34 nuclear region was observed with ALMA in Band 9 during the Early Science Cycle 0 in May and August 2012 (project 2011.0.00182.S, PI: Xu), targeting the CO(6–5) transition ($\nu_{\rm rest-frame} = 691.473$ GHz) and the 435 μm dust continuum. The observing time is split in five Execution Blocks (EBs) with 16 antennas, set up in an extended configuration, and in one EB with 27 antennas set up in both a compact and an extended configuration (the minimum baseline is 21 m, the maximum baseline is 402 m). Hence, at the observing band, the largest angular scale (LAS) recovered by ALMA is $\approx 4''$, corresponding to ~ 2 kpc at NGC 34 distance, while the spatial resolution of the observation is $\theta \simeq 0.2''$, corresponding to ~ 100 pc. The field of view for the used 12 m antennas is FOV $\approx 9''$. The medium precipitable water vapour of all the observing blocks is PWV $\simeq 0.38$ mm. The observation was performed in time division mode with a shallow velocity resolution of 6.8 km s^{-1}, with four spectral windows (SPWs) of ≈ 2 GHz, centered at the sky frequencies of 679.8, 678.0, 676.3 and 674.3 GHz, respectively. The on-source integration time is about 2.25 hr. The phase, bandpass and flux calibrators observed are 2348-165, 3C 454.3 and the asteroid Pallas, respectively, and are the same for all the EBs. The analysis of the data obtained with a standard pipeline was reported by Xu et al. (2014).

Cycle 0 data re-processing is strongly recommended, since, thanks to the new flux model libraries available (*Butler-JPL-Horizons 2012*), a more reliable flux calibration can be obtained (Butler, 2012)[2]. Therefore, we took the raw data from the archive, we generated new reduction scripts and we calibrated the data using CASA 4.5.2, correcting for antenna positions, atmosphere effects and electronics. Since these data are Band 9 observations, the calibrators are faint and the signal-to-noise ratio of the solutions is low, so that a phase solution over 60 s and a bandpass solution over 30 channels can be obtained. In addition, we put the signal-to-noise threshold equal to 1.5 (3 would be the recommended value) to find as many solutions as possible. Then, we applied the more reliable flux calibration, obtaining, for the calibrators, a $\approx 20\%$ higher flux density than the one reported in the archive.

We applied the self calibration, making the image of the emission by selecting only the channels where the emission line was detected, we built a model and we found phase solutions averaged on 600 s (i.e., approximately two scans). Then, we iterated again and we found phase and amplitude solutions, averaging 1200 s and combining scans. We produced the channel map of the CO(6–5) transition with a rms of $\approx 6.5\,\mathrm{mJy/beam}$, subtracting the continuum, binning into channels with a width of $\approx 34\ \mathrm{km s^{-1}}$, in order to increase the signal-to-noise ratio, and iteratively cleaning the dirty image, selecting a natural weighting scheme of the visibilities.

Fig. 4.2 shows the integrated emission of the CO(6–5) transition. Considering the emission within 3σ, contained in a diameter of $\theta \approx 1.2''(\approx 500$ pc), we obtain an integrated flux of $(707 \pm 106)\,\mathrm{Jy\,km\,s^{-1}}$ (i.e., $(1.63 \pm 0.24) \times 10^{-14}\,\mathrm{erg\,s^{-1}\,cm^{-2}}$) with a peak of $(213 \pm 32)\,\mathrm{Jy\,km\,s^{-1}}$. The rms of the image is ≈ 1.5 Jy/beam km $\mathrm{s^{-1}}$. The errors are totally dominated by the calibration error, that is the 15% of the total flux in Band 9 for Cycle 0 Data. Our integrated flux is $\approx 30\%$ lower than the one reported by Xu et al. (2014). The cause of this discrepancy is likely due to the different flux calibration and the use of the new version of the CASA software in our analysis.

---

[2] Butler (2012) contend that many of the models used to calculate the flux density of solar system bodies in the 2010 version were inaccurate with respect to the new ones of 2012, that use new brightness temperature models and a new flux calculation code that replaces the "Butler-JPL-Horizons 2010" standard used before.

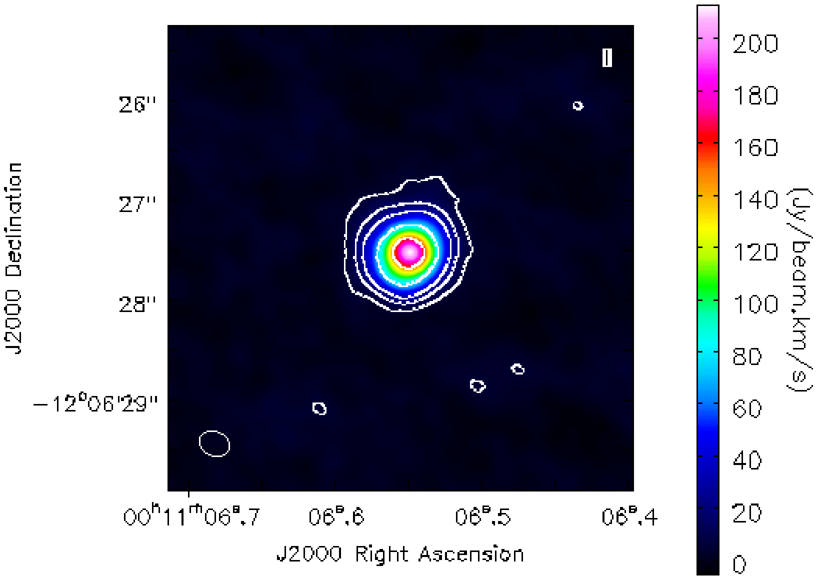

Figure 4.2: Integrated emission of the CO(6–5) line. The wedge on the right shows the color-scale of the map in Jy beam^{-1} km s^{-1}. The integrated flux density is (707 ± 106) Jy km s^{-1}. The contours at [3,10,20,50,100] are set in units of the rms noise level of the image, rms $\approx$ 1.5 Jy beam^{-1} km s^{-1}.

4.1.4 CO data

NGC 34 CO SLED is shown in Fig. 4.3, where the CO rotational transitions up to $J_{\rm up}$ = 13 are reported. The low-J transitions are ground-based observations. The CO(1–0) transition (blue square) was observed by CARMA, that covered a FOV $\approx 1.7'$, detecting a regularly rotating disk of molecular gas with a diameter of 2.1 kpc (Fernández et al., 2014). The CO(2–1) transition (yellow triangle) was observed by the Submillimeter Array (SMA) with a FOV $\approx 22''$(Ueda et al., 2014). By comparing the observed flux with the single-dish measurement made with the Swedish ESO Submillimeter Telescope (SEST), that covered a FOV $\approx 1'$ (Albrecht et al., 2007), we note that SMA recovered all the flux (Ueda et al., 2014). The observation of the CO(3–2) transition (purple pentagon) was conducted with the Submillimeter Telescope (SMT) with a FOV $\approx 22''$and the measure was corrected for subsequent comparison to Herschel CO lines (Kamenetzky et al., 2016). The CO(6–5) transition (red diamond) was observed by ALMA and re-calibrated through the procedure outlined in Sec. 4.1.3, while the transitions from $J_{\rm up} = 4$ to $J_{\rm up} = 13$ (green circles) are Herschel/SPIRE observations, sparsely covering a FOV $\approx$ 2' (Rosenberg et al., 2015). NGC 34 appears point-like in the Herschel/SPIRE photometric bands (from 250 to 500 μm), characterised by a beam size of $17'' - 42''$($\approx 7-20$ kpc). Assuming that the dust (sampled by the SPIRE photometric observations) and the gas (sampled by SPIRE/FTS observations) are almost co-spatial, it can be argued that all the CO fluxes correspond to the integrated emission of the galaxy. By comparing the two different data sets for the CO(6–5) transition, we find a good agreement within 1σ. This allows us to be confident that the ALMA observation has recovered all the flux, which means that no flux related to the CO(6–5) emission comes from a region larger than the one observed with ALMA. Moreover, since ALMA LAS is comparable in size to the CO(1–0) disk (LAS $\approx$ 2 kpc, see Sec. 4.1.3), we can assume that no flux has been lost on the largest scales. Hence, all the data taken from the literature map the source entirely and are thus comparable in size.

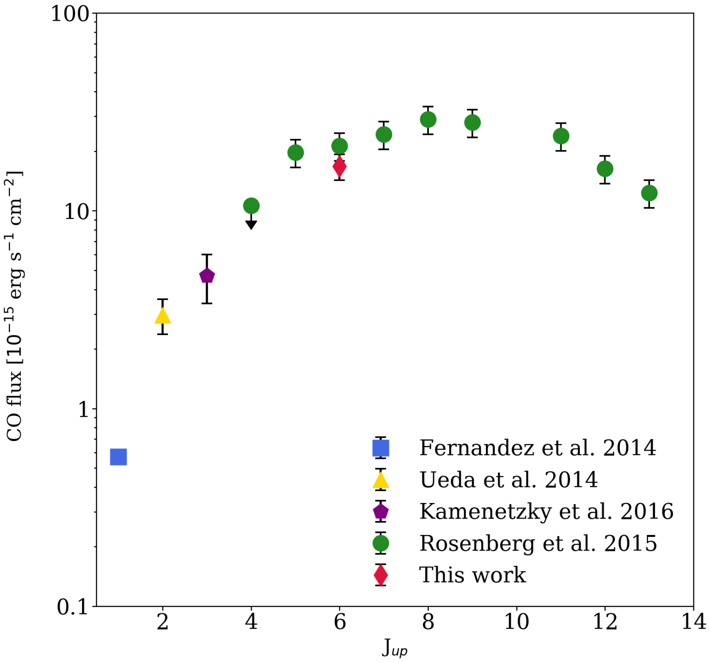

Figure 4.3: Observed CO flux of NGC 34 as a function of the upper J rotational level. The blue square, yellow triangle and purple pentagon represent the ground-based observations (Fernández et al. 2014; Ueda et al. 2014; Kamenetzky et al. 2016), the red diamond the CO(6–5) transition observed with ALMA and the green circles the Herschel/SPIRE FTS data from $J_{\rm up} = 4$ to $J_{\rm up} = 13$ (Rosenberg et al., 2015).

4.2 Interpreting the CO SLED of NGC 34

To fit and interpret the CO SLED of NGC 34, we have modelled the effect of the FUV and X-ray radiation on the molecular gas with the version c13.03 of CLOUDY (Ferland et al., 2013), and the effect of the mechanical heating by adopting the shock models of Flower & Pineau des Forêts (2015). In what follows we separately discuss their main features.

4.2.1 PDR and XDR modelling

We run a grid of CLOUDY PDR and XDR models that span ranges in density (n), distance between the source and the illuminated slab of the cloud (d)[3], and column density ($N_{\rm H}$). In these models, the external radiation field impinges the illuminated face of the cloud, that is assumed to be a 1-D gas slab with a constant density, at a fixed distance from the central source (i.e., the collective light of stars in PDRs and an X-ray point-like source in XDRs).

For the PDR models the SED of the stellar component is obtained using the stellar population synthesis code Starburst99, assuming a Salpeter Initial Mass Function in the range 1-100 $M_{\odot}$, Lejeune-Schmutz stellar atmospheres (Schmutz et al. 1992b, Lejeune et al. 1997b), solar metallicity and a continuous SF mode, that is normalised to NGC 34 SFR ($\simeq 24\,{\rm M_{\odot}\,yr^{-1}}$, Gruppioni et al. 2016). We assume a Milky Way gas-to-dust ratio of ≈ 160 (e.g., Zubko et al. 2004) for the gas slab. We run 21 PDR models, varying n in the range $\log({\rm n/cm^{-3}}) = [2 - 4.5]$ and the distance of the gas slab from the radiation source in the range $d = [100 - 500]$ pc. These values of distances translate into a flux in the FUV band normalised to that observed in the solar neighbourhood ($1.6 \times 10^{-3}\,{\rm erg\,s^{-1}\,cm^{-2}}$, Habing 1968), in the range $[10^4 - 10^3]$ ${\rm G_0}$, respectively. The code computes the radiative transfer through the slab spanning a hydrogen column density range $\log(N_{\rm H}/{\rm cm^{-2}}) = [19 - 23]$. The densities and column densities are chosen to cover the typical values in giant MCs (McKee & Ostriker, 1977). We constrain the range of distances to be larger than the ALMA minimum recoverable scale (≈ 100 pc, see Sec. 4.1.3).

In the XDR models, the AGN radiation field is modelled following the default `table AGN` CLOUDY command (Korista et al., 1997), and its spectrum is normalised so that the 1-100 keV X-ray luminosity matches the observed one $L_{1-100\,{\rm keV}} \simeq 4 \times 10^{42}$

---

[3] A larger distance from the source implies a lower incident radiation field, since the flux is proportional to d^{-2}. Hence, taking into account different values of distance means to vary the incident radiation field.

erg s^{-1} (see Sec. 4.1.2). We run 9 models, adopting a slightly higher range of densities $\log(n/cm^{-3}) = [3.5 - 5.5]$ and the same values of column densities and distances, that translate into an X-ray flux at the cloud surface $F_X \simeq 2.2 - 0.2$ erg cm^{-2} s^{-1}.

4.2.2 Shock modelling

The Flower & Pineau des Forêts (2015) shock code simulates shocks in the ISM as a function of the physical conditions in the ambient gas, providing the CO line intensities (i.e. fluxes per unit of the emitting area where the shock acts, A). Shock waves in the ISM can be distinguished in "jump" (J) or "continuous" (C) types, according to the strength of the magnetic field and the ionisation degree of the medium in which they propagate (see e.g. Fig. 1 in Draine, 1980). In J-shocks the variation in the fluid properties (density, temperature, and velocity) occurs sharply and can be approximated as a discontinuity. In C-shock models, instead, the influence of the magnetic field on the ionised gas causes the ions to diffuse upstream of the shock front, thus eliminating the discontinuities in the fluid variables (Draine & McKee, 1993; Pon et al., 2012). These differences cause the J-shock temperature ($T \approx 10^4$ K) to be far higher than the one characterising C-shock ($T \approx 10^3$ K), inducing the dissociation of H_2 molecules (Flower & Pineau Des Forêts, 2010). This is the reason why C-type shocks are preferentially invoked to affect the CO emission in molecular clouds (e.g., Smith & Mac Low 1997, Hailey-Dunsheath et al. 2012).

In this chapter, we compare the observed CO SLED with two grids of C- and J-shock models, respectively. We let the shock velocity[4] vary in the range $v_{sh} = [10-40]$ km s^{-1}, and the pre-shock density in $\log(n/cm^{-3}) = [3-6]$. The transverse magnetic field scales with the density through the relation $B \sim bn^{1/2}$, where $b = 1$ for C-shocks, and $b = 0.1$ for J-shocks (Flower & Pineau des Forêts, 2015).

4.2.3 CO SLED fitting

Despite the good spatial resolution of ALMA (see Sec. 4.1.3), individual clouds in extragalactic sources cannot be resolved. Each resolution element in ALMA observations measures the combined emission from a large ensemble of molecular clouds. Moreover, as pointed out at the beginning of this Chapter, low-J CO transitions are generally excited in the cold diffuse component of molecular gas while mid- and high-J transitions are associated to a warmer and denser component. The observed CO SLED of NGC 34 can

---

[4] Shock velocities greater than 50 km s^{-1} are known to be fast enough to destroy molecules (Hollenbach et al., 1989).

then be reproduced by summing a low-density PDR component (e.g., $\log(n/\mathrm{cm}^{-3}) \simeq 2 - 2.5$) that accounts for the low-J transitions, to a second component for the high-J transitions. Given the spatial constraints on the CO(1–0) emission (see Sec. 4.1.4), the low-density PDR must account for the emission of MCs located within $d < 1$ kpc from the centre of the galaxy. In addition, we fixed the gas column density of the low-density PDR to $\log(N_{\mathrm{H}}/\mathrm{cm}^{-2}) \simeq 21.8$, that is slightly above that ($\log(N_{\mathrm{H}}/\mathrm{cm}^{-2}) \simeq 21.6$) required to have CO molecules (van Dishoeck & Black, 1988). The CO(6–5) emission line allows to constrain the high-density component in a region of $d < 250$ pc from the centre. We have adopted three different approaches to model this second component, that can be either produced by:

- a high-density PDR (PDR1+PDR2 model);
- the shock heated gas (PDR+shock model);
- an XDR (PDR+XDR model).

The PDR1+PDR2 and the PDR+shock models are shown in Fig. 4.4, in the upper and lower panels, respectively. The black solid line represents the sum of the components, while the 1σ confidence levels on the normalisations have been obtained by marginalising over the other parameters and considering a $\Delta\chi^2 = 2.3$ (Lampton et al., 1976). The PDR+XDR model is shown in Fig. 4.5. All the parameters taken into account and their BF values are summarised in Tab. 4.1.

The PDR1+PDR2 best-fit (BF) model is characterised by a value of the reduced-χ^2 ($\tilde{\chi}^2$), defined as the ratio between the computed χ^2 and the related degrees of freedom, of $\tilde{\chi}^2_{BF} = 3.3$. Such a high value made us infer that the high-density PDR cannot reproduce completely the high-J transitions.

The PDR+C-shock BF model has instead a slightly lower $\tilde{\chi}^2_{BF}$ (= 2.0). However, the best-fit for the C-shock-heated component, accounting for the high-J CO emission, returns an emitting area (A=785^2 pc^2) that is 10x larger than the CO(6-5) emitting region[5].

The PDR+XDR BF has the lowest $\tilde{\chi}^2_{BF}$ among all the combinations tested in this chapter ($\tilde{\chi}^2_{BF} = 1.6$), therefore it is our fiducial model. It is composed by a "cold" and diffuse PDR ($T \simeq 30$ K, $\log(\mathrm{n}/\mathrm{cm}^{-3}) \simeq 2.5$), that accounts for the CO(1–0) and the CO(2–1) transitions, produced by clouds located at a typical distance $d \simeq 500$ pc from the source of the FUV radiation (i.e., OB stars), and by a "warm" and dense

---

[5] Note that in case of a J-shock the emitting area A required to fit the data would be 1000x larger than the CO(6-5) emitting region. That is why we decided not to show the PDR+J-shock BF model.

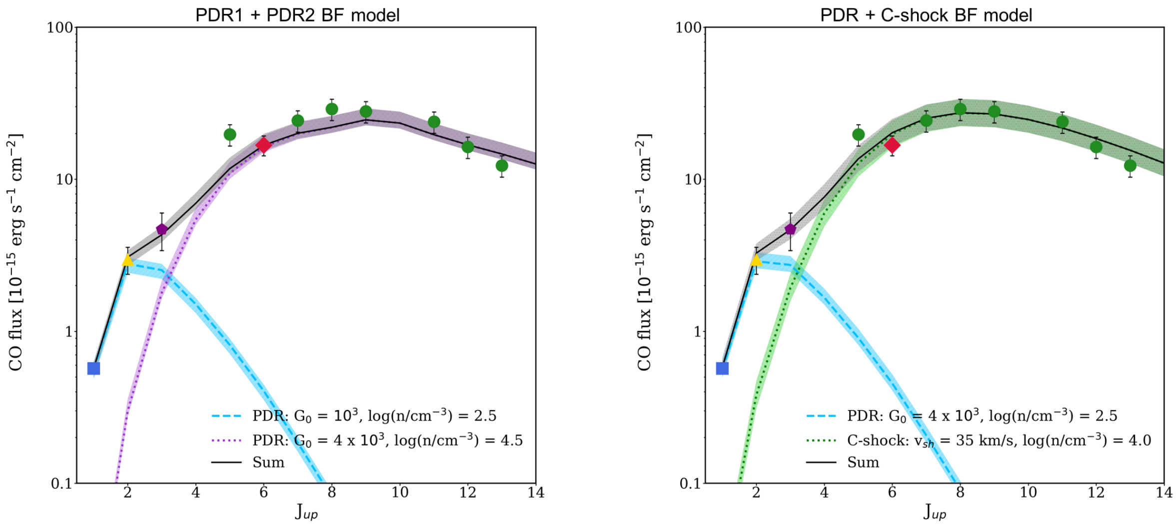

Figure 4.4: Top panel: PDR1+PDR2 BF model, overplotted to the observed data. The light-blue dashed line and the purple dotted line represent the low-density and high-density PDR, respectively. Low panel: PDR+C-shock BF model, overplotted to the observed data. The light-blue dashed line and the green dotted line indicate the low-density PDR and the C-shock component, respectively. In these figures, the black solid line indicates the sum of the two components and the shaded areas indicate the $\pm 1\sigma$ uncertainty range on the normalisation of each component.

XDR ($T \simeq 65$ K, $\log(\mathrm{n/cm^{-3}}) \simeq 4.5$), composed by clouds located at $d \simeq 100$ pc from the central X-ray source. In this case, we fixed the XDR column density to a typical value of $\log(N_{\mathrm{H}}/\mathrm{cm^{-2}}) \simeq 23.0$, since X-rays can penetrate deeper into the molecular gas (e.g., Meijerink & Spaans 2005). The radiation penetrates up to a depth $l \approx 5.0$ pc for the PDR, and up to $l \approx 0.3$ pc, for the XDR. These values are in line with the typical environment sizes of giant MCs, and clumps and cores, respectively, as reported by McKee & Ostriker (2007). From our fiducial modelling, we estimate a total mass $\mathrm{M_{gas}} \simeq 3.1 \times 10^9$ $\mathrm{M_\odot}$ (typical value of LIRGs, e.g., Papadopoulos 2010), that appears to be completely dominated by the low-density component that accounts for $\mathrm{M} = (2.9^{+0.9}_{-0.8}) \times 10^9$ $\mathrm{M_\odot}$, whereas the warm component contribution is $\mathrm{M} = (2.3^{+0.4}_{-0.5}) \times 10^8$ $\mathrm{M_\odot}$. This value is consistent with the total molecular mass found by Fernández et al. (2014), who estimated $\mathrm{M_{gas}} = (2.1 \pm 0.2) \times 10^9$ $\mathrm{M_\odot}$, considering the CO(1–0) luminosity and the standard conversion factor for starburst systems $\alpha_{\mathrm{CO}} \simeq 0.8\,\mathrm{M_\odot/(K\,km\,s^{-1}\,pc^2)}$ (Solomon et al., 1997). From our estimate of the total mass, we infer that in NGC 34 $\alpha_{\mathrm{CO}} \simeq 1.1\,\mathrm{M_\odot/(K\,km\,s^{-1}\,pc^2)}$. This value is consistent with what reported by Bolatto et al. (2013) concerning LIRGs.

To complete our analysis, we also explored the possibility of a three-component

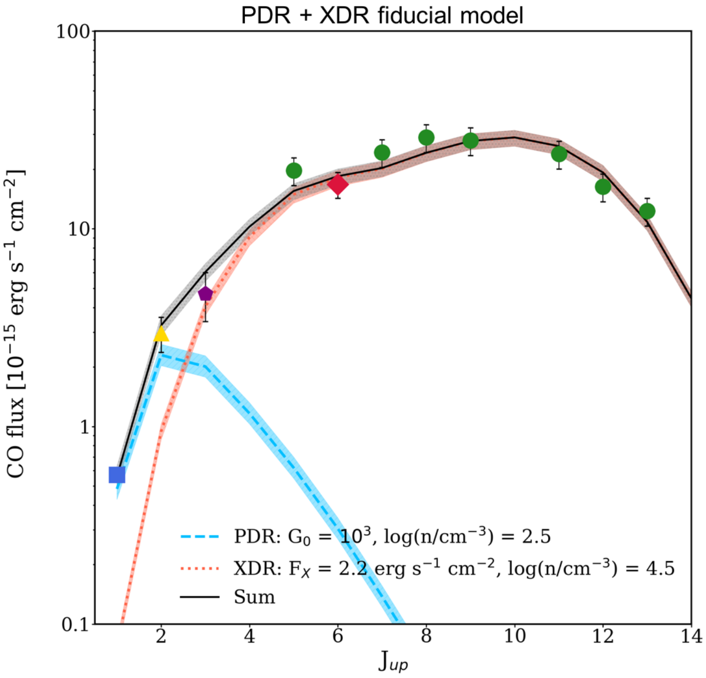

Figure 4.5: Fiducial model (PDR+XDR), overplotted to the observed data. The light-blue dashed line and the red dotted line represent the low-density PDR and the high-density XDR, respectively. The black solid line indicates the sum of the two components and the shaded areas indicate the $\pm 1\sigma$ uncertainty range on the normalisation of each component.

model accounting for the PDR, XDR, and shock heating contribution. We fixed the column densities of the PDR and the XDR to $\log(N_{\rm H}/{\rm cm}^{-2}) = 21.8$ and $\log(N_{\rm H}/{\rm cm}^{-2}) = 23.0$, respectively, and the shock-related emitting area to the CO(6–5) emission size ($\sim 250^2$ pc^2). The BF model has a $\tilde{\chi}^2_{BF} = 2.4$ and is shown in Fig. 4.6, while its parameters are reported in Tab. 4.2. We compare this new configuration with our fiducial PDR+XDR model, taking advantage of the Fisher-test, as presented by Bevington & Robinson (2003). We find a value of $f = 0.66$ that corresponds to a probability $P(F \leq f) = 70\%$, which means that the addition of a third component brings a negligible improvement in the CO SLED fit. This does not mean that shocks are completely absent within the galaxy, but that they do not play a significant role in exciting the high-J CO transitions, more likely powered by the central AGN.

Table 4.1: PDR1+PDR2 and PDR+C-shock BF models, and PDR+XDR fiducial model parameters. For PDRs and XDRs, the distance from the source, the density and the column density values are reported. Density and column density values are given in logarithm. For C-shocks, the shock velocity, the pre-shock density and the shock-related emitting area are reported. The * means that the value was fixed in the chi-square analysis. Finally, the χ^2 and degrees of freedom (dof) values are indicated.

Best-fit	d [pc]	n [cm^{-3}]	N [cm^{-2}]
PDR1	500	2.5	21.8*
PDR2	250	4.5	21.7
χ^2/dof		13.2/4	
Best-fit	d [pc]	n [cm^{-3}]	N [cm^{-2}]
PDR	500	2.5	21.8*
	v$_{sh}$ [km s^{-1}]	n [cm^{-3}]	A [pc^2]
C-shock	35	4.0	(785)^2
χ^2/dof		9.9/5	
Best-fit	d [pc]	n [cm^{-3}]	N [cm^{-2}]
PDR	500	2.5	21.8*
XDR	100	4.5	23.0*
χ^2/dof		7.8/5	

Table 4.2: BF model (PDR+XDR+C-shock) parameters. For PDRs and XDRs, the values reported are the distance from the source, the density and the column density, respectively. Density and column density values are given in logarithm. For C-shocks, the shock velocity, the pre-shock density and the shock-related emitting area are reported. The * means that the value was fixed in the chi-square analysis. Finally, the χ^2 and degrees of freedom (dof) value is indicated.

Best-fit	d [pc]	n [cm^{-3}]	N [cm^{-2}]
PDR	500	2.5	21.8*
XDR	100	3.5	23.0*
	v$_{sh}$ [km s^{-1}]	n [cm^{-3}]	A [pc^2]
C-SHOCK	15	5.0	(250)^{2*}
χ^2/dof		7.1/3	

4.2.4 Discussion and comparison with previous works

The CO SLED of NGC 34 has been extensively studied by others authors (e.g., Rosenberg et al. 2015; Pereira-Santaella et al. 2014). Rosenberg et al. (2015) analysed a

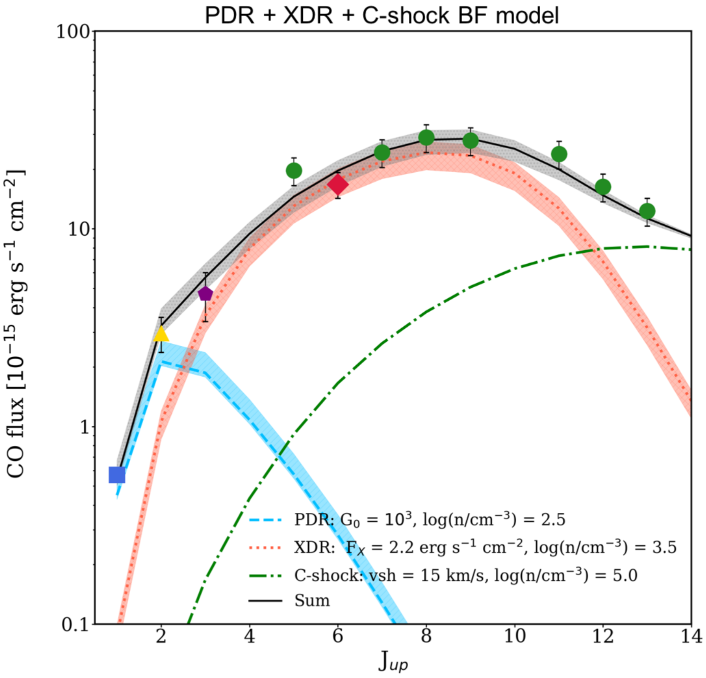

Figure 4.6: PDR+XDR+C-shock BF model overplotted to the observed data. The light-blue dashed line and the red dotted one indicate the low-density PDR and the XDR, respectively, whereas the green dotted-dashed line represents the C-shock. The solid black line indicates the sum of the three components and the shaded areas indicate the $\pm1\sigma$ uncertainty range on the normalisation of each component.

sample of LIRGs, including NGC 34, suggesting a qualitative separation on the basis of the shape of the CO ladder, the CO(1–0) linewidth and the AGN contribution, trying to indicate which mechanisms are responsible for gas heating. They identify NGC 34 as a galaxy with a very flat CO ladder beyond the CO(7-6) transition, which indicates a significant emission by warm and dense molecular gas, that is due to another heating mechanism besides UV heating. This galaxy appears to have an inclination corrected CO(1–0) linewidth of $\simeq$ 600 km/s and a low AGN contribution of the bolometric luminosity ($\simeq$ 30%), and thus they infer that the molecular gas in NGC 34 is experiencing shock excitation.

Pereira-Santaella et al. (2014) have presented a CO emission modelling for NGC 34, using the non-equilibrium radiative transfer code RADEX (van der Tak et al., 2007), along with CLOUDY c13.02 PDR and shock models. They infer that a combination of both PDR and shock models is needed to reproduce the observed CO SLED in NGC 34. They also contend that, although X-ray heating can play a role in AGN, its contribution in LIRGs with high SFR and IR luminosity is negligible in the integrated spectra of the galaxy.

Our work, on the contrary, suggests that X-rays are important in the CO excitation in NGC 34, even though we do not completely exclude the contribution of shock heating. In Sec. 4.2.3, we show that, in order to reproduce the high-J CO emission only with shock models, we need a shock-emitting area far greater than the size of the CO(6–5) area observed with ALMA. This points towards a scenario in which X-ray heating of high-density gas is favourite against shocks to be the primary source of excitation of high-J CO lines. Even though it can be rather difficult to distinguish among shock and XDR heating, Meijerink et al. (2013) and Gallerani et al. (2014) suggest that the CO-to-IR continuum ratio ($L_{\rm CO}/L_{\rm IR}$) can be a key diagnostic for the presence of shocks. Shocks only heat the gas without affecting the temperature of dust grains, that are the primary source of the IR emission (Hollenbach et al., 1989; Meijerink et al., 2013) and thus produce high values ($L_{\rm CO}/L_{\rm IR} > 10^{-4}$) for the CO-to-IR continuum ratio. NGC 34 has an observed CO-to-IR continuum ratio of $L_{\rm CO}/L_{\rm IR} \simeq 2.7 \times 10^{-5}$, that is almost a factor 4 lower than the threshold. This supports our conclusion that even though shocks are expected to be frequent in the highly supersonic turbulent molecular gas found in LIRGs, they are probably not dominant in the powering of high-J transitions in the observed CO SLED of NGC 34. In this scenario, the large linewidth of the CO(1–0) would not be indicative of shocks, but probably traces the rotation of the 2.1 kpc disk resolved by Fernández et al. (2014). We stress that our result is not in contradiction with the relatively low fraction ($L_{\rm X}/L_{\rm bol} \sim 10$ %) of NGC 34, as in our XDR modelling we have properly scaled our AGN radiation to reproduce the X-ray luminosity of the galaxy.

We drew similar conclusions in Pozzi et al. (2017) for NGC 7130, a nearby "ambiguous" LIRG similar to NGC 34, modelling the observed CO SLED with CLOUDY PDR and XDR models, and finding that the higher rotational ladder requires X-ray heating by the AGN as a source of excitation (Fig. 4.7). In the local Universe, a modelling that requires an XDR component to explain the high-J transitions has been proposed also by van der Werf et al. (2010) for the nearby ULIRG Mrk 231. Both NGC 7130 and Mrk 231 are obscured objects with an intrinsic X-ray luminosity of $\sim 10^{43}$ erg s^{-1}, and thus NGC 34, characterised by $L_{2-10\,{\rm keV}} \sim 10^{42}$ erg s^{-1}, would extend the importance of an XDR component to galaxies with a lower X-ray luminosity.

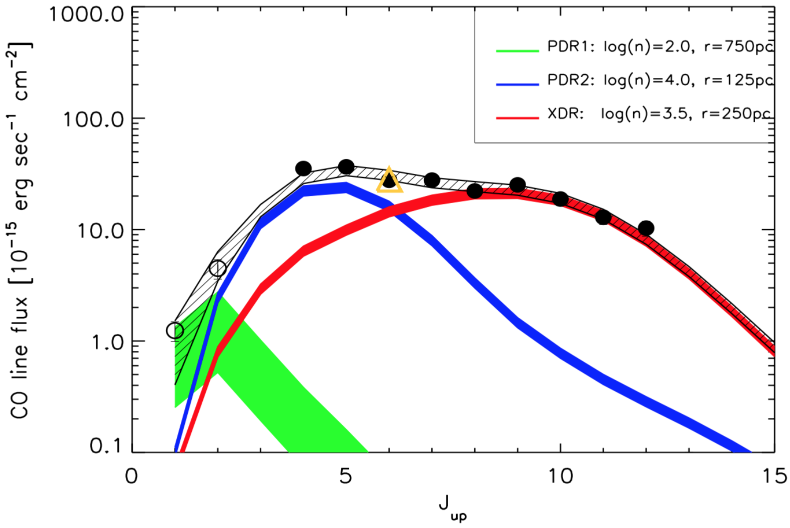

Figure 4.7: Observed CO SLED of NGC 7130 and best-fit model over-plotted. The low-J transition (open circles) are from the SEST telescope, while the mid/high-J transition levels (filled circles) are from Herschel SPIRE/FTS observations. The CO(6–5) ALMA data is highlighted as a yellow triangle. The green, blue and red lines correspond to the PDRs+XDR model components, whose parameters are reported in the legend. The black line represents the sum of the three components and the shaded areas indicate the $\pm 1\sigma$ uncertainty range on the normalisation of each component. This figure is taken from Pozzi et al. (2017).

4.3 Conclusions

In this chapter, we analysed archival XMM-*Newton*, NuSTAR, ALMA and Herschel data and investigated the molecular CO emission as a function of the rotational level (CO SLED), in order to probe the physical properties of the gas, such as density, temperature and the main source that causes the emission (SF, AGN or shocks) in the Seyfert 2 and LIRG galaxy NGC 34, comparing PDR, XDR and shock models with the observations. The main steps of our work and our main conclusions can be summarised as follows.

- The same model has been assumed simultaneously for XMM-*Newton* and NuSTAR data over a broad energy range, fixing the power-law photon indices to $\Gamma = 1.9$. We find an obscuration of $N_{\rm H} = 5.2^{+1.3}_{-1.1} \times 10^{23}$ cm^{-2}, an observed 2–10 keV flux of 3.2×10^{-13} erg cm^{-2} s^{-1} and an intrinsic (i.e., corrected for the obscuration) rest-frame 2–10 keV and 1–100 keV luminosities of 1.3×10^{42} erg s^{-1} and 4.0×10^{42} erg s^{-1}, respectively. The 1–100 keV luminosity is used to run CLOUDY XDR models.

- ALMA Cycle 0 data of the CO(6–5) line emission have been analysed starting from the raw data available in the archive. The CO(6–5) integrated flux results to be $(707 \pm 106)\,\mathrm{Jy\,km\,s^{-1}}$ with a peak of $(213 \pm 32)\,\mathrm{Jy\,km\,s^{-1}}$. The emission comes from a region with a diameter of $\theta \approx 1.2''$, that corresponds to a physical scale of ≈ 500 pc.

- We infer that a PDR1+PDR2 or a PDR+shock models are unlikely to reproduce the observed CO SLED. The former is discarded because of the high value of the $\tilde{\chi}^2$, while the latter has a BF value of the shock-emitting area that appears to be at least 10x higher than the region associated to the CO(6–5) emission, while shocks are expected to account for the high-J transitions.
- The observed CO SLED of NGC 34 can be explained by a cold and diffuse PDR ($T \simeq 30$ K, $\log(n/\mathrm{cm}^{-3}) \simeq 2.5$, $\mathrm{G}_0 = 10^3$), that accounts for the low-J transitions and a warmer and denser XDR ($T \simeq 65$ K, $\log(n/\mathrm{cm}^{-3}) \simeq 4.5$, $\mathrm{F}_X \simeq 2.2$ $\mathrm{erg\,cm^{-2}\,s^{-1}}$), necessary to explain the high-J transitions. The existence of a warm XDR component is supported by the χ^2-square analysis and by all the pieces of evidence of a possible AGN in the central region of NGC 34 discussed in Sec. 4.1.1. We conclude that the AGN contribution is significant in heating the molecular gas in NGC 34.
- The estimated molecular gas mass is $\mathrm{M_{gas}} \simeq 3.1 \times 10^9\ \mathrm{M_\odot}$. We note that the diffuse component contribution to the total mass is dominant compared to the warmer component (one order of magnitude lower). From our total mass estimate, we infer an α_{CO} of $1.1\,\mathrm{M_\odot/(K\,km\,s^{-1}\,pc^2)}$ for NGC 34.
- According to the F-test analysis, a three component model composed by a PDR, a XDR and a C-shock is not significantly improved with respect to our fiducial model (PDR+XDR).

Our results shed light on the great potential of combining self-consistent multi-band and multi-resolution data in order to assess the importance of AGN and SF activity, and mechanical heating produced by shocks for the physics of molecular gas. Papadopoulos et al. (2012), Imanishi et al. (2016) proposed that, in addition to CO rotational lines, a combination of low- to mid-J rotational lines of heavy rotor molecules with high critical densities, such as $\mathrm{HCO^+}$, HCN, HNC and CN, can be used to probe the large range of physical properties within MCs ($\mathrm{T_{kin}} \sim 15 - 100\,\mathrm{K}$, $\mathrm{n(H_2)} \sim 10^2 - 10^6\,\mathrm{cm^{-3}}$, e.g. McKee & Ostriker 2007). For instance, $\mathrm{HCO^+}$ lines appears to be stronger in XDRs than in PDRs by a factor of at least three, while CN/HCN ratio is far higher in PDRs than in XDRs, where it is expected to be $\sim 5 - 10$ (Meijerink et al., 2007).

Chapter 5

Concluding remarks

This Thesis focuses on the study of interstellar medium (ISM) properties and feedback mechanisms in a wide variety of galaxy types, ranging from ellipticals to spiral galaxies and dwarfs – some dominated by active galactic nuclei (AGN) activity, and other by star formation (SF) – and in different conditions within a galaxy, through the use of Integral Field Spectroscopy (IFS). In the following, I summarise the main projects carried out during these three years of research activity, with a highlight on future perspectives.

ISM properties in the nuclear region of AGN hosts and in their outflows

Galaxy-scale outflows driven by AGN activity are thought to be so powerful to sweep away most of the gas of the host galaxy, providing a mechanism for the central black hole (BH) to possibly regulate SF activity. This mechanism, the so-called negative feedback, could potentially explain the relation between the BH mass and the galaxy bulge properties (e.g. Silk & Rees 1998; Fabian 2012). Recently, models and observations have revealed that outflows and jets can also have a positive feedback effect, triggering SF in the galaxy disk and also within the outflowing gas itself (e.g. Silk 2013; Cresci et al. 2015b; Maiolino et al. 2017). Outflows are now routinely detected in luminous active galaxies on different physical scales and in different gas phases (e.g., ionised, atomic and molecular gas; Cresci et al. 2015b; Concas et al. 2019; Cicone et al. 2014), even though understanding their role in galaxy evolution is a challenging task. Indeed, further detailed investigations of outflow properties and how they are related to SF are required.

A poor or absent spatial resolution in outflow observations introduces large uncertainties in the estimate of outflow properties or forces to directly make assumptions on some of outflow physical quantities. Instruments such as the Multi Unit Spectroscopic Explorer (MUSE) at the Very Large Telescope (VLT) provide the unprecedented combination of spatial and spectral coverage needed for this kind of studies. Nearby galaxies do not host outflows as powerful as those observed in quasars around $z \sim 2$, but, thanks to their vicinity, are ideal laboratories to explore in high detail outflow properties, their formation and acceleration mechanisms, as well as the effects of SF and AGN activities on host galaxies.

In Chapter 2, I presented a sample of nine local Seyfert galaxies: the Measuring AGN Under MUSE Microscope (MAGNUM) survey (P.I. Marconi; see e.g. Cresci et al. 2015b; Venturi et al. 2017, 2018; Mingozzi et al. 2019, Venturi Ph.D. Thesis, Venturi et al. in preparation). Our MAGNUM survey aims at observing nearby galaxies hosting an AGN to investigate the physical conditions of the narrow line region (NLR), the interplay between nuclear activity and SF, and the effects and acceleration mechanisms of outflows. Specifically, I performed the data analysis, from stellar continuum subtraction to emission line fit with multiple Gaussians in order to reproduce the asymmetric line profiles. Then, I created spatially and kinematically resolved maps, by dividing the emission lines in velocity bins, associating the core of the lines (centred on the stellar velocity in each spaxel) to the disk, and the redshifted and the blueshifted wings to the outflow. This innovative approach, made possible by the unprecedented combination of spatial and spectral coverage of MUSE, gave us new insights on the outflow properties and structure. In general, the main source of excitation, density, level of ionisation and dust extinction of the ISM can be explored for both the gas in the host galaxy and in the outflow, down to scales of $\sim 20-240$ pc for distances of $\sim 4-50$ Mpc, respectively, using selected line ratios among the measured emission lines, across the MUSE field of view.

I found that the outflowing gas is characterised by higher values of density and ionisation parameter (i.e. a measure of the intensity of the radiation field, relative to gas density) than the disk, which is instead more affected by dust extinction. Interestingly, our median outflow density is lower with respect to what is found in the literature, but a more consistent value can be obtained calculating the median density weighting for the [S II] line flux. This means that many values of outflow density found in the literature could be biased towards higher densities because they are based only on the most luminous outflowing regions, characterised by a higher signal-to-noise ratio.

Using the Baldwin, Phillips & Telervich (BPT) diagrams (Baldwin et al., 1981; Veilleux & Osterbrock, 1987), I distinguished high- from low-ionisation regions across the spatially resolved NLR traced by the outflowing gas. The former, characterised by the lowest [N II]$\lambda\lambda$6548,6584/Hα and [S II]$\lambda\lambda$6717,6731/Hα line ratios, generally traces the inner parts along the emitting cone axis where the [S III]$\lambda\lambda$9068,9532/[S II]$\lambda\lambda$6717,6731 line ratio is enhanced (i.e. high excitation), while the latter follows the cone edges and/or the regions perpendicular to the outflow axis, characterised also by a higher [O III] velocity dispersion.

A possible explanation for the observed features identified in the outflow is to take into account different proportions of two distinct populations of line emitting clouds (e.g. Binette 1996). One is optically thin to the radiation and characterised by the highest excitation, while the other, optically thick, is impinged by a filtered - and then harder - radiation field, which makes it dominated by low-excitation lines and characterised by lower [S III]/[S II] line ratios. The highest values of [N II]/Hα and [S II]/Hα line ratios may be due to shocks and/or to a hard-filtered radiation field from the AGN. These results are reported in Mingozzi et al. (2019).

Separating the outflow and disk components allowed us to detect in one of the sources of our sample, Centaurus A, two blobs dominated by star forming ionisation, apparently embedded in the AGN ionisation cone, possibly tracing the two modes of positive feedback. One has a velocity consistent with the gas in the disk (e.g. Cresci et al. 2015b), while the other has a higher velocity, compatible with the outflowing gas (e.g. Maiolino el a. 2017). Our X-SHOOTER proposal (P.I. Mingozzi) on the observations of these two clumps was accepted and I will soon analyse these data with the aim of completely discarding AGN/shock excitation through infrared diagnostics and of obtaining an independent confirmation of young stars in the outflow from the analysis of the stellar kinematics (Mingozzi et al. in preparation).

Since MUSE data of 18 new objects compatible with the selection criteria of the first nine galaxies already analysed are now available in the ESO archive, it is possible to extend the current sample to have a more complete and detailed view of the central kiloparsecs of nearby Seyferts, and to assess the global role of positive feedback. In this context, it would also be interesting to investigate their metal content in order to understand how metallicity relates with outflows (e.g. using NebulaBayes, Thomas et al. 2018). This could allow to understand the role that outflows play in creating metallicity gradients (e.g. Chisholm et al. 2018).

Metallicity and ionisation parameter in local star forming galaxies

The observed content of gas-phase metallicity in the ISM stems from stellar evolution, modulated by gas flows into and out of galaxies. Furthermore, different chemical elements are enriched on different timescales by different stellar populations. Hence, investigating the time evolution of metallicity and how metallicity relates to other observables provides unique information on the evolutionary processes driving galaxy evolution (Maiolino & Mannucci, 2019). The recent development of powerful integral field unit (IFU) spectrographs has allowed us to analyse how metallicity and chemical abundances change on spatially resolved scales, emphasising their dependence both on the mass of the galaxy and the location within the galaxy (e.g. Sánchez et al. 2014; Belfiore et al. 2017).

Oxygen is commonly used to trace gas-phase metallicity because of its abundance and the ability to observe in the optical wavelength range key temperature-sensitive lines (auroral lines), that allows a calculation of the ionisation structure of the nebula and metal content with minimal assumptions. Unfortunately, auroral lines are often too weak to be detected in extragalactic sources at even modest redshifts. Therefore, more indirect calibrations for the oxygen abundance, based on strong optical nebular lines, have been devised. However, the intensity of nebular lines depends both on the metallicity and the ionisation parameter (i.e. measure of the intensity of the radiation field, relative to gas density) of the gas. A wide variety of metallicity calibrations from strong line ratios are available (e.g., Curti et al. 2017), based either on empirical datasets or on photoionisation models. The effect of ionisation parameter variations is, however, difficult to take into account in these calibrations.

In the first part of Chapter 3, I presented a work I was involved with, focused on the study of ISM properties with MUSE in a local H II galaxy, He 2-10 (Cresci et al., 2017). The central regions of this object are characterised by a strong SF activity, and have the highest values of electron density, ionisation parameter and metallicity. This works highlights the importance of taking into account the ionisation parameter variations to measure the gas metallicity to avoid misleading conclusions.

The second part of Chapter 3 deals with a project focused on studying simultaneously gas metallicity and ionisation parameter with the Mapping Nearby Galaxies at APO (MaNGA) survey (P.I Bundy), carried out to assess whether the results obtained for He 2-10 are valid on a statistically significant sample of galaxies. This project was started in collaboration with Dr. Kevin Bundy and Dr. Francesco Belfiore at the University of California Santa Cruz. The primary aims are to investigate how the still poorly understood ionisation parameter varies within galaxies of different stellar masses and types and to study the nature of the observed relation between metallicity and ionisation parameter. In addition, I want to understand to what extent the inclusion of the [S III]$\lambda\lambda$9069,9532 lines can help with the determination of metallicity and ionisation parameter. In fact, theoretically the [S III]$\lambda\lambda$9069,9532/[S II]$\lambda\lambda$6717,31 line ratio provides a superior measure of the ionisation parameter (Kewley & Dopita, 2002). Until recently, however, no large spectroscopic survey of nearby galaxies covered the required [S III] emission lines in the near-IR.

Specifically, I used a sample of 2139 local star forming galaxies, spanning the stellar mass range $M_\star = 10^9 - 10^{11}$ M$_\odot$ from the fifteenth SDSS-IV MaNGA data release (Aguado et al., 2019). The method used to derive the gas metallicity 12+log(O/H) and ionisation parameter q of ionised nebulae is inspired by the software tool IZI (Blanc et al., 2015), which compares an arbitrary observed strong emission lines set with photoionisation model grids through a Bayesian analysis. Our revisited version peculiarity is the simultaneous estimate of a third parameter, the dust extinction E(B-V), meaning that it does not assume a fixed unattenuated Case B ratio (i.e., Hα/Hβ = 2.86, appropriate for an electron density of $n_e = 100$ cm^{-3} and electron temperature $T_e = 10^4$ K; Osterbrock & Ferland 2006), that would neglect the effect of metallicity and ionisation state.

Interestingly, current photoionisation models, based on both CLOUDY and MAPPINGS, globally reproduce the observed range in optical line ratios, while substantially over-predict the [S III] lines. Furthermore, I argued that the set of emission lines comprising [O II]$\lambda\lambda$3727,29, Hβ, [O III]$\lambda\lambda$4959,5007, [N II]$\lambda\lambda$6548,84, Hα, [S II]λ6717 and [S II]λ6731 is not sufficient to break the degeneracy between metallicity and ionisation parameter with the current photoionisation models, and thus the introduction of a prior on the ionisation parameter based on the [S III]/[S II] line ratio is needed. One of the results that I obtained is that ionisation parameter radial profiles are approximately flat at low stellar masses, and tends to steepen (more positive slopes) at increasing stellar masses. The slopes of the ionisation parameter radial profiles can be interpreted on the basis of the tight correlation between the equivalent width of Hα EW(Hα) (a proxy for specific star formation rate) and log(q), that I observe at all stellar masses. Indeed, EW(Hα) gradients show a similar trend with radius. In low massive galaxies, the star forming regions traced by EW(Hα) are located all across the field of view observed by MaNGA, and the ionisation parameter does not show a radial distribution, but is set in structures, with a similar distribution. This behaviour explains the flat radial profiles of log(q) at low stellar mass, showing that they might not be ideal to understand the variations of q across the galaxy discs. In higher massive galaxies instead, the central regions are dominated by older stars, showing a decrease of EW(Hα), and thus a decrease of log(q) with respect to the outskirts. I also found a correlation between ionisation parameter and metallicity, at fixed EW(Hα) up to EW(Hα) < 150 Å, while beyond this value the two parameters seem to be unrelated. These results are summarised in a paper that has just been resubmitted to A&A (Mingozzi et al., 2020).

The next steps of this investigation are the implementation of new parameters in our revisited IZI code, such as the N/O variation and the effective temperature of the exciting stars, to give a more complete and detailed view of the ISM in star forming galaxies. However, a fundamental tool to do this is the development of new generation photoionisation models able to better reproduce the observed emission lines, such as sulfur lines, and to predict oxygen abundances more consistent with those based on the direct method (see e.g. Kewley & Ellison 2008; Curti et al. 2019b).

Investigating local galaxies ISM by exploiting CO excitation

The molecular gas plays a crucial role in the physics of galaxies, fuelling both SF and accretion onto the super massive BH, when the latter is present. The study of the so-called Carbon Monoxide Spectral Line Energy Distribution (CO SLED) – i.e. the CO line luminosity as a function of the CO upper rotational quantum level J – allows to constrain the physical properties of the molecular gas, both at high-redshift (e.g. Gallerani et al. 2014; Daddi et al. 2015), thanks to submillimeter facilities such as CARMA and IRAM-PdBI interferometers, and in local sources (e.g. Rosenberg et al. 2015; Pereira-Santaella et al. 2014), with Herschel. ALMA advent has represented a breakthrough making possible to reach a spatial resolution down to molecular cloud scales when targeting CO lines in the nearby Universe.

The CO(1–0) is the most sensitive transition to the total gas reservoir, being excited in the diffuse cold molecular component. The higher-J transitions ($J_{up} > 1$) are, instead, increasingly luminous in the warm dense ($n_{crit} \sim 0.01 - 2 \times 10^6$ cm^{-3}, $T_{ex} \sim 16.6 - 7000$ K) star forming regions within molecular clouds (Carilli & Walter, 2013). The heating agents can be either far-ultraviolet photons, mainly related to star forming regions, X-ray photons, due to AGN activity, or shocks, originating from the supersonic injection of mass into the ISM by stellar winds, supernovae, and/or young stellar objects (e.g. Narayanan & Krumholz 2014). The CO SLED shape is determined primarily by the gas density and the heating mechanism acting on the molecular gas, and thus its analysis can shed light on the physical properties (e.g. density, temperature, gas mass) and the main excitation source of the molecular gas (SF, AGN or shocks).

In Chapter 4, I described a project about the analysis of the molecular and X-ray data in a nearby Seyfert galaxy, NGC 34. Specifically, I reduced from scratch archival ALMA data for the CO(6–5) transition, and then, taking into account also archival Herschel data, I modelled the observed CO SLED with photoionisation and shock models, demonstrating that also the influence of the AGN is needed to reproduce the observed molecular emission (Mingozzi et al., 2018). The CO emission, traced by ALMA in the central region of the galaxy with a very high spatial resolution, is crucial to spatially constrain the region where the contribution of the AGN could actually dominate. A similar work that I was involved with is about the local Seyfert galaxy NGC 7130, published by Pozzi et al. (2017).

The works presented in Mingozzi et al. (2018) and Pozzi et al. (2017) are a starting point to a larger project, that can be potentially extended to the sample of 76 AGN presented in Gruppioni et al. (2016), from which NGC 34 and NGC 7130 were selected. Furthermore, new constraints on our modelling can be given by including a combination of low- to mid-J rotational lines of heavy rotor molecules with high critical densities (e.g. HCO^+, HCN), able to probe the densest conditions within molecular clouds (McKee & Ostriker, 2007; Papadopoulos et al., 2014). In this context, there are already APEX data for the HCO^+(2–1), HCN(2–1) in NGC 34 and NGC 7130 (P.I. Pozzi) that will be soon analysed. In this context, it would be interesting to test the new set of photoionisation models of realistic clouds (i.e. exploring their internal structure, with different densities), impinged by AGN radiation, partly obscured by a torus with variable column density and inclination recently proposed by Vallini et al. (2019).

This Thesis highlights the crucial role that multi-wavelength IFS studies can play in exploring in detail the properties of different ISM phases in local galaxies. Making use of different ISM diagnostics (from optical to submillimeter wavelengths) allows to trace the processes that affect ISM conditions across both AGN and star forming galaxies, to assess their impact on the evolution of their hosts. Overall, given the unprecedented detail of the analysed data as well as some limitations of current models highlighted in this work, the results of the three projects described above represent a unique test bench for the new generation of photoionisation models.

Bibliography

Aalto, S., Garcia-Burillo, S., Muller, S., et al. 2015, Astronomy and Astrophysics, 574, A85 18

Aalto, S., Garcia-Burillo, S., Muller, S., et al. 2012, Astronomy and Astrophysics, 537, A44 18

Aguado, D. S., Ahumada, R., Almeida, A., et al. 2019, Astrophysical Journal, Supplement, 240, 23 105, 141, 168

Aird, J., Coil, A. L., Georgakakis, A., et al. 2015, Monthly Notices of the RAS, 451, 1892 16

Aird, J., Nandra, K., Laird, E. S., et al. 2010, Monthly Notices of the RAS, 401, 2531 16

Albrecht, M., Krügel, E., & Chini, R. 2007, Astronomy and Astrophysics, 462, 575 153

Alexander, D. M. & Hickox, R. C. 2012, New Astronomy Review, 56, 93 17

Ali, B., Blum, R. D., Bumgardner, T. E., et al. 1991, Publications of the ASP, 103, 1182 115

Allen, D. A., Wright, A. E., & Goss, W. M. 1976, Monthly Notices of the RAS, 177, 91 93

Allen, J. T., Croom, S. M., Konstantopoulos, I. S., et al. 2015, Monthly Notices of the RAS, 446, 1567 38

Allen, M. G., Dopita, M. A., Tsvetanov, Z. I., & Sutherland, R. S. 1999, Astrophysical Journal, 511, 686 43, 65

Allen, M. G., Groves, B. A., Dopita, M. A., Sutherland, R. S., & Kewley, L. J. 2008, Astrophysical Journal, Supplement, 178, 20 38, 68, 69

Alloin, D., Collin-Souffrin, S., Joly, M., & Vigroux, L. 1979, Astronomy and Astrophysics, 78, 200 7, 22, 69, 91, 101, 117

Alonso-Herrero, A., Pereira-Santaella, M., García-Burillo, S., et al. 2018, Astrophysical Journal, 859, 144 44

Anders, E. & Grevesse, N. 1989, Geochimica Cosmochimica Acta, 53, 197 114

Andrews, B. H. & Martini, P. 2013, Astrophysical Journal, 765, 140 23, 100

Arnaud, K. A. 1996, Astronomical Society of the Pacific Conference Series, 101, 17 150

Arribas, S., Colina, L., Bellocchi, E., Maiolino, R., & Villar-Martín, M. 2014, Astronomy and Astrophysics, 568, A14 17, 58

Asplund, M., Grevesse, N., Sauval, A. J., & Scott, P. 2009, Annual Review of Astron and Astrophys, 47, 481 7, 110, 114

Avni, Y. 1976, Astrophysical Journal, 210, 642 150

Axon, D. J., Marconi, A., Macchetto, F. D., Capetti, A., & Robinson, A. 1997, Astrophysics and Space Science, 248, 69 42

Azimlu, M., Marciniak, R., & Barmby, P. 2011, Astronomical Journal, 142, 139 114

Bacon, R., Accardo, M., Adjali, L., et al. 2010, in Proceedings of the SPIE, Vol. 7735, Ground-based and Airborne Instrumentation for Astronomy III, 773508 33, 39

Baldwin, J. A., Phillips, M. M., & Terlevich, R. 1981, Publications of the ASP, 93, 5 26, 97, 105, 149, 166

Barbosa, F. K. B., Storchi-Bergmann, T., McGregor, P., Vale, T. B., & Rogemar Riffel, A. 2014, Monthly Notices of the RAS, 445, 2353 42

Baumgartner, W. H., Tueller, J., Markwardt, C. B., et al. 2013, Astrophysical Journal, Supplement, 207, 19 39

Beck, S. C., Kelly, D. M., & Lacy, J. H. 1997, Astronomical Journal, 114, 585 94

Belfiore, F., Maiolino, R., Bundy, K., et al. 2018, Monthly Notices of the RAS, 477, 3014 34, 105, 132

Belfiore, F., Maiolino, R., Maraston, C., et al. 2016, Monthly Notices of the RAS, 461, 3111 26, 27, 28, 34, 60, 97, 105, 108, 139

Belfiore, F., Maiolino, R., Tremonti, C., et al. 2017, Monthly Notices of the RAS, 469, 151 12, 127, 128, 129, 130, 131, 140, 167

Belfiore, F., Vincenzo, F., Maiolino, R., & Matteucci, F. 2019, MNRAS, 487, 456 13, 128, 130

Belfiore, F., Westfall, K. B., Schaefer, A., et al. 2019, arXiv e-prints, arXiv:1901.00866 105, 106, 107, 108, 141

Bell, E. F. & de Jong, R. S. 2000, Monthly Notices of the RAS, 312, 497 137

Bell, E. F., McIntosh, D. H., Katz, N., & Weinberg, M. D. 2003, Astrophysical Journal, Supplement, 149, 289 15

Belley, J. & Roy, J.-R. 1992, Astrophysical Journal, Supplement, 78, 61 130

Benson, A. J., Bower, R. G., Frenk, C. S., et al. 2003, Astrophysical Journal, 599, 38 15

Bershady, M. A., Verheijen, M. A. W., Swaters, R. A., et al. 2010, Astrophysical Journal, 716, 198 33

Bevington, P. R. & Robinson, D. K. 2003, Data reduction and error analysis for the physical sciences 159

Bian, F., Kewley, L. J., Dopita, M. A., & Juneau, S. 2016, Astrophysical Journal, 822, 62 59, 131

Bieri, R., Dubois, Y., Silk, J., Mamon, G. A., & Gaibler, V. 2016, Monthly Notices of the RAS, 455, 4166 18, 37

Binette, L., Wilson, A. S., & Storchi-Bergmann, T. 1996, Astronomy and Astrophysics, 312, 365 63, 65, 76

Binney, J. & Tremaine, S. 2008, Galactic Dynamics: Second Edition 48

Blanc, G. A., Kewley, L., Vogt, F. P. A., & Dopita, M. A. 2015, Astrophysical Journal, 798, 99 23, 24, 104, 108, 109, 110, 139, 169

Blanc, G. A., Lu, Y., Benson, A., Katsianis, A., & Barraza, M. 2019, Astrophysical Journal, 877, 6 122

Blanc, G. A., Weinzirl, T., Song, M., et al. 2013, Astronomical Journal, 145, 138 33, 131

Blanco, V. M., Graham, J. A., Lasker, B. M., & Osmer, P. S. 1975, Astrophysical Journal, Letters, 198, L63 40, 71

Bland-Hawthorn, J. & Kedziora-Chudczer, L. 2003, Publications of the Astron. Soc. of Australia, 20, 242 40, 71

Bland-Hawthorn, J., Lumsden, S. L., Voit, G. M., Cecil, G. N., & Weisheit, J. C. 1997, Astrophysics and Space Science, 248, 177 42

Blanton, M. R., Bershady, M. A., Abolfathi, B., et al. 2017, Astronomical Journal, 154, 28 104

Blanton, M. R., Kazin, E., Muna, D., Weaver, B. A., & Price-Whelan, A. 2011, Astronomical Journal, 142, 31 104

Blitz, L. 1993, in Protostars and Planets III, ed. E. H. Levy & J. I. Lunine, 125–161 3

Boissier, S. & Prantzos, N. 1999, Monthly Notices of the RAS, 307, 857 12, 128

Bolatto, A. D., Wolfire, M., & Leroy, A. K. 2013, Annual Review of Astron and Astrophys, 51, 207 3, 158

Bournaud, F., Daddi, E., Weiß, A., et al. 2015, Astronomy and Astrophysics, 575, A56 31

Bower, R. G., Benson, A. J., & Crain, R. A. 2012, Monthly Notices of the RAS, 422, 2816 15

Bresolin, F. 2019, Monthly Notices of the RAS, 488, 3826 131

Brightman, M. & Nandra, K. 2011a, Monthly Notices of the RAS, 413, 1206 149, 150

Brightman, M. & Nandra, K. 2011b, Monthly Notices of the RAS, 414, 3084 149

Brinchmann, J., Charlot, S., White, S. D. M., et al. 2004, Monthly Notices of the RAS, 351, 1151 31, 104, 109, 137

Brinchmann, J., Pettini, M., & Charlot, S. 2008, Monthly Notices of the RAS, 385, 769 131

Bruhweiler, F. C., Truong, K. Q., & Altner, B. 1991, Astrophysical Journal, 379, 596 42

Brusa, M., Perna, M., Cresci, G., et al. 2016, Astronomy and Astrophysics, 588, A58 66

Bundy, K., Bershady, M. A., Law, D. R., et al. 2015, Astrophysical Journal, 798, 7 12, 34, 38, 93

Butler, B. 2012, ALMA memo 594: Flux Density Models for Solar System Bodies in CASA, ALMA memo series (NRAO) 152

Byler, N., Dalcanton, J. J., Conroy, C., & Johnson, B. D. 2017, Astrophysical Journal, 840, 44 112, 113, 114

Calzetti, D. 1997, Astronomical Journal, 113, 162 109

Calzetti, D., Armus, L., Bohlin, R. C., et al. 2000, Astrophysical Journal, 533, 682 26, 54, 77, 97, 109, 112

Calzetti, D., Kennicutt, R. C., J., Bianchi, L., et al. 2005, Astrophysical Journal, 633, 871 133

Calzetti, D., Liu, G., & Koda, J. 2012, Astrophysical Journal, 752, 98 133

Cano-Díaz, M., Maiolino, R., Marconi, A., et al. 2012, Astronomy and Astrophysics, 537, L8 6, 17, 39

Cappellari, M. & Copin, Y. 2003, Monthly Notices of the RAS, 342, 345 45, 96

Cappellari, M. & Emsellem, E. 2004, Publications of the ASP, 116, 138 45, 96

Cappellari, M., Emsellem, E., Krajnović, D., et al. 2011, Monthly Notices of the RAS, 413, 813 33

Cappellari, M., McDermid, R. M., Alatalo, K., et al. 2013, MNRAS, 432, 1862 122, 123

Cardelli, J. A., Clayton, G. C., & Mathis, J. S. 1989, Astrophysical Journal, 345, 245 25

Carilli, C. L. & Walter, F. 2013, Annual Review of Astron and Astrophys, 51, 105 30, 147, 170

Carniani, S., Marconi, A., Maiolino, R., et al. 2016, Astronomy and Astrophysics, 591, A28 6, 17, 18, 33, 39

Cecil, G., Bland, J., & Tully, R. B. 1990, Astrophysical Journal, 355, 70 42

Cecil, G., Dopita, M. A., Groves, B., et al. 2002, Astrophysical Journal, 568, 627 42, 52

Charlot, S. & Longhetti, M. 2001, Monthly Notices of the RAS, 323, 887 104

Chevallard, J. & Charlot, S. 2016, Monthly Notices of the RAS, 462, 1415 23, 24

Chisholm, J., Tremonti, C., & Leitherer, C. 2018, Monthly Notices of the RAS, 481, 1690 9, 167

Choi, J., Dotter, A., Conroy, C., et al. 2016, Astrophysical Journal, 823, 102 114

Cicone, C., Brusa, M., Ramos Almeida, C., et al. 2018, Nature Astronomy, 2, 176 6

Cicone, C., Maiolino, R., Sturm, E., et al. 2014, Astronomy and Astrophysics, 562, A21 6, 18, 165

Colbert, E. J. M., Baum, S. A., Gallimore, J. F., O'Dea, C. P., & Christensen, J. A. 1996a, Astrophysical Journal, 467, 551 44

Colbert, E. J. M., Baum, S. A., Gallimore, J. F., et al. 1996b, Astrophysical Journal, Supplement, 105, 75 44

Cole, S., Lacey, C. G., Baugh, C. M., & Frenk, C. S. 2000, Monthly Notices of the RAS, 319, 168 15

Colina, L., Fricke, K. J., Kollatschny, W., & Perryman, M. A. C. 1987, Astronomy and Astrophysics, 178, 51 43

Colina, L., Piqueras López, J., Arribas, S., et al. 2015, Astronomy and Astrophysics, 578, A48 75

Colina, L., Sparks, W. B., & Macchetto, F. 1991, Astrophysical Journal, 370, 102 42

Concas, A., Popesso, P., Brusa, M., Mainieri, V., & Thomas, D. 2019, Astronomy and Astrophysics, 622, A188 165

Conroy, C., Gunn, J. E., & White, M. 2009, Astrophysical Journal, 699, 486 114

Considère, S., Coziol, R., Contini, T., & Davoust, E. 2000, Astronomy and Astrophysics, 356, 89 7, 69

Contini, T., Garilli, B., Le Fèvre, O., et al. 2012, Astronomy and Astrophysics, 539, A91 38

Cowie, L. L., Songaila, A., Hu, E. M., & Cohen, J. G. 1996, Astronomical Journal, 112, 839 10

Crenshaw, D. M. & Kraemer, S. B. 2000, Astrophysical Journal, Letters, 532, L101 38

Crenshaw, D. M., Kraemer, S. B., Schmitt, H. R., et al. 2010, Astronomical Journal, 139, 871 38

Cresci, G., Mainieri, V., Brusa, M., et al. 2015a, Astrophysical Journal, 799, 82 6, 17, 18, 33, 39

Cresci, G. & Maiolino, R. 2018, Nature Astronomy, 2, 179 17, 37

Cresci, G., Marconi, A., Zibetti, S., et al. 2015b, Astronomy and Astrophysics, 582, A63 18, 38, 39, 44, 71, 96, 165, 166

Cresci, G., Vanzi, L., Sauvage, M., Santangelo, G., & van der Werf, P. 2010, Astronomy and Astrophysics, 520, A82 38, 94, 97, 100

Cresci, G., Vanzi, L., Telles, E., et al. 2017, Astronomy and Astrophysics, 604, A101 92, 94, 95, 97, 98, 99, 102, 103, 117, 136, 168

Crockett, R. M., Shabala, S. S., Kaviraj, S., et al. 2012, Monthly Notices of the RAS, 421, 1603 71

Croom, S. M., Lawrence, J. S., Bland-Hawthorn, J., et al. 2012, Monthly Notices of the RAS, 421, 872 34

Curti, M., Cresci, G., Mannucci, F., et al. 2017, Monthly Notices of the RAS, 465, 1384 23, 66, 91, 100, 102, 168

Curti, M., Maiolino, R., Cirasuolo, M., et al. 2019a, arXiv e-prints, arXiv:1910.13451 34

Curti, M., Mannucci, F., Cresci, G., & Maiolino, R. 2019b, arXiv e-prints, arXiv:1910.00597 23, 123, 124, 128, 170

Cyburt, R. H., Fields, B. D., Olive, K. A., & Yeh, T.-H. 2016, Reviews of Modern Physics, 88, 015004 2

Daddi, E., Dannerbauer, H., Liu, D., et al. 2015, Astronomy and Astrophysics, 577, A46 29, 31, 147, 170

D'Agostino, J. J., Kewley, L. J., Groves, B., et al. 2019, The Astrophysical Journal, 878, 2 104

Das, V., Crenshaw, D. M., Kraemer, S. B., & Deo, R. P. 2006, Astronomical Journal, 132, 620 38

Dasyra, K. M., Bostrom, A. C., Combes, F., & Vlahakis, N. 2015, Astrophysical Journal, 815, 34 42

Davé, R., Finlator, K., & Oppenheimer, B. D. 2011, Monthly Notices of the RAS, 416, 1354 13, 128

de Zeeuw, P. T., Bureau, M., Emsellem, E., et al. 2002, Monthly Notices of the RAS, 329, 513 33

Dekel, A. & Silk, J. 1986, Astrophysical Journal, 303, 39 14

Delvecchio, I., Gruppioni, C., Pozzi, F., et al. 2014, Monthly Notices of the RAS, 439, 2736 16

Denicoló, G., Terlevich, R., & Terlevich, E. 2002, Monthly Notices of the RAS, 330, 69 23

Diamond-Stanic, A. M. & Rieke, G. H. 2012, Astrophysical Journal, 746, 168 73

Díaz, A. I. & Pérez-Montero, E. 2000, Monthly Notices of the RAS, 312, 130 92

Diaz, A. I., Terlevich, E., Vilchez, J. M., Pagel, B. E. J., & Edmunds, M. G. 1991, Monthly Notices of the RAS, 253, 245 56, 59, 79, 116, 117, 118, 119

Dinerstein, H. L. & Shields, G. A. 1986, Astrophysical Journal, 311, 45 115

D'Odorico, S., Dekker, H., Mazzoleni, R., et al. 2006, in Proceedings of the SPIE, Vol. 6269, 626933 75

Dopita, M. A. & Evans, I. N. 1986, Astrophysical Journal, 307, 431 10, 24, 91, 135

Dopita, M. A., Fischera, J., Sutherland , R. S., et al. 2006a, The Astrophysical Journal Supplement Series, 167, 177 23, 111, 117, 140

Dopita, M. A., Fischera, J., Sutherland, R. S., et al. 2006b, Astrophysical Journal, 647, 244 11, 131, 135, 140

Dopita, M. A., Fischera, J., Sutherland, R. S., et al. 2006c, Astrophysical Journal, 647, 244 59

Dopita, M. A., Groves, B. A., Fischera, J., et al. 2005, Astrophysical Journal, 619, 755 110

Dopita, M. A., Groves, B. A., Sutherland, R. S., & Kewley, L. J. 2003, Astrophysical Journal, 583, 727 109

Dopita, M. A., Kewley, L. J., Heisler, C. A., & Sutherland , R. S. 2000, Astrophysical Journal, 542, 224 114, 115

Dopita, M. A., Kewley, L. J., Sutherland, R. S., & Nicholls, D. C. 2016, Astrophysics and Space Science, 361, 61 22, 23, 100, 101, 102, 103

Dopita, M. A., Rich, J., Vogt, F. P. A., et al. 2014, Astrophysics and Space Science, 350, 741 11, 131, 135

Dopita, M. A. & Sutherland, R. S. 1995, Astrophysical Journal, 455, 468 38, 60, 68

Dopita, M. A. & Sutherland, R. S. 1996, Astrophysical Journal, Supplement, 102, 161 38

Dopita, M. A., Sutherland, R. S., Nicholls, D. C., Kewley, L. J., & Vogt, F. P. A. 2013, Astrophysical Journal, Supplement, 208, 10 22, 23, 24, 109, 110, 111, 112, 113, 114, 131

Dotter, A. 2016, Astrophysical Journal, Supplement, 222, 8 114

Draine, B. T. 1980, Astrophysical Journal, 241, 1021 156

Draine, B. T. 2003, Annual Review of Astron and Astrophys, 41, 241 7

Draine, B. T. & Kreisch, C. D. 2018, Astrophysical Journal, 862, 30 110

Draine, B. T. & McKee, C. F. 1993, Annual Review of Astron and Astrophys, 31, 373 156

Drory, N., MacDonald, N., Bershady, M. A., et al. 2015, Astronomical Journal, 149, 77 105

Dugan, Z., Bryan, S., Gaibler, V., Silk, J., & Haas, M. 2014, Astrophysical Journal, 796, 113 18, 38

Ebeling, H., Stephenson, L. N., & Edge, A. C. 2014, Astrophysical Journal, Letters, 781, L40 33

Edmunds, M. G., Taylor, K., & Turtle, A. J. 1988, Monthly Notices of the RAS, 234, 155 47

Eisenhauer, F., Abuter, R., Bickert, K., et al. 2003, in Proceedings of the SPIE, Vol. 4841, Instrument Design and Performance for Optical/Infrared Ground-based Telescopes, ed. M. Iye & A. F. M. Moorwood, 1548–1561 33

El-Badry, K., Wetzel, A., Geha, M., et al. 2016, Astrophysical Journal, 820, 131 18, 38

Ellison, S. L., Patton, D. R., Simard, L., & McConnachie, A. W. 2008, Astrophysical Journal, Letters, 672, L107 10

Erb, D. K., Shapley, A. E., Pettini, M., et al. 2006, Astrophysical Journal, 644, 813 10

Esteban, C., García-Rojas, J., Carigi, L., et al. 2014, Monthly Notices of the RAS, 443, 624 100

Fabian, A. C. 2012, Annual Review of Astron and Astrophys, 50, 455 14, 16, 37, 165

Falcón-Barroso, J., Sánchez-Blázquez, P., Vazdekis, A., et al. 2011, Astronomy and Astrophysics, 532, A95 106

Ferguson, J. W., Korista, K. T., Baldwin, J. A., & Ferland, G. J. 1997, Astrophysical Journal, 487, 122 38

Ferland, G. J., Chatzikos, M., Guzmán, F., et al. 2017, Revista Mexicana de Astronomia y Astrofisica, 53, 385 22, 77

Ferland, G. J., Porter, R. L., van Hoof, P. A. M., et al. 2013, Revista Mexicana de Astronomia y Astrofisica, 49, 137 114, 117, 155

Fernández, X., Petric, A. O., Schweizer, F., & van Gorkom, J. H. 2014, Astronomical Journal, 147, 74 153, 154, 158, 162

Ferrarese, L. & Merritt, D. 2000, Astrophysical Journal, Letters, 539, L9 13

Ferruit, P., Wilson, A. S., & Mulchaey, J. 2000, Astrophysical Journal, Supplement, 128, 139 43, 52

Feruglio, C., Maiolino, R., Piconcelli, E., et al. 2010, Astronomy and Astrophysics, 518, L155 6, 18

Field, G. B., Goldsmith, D. W., & Habing, H. J. 1969, Astrophysical Journal, Letters, 155, L149 2, 3

Fischer, T. C., Crenshaw, D. M., Kraemer, S. B., & Schmitt, H. R. 2013, Astrophysical Journal, Supplement, 209, 1 18, 44

Flower, D. R. & Pineau Des Forêts, G. 2010, Monthly Notices of the RAS, 406, 1745 156

Flower, D. R. & Pineau des Forêts, G. 2015, Astronomy and Astrophysics, 578, A63 155, 156

Fluetsch, A., Maiolino, R., Carniani, S., et al. 2019, Monthly Notices of the RAS, 483, 4586 18

Forbes, D. A. & Norris, R. P. 1998, Monthly Notices of the RAS, 300, 757 48

Foreman-Mackey, D., Hogg, D. W., Lang, D., & Goodman, J. 2013, Publications of the ASP, 125, 306 109

Förster Schreiber, N. M., Genzel, R., Bouché, N., et al. 2009, Astrophysical Journal, 706, 1364 33, 38

Förster Schreiber, N. M., Renzini, A., Mancini, C., et al. 2018, Astrophysical Journal, Supplement, 238, 21 39

Förster Schreiber, N. M., Shapley, A. E., Erb, D. K., et al. 2011, Astrophysical Journal, 731, 65 98

Förster Schreiber, N. M., Übler, H., Davies, R. L., et al. 2019, Astrophysical Journal, 875, 21 58

Freitas-Lemes, P., Rodrigues, I., Dors, O. L., Faúndez-Abans, M., & Pérez-Montero, E. 2014, Monthly Notices of the RAS, 441, 1086 10, 91

Friedrich, S., Davies, R. I., Hicks, E. K. S., et al. 2010, Astronomy and Astrophysics, 519, A79 43

Gaibler, V., Khochfar, S., Krause, M., & Silk, J. 2012, Monthly Notices of the RAS, 425, 438 18, 38

Gallagher, R., Maiolino, R., Belfiore, F., et al. 2019, Monthly Notices of the RAS, 485, 3409 19, 75

Gallerani, S., Ferrara, A., Neri, R., & Maiolino, R. 2014, Monthly Notices of the RAS, 445, 2848 147, 162, 170

Gallimore, J. F., Baum, S. A., O'Dea, C. P., Brinks, E., & Pedlar, A. 1994, Astrophysical Journal, Letters, 422, L13 42

Gallimore, J. F., Elitzur, M., Maiolino, R., et al. 2016, Astrophysical Journal, Letters, 829, L7 42

Gandhi, P., Horst, H., Smette, A., et al. 2009, Astronomy and Astrophysics, 502, 457 149

García-Burillo, S., Combes, F., Usero, A., et al. 2015, Astronomy and Astrophysics, 580, A35 18

García-Burillo, S., Combes, F., Usero, A., et al. 2014, Astronomy and Astrophysics, 567, A125 42, 52

Garnett, D. R. 1989, Astrophysical Journal, 345, 282 115

Garnett, D. R. 1992, Astronomical Journal, 103, 1330 20

Gebhardt, K., Bender, R., Bower, G., et al. 2000, Astrophysical Journal, Letters, 539, L13 13

Gibson, B. K., Pilkington, K., Brook, C. B., Stinson, G. S., & Bailin, J. 2013, Astronomy and Astrophysics, 554, A47 13, 128

Graham, J. A. 1998, Astrophysical Journal, 502, 245 71

Graham, J. A. & Price, R. M. 1981, Astrophysical Journal, 247, 813 71

Granato, G. L., De Zotti, G., Silva, L., Bressan, A., & Danese, L. 2004, Astrophysical Journal, 600, 580 14, 15

Greene, J. E., Zakamska, N. L., & Smith, P. S. 2012, Astrophysical Journal, 746, 86 38

Gruppioni, C., Berta, S., Spinoglio, L., et al. 2016, Monthly Notices of the RAS, 458, 4297 149, 155, 171

Guainazzi, M., Matt, G., Brandt, W. N., et al. 2000, Astronomy and Astrophysics, 356, 463 44

Guainazzi, M., Matt, G., & Perola, G. C. 2005, Astronomy and Astrophysics, 444, 119 150

Gunn, J. E., Siegmund, W. A., Mannery, E. J., et al. 2006, Astronomical Journal, 131, 2332 104

Gutiérrez, L., Beckman, J. E., & Buenrostro, V. 2011, Astronomical Journal, 141, 113 114

Gutkin, J., Charlot, S., & Bruzual, G. 2016, Monthly Notices of the RAS, 462, 1757 23

Habing, H. J. 1968, Bulletin Astronomical Institute of the Netherlands, 19, 421 155

Hailey-Dunsheath, S., Sturm, E., Fischer, J., et al. 2012, Astrophysical Journal, 755, 57 156

Hardcastle, M. J., Worrall, D. M., Kraft, R. P., et al. 2003, Astrophysical Journal, 593, 169 40, 52, 70, 71, 73

Harrison, C. M., Alexander, D. M., Mullaney, J. R., et al. 2016, Monthly Notices of the RAS, 456, 1195 39

Haworth, T. J., Glover, S. C. O., Koepferl, C. M., Bisbas, T. G., & Dale, J. E. 2018, New Astronomy Review, 82, 1 4

Heckman, T. M. 1980, Astronomy and Astrophysics, 87, 152 26

Heckman, T. M., Robert, C., Leitherer, C., Garnett, D. R., & van der Rydt, F. 1998, Astrophysical Journal, 503, 646 137

Hickox, R. C. & Alexander, D. M. 2018, Annual Review of Astron and Astrophys, 56, 625 6, 27

Hillier, D. J. & Miller, D. L. 1998, Astrophysical Journal, 496, 407 112

Hinshaw, G., Larson, D., Komatsu, E., et al. 2013, Astrophysical Journal, Supplement, 208, 19 15

Hjelm, M. & Lindblad, P. O. 1996, Astronomy and Astrophysics, 305, 727 48

Ho, I.-T., Kewley, L. J., Dopita, M. A., et al. 2014, Monthly Notices of the RAS, 444, 3894 67

Ho, I. T., Kudritzki, R.-P., Kewley, L. J., et al. 2015, Monthly Notices of the RAS, 448, 2030 13, 127, 131, 135

Ho, L. C., Li, Z.-Y., Barth, A. J., Seigar, M. S., & Peng, C. Y. 2011, Astrophysical Journal, Supplement, 197, 21 41, 44

Hollenbach, D. J., Chernoff, D. F., & McKee, C. F. 1989, in ESA Special Publication, Vol. 290, Infrared Spectroscopy in Astronomy, ed. E. Böhm-Vitense 148, 156, 162

Hollenbach, D. J. & Tielens, A. G. G. M. 1999, Reviews of Modern Physics, 71 2, 3, 148

Holt, J., Tadhunter, C. N., Morganti, R., & Emonts, B. H. C. 2011, Monthly Notices of the RAS, 410, 1527 57, 58

Hoopes, C. G., Heckman, T. M., Salim, S., et al. 2007, Astrophysical Journal, Supplement, 173, 441 10

Hoopes, C. G. & Walterbos, R. A. M. 2003, Astrophysical Journal, 586, 902 5, 108

Hopkins, P. F., Grudic, M. Y., Wetzel, A. R., et al. 2018, arXiv e-prints, arXiv:1811.12462 13

Hopkins, P. F., Hernquist, L., Cox, T. J., Robertson, B., & Krause, E. 2007, Astrophysical Journal, 669, 45 13

Hopkins, P. F., Quataert, E., & Murray, N. 2012, Monthly Notices of the RAS, 421, 3522 14

Hutchings, J. B., Crenshaw, D. M., Kaiser, M. E., et al. 1998, Astrophysical Journal, Letters, 492, L115 38

Imanishi, M., Nakanishi, K., & Izumi, T. 2016, Astronomical Journal, 152, 218 164

Ishibashi, W. & Fabian, A. C. 2012, Monthly Notices of the RAS, 427, 2998 18, 38

Ishibashi, W. & Fabian, A. C. 2014, Monthly Notices of the RAS, 441, 1474 18, 38

Ishibashi, W., Fabian, A. C., & Canning, R. E. A. 2013, Monthly Notices of the RAS, 431, 2350 18, 38

Israel, F. P. 1998, Astronomy and Astrophysics Reviews, 8, 237 70, 71

Israel, F. P., Güsten, R., Meijerink, R., Requena-Torres, M. A., & Stutzki, J. 2017, Astronomy and Astrophysics, 599, A53 71

Johansson, I. 1987, Astronomy and Astrophysics, 182, 179 93

Johansson, J., Thomas, D., & Maraston, C. 2012, Monthly Notices of the RAS, 421, 1908 31

Johnson, K. E. & Kobulnicky, H. A. 2003, Astrophysical Journal, 597, 923 94, 95

Johnson, K. E., Leitherer, C., Vacca, W. D., & Conti, P. S. 2000, Astronomical Journal, 120, 1273 94

Kaasinen, M., Kewley, L., Bian, F., et al. 2018, Monthly Notices of the RAS, 477, 5568 131, 133

Kakkad, D., Groves, B., Dopita, M., et al. 2018, Astronomy and Astrophysics, 618, A6 57

Kamenetzky, J., Rangwala, N., Glenn, J., Maloney, P. R., & Conley, A. 2016, Astrophysical Journal, 829, 93 153, 154

Kaplan, K. F., Jogee, S., Kewley, L., et al. 2016, Monthly Notices of the RAS, 462, 1642 131, 135

Karouzos, M., Woo, J.-H., & Bae, H.-J. 2016a, Astrophysical Journal, 819, 148 39

Karouzos, M., Woo, J.-H., & Bae, H.-J. 2016b, Astrophysical Journal, 833, 171 29, 39, 60

Kauffmann, G., Heckman, T. M., Tremonti, C., et al. 2003a, Monthly Notices of the RAS, 346, 1055 26, 31, 60

Kauffmann, G., Heckman, T. M., Tremonti, C., et al. 2003b, Monthly Notices of the RAS, 346, 1055 31, 105, 106, 111

Kauffmann, G., White, S. D. M., & Guiderdoni, B. 1993, Monthly Notices of the RAS, 264, 201 15

Kehrig, C., Vílchez, J. M., Telles, E., Cuisinier, F., & Pérez-Montero, E. 2006, Astronomy and Astrophysics, 457, 477 92

Kennicutt, Robert C., J. 1998, Annual Review of Astron and Astrophys, 36, 189 73

Kennicutt, R. C. & Evans, N. J. 2012, Annual Review of Astron and Astrophys, 50, 531 98

Kewley, L. J. & Dopita, M. A. 2002, Astrophysical Journal, Supplement, 142, 35 20, 21, 22, 23, 59, 92, 100, 127, 168

Kewley, L. J., Dopita, M. A., Sutherland, R. S., Heisler, C. A., & Trevena, J. 2001, Astrophysical Journal, 556, 121 26, 60, 106, 111

Kewley, L. J. & Ellison, S. L. 2008, Astrophysical Journal, 681, 1183 23, 59, 109, 170

Kewley, L. J., Groves, B., Kauffmann, G., & Heckman, T. 2006, Monthly Notices of the RAS, 372, 961 26, 27, 31, 60, 97, 105, 111

Kewley, L. J., Nicholls, D. C., & Sutherland, R. S. 2019, Annual Review of Astron and Astrophys, 57, 511 19, 111, 115

Kewley, L. J., Zahid, H. J., Geller, M. J., et al. 2015, Astrophysical Journal, Letters, 812, L20 131, 133

King, A. 2014, Space Science Reviews, 183, 427 70

King, A. R. 2010, Monthly Notices of the RAS, 402, 1516 14

Klessen, R. S. & Glover, S. C. O. 2016, Saas-Fee Advanced Course, 43, 85 1, 2, 3, 7

Kobulnicky, H. A., Dickey, J. M., Sargent, A. I., Hogg, D. E., & Conti, P. S. 1995a, Astronomical Journal, 110, 116 94

Kobulnicky, H. A., Dickey, J. M., Sargent, A. I., Hogg, D. E., & Conti, P. S. 1995b, Astronomical Journal, 110, 116 94, 97

Kobulnicky, H. A., Kennicutt, Robert C., J., & Pizagno, J. L. 1999, Astrophysical Journal, 514, 544 98

Kobulnicky, H. A. & Kewley, L. J. 2004, Astrophysical Journal, 617, 240 22, 24, 92, 130, 131

Komossa, S. & Schulz, H. 1997, Astronomy and Astrophysics, 323, 31 38

Korista, K., Ferland, G., & Baldwin, J. 1997, Astrophysical Journal, 487, 555 155

Kormendy, J., Bender, R., Magorrian, J., et al. 1997, Astrophysical Journal, Letters, 482, L139 13

Kormendy, J. & Ho, L. C. 2013, Annual Review of Astron and Astrophys, 51, 511 15

Kraemer, S. B., Schmitt, H. R., & Crenshaw, D. M. 2008, Astrophysical Journal, 679, 1128 70

Kraft, R. P., Hardcastle, M. J., Sivakoff, G. R., et al. 2008, Astrophysical Journal, Letters, 677, L97 40, 70

Kreckel, K., Faesi, C., Kruijssen, J. M. D., et al. 2018, Astrophysical Journal, Letters, 863, L21 33

Kreckel, K., Ho, I. T., Blanc, G. A., et al. 2019, arXiv e-prints, arXiv:1910.07190 112, 113, 115

Kristen, H., Jorsater, S., Lindblad, P. O., & Boksenberg, A. 1997, Astronomy and Astrophysics, 328, 483 48

Krühler, T., Kuncarayakti, H., Schady, P., et al. 2017, Astronomy and Astrophysics, 602, A85 101, 117

Kruijssen, J. M. D., Schruba, A., Chevance, M., et al. 2019, Nature, 569, 519 33

Lacerda, E. A. D., Cid Fernandes, R., Couto, G. S., et al. 2018, Monthly Notices of the RAS, 474, 3727 108, 133

Lampton, M., Margon, B., & Bowyer, S. 1976, Astrophysical Journal, 208, 177 157

Laor, A. 1998, Astrophysical Journal, Letters, 496, L71 70

Larson, R. B. 1974, Monthly Notices of the RAS, 169, 229 12

Law, D. R., Cherinka, B., Yan, R., et al. 2016, Astronomical Journal, 152, 83 105

Law, D. R., Steidel, C. C., Erb, D. K., et al. 2009, Astrophysical Journal, 697, 2057 33, 38

Law, D. R., Yan, R., Bershady, M. A., et al. 2015, Astronomical Journal, 150, 19 105

Lee, H.-H., Bettens, R. P. A., & Herbst, E. 1996, Astronomy and Astrophysics, Supplement, 119, 111 147

Lee, J. C., Gil de Paz, A., Tremonti, C., et al. 2009, Astrophysical Journal, 706, 599 73

Leitherer, C. 2005, in American Institute of Physics Conference Series, Vol. 783, The Evolution of Starbursts, ed. S. Hüttmeister, E. Manthey, D. Bomans, & K. Weis, 280–295 132

Leitherer, C., Schaerer, D., Goldader, J. D., et al. 1999, Astrophysical Journal, Supplement, 123, 3 110

Lejeune, T., Cuisinier, F., & Buser, R. 1997a, Astronomy and Astrophysics, Supplement, 125 110

Lejeune, T., Cuisinier, F., & Buser, R. 1997b, Astronomy and Astrophysics, Supplement, 125 155

Lena, D., Robinson, A., Storchi-Bergman, T., et al. 2015, Astrophysical Journal, 806, 84 43, 52

Lequeux, J., Peimbert, M., Rayo, J. F., Serrano, A., & Torres-Peimbert, S. 1979, Astronomy and Astrophysics, 500, 145 9, 122

Lester, D. F., Joy, M., Harvey, P. M., Ellis, Jr., H. B., & Parmar, P. S. 1987, Astrophysical Journal, 321, 755 42

Levesque, E. M., Kewley, L. J., & Larson, K. L. 2010, Astronomical Journal, 139, 712 111, 112, 113, 114, 122

Li, A. 2006, in 25

Lian, J., Thomas, D., Maraston, C., et al. 2018, Monthly Notices of the RAS, 476, 3883 10

Liang, Y. C., Yin, S. Y., Hammer, F., et al. 2006, Astrophysical Journal, 652, 257 59

Lilly, S. J., Carollo, C. M., Pipino, A., Renzini, A., & Peng, Y. 2013, Astrophysical Journal, 772, 119 91

Lindblad, P. O. 1999, Astronomy and Astrophysics Reviews, 9, 221 42, 48

Liu, C., Yuan, F., Ostriker, J. P., Gan, Z., & Yang, X. 2013, Monthly Notices of the RAS, 434, 1721 39

Lu, N., Zhao, Y., Díaz-Santos, T., et al. 2017, ArXiv e-prints 147

Luridiana, V., Morisset, C., & Shaw, R. A. 2015, Astronomy and Astrophysics, 573, A42 106, 115, 141

Ma, X., Hopkins, P. F., Faucher-Giguère, C.-A., et al. 2016, Monthly Notices of the RAS, 456, 2140 10

Macchetto, F., Capetti, A., Sparks, W. B., Axon, D. J., & Boksenberg, A. 1994, Astrophysical Journal, Letters, 435, L15 42

Madau, P. & Dickinson, M. 2014, Annual Review of Astron and Astrophys, 52, 415 16

Magorrian, J., Tremaine, S., Richstone, D., et al. 1998, Astronomical Journal, 115, 2285 13

Maio, U., Dolag, K., Ciardi, B., & Tornatore, L. 2007, Monthly Notices of the RAS, 379, 963 7, 8

Maiolino, R. & Mannucci, F. 2019, Astronomy and Astrophysics Reviews, 27, 3 1, 2, 9, 22, 91, 92, 130, 167

Maiolino, R., Nagao, T., Grazian, A., et al. 2008, Astronomy and Astrophysics, 488, 463 10, 130

Maiolino, R. & Rieke, G. H. 1995, Astrophysical Journal, 454, 95 39

Maiolino, R., Russell, H. R., Fabian, A. C., et al. 2017, Nature, 544, 202 19, 71, 75, 165

Mallery, R. P., Kewley, L., Rich, R. M., et al. 2007, Astrophysical Journal, Supplement, 173, 482 7, 69

Maloney, P. R., Hollenbach, D. J., & Tielens, A. G. G. M. 1999, Astrophysical Journal 3, 148

Mannucci, F., Cresci, G., Maiolino, R., Marconi, A., & Gnerucci, A. 2010, Monthly Notices of the RAS, 408, 2115 10, 11, 31, 100, 108

Marconi, A., Moorwood, A. F. M., Origlia, L., & Oliva, E. 1994, The Messenger, 78, 20 42

Marconi, A., Oliva, E., van der Werf, P. P., et al. 2000, Astronomy and Astrophysics, 357, 24 44, 65

Marino, R. A., Rosales-Ortega, F. F., Sánchez, S. F., et al. 2013, Astronomy and Astrophysics, 559, A114 22, 23

Markwardt, C. B. 2009, in Astronomical Society of the Pacific Conference Series, Vol. 411, Astronomical Data Analysis Software and Systems XVIII, ed. D. A. Bohlender, D. Durand, & P. Dowler, 251 47, 106

Marquart, T., Fathi, K., Östlin, G., et al. 2007, Astronomy and Astrophysics, 474, L9 94

Martin, P. & Roy, J.-R. 1995, Astrophysical Journal, 445, 161 130

Mashian, N., Sturm, E., Sternberg, A., et al. 2015, Astrophysical Journal, 802, 81 29, 30, 147

Mast, D., Rosales-Ortega, F. F., Sánchez, S. F., et al. 2014, Astronomy and Astrophysics, 561, A129 28

Mathis, J. S. 1982, Astrophysical Journal, 261, 195 20, 92

Mathis, J. S. 1985, Astrophysical Journal, 291, 247 20, 92

Mathis, J. S., Rumpl, W., & Nordsieck, K. H. 1977, Astrophysical Journal, 217, 425 110

Matt, G., Fabian, A. C., Guainazzi, M., et al. 2000, Monthly Notices of the RAS, 318, 173 42

Matteucci, F. & Francois, P. 1989, Monthly Notices of the RAS, 239, 885 12, 128

McConnell, N. J. & Ma, C.-P. 2013, Astrophysical Journal, 764, 184 13, 14

McElroy, R., Croom, S. M., Pracy, M., et al. 2015, Monthly Notices of the RAS, 446, 2186 29, 39, 60, 68, 70

McKee, C. F. & Ostriker, E. C. 1977, Astrophysical Journal, 218, 148 3, 155

McKee, C. F. & Ostriker, E. C. 2007, Annual Review of Astron and Astrophys, 45, 565 147, 158, 164, 171

McLeod, A. F., Dale, J. E., Ginsburg, A., et al. 2015, Monthly Notices of the RAS, 450, 1057 57

McQuinn, M. 2016, Annual Review of Astron and Astrophys, 54, 313 1

Meijerink, R., Kristensen, L. E., Weiß, A., et al. 2013, Astrophysical Journal, Letters, 762, L16 162

Meijerink, R., Spaans, M., & Israel, F. P. 2007, Astronomy and Astrophysics, 461, 793 164

Meijerink, R. & Spaans, M. S. 2005, Astronomy and Astrophysics158

Méndez, D. I., Esteban, C., Filipović, M. D., et al. 1999, Astronomy and Astrophysics, 349, 801 94

Minchev, I., Famaey, B., Combes, F., et al. 2011, Astronomy and Astrophysics, 527, A147 130

Minchev, I., Famaey, B., Quillen, A. C., et al. 2012, Astronomy and Astrophysics, 548, A126 130

Mingozzi, M., Belfiore, F., Cresci, G., et al. 2020, arXiv e-prints, arXiv:2002.05744 169

Mingozzi, M., Cresci, G., Venturi, G., et al. 2019, Astronomy and Astrophysics, 622, A146 92, 166, 167

Mingozzi, M., Vallini, L., Pozzi, F., et al. 2018, Monthly Notices of the RAS, 474, 3640 170

Molla, M., Ferrini, F., & Diaz, A. I. 1996, Astrophysical Journal, 466, 668 12, 128

Mollá, M., García-Vargas, M. L., & Bressan, A. 2009, Monthly Notices of the RAS, 398, 451 114

Monreal-Ibero, A., Arribas, S., & Colina, L. 2006, Astrophysical Journal, 637, 138 67

Monreal-Ibero, A., Arribas, S., Colina, L., et al. 2010, Astronomy and Astrophysics, 517, A28 67

Moorwood, A. F. M., Lutz, D., Oliva, E., et al. 1996, Astronomy and Astrophysics, 315, L109 42

Morganti, R. 2010, Publications of the Astron. Soc. of Australia, 27, 463 40, 50, 70

Morganti, R., Oosterloo, T., & Tsvetanov, Z. 1998, Astronomical Journal, 115, 915 42

Morganti, R., Robinson, A., Fosbury, R. A. E., et al. 1991, Monthly Notices of the RAS, 249, 91 71

Morisset, C., Delgado-Inglada, G., Sánchez, S. F., et al. 2016, Astronomy and Astrophysics, 594, A37 59, 117, 118, 119, 120

Mould, J. R., Ridgewell, A., Gallagher, John S., I., et al. 2000, Astrophysical Journal, 536, 266 71

Mukherjee, D., Bicknell, G. V., Wagner, A. e. Y., Sutherland, R. S., & Silk, J. 2018, Monthly Notices of the RAS, 479, 5544 18, 38

Mulchaey, J. S., Wilson, A. S., & Tsvetanov, Z. 1996, Astrophysical Journal, Supplement, 102, 309 149

Nagao, T., Maiolino, R., & Marconi, A. 2006, Astronomy and Astrophysics, 459, 85 24

Nakajima, K. & Ouchi, M. 2014, Monthly Notices of the RAS, 442, 900 11, 20, 59

Narayanan, D. & Krumholz, M. R. 2014, Monthly Notices of the Royal Astronomical Society, 442, 1411–1428 29, 30, 31, 148, 170

Nayakshin, S. & Zubovas, K. 2012, Monthly Notices of the RAS, 427, 372 18, 37

Nesvadba, N. 2018, in American Astronomical Society Meeting Abstracts, Vol. 231, American Astronomical Society Meeting Abstracts #231, 125.08 66

Netzer, H. 2015, Annual Review of Astron and Astrophys, 53, 365 38, 70

Nguyen, D. D., Seth, A. C., Reines, A. E., et al. 2014, Astrophysical Journal, 794, 34 93, 94

Nicholls, D. C., Dopita, M. A., Sutherland , R. S., Kewley, L. J., & Palay, E. 2013, Astrophysical Journal, Supplement, 207, 21 110

Nicholls, D. C., Sutherland, R. S., Dopita, M. A., Kewley, L. J., & Groves, B. A. 2017, Monthly Notices of the RAS, 466, 4403 23

O'Donnell, J. E. 1994, Astrophysical Journal, 422, 158 106

Oey, M. S., Meurer, G. R., Yelda, S., et al. 2007, Astrophysical Journal, 661, 801 5, 108

Oliva, E., Marconi, A., Maiolino, R., et al. 2001, Astronomy and Astrophysics, 369, L5 75

Oliva, E., Salvati, M., Moorwood, A. F. M., & Marconi, A. 1994, Astronomy and Astrophysics, 288, 457 42

Oosterloo, T., Raymond Oonk, J. B., Morganti, R., et al. 2017, Astronomy and Astrophysics, 608, A38 42

Oosterloo, T. A. & Morganti, R. 2005, Astronomy and Astrophysics, 429, 469 71

Osterbrock, D. E. 1989, Astrophysics of gaseous nebulae and active galactic nuclei 97, 109

Osterbrock, D. E. & Ferland, G. J. 2006, Astrophysics of gaseous nebulae and active galactic nuclei 21, 26, 54, 66, 70, 79, 106, 169

Pagel, B. E. J., Edmunds, M. G., Blackwell, D. E., Chun, M. S., & Smith, G. 1979, Monthly Notices of the RAS, 189, 95 22, 23, 91, 117

Papadopoulos, P. P. 2010, Astrophysical Journal, 720, 226 158

Papadopoulos, P. P., van der Werf, P. P., Xilouris, E. M., et al. 2012, Monthly Notices of the RAS, 426, 2601 3, 31, 164

Papadopoulos, P. P., Zhang, Z.-Y., Xilouris, E. M., et al. 2014, Astrophysical Journal, 788, 153 171

Pauldrach, A. W. A., Hoffmann, T. L., & Lennon, M. 2001, Astronomy and Astrophysics, 375, 161 112

Peimbert, M. & Costero, R. 1969, Boletin de los Observatorios Tonantzintla y Tacubaya, 5, 3 22

Peimbert, M., Peimbert, A., & Delgado-Inglada, G. 2017, Publications of the ASP, 129, 082001 22

Pellegrini, E. W., Rahner, D., Reissl, S., et al. 2019, arXiv e-prints, arXiv:1909.09651 133, 140

Pereira-Santaella, M., Colina, L., García-Burillo, S., et al. 2016, Astronomy and Astrophysics, 594, A81 18

Pereira-Santaella, M., Spinoglio, L., van der Werf, P. P., & Piqueras López, J. 2014, Astronomy and Astrophysics, 566, A49 147, 160, 161, 170

Pérez-Beaupuits, J. P., Spoon, H. W. W., Spaans, M., & Smith, J. D. 2011, Astronomy and Astrophysics, 533, A56 44

Pérez-Montero, E. 2014, Monthly Notices of the RAS, 441, 2663 10, 24, 91, 112, 113, 114, 140

Pérez-Montero, E. 2017, Publications of the ASP, 129, 043001 21, 22, 24

Pérez-Montero, E. & Díaz, A. I. 2005, Monthly Notices of the RAS, 361, 1063 20, 140

Pérez-Montero, E. & Vílchez, J. M. 2009, Monthly Notices of the RAS, 400, 1721 24

Perna, M., Brusa, M., Salvato, M., et al. 2015, Astronomy and Astrophysics, 583, A72 39

Perna, M., Cresci, G., Brusa, M., et al. 2019, Astronomy and Astrophysics, 623, A171 66

Perna, M., Lanzuisi, G., Brusa, M., Cresci, G., & Mignoli, M. 2017, Astronomy and Astrophysics, 606, A96 54, 58, 66, 68, 70

Pettini, M. & Pagel, B. E. J. 2004, Monthly Notices of the RAS, 348, L59 12, 22, 23, 91, 101, 131

Piconcelli, E., Jimenez-Bailón, E., Guainazzi, M., et al. 2005, Astronomy and Astrophysics, 432, 15 150

Pilkington, K., Few, C. G., Gibson, B. K., et al. 2012, Astronomy and Astrophysics, 540, A56 13, 128

Pillepich, A., Springel, V., Nelson, D., et al. 2018, Monthly Notices of the RAS, 473, 4077 17

Pilyugin, L. S. & Mattsson, L. 2011, Monthly Notices of the RAS, 412, 1145 23

Pilyugin, L. S. & Thuan, T. X. 2005, Astrophysical Journal, 631, 231 22, 23

Pilyugin, L. S., Vílchez, J. M., Mattsson, L., & Thuan, T. X. 2012, Monthly Notices of the RAS, 421, 1624 22, 23

Poetrodjojo, H., Groves, B., Kewley, L. J., et al. 2018, Monthly Notices of the RAS, 479, 5235 11, 130, 131, 135

Poggianti, B. M., Moretti, A., Gullieuszik, M., et al. 2017, Astrophysical Journal, 844, 48 33

Pon, A., Johnstone, D., & Kaufman, M. J. 2012, Astrophysical Journal, 748, 25 156

Pozzi, F., Vallini, L., Vignali, C., et al. 2017, Monthly Notices of the RAS147, 162, 163, 170

Prantzos, N. & Boissier, S. 2000, Monthly Notices of the RAS, 313, 338 13, 128

Privon, G. C., Aalto, S., Falstad, N., et al. 2017, Astrophysical Journal, 835, 213 18

Rahner, D., Pellegrini, E. W., Glover, S. C. O., & Klessen, R. S. 2017, Monthly Notices of the RAS, 470, 4453 140

Ranalli, P., Comastri, A., & Setti, G. 2003, Astronomy and Astrophysics, 399, 39 149

Read, J. I. & Trentham, N. 2005, Philosophical Transactions of the Royal Society of London Series A, 363, 2693 15

Reddy, N. A., Erb, D. K., Pettini, M., Steidel, C. C., & Shapley, A. E. 2010, Astrophysical Journal, 712, 1070 137

Rees, M. J. 1989, Monthly Notices of the RAS, 239, 1P 18, 37

Reines, A. E., Sivakoff, G. R., Johnson, K. E., & Brogan, C. L. 2011, Nature, 470, 66 93, 94, 99

Ricci, C., Bauer, F. E., Treister, E., et al. 2017, ArXiv e-prints 150

Rich, J. A., Kewley, L. J., & Dopita, M. A. 2011, Astrophysical Journal, 734, 87 67

Rich, J. A., Kewley, L. J., & Dopita, M. A. 2015, Astrophysical Journal, Supplement, 221, 28 67

Riffel, R., Rodríguez-Ardila, A., & Pastoriza, M. G. 2006, Astronomy and Astrophysics, 457, 61 149

Riffel, R. A., Storchi-Bergmann, T., & Winge, C. 2013, Monthly Notices of the RAS, 430, 2249 39

Risaliti, G., Maiolino, R., & Salvati, M. 1999, Astrophysical Journal, 522, 157 39

Rodríguez del Pino, B., Arribas, S., Piqueras López, J., Villar-Martín, M., & Colina, L. 2019, Monthly Notices of the RAS, 486, 344 75

Rosa, D. A., Dors, O. L., Krabbe, A. C., et al. 2014, Monthly Notices of the RAS, 444, 2005 10, 91

Rosenberg, M. J. F., van der Werf, P. P., Aalto, S., et al. 2015, Astrophysical Journal, 801, 72 147, 153, 154, 160, 170

Roy, J. R. & Walsh, J. R. 1997, Monthly Notices of the RAS, 288, 715 130

Salim, S., Rich, R. M., Charlot, S., et al. 2007, Astrophysical Journal, Supplement, 173, 267 31

Sánchez, S. F., Avila-Reese, V., Hernandez-Toledo, H., et al. 2018, Revista Mexicana de Astronomia y Astrofisica, 54, 217 107, 141

Sánchez, S. F., Kennicutt, R. C., Gil de Paz, A., et al. 2012, Astronomy and Astrophysics, 538, A8 13, 34, 38

Sánchez, S. F., Pérez, E., Sánchez-Blázquez, P., et al. 2016, Revista Mexicana de Astronomia y Astrofisica, 52, 171 107, 141

Sánchez, S. F., Rosales-Ortega, F. F., Iglesias-Páramo, J., et al. 2014, Astronomy and Astrophysics, 563, A49 13, 108, 127, 128, 167

Sánchez Almeida, J., Morales-Luis, A. B., Muñoz-Tuñón, C., et al. 2014, Astrophysical Journal, 783, 45 100

Sánchez-Blázquez, P., Peletier, R. F., Jiménez-Vicente, J., et al. 2006, Monthly Notices of the RAS, 371, 703 96, 106

Sánchez-Menguiano, L., Sánchez, S. F., Pérez, I., et al. 2016, Astronomy and Astrophysics, 587, A70 13, 128

Sanders, D. B., Mazzarella, J. M., Kim, D.-C., Surace, J. A., & Soifer, B. T. 2003, Astronomical Journal, 126, 1607 149

Sanders, D. B. & Mirabel, I. F. 1996, Annual Review of Astron and Astrophys, 34, 749 30

Sanders, R. L., Shapley, A. E., Zhang, K., & Yan, R. 2017, Astrophysical Journal, 850, 136 5, 108

Santoro, F., Oonk, J. B. R., Morganti, R., & Oosterloo, T. 2015a, Astronomy and Astrophysics, 574, A89 71

Santoro, F., Oonk, J. B. R., Morganti, R., Oosterloo, T. A., & Tadhunter, C. 2016, Astronomy and Astrophysics, 590, A37 71

Santoro, F., Oonk, J. B. R., Morganti, R., Oosterloo, T. A., & Tremblay, G. 2015b, Astronomy and Astrophysics, 575, L4 71

Sauvage, M., Thuan, T. X., & Lagage, P. O. 1997, Astronomy and Astrophysics, 325, 98 93

Schaefer, A. L., Tremont, C., Belfiore, F., et al. 2019, arXiv e-prints, arXiv:1911.00581 140

Schaerer, D., Contini, T., & Pindao, M. 1999, Astronomy and Astrophysics, Supplement, 136, 35 93

Schaller, G., Schaerer, D., Meynet, G., & Maeder, A. 1992, Astronomy and Astrophysics, Supplement, 96, 269 112

Schechter, P. 1976, Astrophysical Journal, 203, 297 15

Schlegel, D. J., Finkbeiner, D. P., & Davis, M. 1998, Astrophysical Journal, 500, 525 106

Schleicher, D. R. G., Spaans, M., & Klessen, R. S. 2010, Astronomy and Astrophysics, 513, A7 148

Schmitt, H. R., Storchi-Bergmann, T., & Baldwin, J. A. 1994, Astrophysical Journal, 423, 237 18, 44

Schmutz, W., Leitherer, C., & Gruenwald, R. 1992a, Publications of the ASP, 104, 1164 110

Schmutz, W., Leitherer, C., & Gruenwald, R. 1992b, Publications of the ASP, 104, 1164 155

Scoville, N. Z., Matthews, K., Carico, D. P., & Sanders, D. B. 1988, Astrophysical Journal, Letters, 327, L61 42

Shankar, F., Weinberg, D. H., & Miralda-Escudé, J. 2009, Astrophysical Journal, 690, 20 16

Sharp, R. G. & Bland-Hawthorn, J. 2010, Astrophysical Journal, 711, 818 29, 38, 42, 48

Sharples, R., Bender, R., Bennett, R., et al. 2006, New Astronomy Review, 50, 370 34

Shlosman, I. 1996, Dynamics of Inner Galactic Disks: The Striking Case of M 100, ed. A. Sandqvist & P. O. Lindblad, Vol. 474, 141 48

Silk, J. 2013, Astrophysical Journal, 772, 112 18, 38, 44, 165

Silk, J. & Rees, M. J. 1998, Astronomy and Astrophysics, 331, L1 13, 14, 37, 165

Simpson, C., Wilson, A. S., Bower, G., et al. 1997, Astrophysical Journal, 474, 121 18, 44

Singh, R., van de Ven, G., Jahnke, K., et al. 2013, Astronomy and Astrophysics, 558, A43 60

Smee, S. A., Gunn, J. E., Uomoto, A., et al. 2013, Astronomical Journal, 146, 32 105

Smith, M. D. & Mac Low, M.-M. 1997, Astronomy and Astrophysics, 326, 801 156

Solomon, P. M., Downes, D., Radford, S. J. E., & Barrett, J. W. 1997, Astrophysical Journal 158

Springel, V., Di Matteo, T., & Hernquist, L. 2005, Monthly Notices of the RAS, 361, 776 15

Stasińska, G. 2004, in Cosmochemistry. The melting pot of the elements, ed. C. Esteban, R. García López, A. Herrero, & F. Sánchez, 115–170 22

Stasińska, G. 2005, Astronomy and Astrophysics, 434, 507 22

Stasińska, G. 2006, Astronomy and Astrophysics, 454, L127 23, 112, 113

Stasińska, G., Vale Asari, N., Cid Fernandes, R., et al. 2008, Monthly Notices of the RAS, 391, L29 27, 108

Storchi-Bergmann, T. & Bonatto, C. J. 1991, Monthly Notices of the RAS, 250, 138 47

Storchi-Bergmann, T., Calzetti, D., & Kinney, A. L. 1994, Astrophysical Journal, 429, 572 23

Storchi-Bergmann, T., Lopes, R. D. S., McGregor, P. J., et al. 2010, Monthly Notices of the RAS, 402, 819 38

Storchi-Bergmann, T., Wilson, A. S., & Baldwin, J. A. 1992, Astrophysical Journal, 396, 45 38

Storey, P. J. & Zeippen, C. J. 2000, Monthly Notices of the RAS, 312, 813 45

Stott, J. P., Swinbank, A. M., Johnson, H. L., et al. 2016, Monthly Notices of the RAS, 457, 1888 38

Sun, A.-L., Greene, J. E., & Zakamska, N. L. 2017, Astrophysical Journal, 835, 222 38

Sun, A.-L., Greene, J. E., Zakamska, N. L., et al. 2018, Monthly Notices of the RAS, 480, 2302 38

Tadhunter, C., Morganti, R., Rose, M., Oonk, J. B. R., & Oosterloo, T. 2014, Nature, 511, 440 42

Thomas, A. D., Dopita, M. A., Kewley, L. J., et al. 2018, Astrophysical Journal, 856, 89 167

Thronson, Jr., H. A., Hereld, M., Majewski, S., et al. 1989, Astrophysical Journal, 343, 158 42

Tommasin, S., Spinoglio, L., Malkan, M. A., & Fazio, G. 2010, Astrophysical Journal, 709, 1257 149

Trager, S. C., Faber, S. M., Worthey, G., & González, J. J. 2000, Astronomical Journal, 120, 165 10

Tremonti, C. A., Heckman, T. M., Kauffmann, G., et al. 2004, Astrophysical Journal, 613, 898 9, 10, 22, 31, 100, 104, 122, 128

Trippe, M. L., Crenshaw, D. M., Deo, R., & Dietrich, M. 2008, Astronomical Journal, 135, 2048 43

Tully, R. B., Courtois, H. M., Dolphin, A. E., et al. 2013, Astronomical Journal, 146, 86 93

Turner, O. J., Cirasuolo, M., Harrison, C. M., et al. 2017, Monthly Notices of the RAS, 471, 1280 38

Ueda, J., Iono, D., Yun, M. S., et al. 2014, Astrophysical Journal, Supplement, 214, 1 153, 154

Vacca, W. D. & Conti, P. S. 1992, Astrophysical Journal, 401, 543 93

Vale Asari, N., Couto, G. S., Cid Fernandes, R., et al. 2019, arXiv e-prints, arXiv:1907.08635 4, 108

Vallini, L., Tielens, A. G. G. M., Pallottini, A., et al. 2019, Monthly Notices of the RAS, 490, 4502 171

van der Tak, F. F. S., Black, J. H., Schöier, F. L., Jansen, D. J., & van Dishoeck, E. F. 2007, Astronomy and Astrophysics, 468, 627 161

van der Werf, P. P., Isaak, K. G., Meijerink, R., et al. 2010, Astronomy and Astrophysics, 518, L42 162

van Dishoeck, E. F. & Black, J. H. 1988, Astrophysical Journal, 334, 771 148, 157

Vanzi, L., Combes, F., Rubio, M., & Kunth, D. 2009, Astronomy and Astrophysics, 496, 677 94

Vanzi, L. & Rieke, G. H. 1997, Astrophysical Journal, 479, 694 93

Vanzi, L. & Sauvage, M. 2006, Astronomy and Astrophysics, 448, 471 98

Vaona, L., Ciroi, S., Di Mille, F., et al. 2012, Monthly Notices of the RAS, 427, 1266 38

Vardoulaki, E., Charmandaris, V., Murphy, E. J., et al. 2015, Astronomy and Astrophysics, 574, A4 149

Vazdekis, A., Ricciardelli, E., Cenarro, A. J., et al. 2012, Monthly Notices of the RAS, 424, 157 141

Vazdekis, A., Sánchez-Blázquez, P., Falcón-Barroso, J., et al. 2010, Monthly Notices of the RAS, 404, 1639 45

Vázquez, G. A. & Leitherer, C. 2005, Astrophysical Journal, 621, 695 112

Veilleux, S. & Bland-Hawthorn, J. 1997, Astrophysical Journal, Letters, 479, L105 42

Veilleux, S. & Osterbrock, D. E. 1987, Astrophysical Journal, Supplement, 63, 295 26, 105, 166

Veilleux, S., Shopbell, P. L., & Miller, S. T. 2001, Astronomical Journal, 121, 198 44

Veilleux, S., Shopbell, P. L., Rupke, D. S., Bland -Hawthorn, J., & Cecil, G. 2003, Astronomical Journal, 126, 2185 47

Venturi, G., Marconi, A., Mingozzi, M., et al. 2017, Frontiers in Astronomy and Space Sciences, 4, 46 39, 44, 53, 166

Venturi, G., Nardini, E., Marconi, A., et al. 2018, A&A, 619, A74 38, 39, 42, 47, 48, 49, 50, 52, 57, 166

Vernet, J., Dekker, H., D'Odorico, S., et al. 2011, Astronomy and Astrophysics, 536, A105 75

Vilchez, J. M. & Esteban, C. 1996, Monthly Notices of the RAS, 280, 720 59, 100, 130

Villar Martín, M., Bellocchi, E., Stern, J., et al. 2015, Monthly Notices of the RAS, 454, 439 57, 58

Villar Martín, M., Emonts, B., Humphrey, A., Cabrera Lavers, A., & Binette, L. 2014, Monthly Notices of the RAS, 440, 3202 57, 58, 66

Wake, D. A., Bundy, K., Diamond-Stanic, A. M., et al. 2017, Astronomical Journal, 154, 86 105

Walter, F., Bolatto, A. D., Leroy, A. K., et al. 2017, Astrophysical Journal, 835, 265 18

Ward, M., Penston, M. V., Blades, J. C., & Turtle, A. J. 1980, Monthly Notices of the RAS, 193, 563 43

Weiss, A., Downes, D., Walter, F., & Henkel, C. 2007, in Astronomical Society of the Pacific Conference Series, Vol. 375, From Z-Machines to ALMA: (Sub)Millimeter Spectroscopy of Galaxies, ed. A. J. Baker, J. Glenn, A. I. Harris, J. G. Mangum, & M. S. Yun, 25 147

Weller, J., Ostriker, J. P., Bode, P., & Shaw, L. 2005, Monthly Notices of the RAS, 364, 823 15

Westfall, K. B., Cappellari, M., Bershady, M. A., et al. 2019, arXiv e-prints, arXiv:1901.00856 105

Westmoquette, M. S., Clements, D. L., Bendo, G. J., & Khan, S. A. 2012, Monthly Notices of the RAS, 424, 416 60

Westmoquette, M. S., Dale, J. E., Ercolano, B., & Smith, L. J. 2013, Monthly Notices of the RAS, 435, 30 57

Westmoquette, M. S., Smith, L. J., & Gallagher, III, J. S. 2011, Monthly Notices of the RAS, 414, 3719 57

Whitmore, B. C., Chandar, R., Kim, H., et al. 2011, Astrophysical Journal, 729, 78 114

Wisnioski, E., Förster Schreiber, N. M., Wuyts, S., et al. 2015, Astrophysical Journal, 799, 209 38

Wootten, A. & Thompson, A. R. 2009, IEEE Proceedings, 97, 1463 33

Wylezalek, D., Zakamska, N. L., Greene, J. E., et al. 2018, Monthly Notices of the RAS, 474, 1499 108

Xu, C. K., Cao, C., Lu, N., et al. 2015, Astrophysical Journal, 799, 11 147

Xu, C. K., Cao, C., Lu, N., et al. 2014, Astrophysical Journal, 787, 48 147, 152

Yan, R., Bundy, K., Law, D. R., et al. 2016, Astronomical Journal, 152, 197 105

York, D. G., Adelman, J., Anderson, Jr., J. E., et al. 2000, Astronomical Journal, 120, 1579 9

Zahid, H. J., Bresolin, F., Kewley, L. J., Coil, A. L., & Davé, R. 2012, Astrophysical Journal, 750, 120 9

Zahid, H. J., Yates, R. M., Kewley, L. J., & Kudritzki, R. P. 2013, Astrophysical Journal, 763, 92 137

Zhang, K., Yan, R., Bundy, K., et al. 2017, Monthly Notices of the RAS, 466, 3217 5, 108

Zhao, Y., Lu, N., Xu, C. K., et al. 2016, Astrophysical Journal, 820, 118 147

Zinchenko, I. A., Pilyugin, L. S., Grebel, E. K., Sánchez, S. F., & Vílchez, J. M. 2016, Monthly Notices of the RAS, 462, 2715 12, 130

Zubko, V., Dwek, E., & Arendt, R. G. 2004, Astrophysical Journal, Supplement, 152, 211 155

Zubovas, K. & King, A. 2016, Monthly Notices of the RAS, 462, 4055 18, 37

Zubovas, K. & King, A. R. 2014, Monthly Notices of the RAS, 439, 400 18, 38

Zubovas, K., Nayakshin, S., Sazonov, S., & Sunyaev, R. 2013, Monthly Notices of the RAS, 431, 793 18, 38